Modelling non-alcoholic fatty liver disease (NAFLD) using human induced pluripotent stem cell (hiPSC)-derived hepatocytes

Submitted by

Peggy Cho Kiu Lo

MSc, BSc

School of Medicine
Division of Cancer and Stem Cells
The University of Nottingham

Principal supervisor: Dr Nicholas R. F. Hannan
Secondary supervisor: Professor Guruprasad Aithal

April 2021

Thesis submitted to The University of Nottingham for the Degree of Doctor in Philosophy

Acknowledgements

First of all, I would like to thank my principal supervisor Dr Nicholas R.F. Hannan, for his support and guidance throughout my PhD journey. He is absolutely the best supervisor anyone could ask for and I am so grateful to be one of his students. I also thank my secondary supervisor Professor Guruprasad P. Aithal, as well as our collaborators Dr Jane I. Grove and Professor Andrew M. Salter for giving their scientific knowledge and clinical samples, making it possible for us to complete this project.

This work was the product of the combined efforts of many extraordinary scientists. I would like to therefore acknowledge Dr Dong-Hyun Kim, Mr Salah Abdelrazig, Dr Laudina Safo and Dr Thais Fedatto Abelha for their help in metabolomics work and data analysis. I thank Dr Andrew Bennett, Ms Monika Owen, Ms Nicola De Vivo from the FRAME Alternatives Laboratory for teaching me how to prepare fatty acid complex. I would also like to thank Ms Katarzyna Lis-Slimak for all the help in high-content Operetta imaging. Our former laboratory managers Ms Maria Barbadillo-Munoz and Mr Jayson Bispham for their technical support and managing the labs. I would also like to specially thank Ms Caroline Reffin, Ms Paula Olsen and Ms Penny Howick for their kindness and warmth, they have always been very helpful to students. Professor Chris Denning for giving his extensive scientific knowledge and care for the whole stem cell department.

A big thank you to all my colleagues, members of Hannan lab, Denning lab, Ruzov lab, Thompson lab and Sottile lab. Especially Jamie B., Paulina, Emma, Analy, Sara B., Maria E., Sara PG., Diogo, Smithy, Liz, Jordan, Liam, Paige, all the past and present members in the department of Stem Cells. You guys have made my PhD journey very enjoyable and I have learnt so much from every single one of you, thank you once again!

A special thanks to my Superbrain team, Elisa, Francesca, Yousuf, Nick and Zeeny, you guys have made me a better person and thank you for teaching me so many valuable lessons in life, I am super grateful.

Finally, I would like to thank my family, especially my mum and my late uncle. Thank you for always believing in me, supporting, and encouraging me. Distance can't keep us apart. 媽媽，大舅舅，和我的家人們，我很感激你們一直以來對我的愛護。謝謝你們，是你們成就了我。我愛你們，也希望你們感到幸福快樂。

The year of 2020 with the COVID-19 pandemic hasn't been the easiest year for everyone, but it has definitely brought out the best in many people. I have met a lot of wonderful people who have shown compassion, kindness, empathy and offering a helping hand to others during this extraordinary time. I wish you all well and healthy, god bless you!

Declaration

I hereby declare that this thesis has been composed by myself and has not been submitted for any other degree previously. Acknowledgements of specific procedures not performed by myself are stated; otherwise, the work described is my own.

Signature:



Peggy Cho Kiu Lo

Date:

22nd April 2021

Abstract

Non-alcoholic fatty liver disease (NAFLD) refers to a spectrum of disorders caused by accumulation of excess dietary lipids within the liver. NAFLD is the fastest growing chronic liver disease and without intervention can progress to liver cancer and liver failure. Poor prognosis and limited therapeutic options for patients is hindered by the absence of robust, human specific platforms for modelling NAFLD. We have access to a large three-generation family patient cohort that display a high rate of cirrhosis and hepatocellular carcinoma. The family have full range of manifestations of NAFLD and therefore represent a unique and ideal opportunity to investigate the pathogenesis of NAFLD. Whole exome sequencing of affected individuals has identified a rare, novel missense variant in microsomal triglyceride transfer protein (*MTTP*, 4q23). To address this need we have created an *in vitro* human model of NAFLD using hiPSCs derived from patients inherited NAFLD with *MTTP*-p.I564T single nucleotide variation. In this study, we have improved our differentiation protocol to differentiate hiPSCs into HLCs that are more similar to primary human hepatocytes than foetal hepatocytes. We demonstrated higher expression of cytochrome P450 enzymes as well as many genes involved in a broad range of metabolic processes including lipid biosynthesis and metabolism via transcriptomic analysis. We have then applied this more advanced platform to model NAFLD by inducing lipid accumulation in $MTTP^{WT/WT}$ and $MTTP^{VAR/VAR}$ hepatocytes using palmitic acid (PA). PA replicates a western high fat diet, we observed both control and $MTTP^{VAR/VAR}$ -HLCs demonstrate key features of hepatic steatosis such as intracellular accumulation of lipid droplets within the cytoplasmic space, as well as reduction of apolipoprotein B (apoB) secretion. $MTTP^{VAR/VAR}$ -HLCs when compared to healthy hepatocytes treated with PA show unique differences in their inflammatory and fibrotic gene expression profiles. We also detected significant reduction of eNOS phosphorylation in $MTTP^{MUT/MUT}$-HLCs compared to healthy cell line, this may represent biomarkers for people with genetic predisposition to NAFLD, as well as novel interventions for familial-*MTTP*-p.I564T NAFLD patient. Finally, we also observe significant demand in metabolic profiles and mitochondrial functionality in $MTTP^{VAR/VAR}$ -HLCs overall, however, PA-treated condition in both wildtype and $MTTP^{VAR/VAR}$-HLCs is associated with

decreased mitochondrial maximal respiration. These findings may represent new mechanisms that drive the spectrum of clinical observations in the pathogenesis of NAFLD with *MTTP*-p.I564T genetic influence. Our study demonstrates the potential of hiPSC-HLCs to provide mechanistic insight and discovery of novel biomarkers and drug targets for NAFLD.

Table of Contents

ACKNOWLEDGEMENTS ..... **II**

DECLARATION ..... **III**

ABSTRACT ..... **IV**

TABLE OF CONTENTS ..... **VI**

LIST OF FIGURES ..... **X**

LIST OF TABLES ..... **XIII**

ABBREVIATIONS ..... **XIV**

CHAPTER 1. GENERAL INTRODUCTION 20

1.1 Thesis Rationale & Objectives *20*

1.2 The liver *23*

1.2.1 Anatomy and functions of the liver 23

1.2.2 Lipid metabolism 26

1.3 Non-Alcoholic Fatty Liver Disease (NAFLD) *29*

1.3.1 Pathology and clinical diagnosis of NAFLD 29

1.3.2 Epidemiology and economic impact of NAFLD 30

1.3.3 Hepatic pathogenesis of NAFLD 31

Role of lipotoxicity in the pathogenesis of NAFLD/ NASH 32

1.3.4 Genetic predisposition influences on lipid metabolism and NAFLD 36

Potential implication of novel MTTP-p.I564T single nucleotide variation in NAFLD progression 38

1.4 Disease models for NAFLD *43*

1.5 Hypothesis and aims *47*

CHAPTER 2. MATERIALS AND METHODS 49

2.1 Cell culture *49*

2.1.1 Media 49

2.1.2 Isolation and derivation of human fibroblasts from human dermal tissue 52

2.1.3 Generation of hiPSC in feeder-free condition 53

2.1.4 Colony isolation using EDTA or ReLeSR 54

2.1.5 Human induced pluripotent stem cell (hiPSC) culture and maintenance 55

2.1.6 Differentiation of hiPSCs 55

Formation of mesodermal and ectodermal progenitor cells 55

Formation of definitive endoderm, foregut, hepatic endoderm, and hepatocyte-like cells (HLCs) . 56

Optimisation of hepatocyte maturation using small molecules 57

Formation of hindgut and intestinal organoids 57

2.1.7 Fatty acid (FA) preparation and treatment 58

Preparation of 24% (w/v) fatty-acid-free bovine serum albumin (BSA) for fatty acid binding 58

Preparation of 10mM BSA-conjugated palmitic acid stock solution 59
FA treatment to hiPSC-HLCs or hiPSC-IOs 59
2.2 CRISPR/Cas9 knockout (KO) strategy for gene editing 59
2.2.1 CRISPR/Cas9 guide RNA (gRNA) and targeting construct 59
2.2.2 Transformation and plasmid DNA preparation 60
2.2.3 Transfection of hiPSCs and antibiotic selection 60
2.2.4 DNA extraction from cultured mammalian cells 62
2.2.5 Polymerase chain reaction (PCR) genotyping, gel electrophoresis and purification 62
2.3 Molecular biology 63
2.3.1 RNA extraction and cDNA synthesis 63
2.3.2 Real-time quantitative polymerase chain reaction (qPCR) 64
2.3.3 Allele- specific PCR (ASPCR), restriction digestion and band densitometry 66
2.3.4 Karyotype assessment of hiPSCs 67
2.3.5 Immunocytochemistry (ICC) and Image acquisition 67
2.4 Lipid detection and quantification 69
2.4.1 Oil Red O (ORO) staining 69
2.4.2 Nile Red Assay 69
2.5 Lipoprotein separation via ultracentrifugation 70
2.6 Measurement of ApoB-100 levels by sandwich ELISA 70
2.7 Detection and Quantification of mitochondrial content and Reactive Oxygen Species (ROS) in live cells 71
2.8 Measurement of mitochondrial respiration using Seahorse analyser 72
2.9 Transcriptomic analysis 73
2.9.1 rRNA removal and mRNA library preparation 73
2.9.2 mRNA sequencing and bioinformatics data analysis 73
2.10 Proteome profiler antibody array analysis 74
2.11 Metabolomic analysis 75
2.11.1 Metabolite extraction 75
2.11.2 Mass spectrometry, metabolites identification and data interpretation 75
2.12 Statistical analysis 76
CHAPTER 3. GENERATION AND CHARACTERISATION OF HIPSCS FROM DONOR-DERIVED DERMAL FIBROBLASTS . 78
3.1 Introduction 78
3.1.1 Implication of rare MTTP-p.I564T in NAFLD pathophysiology 78
3.1.2 HiPSC reprogramming strategies 79
3.1.3 Genetic manipulations of patient-derived hiPSCs 82
3.2 Chapter aims and objectives 82
3.3 Results 83
3.3.1 Derivation of human dermal fibroblasts from skin punch biopsy 83
3.3.2 HiPSC reprogramming using Sendai-virus based vectors 85
3.3.3 Characterisation of reprogrammed hiPSC lines 87

Chromosome analysis 87
Stable pluripotency throughout cell culture media transition 87
Assessment of pluripotency markers and trilineage differentiation 91
Validation of pre-existing MTTP SNVs remain intact post-reprogramming 94
3.3.4 Using CRISPR/Cas9 approach to create MTTP knockout hiPSCs as a NAFLD positive control 96
Determination and optimisation of transfection agent for high efficiency CRISPR/Cas9 targeting . 96
Determination of optimal dosage for colony antibiotic selection 99
MTTP KO in LOPCK hiPSCs using CRISPR/Cas9 technology and genotypic characterisation of targeted clones 100
Genotypic characterisation of targeted clones using PCR 101
3.4 Discussion 105
CHAPTER 4. DEVELOPMENT AND OPTIMISATION OF DIFFERENTIATION METHOD TOWARDS HEPATOCYTE FATE 112
4.1 Introduction 112
4.1.1 Manipulation of cell signalling using culture media and supplements 112
4.1.2 2D vs 3D culture system 114
4.2 Chapter Aims and Objectives 115
4.3 Results 117
4.3.1 48 hours induction is sufficient to generate anterior foregut (FG) endoderm population .. 117
4.3.2 Cell line optimisation 119
Seeding density 119
BMP4 concentration is cell-line specific during hepatic specification stage 121
4.3.3 Explore the use of small molecule-based directed hepatic differentiation approach 123
Small molecule candidates screening for the optimisation of hepatic differentiation 123
Hepatic differentiation efficiency comparison using small molecule cocktail and recombinant growth factors 126
4.3.4 New developed platform produces HLCs with a relatively more mature phenotype compared to old differentiation approach 128
Cell morphology 128
Protein expression profile 129
Gene expression profile 129
mRNA sequencing – Correlation tree 134
mRNA sequencing – Multi-dimensional analysis 136
mRNA sequencing – Gene expression distribution 137
mRNA sequencing – Liver-related genes 139
Metabolomic profiling for Old and New maturation media culture 141
4.4 Discussion 144
CHAPTER 5. VALIDATION AND PHENOTYPING OF HIPSC-HLCS AS NAFLD DISEASE MODEL 154
5.1 Introduction 154
5.2 Chapter aims and objectives 156
5.3 Results 157
5.3.1 In vitro screening of fatty acid candidates for steatosis induction 157

Simulation of Western diet using fatty acid (FA) cocktail in vitro 157
Potential beneficial effects of oleic acid (OA) in hepatocyte maturation 158
Palmitic acid (PA) is the ideal fatty acid candidate to simulate hepatic steatosis 159
5.3.2 Phenotype validation of LOPCK ($MTTP^{WT/WT}$) and MOPIK ($MTTP^{VAR/VAR}$) as NAFLD disease models 165
LOPCK and MOPIK HLCs expressed liver-related proteins at comparable levels 165
Detection of MTTP gene transcript and protein level 167
Validation of apolipoprotein B-100 levels in HLCs compared to hiPSC-derived intestinal organoids and patient plasma serum 169
MOPIK ($MTTP^{VAR/VAR}$)-HLCs have lower lipid metabolising efficiency and accumulate intracellular lipid inherently 171
MOPIK ($MTTP^{VAR/VAR}$)-HLCs sustained higher degree of ER stress 173
NFκB inflammatory pathway is activated in MOPIK ($MTTP^{VAR/VAR}$)-HLCs 175
Increased cellular and mitochondrial ROS production in MOPIK ($MTTP^{VAR/VAR}$)-HLCs 179
Altered mitochondrial respiration in MOPIK ($MTTP^{VAR/VAR}$)-HLCs 181
Transcriptomic profiling of healthy and disease cell lines in response to lipid challenge 186
High throughput proteomics profiling using antibody microarrays 198
Metabolomics profiling of LOPCK ($MTTP^{WT/WT}$) and MOPIK ($MTTP^{VAR/VAR}$) 207
5.4 Discussion 210
CHAPTER 6. GENERAL DISCUSSION 220
6.1 Fulfilment of thesis objectives 220
6.2 Proposed mechanistic model of MTTP-p.I564T NAFLD 224
6.3 Study limitations and improvements 228
6.4 Conclusion and future perspective 230
REFERENCES 232
APPENDIX I – PUBLICATIONS 260
APPENDIX II – OTHER SCIENTIFIC CONTRIBUTIONS 261

List of Figures

Figure 1.1 PhD project workflow. 22
Figure 1.2 Architecture of the liver. 26
Figure 1.3 Overview of lipid metabolism. 28
Figure 1.4 Histological features of NAFLD/NASH. 30
Figure 1.5. Imbalance between lipid supply and demand can lead to NAFLD and NASH. 35
Figure 1.6. Overview of the genetic variants that may be involved in NAFLD susceptibility and progression. 37
Figure 1.7 Role of MTP in apoB-containing lipoproteins assembly and secretion to the bloodstream. 39
Figure 1.8 Impact of *MTTP*-p.I564T SNV upon MTP protein structure. 41
Figure 2.1 Schematic timeline of the protocol used to obtain iPSCs by the transduction of sendai virus vectors. 54
Figure 2.2 Schematic diagram of the four-stage stepwise strategy to induce hiPSC differentiation into HLCs, which takes total of 21 days (from seeding D-2). 57
Figure 3.1 Overview of common hiPSC reprogramming approaches. 81
Figure 3.2 Isolation of human dermal fibroblasts from skin biopsy. (A) Pedigree of the investigated family. Square: male; circle: female; slashed 84
Figure 3.3 Derivation of hiPSCs from dermal fibroblasts. 86
Figure 3.4 Karyotype of reprogrammed hiPSC lines. 87
Figure 3.5 Sequential adaptation of media transition from TeSR-E8 to HB E8. 90
Figure 3.6 Fibroblast-derived hiPSCs are pluripotent. 93
Figure 3.7 Allele-specific expression of the *MTTP* gene. 94
Figure 3.8 Transfection efficiency comparison between lipofectamine and Amaxa™ 4D nucleofection using GFP plasmid on LOPCK hiPSCs. 98
Figure 3.9 Puromycin titration on LOPCK hiPSCs to determine optimal selection concentration. 100
Figure 3.10 Overview of CRISPR/Cas9 KO targeting workflow. 103
Figure 3.11 PCR genotypic characterisation of genome-edited LOPCK hiPSCs. 104
Figure 4.1 Overview of different aspects to consider for direct differentiation toward hepatocyte-like cells. 116
Figure 4.2 Foregut endoderm markers are upregulated after 48 h induction. 118
Figure 4.3 Different cell lines require different seeding densities 121

Figure 4.4 Different hiPSC lines require different dosage of BMP4 during hepatic specification. 122
Figure 4.5 Initial dose response screening of the small molecule candidates. 125
Figure 4.6 20-day maturation time course to assess developmental trajectory of small molecule versus recombinant protein approach..... 127
Figure 4.7 Morphological changes of cells cultured under Old and New formulated media during hepatocyte maturation stage. 131
Figure 4.8 HLCs generated using New maturation media expressed higher levels of mature markers. 131
Figure 4.9 Mature liver-related genes are relatively more upregulated in New media-cultured HLCs. 133
Figure 4.10 Overall similarity of differentially expressed genes between REBLPAT hiPSCs, Old-, New-maturation generated HLCs, foetal and adult liver samples. 136
Figure 4.11 Multi-dimensional PCA and t-SNE analyses of similaities between sample groups. 136
Figure 4.12 Gene expression profile of HLCs generated by New maturation medium is more closely related to liver cell type. 138
Figure 4.13 Expression profile of liver-related genes that are upregulated in New medium samples. 140
Figure 4.14 Extracellular metabolite profiling between Old and New maturation media using LC-MS-based method..... 143
Figure 4.15 Schematic illustration of the experimental timeline of chapter 4. 144
Figure 5.1 Classification of fatty acids according to their degree of saturation and unsaturation..... 156
Figure 5.2 Simulation of Western diet using fatty acid (FA) cocktail in REBLPAT-HLCs..... 161
Figure 5.3 Effects of OA treatment at different dosages on LOPCK-HLCs. 162
Figure 5.4 Effects of 48-hour PA treatment at different dosages on HLCs lipid induction.. 164
Figure 5.5 48-hour Palmitic acid treatment can induce lipid accumulation in hiPSC-derived HLCs at 300 µM while maintaining cellular architecture. 164
Figure 5.6 LOPCK and MOPIK HLCs expressed liver markers at similar levels. 165
Figure 5.7 *MTTP* gene expression is highly upregulated in MOPIK ($MTTP^{VAR/VAR}$) HLCs but with relatively lower MTTP protein expression compared to that of LOPCK ($MTTP^{WT/WT}$) HLCs..... 168
Figure 5.8 ApolipoproteinB-100 (ApoB-100) quantification by ELISA. 170

Figure 5.9 MOPIK (*MTTP*$^{VAR/VAR}$) HLCs are relatively more mature than LOPCK(*MTTP*$^{WT/WT}$) HLCs, with various expression levels of genes related to lipid metabolism. 177
Figure 5.10 MOPIK (MTTP$^{VAR/VAR}$) HLCs show a relatively higher degree of inflammatory gene upregulation and activated unfolded protein response (UPR). 178
Figure 5.11 MOPIK (*MTTP*$^{VAR/VAR}$) HLCs display signs of cellular and mitochondrial oxidative stress. 181
Figure 5.12 Functional analysis of mitochondrial respiration in LOPCK (*MTTP*$^{WT/WT}$)- and MOPIK (*MTTP*$^{VAR/VAR}$)-HLCs using the Seahorse platform. 183
Figure 5.13 Mitochondrial respiration parameters of LOPCK- and MOPIK-HLCs in untreated and PA-treated conditions, measured using the Seahorse platform. 184
Figure 5.14 Multi-dimensional principal component analysis (PCA) and t-SNE analyses of differentially expressed genes similarities between sample sets. 188
Figure 5.15 Pairwise comparison of untreated and PA-treated HLCs derived from LOPCK (MTTP$^{WT/WT}$) and MOPIK (MTTP$^{VAR/VAR}$) cell lines. 188
Figure 5.16 Differentially expressed gene profiles between LOPCK (*MTTP*$^{WT/WT}$)- and MOPIK (*MTTP*$^{VAR/VAR}$)-HLCs in 48-hour untreated and PA-treated conditions at maturation day 10 (M10, equivalent to differentiation D19). 195
Figure 5.17 Gene list term enrichment analysis based on functional annotations and protein interactions network. 197
Figure 5.18 Expression of NFκB-associated signalling proteins in HLCs under different PA treatments at maturation day 10 (M10). 204
Figure 5.19 Protein phosphorylation in HLCs, normalised to untreated LOPCK (*MTTP*$^{WT/WT}$)-HLCs quantified using densitometry of phosphokinase array. 204
Figure 5.20 Cytokine proteome array Levels of proteins secreted into tissue culture medium in HLCs. 207
Figure 5.21 Extracellular metabolite profiling between LOPCK- and MOPIK-HLCs in untreated and PA-treated conditions using LC-MS-based method. 208
Figure 5.22 Schematic illustration of the experimental timeline of chapter 5. 210
Figure 6.1 Schematic illustration of the experimental timeline of chapter 3 to 5. 223

List of Tables

Table 1.1 Summary of advantages and challenges of different approaches for modelling NAFLD..... 46
Table 2.1 Composition of culture media..... 49
Table 2.2 Standard PCR reaction mix..... 63
Table 2.3 Sequence of primers used for genotyping the genome-edited hiPSC clones..... 63
Table 2.4 Primer sequences used for qPCR. 64
Table 2.5 Primary and secondary antibodies used. 68
Table 4.1 Characteristics and measurement parameters of mature human hepatocytes.. 149
Table 5.1 Common differentially expressed genes that are upregulated in both LOPCK- and MOPIK-HLCs. 190
Table 5.2 Common differentially expressed genes that are downregulated in both LOPCK- and MOPIK-HLCs. 192

Abbreviations

Abbreviation	Description
%	Percentage
(F)FA	(Free) Fatty Acid
°C	Degree Celsius
Ab	Antibody
ABL	Abetalipoproteinemia
AFLD	Alcoholic Fatty Liver Disease
AFP	Alpha Foetal Protein
ALB	Albumin
ALT	Alanine Aminotransferase
AMP	Adenosine Monophosphate
AMPK	AMP-Activated Protein Kinase
ANOVA	Analysis of Variance
APOB	Apolipoprotein B
AST	Aspartate Aminotransferase
ATP	Adenosine Triphosphate
BMP	Bone Morphogenic Protein
bp	Base Pairs
BSA	Bovine Serum Albumin
Cas9	CRISPR Associated Protein 9
cDNA	Complementary DNA
CRISPR	Clustered Regularly Interspaced Short Palindromic Repeats
CYP	Cytochrome P450
DAPI	Di-Amino Phenyl-Indole
DE	Definitive Endoderm
DKK	Dickkopf-Related Protein
DMEM	Dulbecco's (Modified Eagle's) Minimal Essential Medium
DMSO	Dimethyl Sulfoxide
DNA	Deoxyribonucleic Acid
dNTP	Deoxyribonucleotide Triphosphate
DPBS	Dulbecco’s Phosphate Buffered Saline
DSB	Double-Stranded Break
DTT	Dithiothreitol
E8	Essential 8 Medium
ECM	Extracellular Matrix

EDTA	Ethylene Diamine Tetra-Acetic Acid
EGF	Epidermal Growth Factor
ELISA	Enzyme-Linked Immunosorbent Assay
eNOS	Endothelial Nitric Oxide Synthase
ER	Endoplasmic Reticulum
ETC	Electron Transport Chain
FBS	Foetal Bovine Serum
FCCP	Carbonyl Cyanide 4-(Trifluoromethoxy)Phenylhydrazone
FDR	False Discovery Rate
FG	Foregut
FGF	Fibroblast Growth Factor
FWD	Forward
gDNA	Genomic DNA
GFP	Green Fluorescent Protein
GFR	Growth Factor Reduced
gRNA	Guide RNA
GWAS	Genome-Wide Association Study
HB E8	Homebrew Essential 8
HBSS	Hank's Buffered Salt Solution
HC	Hydrocortisone
HCC	Hepatocellular Carcinoma
HCM	Hypertrophic Cardiomyopathy
HDF	Human Dermal Fibroblast
HDL	High-Density Lipoprotein
HDR	Homology-Directed Repair
HE	Hepatic Endoderm
hESC	Human Embryonic Stem Cell
hESC-HLC	Human Embryonic Stem Cell Derived Hepatocyte-Like Cells
HETIK ($MTTP^{WT/VAR}$)	Heterozygous MTTP-P.I564T Mutant hiPSC Line
HG	Hindgut
HGF	Hepatocyte Growth Factor
hiPSC	Human Induced Pluripotent Stem Cell
hiPSC-HLC	Human Induced Pluripotent Stem Cell Derived Hepatocyte-Like Cells
HLC	Hepatocyte-Like Cells
hPSC	Human Pluripotent Stem Cell

hPSC-HLC	Human Pluripotent Stem Cell Derived Hepatocyte-Like Cells
HSC	Hepatic Stellate Cells
ICC	Immunocytochemistry
IDL	Intermediate-Density Lipoprotein
INS	Insulin
IO	Intestinal Organoids
iPSC	Induced Pluripotent Stem Cell
IRES	Internal Ribosome Entry Site
ITS	Insulin-Transferrin-Selenium
IWP-4	Inhibitor of WNT Production-4
kb	Kilobases
KO	Knockout
LA	Linoleic Acid
LAL	Lysosomal Acid Lipase
LD	Lipid Droplets
LDL	Low-Density Lipoprotein
LDN	Ldn-193189
LHA	Left Homology Arm
LOPCK ($MTTP^{WT/WT}$)	Wild-Type MTTP-P.I564T hiPSC Line
LPL	Lipoprotein Lipase
LPS	Lipopolysaccharides
LSEC	Liver Sinusoidal Endothelial Cells
MOI	Multiplicity of Infection
MOPIK ($MTTP^{VAR/VAR}$)	Homozygous MTTP-P.I564T Variant hiPSC Line
MRI	Magnetic Resonance Imaging
mRNA	Messenger RNA
MTP (Protein) / *MTTP* (Gene)	Microsomal Triglyceride Transfer Protein
MUFA	Monounsaturated Fatty Acids
MUT	Mutant
MW	Molecular Weight Marker
N:C ratio	Nuclear-Cytoplasmic Ratio
NAC	N-Acetyl Cysteine
NADPH	Nicotinamide Adenine Dinucleotide Phosphate
NAFLD	Non-Alcoholic Fatty Liver Disease
NASH	Non-Alcoholic Steatohepatitis
NEAA	Non-Essential Amino Acids
NFW	Nuclease-Free Water

NHEJ	Non-Homologous End Joining
NK	Natural Killer
NKT	Natural Killer T
NM	New Medium
NTC	No Template Control
OA	Oleic Acid
OCR	Oxygen Consumption Rate
ORO	Oil Red O
OSKM	OCT4, SOX2, KLF4 and c-MYC
OSM	Oncostatin-M
OXPHOS	Oxidative Phosphorylation
PA	Palmitic Acid
PBS	Phosphate Buffered Saline
PBST	Phosphate-Buffered Saline with Triton
PCA	Principal Component Analysis
PCR	Polymerase Chain Reaction
PDB	Protein Data Bank
PHH	Primary Human Hepatocyte
PNU	PNU-74654, Wnt-B Catenin Pathway Inhibitor
PUFA	Polyunsaturated Fatty Acids
Puro	Puromycin
QC	Quality Control
qPCR	Quantitative Real-Time Polymerase Chain Reaction
RA	Retinoic Acid
REBLPAT	Wild-Type hiPSC Line
REV	Reverse
RHA	Right Homology Arm
RIN	RNA Integrity Number
RLU	Relative Luminescence Units
RNA	Ribonucleic Acid
ROCKi	Rho-Associated Kinase Inhibitor
ROS	Reactive Oxygen Species
RPMI	Roswell Park Memorial Institute Medium
rRNA	Ribosomal RNA
RT	Room Temperature
RT-PCR	Reverse Transcriptase PCR
SB	Sb431542
SD	Standard Deviation of The Mean

SEM	Standard Error of The Mean
SeV	Sendai Virus
SFA	Saturated Fatty Acid
SM	Small Molecule
SNP	Single Nucleotide Polymorphism
SNV	Single Nucleotide Variation
TG	Triglyceride
TGF-β	Transforming Growth Factor Beta
TLR	Toll-Like Receptor
TNF-α	Tumour Necrosis Factor Alpha
TRAIL	TNF-Related Apoptosis-Inducing Ligand
t-SNE	T-Distributed Stochastic Neighbour Embedding
ULDL	Ultra-Low-Density Lipoprotein
UPR	Unfolded Protein Response
VLDL	Very-Low-Density-Lipoprotein
WFI	Water-For-Injection for Cell Culture
WT	Wild-Type

Chapter 1.

General Introduction

Chapter 1. General Introduction

1.1 Thesis Rationale & Objectives

Non-alcoholic fatty liver disease (NAFLD) refers to a spectrum of disorders that are caused by the accumulation of lipids within the liver in the absence of excessive alcohol consumption. Without intervention, progression of the disease involves hepatic steatosis, steatohepatitis, fibrosis, cirrhosis, and end-stage liver failure. The global prevalence of NAFLD is approximately between 25-30% and it has been increasing rapidly in parallel with the dramatic rise in obesity and type 2 diabetes in both developed and developing countries [1], making NAFLD a novel epidemic as one of the most common forms of liver disease and a major public health burden in the past three decades [2]. Although the precise pathogenesis of NAFLD remains poorly understood, susceptibility and progression of NAFLD can be governed by genetic predisposition, environmental factors and lifestyle. Despite clear evidence that weight loss via lifestyle interventions such as dietary changes and exercise as the primary therapy of NAFLD, many patients struggle to implement and maintain these health behaviour changes long term [3]. There is still a gap in knowledge about the natural history of the disease and modern alternative treatments, therefore it is fundamental to educate the public to improve their attitudes and perceptions toward the condition. The presence of social support can facilitate behaviours to lifestyle change among people with NAFLD consistently. Understanding temporal trends in NAFLD prevalence is also vital to better understand its economic burden, urging appropriate government bodies to create more efficient prevention strategies sooner [4], [5].

An increasing number of studies have identified genes that contribute to the high risk for developing NAFLD, many of these genes including microsomal triglyceride transfer protein (*MTTP*) are involved in the regulation of lipid metabolism, defective of these genes can cause lipid imbalance, which sequentially may lead to hepatic steatosis. In this thesis, an *in vitro* disease model is generated to elucidate the driving mechanisms of hepatic steatosis and the pathogenesis of NAFLD. We have access to

a unique patient cohort of a family found to have a rare *MTTP* single nucleotide polymorphism (SNP) could also contributed to predisposition of NAFLD and disease progression. To better understand the role of intrinsic genetic risk factors and externally-induced cellular stress in this disease, donor-derived dermal fibroblasts are reprogrammed into hiPSCs and undergone hepatic differentiation, HLCs with wild-type (WT) and *MTTP*-p.I564T variant (VAR) background would be used to investigate the underlying mechanisms linking intrahepatic lipid accumulation and subsequent cellular changes in lipid-induced steatosis model through 3 main experimental stages as illustrated in **Figure 1.1**.

Chapter 3 outlines the derivation of human dermal fibroblasts and reprogramming to hiPSCs from donors with different *MTTP*-p.I564T genetic variations. Additionally, to explore the use of CRISPR/Cas9 technology and produce *MTTP* knockout (KO) hiPSC line as a positive control (*MTTP-/-*) in comparison to other donor-derived cell lines.

In chapter 4, we would explore various strategies to improve and optimise hepatic differentiation protocol, in order to produce HLCs that are more mature and functionally relevant to accurately model NAFLD.

In the final result chapter 5, *in vitro* steatosis model would be established; wildtype and *MTTP*-p.I564T variant cell lines would be challenged with extraneous fatty acid, global changes in cellular response and molecular signatures will be examined via multi-omics profiling. This would enable us to better understand the physiological characteristic of these cells, which would potentially allow us to identify disease triggering factors as potential therapeutic targets or diagnostic biomarkers.

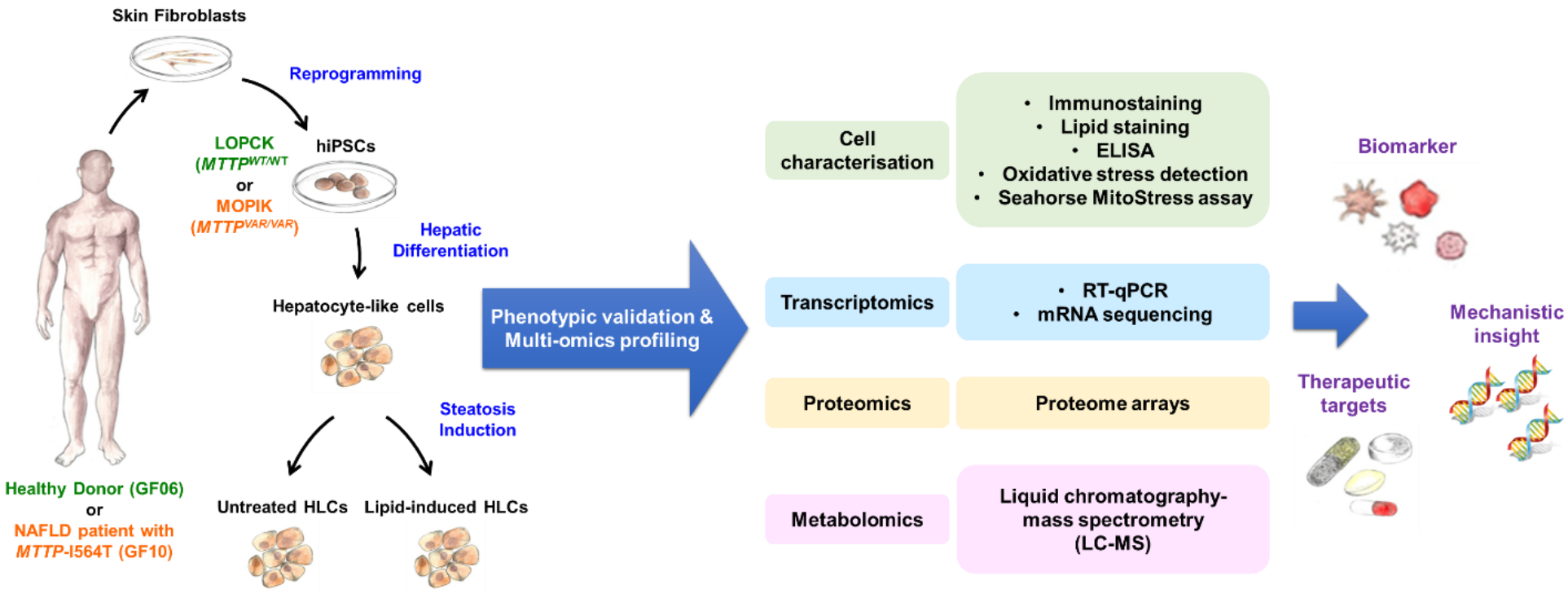


Figure 1.1 PhD project workflow. Human skin biopsy was obtained from healthy individual GF06 and NAFLD patient GF10 with homozygous *MTTP*-p.I564T genetic variation. Derived dermal fibroblasts were then reprogrammed into hiPSCs. HiPSCs were differentiated into hepatocyte-like cells, subsequently cultured in either normal or lipid-exposed conditions for downstream functional and molecular phenotype characterisation, multi-omics profiling was used to depict potential mechanistic insights, identification of early diagnostic biomarker and therapeutic targets.

1.2 The liver

1.2.1 Anatomy and functions of the liver

The liver is an essential hub for numerous physiological processes such as glycogen storage and drug detoxification, it is the largest gland in the body exhibiting both endocrine and exocrine properties, which makes it a central regulator of macronutrient metabolism including glucose, lipid, protein, amino acid and urea [6]–[8]. The liver lobules are the basic architectural units of the liver, which formed into a roughly hexagonal shape with six corners demarcated by a portal triad of vessels consisting of a portal vein, bile duct, and hepatic artery (**Figure 1.2**) [7]. While the lobule represents a more structural anatomical unit, the hepatic acinus is the functional unit of the liver in terms of blood flow [9]. The acinus has an irregular shape, roughly ellipsoidal mass of hepatocytes oriented around the afferent vascular system, aligned around the hepatic arterioles and portal venules just as they anastomose into sinusoids [6]. The acinus is roughly divided into three zones that correspond to distance from the arterial blood supply, connecting two portal triads with a line from which it extends into the direction of the two adjacent central veins [9]. Zone 1 is the periportal zone around the portal triads, consisting of hepatocytes closest to the arterioles and they are best oxygenated. Whereas zone 3 is around the central vein, distinguished as the perivenous or centrilobular zone, with the poorest supply of oxygen. The intermediary zone between periportal and perivenous zones is zone 2 [6], [9], [10].

Each lobule is comprised of plates of hepatocytes lined by sinusoidal capillaries that radiate toward a central efferent vein; oxygenated blood is supplied to the lobule from the hepatic artery, whereas the portal vein carries nutrient-rich blood drained from the gastrointestinal tract, spleen, and pancreas [6]. The blood would then flow through a network of sinusoidal capillaries before draining into branches of the central vein; this organization leads to formation of several gradients including oxygen, hormones, nutrients, and waste products, which are relevant to

consequential metabolic processes [7], [11], [12]. Dynamic interplay of this gradient formation can drive liver zonation and thus contribute to its physiological function, this pattern and consequential organisation of relevant metabolic processes is commonly known as 'metabolic zonation' [10]. Metabolic zonation provides several advantages to main organ and whole body homeostasis, it has been shown for carbohydrate, amino acid, lipid, ammonia, and xenobiotic metabolisms [9]. For example, spatial separation of opposing pathways can prevents competition for a common substrate. In addition, substrate demanding activities such as lipogenesis and ketogenesis can be carried out at site with the best substrate provision when complementing pathways are linked.

The liver is composed of several cell types including hepatocytes, cholangiocytes (biliary epithelial cells), stellate cells, Kupffer cells, and liver sinusoidal endothelial cells; each cell type has its unique biological roles and functions [11]. Hepatocytes are the predominant epithelial cell population that make up majority of the liver volume (~70%) and perform many of the functions ascribed to the liver [7], [11]. Cholangiocytes are the second most abundant epithelial population of the liver (~3%), they formed the bile ducts as well as controlling the rate of bile flow to secrete water and bicarbonate [13]. Hepatic stellate (or Ito) cells (HSCs) are located in the perisinusoidal space (space of Disse) between the hepatocyte cords and sinusoids [11]. HSCs can exist in a quiescent state as the main reservoir of vitamin A in the form of liver droplets, alternatively, upon activation by liver injury or infection they proliferate and progressively lose vitamin A, they can also differentiate into αSMA-expressing myofibroblast-like cells capable of depositing extracellular matrix (ECM) protein such as collagen and directing temporary fibrotic scar formation, eventually may progress to cirrhosis in end stage liver disease [14]–[16]. Kupffer cells are located within the lumen of sinusoids, they are important resident liver macrophages that protect the liver by recognising many pathogenic stimuli introduced through portal circulation, activated Kupffer cells can then secrete pro- or anti-inflammatory cytokines and proteases depending on a number of contributing factors [7], [17]. Finally, liver sinusoidal endothelial cells (LSECs) are the most abundant non-

parenchymal hepatic cell population which line the sinusoidal capillary channels of the liver, they are highly specialised endothelial cells that form the interface between blood derived from the visceral adipose tissue and the gut on one side; hepatocytes and hepatic stellate cells on the other [18]. They have vital physiological and immunological functions, including filtration, exchange of proteins and particles, endocytosis, antigen presentation and leukocyte recruitment. [7], [18], [19].

The liver can influence metabolism in other tissues by secreting autocrine/paracrine and endocrine factors such as insulin-like growth factors (IGFs), angiotensinogen, thrombopoietin, plasma proteins including albumin and apolipoproteins, metabolites, and non-coding RNA (ncRNA); as well as exocrine secretion in the form of bile [7], [20]. Dysregulation of cell behaviours and activities can lead to perturbations in the metabolism and development of metabolic syndrome; urbanisation and industrialised society in many developed countries led to a sedentary lifestyle, excessive dietary intake, stress, and sleep deprivation cab contribute to obesity, metabolic syndrome, and the emerging condition of non-alcoholic fatty liver disease (NAFLD) [21]. NAFLD represents the leading cause of chronic liver disease worldwide in the last decade, current therapeutic options for NAFLD are limited, resulting a huge health and economic burden [22]. Therefore, it is imperative to get a better understanding of the disease pathogenesis if new treatments are to be discovered.

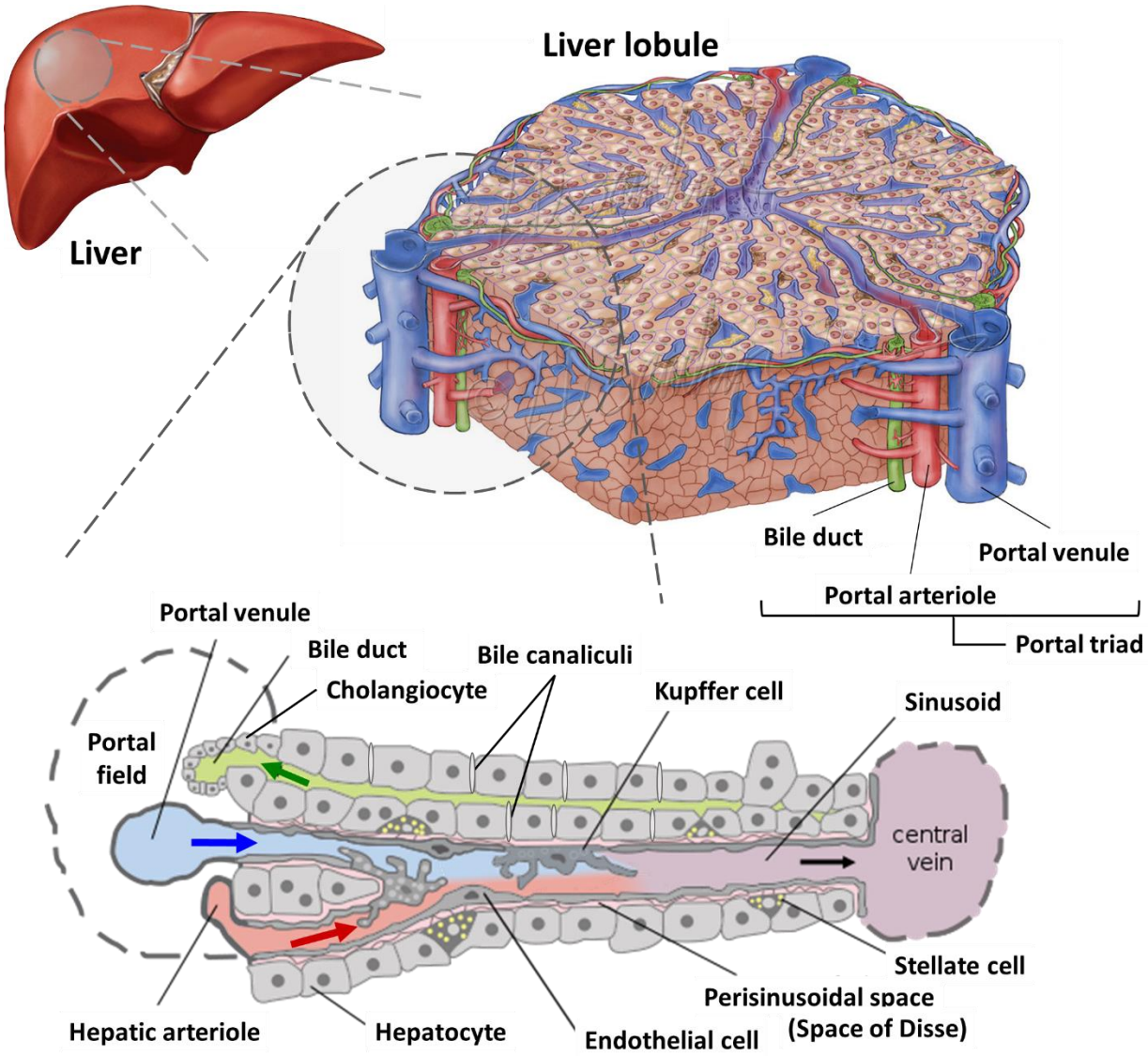


Figure 1.2 Architecture of the liver. Illustration adapted from [11], [23], [24].

1.2.2 Lipid metabolism

Lipids are insoluble in water and therefore must be transported in the plasma in the form of lipoproteins; lipoproteins are complex particles comprised of a central core containing cholesterol esters and triglycerides (TGs), surrounded by a hydrophilic layer in which free cholesterol, phospholipids, or apolipoproteins can be embedded to facilitate lipoprotein formation and functions [25]. Depending on the density size, lipid composition, and apolipoprotein associated, lipids can be classified into five main classes including ultra-low-density lipoprotein (ULDL, or chylomicron) to very-

low-density lipoprotein (VLDL), intermediate-density lipoproteins (IDL) , low-density lipoproteins (LDL), and high-density lipoproteins (HDL); in which chylomicron is the largest in diameter with the lowest density and high TG content [26].

Lipid metabolism consists of three main pathways via exogenous, endogenous and reverse cholesterol transport (**Figure 1.3**). The exogenous pathway starts with the incorporation of dietary lipids into chylomicrons in the intestine, thereby released into the lymph and enter circulation, TGs carried in chylomicrons are then metabolised by lipoprotein lipase (LPL) in the muscle and adipose tissues releasing free fatty acids (FFA), forming chylomicron remnants which subsequently taken up by the liver through remnant receptors and subsequently degraded into FFA and cholesterol [25]. The endogenous pathway refers to the processing of lipids synthesised in the liver, which begins with the formation of VLDL by the action of microsomal triglyceride transfer protein (MTP) [27]. VLDLs are then exported from the liver to the circulation and adipose tissue where they are degraded again through LPL into FFA and IDL, followed by conversion into LDL; cholesterol is delivered to peripheral tissues as well as to the liver when LDL binds to the LDL receptor [41]. Lastly in the reverse cholesterol pathway, excess cholesterol is removed from tissues and returned to the liver via HDL, which later are excreted in the bile [26].

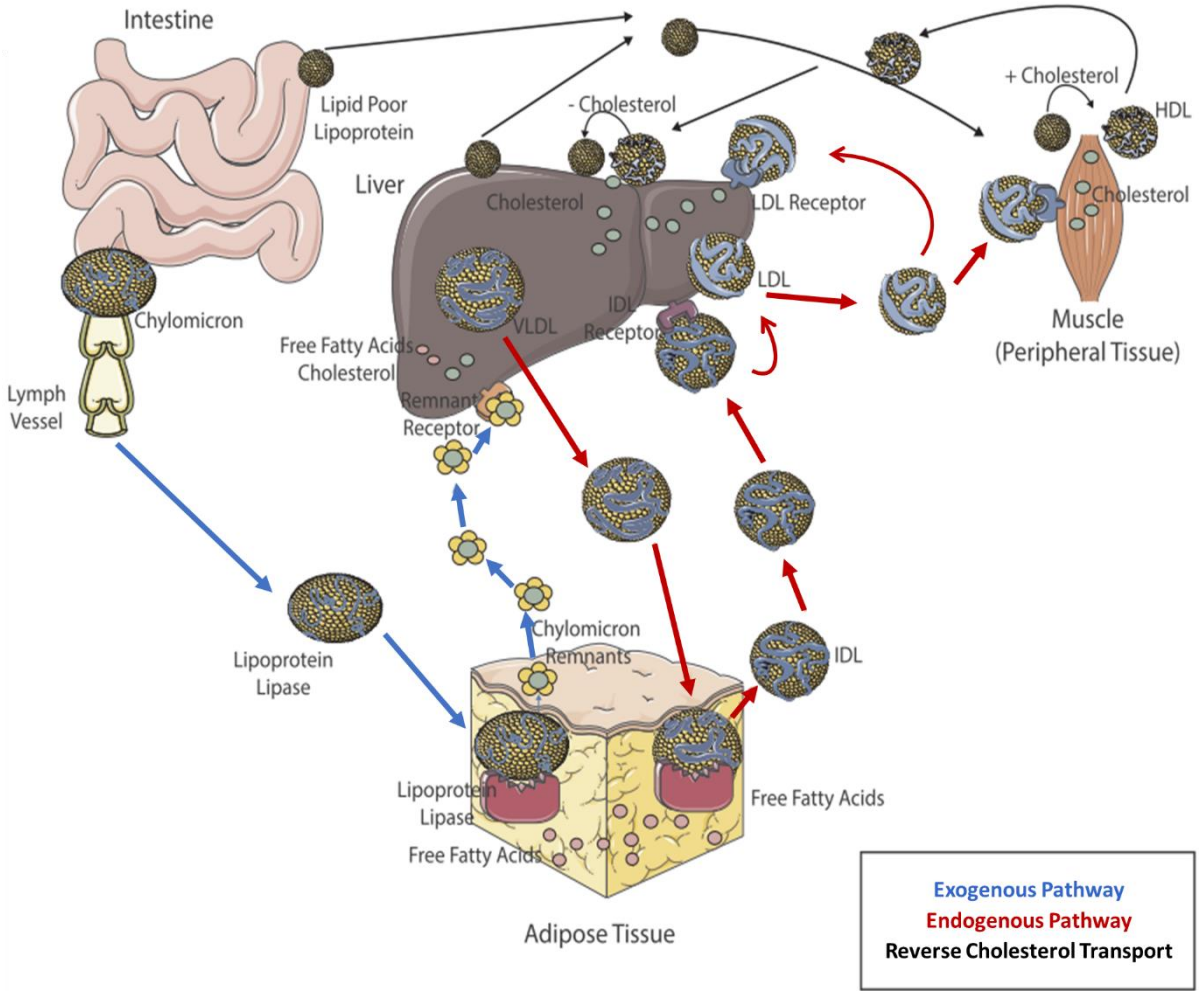


Figure 1.3 Overview of lipid metabolism. The three main pathways of lipid metabolism are the exogenous pathway (arrows in blue), the endogenous pathway (red) and reverse cholesterol transport (black). Very-low-density lipoprotein (VLDL), intermediate-density lipoproteins (IDL), low-density lipoproteins (LDL), high-density lipoproteins (HDL). Adapted from [28].

1.3 Non-Alcoholic Fatty Liver Disease (NAFLD)

1.3.1 Pathology and clinical diagnosis of NAFLD

Alcoholic liver disease (ALD) and non-alcoholic fatty liver disease (NAFLD) have similar pathological spectra, ranging from simple hepatocellular steatosis to the more aggressive form of non-alcoholic steatohepatitis (NASH), with the additional features of hepatic inflammation and variable degrees of fibrosis, which can potentially progress to cirrhosis and hepatocellular carcinoma (HCC) [29], [30]. However, the etiology of these two diseases are very different; ALDs such as fatty liver and alcoholic hepatitis are due to alcohol overconsumption, whereas the severity of the clinicopathologic outcome of NAFLD is hugely influenced by excessive food intake or genetics; notably, both ALD and NAFLD are frequently accompanied by extrahepatic complications such as cardiovascular disease and malignancy.

NAFLD is characterised by the accumulation of hepatocellular triglycerides exceeding 5-10% of liver mass in an individual consuming less than three units/ two units of alcohol per day for men/ women; other lipid metabolites such as free fatty acids, cholesterol, and phospholipids, may also be present and play a role in disease progression [31]. Early stage of NAFLD is asymptomatic, usually it is not until an incidental detection of abnormal elevation of liver enzymes including alanine aminotransferase (ALT) and aspartate aminotransferase (AST), and/or liver-related complications that a systematic examination is initiated [30]. Confirmation of the diagnosis of NAFLD can achieved by non-invasive imaging such as ultrasonography and magnetic resonance imaging (MRI) [32]. Although non-invasive tests are available, a liver biopsy remains the gold standard for identifying hepatic steatosis and NASH, and for fibrosis staging [33], [34] (**Figure 1.4**).

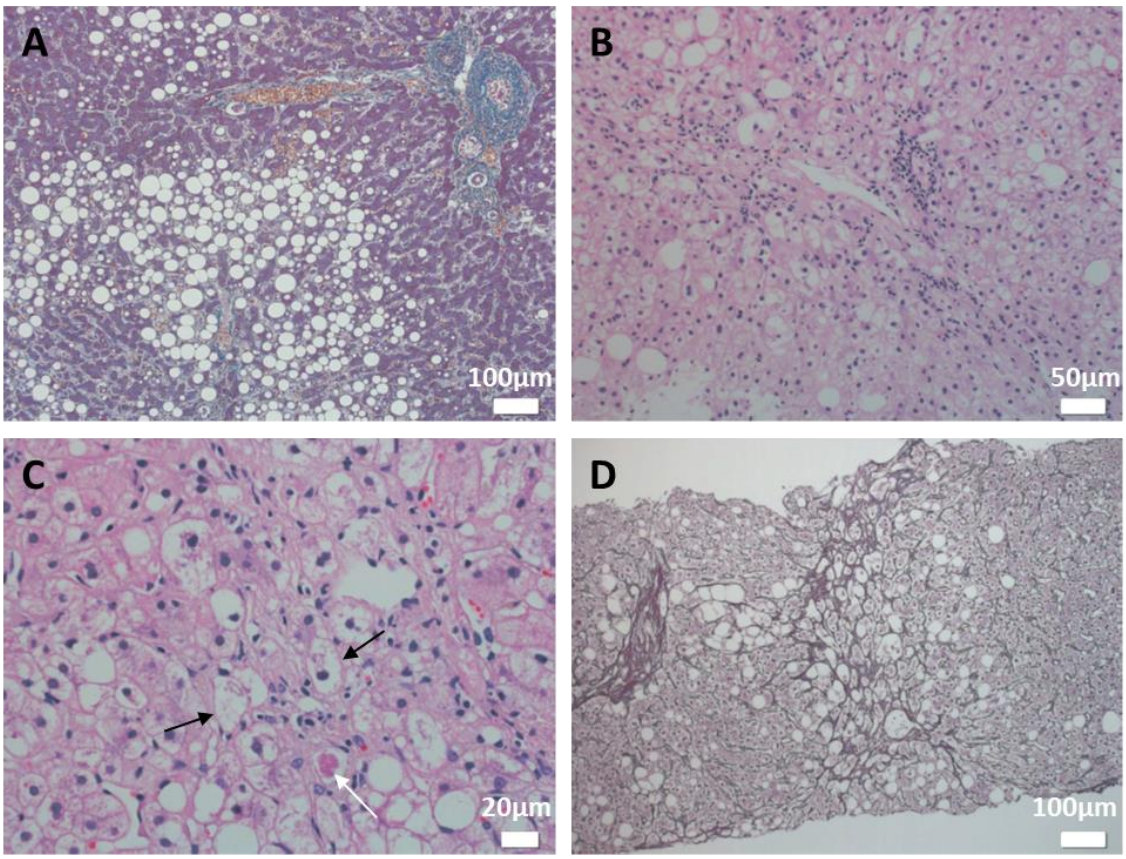


Figure 1.4 Histological features of NAFLD/NASH. **(A)** Macrovesicular steatosis, the intracytoplasmic fat is seen as clear vacuoles (Masson trichrome stain). **(B)** Lobular inflammation in NASH (haematoxylin and eosin staining). **(C)** Ballooned hepatocytes (swollen hepatocytes with rarefied cytoplasm indicated with black arrows) and Mallory-Denk bodies (intracellular deposition of eosinophilic aggregates in the cytoplasm of ballooned hepatocytes indicated with white arrow) in NASH (haematoxylin and eosin staining). **(D)** Characteristic chicken-wire fence pattern of fibrosis in NASH (reticulin staining). Images adapted from [35].

1.3.2 Epidemiology and economic impact of NAFLD

Non-alcoholic fatty liver disease (NAFLD) is the fastest growing chronic liver disease (CLD) in Western countries; linked to the worldwide obesity epidemic, NAFLD is also becoming one of the most prominent causes of CLD in children and adolescents [36]. NAFLD is found to be most prevalent at peak in the Middle East (31.8%) and South America (30.4%), whereas developing countries such as Africa has as low as 13% in comparison [37]. Approximately 33% of the UK population have NAFLD, and 2-5% developed NASH [38], [39]. The prevalence of NAFLD has been increasing rapidly in parallel with the dramatic rise in obesity and the subsequent metabolic disorder

including not only obesity but also depression and type 2 diabetes mellitus, NAFLD poses a significant public health burden by the sheer number of people needing clinical attention in the USA (64 million) and Europe (52 million) [40], [41]. Recent studies showed that there is a changing epidemiology within Asia-Pacific region, there is an upwardly mobile economic drift and a vast geographical spread of NAFLD burden due to its larger and expanding population in these urbanising societies [42]. Diversity of diet and lifestyle amongst different countries and also within countries, as well as genetic factors possibly account for the wide variation of NAFLD prevalence among Asian areas, it varies from 12.5–38% in Mainland China, 23–26% in Japan, 27% in Korea, 12–51% in Taiwan, 28% in Hongkong, 9–32% in India and 5–30% in other areas of South Asia and far East [42]–[45]. Modern sedentary lifestyle and diets high in fat and processed carbohydrates have all contributed to the meteoric trends in the diabesity epidemic and NAFLD. Obesity is one of the key drivers for the growth in burden and mortality for liver disease; according to The Health Survey for England (HSE) data, around a quarter of adults in 2014 were obese and the cost to the NHS was estimated to be £4.2 billion, making it a major public health burden [46]. Death caused by liver disease has increased by 25% between 2001 and 2009 and constitutes the third most common cause of premature death in the UK, while health and life expectancy of many other chronic illnesses such as cardiovascular and respiratory diseases are improving [47]. Interestingly, an additional aspect of NAFLD epidemiology in Asia is the so called “lean or non-obese NAFLD”, around 10% of the NAFLD subjects was initially identified as Asian populations, indicating a remarkable propensity of developing metabolic syndrome-associated clinical conditions without the anthropometric parameters considered as obese; genetic predisposition possibly explain this defiance of classical metrics but following a similar pattern of clinical outcomes [48], [49]. There is a real need to put in efforts in reducing morbidity and mortality by addressing the underlying causes and consequences of liver disease.

1.3.3 Hepatic pathogenesis of NAFLD

NAFLD is strongly associated with a cluster of clinical problems that relates to metabolic syndrome including obesity, insulin resistance, hypertension, and

dyslipidaemia; in fact, excessive visceral adiposity and insulin resistance have been demonstrated to contribute towards the pathogenesis of NAFLD [50]. The pathogenesis of NAFLD was first proposed as a "two-hit" process by Day and James (1998) ; first, insulin resistance causes intrahepatic triglyceride accumulation; second, cellular insults such as oxidative stress, lipid oxidation and inflammation cause hepatocyte apoptosis/necrosis and fibrosis, leading to the progression of NASH [52]. Nonetheless, as the understanding of the pathogenesis of NAFLD and NASH evolves, implicates cell interaction between liver parenchymal and nonparenchymal cells, as well as crosstalk between various immune cell populations in liver. Accumulating studies are more leaning toward the "multi-parallel model" hypothesis, lipotoxicity appears to be the central driver of hepatocellular injury via oxidative stress, endoplasmic reticulum (ER) stress and immune related signalling networks [53], [54]. Cellular injury can activate subsequent immune response, contributing to the progression towards NASH. The cellular sources of various inflammatory related mediators such as endotoxins, chemokines, adipokines, and other inflammatory cytokines can be broad. These molecules can come from hepatocytes, hepatic stellate cells (HSCs), portal fibroblasts and immune cells such as neutrophils, macrophages, natural killer (NK) cells, natural killer T (NKT) cells, and lymphocytes [54] Additionally, genetics may also play a huge role in the pathogenesis and progression of NAFLD/ NASH [55]–[57].

Role of lipotoxicity in the pathogenesis of NAFLD/ NASH

The term lipotoxicity is used to describe the toxic effects of FFA and their metabolites causing cell injury and death, this can affect cellular and molecular functions and consequently sensitising the liver to additional insults [58]. NASH is a result where steatosis occur in parallel with the generation of lipotoxic metabolites of fatty acid, hepatocellular injury can be manifested as mitochondrial damage, endoplasmic reticulum (ER) stress, inflammation, apoptosis, necrosis, and histological features such as ballooning and Mallory-Denk body formation [29], [58].

Hepatic lipid content is regulated by the balance in lipid flux of FFA uptake through lipolysis of adipose tissue (input) and de novo lipogenesis from excess dietary fats and sugars [59], which would then be metabolised via mitochondrial fatty acid beta (β)-oxidation (breakdown) or incorporated into triglycerides exportation as VLDL (output); disproportion between these processes can lead to hepatic steatosis (**Figure 1.5**) [34], [60], [61]. Harmful lipid species may be formed when the liver cannot metabolise FFA efficiently, as a consequent they could potentially activate lipotoxic pathways, leading to hepatocellular injury and exacerbate further lipid accumulation, which can drive progression towards non-alcoholic steatohepatitis (NASH, steatosis plus inflammation and hepatocyte ballooning) to fibrosis (scarring), cirrhosis, hepatocellular carcinoma (HCC) and eventually liver failure [62], [63]. Repeated hepatocellular injury can result in dysregulated wound healing response and lead to fibrosis, this is characterised by the employment of inflammatory mediators to activate hepatic stellate cells to myofibroblasts, which sequentially could migrate into the liver parenchyma and secrete collagen-rich extracellular matrix (ECM) [64]

In an insulin resistance setting, insulin does not suppress peripheral adipose lipolysis to the same extent as in healthy individuals, thereby increasing adipose-derived fatty acid (FA) flux to the liver in the fasting state; postprandially the liver is unable to regulate the changes in lipogenesis from fasted to fed state, which induces de novo lipogenesis and reduces β- oxidation through production of malonyl-CoA (inhibitor of fatty acid oxidation); both leading to increased hepatic triglyceride production [52], [65]. Hepatic lipid can be reduced by mitochondrial fatty-acid oxidation or exported in the form as VLDL; since triglyceride synthesis prevails over VLDL secretion, excess fat accumulates in the form of lipid droplets within hepatocytes leading to fatty liver development [52], [66].

Mitochondria is responsible for maintaining cellular homeostasis by regulating energy production and multiple metabolic pathways. Mitochondrial dysfunction could be due to lipotoxicity as a result of structural defects, this drives the formation of proinflammatory cytokines such as TNFα, IL-6, and of the MCP-1 chemokine and

subsequent activation of hepatic stellate cells, leading to collagen deposition and liver fibrosis, which are all implicated in the progression to NASH [34], [67].

Endoplasmic reticulum (ER) is a membrane-bound organelle responsible for the assembly and post-translational modification of secretory and membrane proteins and lipid biosynthesis [68]. When the demand for protein modification exceeds the capacity of the ER to fold or degrade, unfolded or misfolded proteins accumulate and ER stress is activated in order to restore homeostatic equilibrium; disruption of ER homeostasis will lead to activation of the unfolded protein response (UPR) [55]. UPR is mediated by three transmembrane proteins of the ER: protein kinase RNA-like ER kinase (PERK), activating transcription factor-6 (ATF6) and inositol-requiring enzyme-1 (IRE1); three distinct but inter-related signalling cascades will initiate when these proteins are activated, resulting in a global decrease in protein translation and enhancing ER folding capacity [68]. UPR has the capacity to activate stress signalling pathway including the activation of cellular stress mediator C-Jun NH_2 terminal kinase (JNK) and transcriptional regulator nuclear factor-κB (NFκB), these signalling pathways connect ER stress to inflammation and play an important role in the progression from NAFLD to NASH [55], [68].

Hepatic steatosis is clinically silent, it is an adaptive mechanism that is reversible if the lipid metabolism regains balance. Modern diets often contain *trans*-fatty acid (found in processed food) and fructose (common sweetener), long-term consumption of high-fat, high-fructose diet have been shown to contribute in the development of NAFLD in animal models [69], [70]. Insulin resistance, steatosis, hepatic oxidative damage and inflammation were observed in rats and mice fed on high-fat diet after 3-8 weeks, however these abnormal symptoms were alleviated by using a restricted dietary consumption program, implicating that diet has a direct association to the progression of NAFLD [70]. In humans, a high-fructose diet can lead to more severe hepatic inflammation and fibrosis in subjects with NAFLD [71]. Combination of diet high in fat and fructose can induce a more advanced form of NAFLD and NASH [72]. Although NAFLD can be stimulated by a number of exogenous

factors, endogenous genetic risk factors may also contribute to the pathogenesis and disease progress of NAFLD. Multiple genome-wide association studies (GWAS) and large-scale candidate gene studies have enriched our understanding of the genetic aspects of NAFLD.

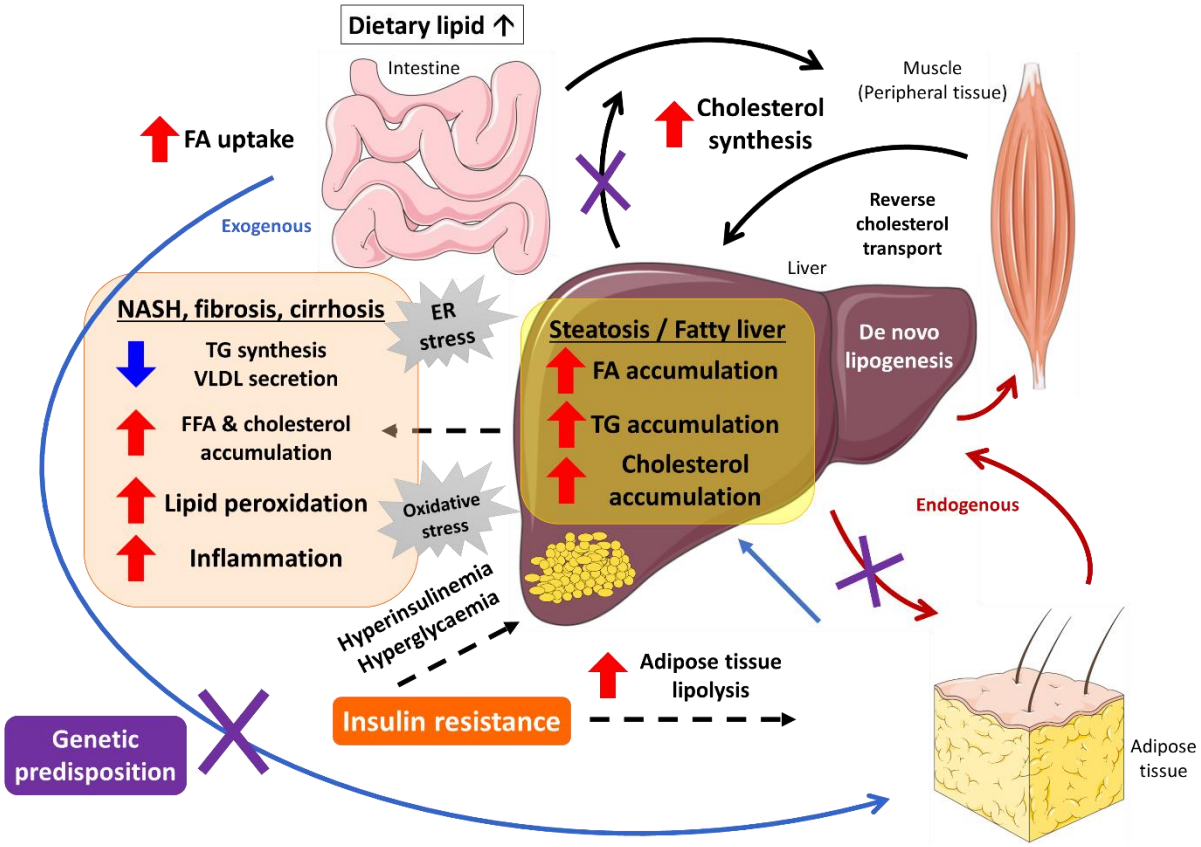


Figure 1.5. Imbalance between lipid supply and demand can lead to NAFLD and NASH. Insulin resistance and hyperglycaemia/hyperinsulinemia can promote NAFLD by increasing the release of FFAs from adipose tissue, which then induces hepatic de novo lipogenesis. Excess dietary fat intake also has a contribution to lipid overload and fat accumulation. Hepatic steatosis is also associated with developing/exacerbating systemic insulin resistance by direct and indirect mechanisms. Genetic predisposition (purple crosses) could influence lipid metabolism potentially by reducing lipase activity, decrease apolipoprotein secretion, inefficient conversion of lipoproteins, subsequently inducing more ER stress and oxidative stress, leading to further inflammation, fibrogenesis and eventually cirrhosis. Free fatty acid (FFA), triglyceride (TG), very-low-density-lipoprotein (VLDL).

1.3.4 Genetic predisposition influences on lipid metabolism and NAFLD

Excessive intrahepatic triglyceride accumulation is the hallmark of NAFLD; genetic variation of genes involved in lipid metabolism may lead to functional alterations that predispose individual to NAFLD susceptibility and progression (**Figure 1.6**). Some of the well-known genetic mutations/variations are identified using GWAS screening for genes in patients at risk of NAFLD and its progression, these genes include patatin-like phospholipase domain-containing 3 (*PNPLA3*)-I148M single nucleotide polymorphism (SNP; rs738409) [73]; transmembrane 6 superfamily member 2 (*TM6SF2*)-E167K variant (rs58542926) [74]; glucokinase regulator (*GCKR*)-P446L variant (rs1260326) [75]; and membrane bound O-acyltransferase domain-containing 7 (*MBOAT7;* rs641738). These genetic variants can increase risk of NAFLD by involving different aspects of lipid metabolism.

PNPLA3 encodes for a protein called adiponutrin that is highly expressed on the ER and lipid membranes of hepatocytes and adipose tissue [76], under glucose and insulin regulation it exhibits triglyceride hydrolase activity towards TG and retinyl ester; disruption of this hydrolase activity due to the I148M variation can sequentially cause lipid droplets to accumulate [73]. The nonsynonymous substitution rs58542926 (c.449 C>T) within *TM6SF2* at the 19p13.11 locus, encodes an E167K amino acid substitution, it is associated with reduced hepatic lipid secretion via VLDL, resulting in hepatic steatosis and progressive fibrosis [74]. The enzyme lysophosphatidylinositol acyltransferase 1 (LPIAT1) is encoded by the *MBOAT7* gene, which catalyses the incorporation of arachidonic acid into phosphatidylinositol, it participates in the regulation of triglyceride metabolism through the phosphatidylinositol acyl-chain remodelling; rs641738 C > T polymorphism has been shown to predisposes individuals to fibrosis and cirrhosis in the case of alcohol misuses [77], [78]

NAFLD is a complex disease, any one genetic variant alone is insufficient for risk stratification, however, the combination of multiple genetic variants or even just with

an additional parameter such as exogenous dietary intake can compromise cellular metabolic activities, which would have an implication in the development and progression of NAFLD.

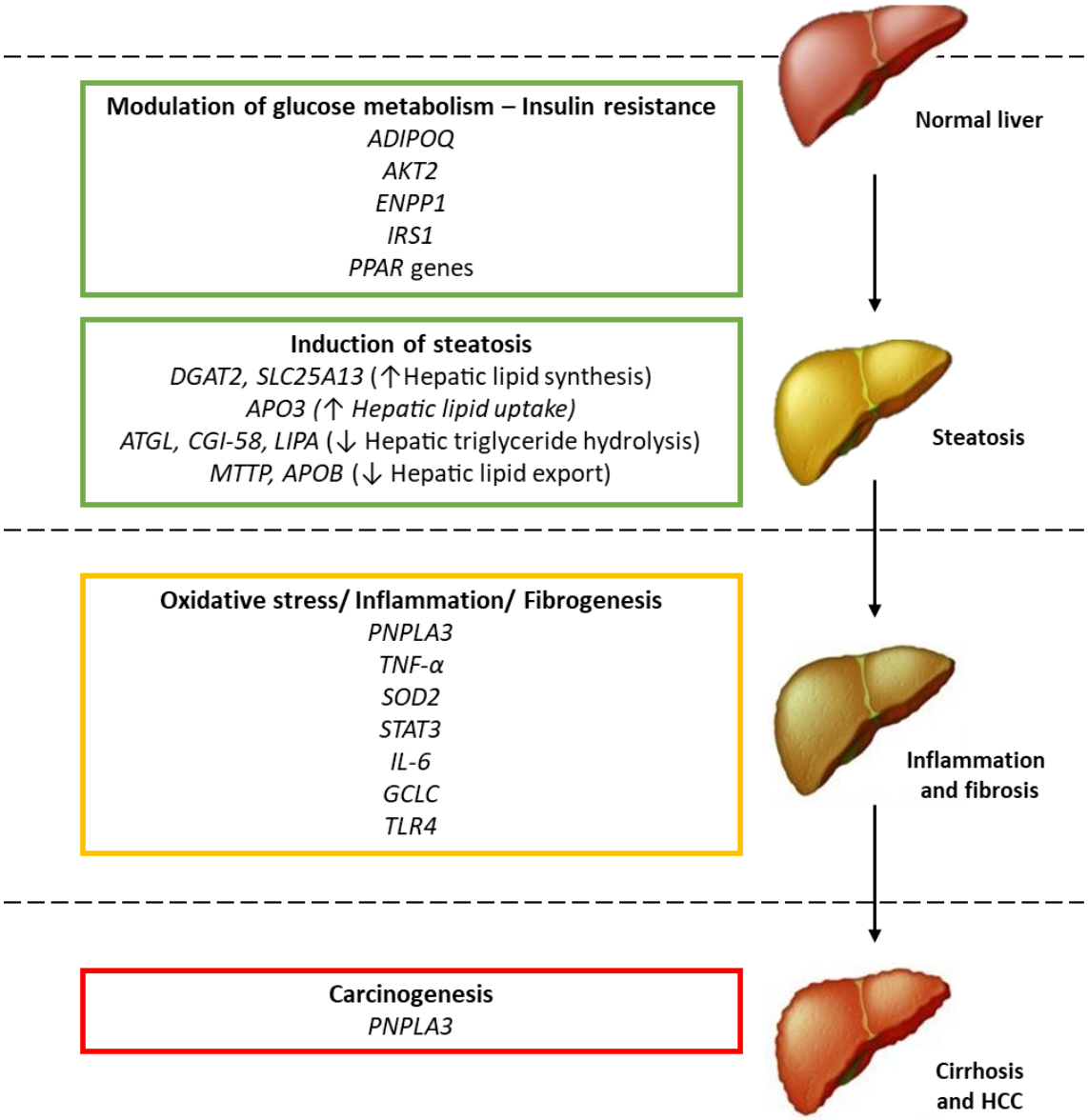


Figure 1.6. Overview of the genetic variants that may be involved in NAFLD susceptibility and progression. Illustration adapted from [79], [80].

Potential implication of novel MTTP-p.I564T single nucleotide variation in NAFLD progression

In addition to lifestyle and environmental factors, genetic predispositions of genes involved in lipid metabolism can often contribute to the higher risks of susceptibility and severity of NAFLD. One of the genetic variants that have been identified in modifying lipid metabolism is *MTTP*; the enzyme microsomal triglyceride transfer protein (MTP) is ubiquitously found in the lumen of the endoplasmic reticulum and, to a lesser extent, in the Golgi apparatus, of both hepatocytes and enterocytes [81]. MTP is a major cellular protein that catalyses the transfer of neutral lipids (triglycerides and cholesterol esters) between membrane vesicles by assisting the assembly and secretion of apolipoprotein B (apoB) [27]. MTP is an essential chaperone incorporating hepatic triglycerides into apoB-containing very-low-density lipoprotein (VLDL) for lipid export from the liver to blood circulation [82].

The main role of MTP is to shuttle small amount of lipids such as triglycerides (TGs), cholesteryl esters (CEs) and phospholipids from the ER membrane to the nascent apoB (apoB-48 in the intestine and apoB-100 in the liver) during translocation to form a primordial apoB particle. These lipid droplets would then be added to the primordial apoB particle and secreted as chylomicrons or VLDL post-translationally [83]. Defect of the MTP protein would limit the transfer enzymatic activity and cause a significant reduction in apolipoproteins B-48 and B-100, which are used in the synthesis and exportation of chylomicrons and VLDL to the plasma, this can subsequently lead to TG accumulation within the liver, resulting in hepatic steatosis (**Figure 1.7**).

Clinically, it has been shown that defective or missing MTP function may lead to a rare autosomal recessive disorder called abetalipoproteinemia (ABL; Online Mendelian Inheritance in Man database 200100) [84]; failure of apoB-containing lipoproteins assembly and secretion would result in fat malabsorption, lipo-soluble vitamin deficiency, subsequent steatorrhea, as well as fat-filled hepatocytes and enterocytes [27]. Multiple point mutations within the *MTTP* gene have been

identified causing various conditions; such as ABL [85], hypocholesterolaemia and hypotriglyceridaemia [86], increased risk of ischemic heart disease [87], hepatic steatosis [88], NASH and fibrosis [89].

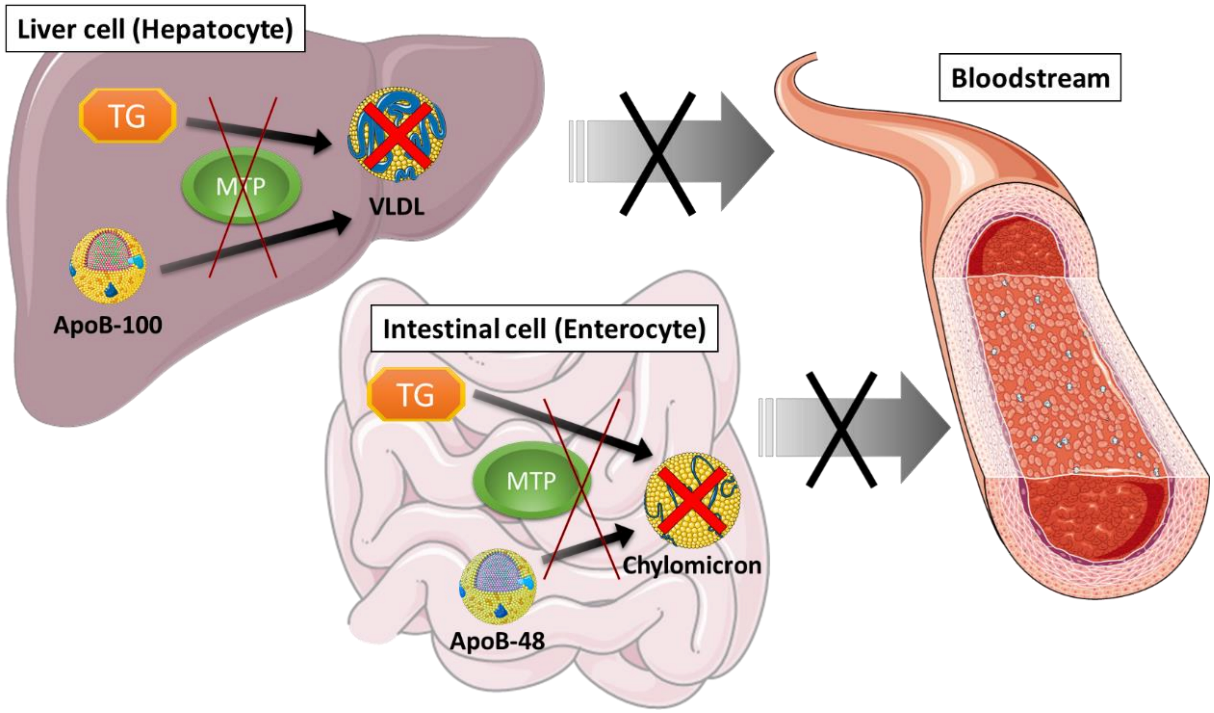


Figure 1.7 Role of MTP in apoB-containing lipoproteins assembly and secretion to the bloodstream. MTP is responsible for transferring triglycerides (TGs) onto apoBs (apoB-100 in liver, apoB-48 in intestine) in the assembly of hepatic very-low-density lipoprotein (VLDL) and intestinal chylomicron, which would then be secreted into the bloodstream. Basic structure is thought to be similar to that of cytoplasmic lipid droplets as they both contain a lipid ester core and the surface phospholipid monolayer. The VLDL formation in hepatocytes starts by co-translational lipidation of apoB, which makes the primordial lipoprotein particle, or pre-VLDL. The pre-VLDL then acquires additional lipids by fusing with apoB-free lipid particles in the ER or in post-ER compartments, the mature VLDL is then ready for exocytosis. MTP is an important enzyme for the formation of pre-VLDL and the apoB-free lipid particles. If insufficient lipid is transferred due to a defect or absence of MTP, the emerging apoB will be destroyed and inhibit lipoprotein secretion, which consequently lowers plasma lipids.

We have identified an atypical *MTTP* genetic variant that can cause hereditary and progressive NAFLD, but without any manifestations of ABL, which has not been previously described. We have access to a unique patient cohort of a large four generation family that has multiple members with a rare *MTTP*-p.I564T (c.1691T>C; rs745447480) single nucleotide variation (SNV), causing a missense point mutation

changing from a T to C nucleotide resulting a replacement of isoleucine (Ile) to threonine (Thr) at residue position 564 on the G chain of MTP protein (**Figure 1.8A**). Family members with different homozygous and heterozygous *MTTP*-p.I564T variant experienced different degrees of NAFLD, several of the homozygous individual have progressed to NASH, cirrhosis, HCC, and even liver failure, which subsequently would have to undergo liver transplantation.

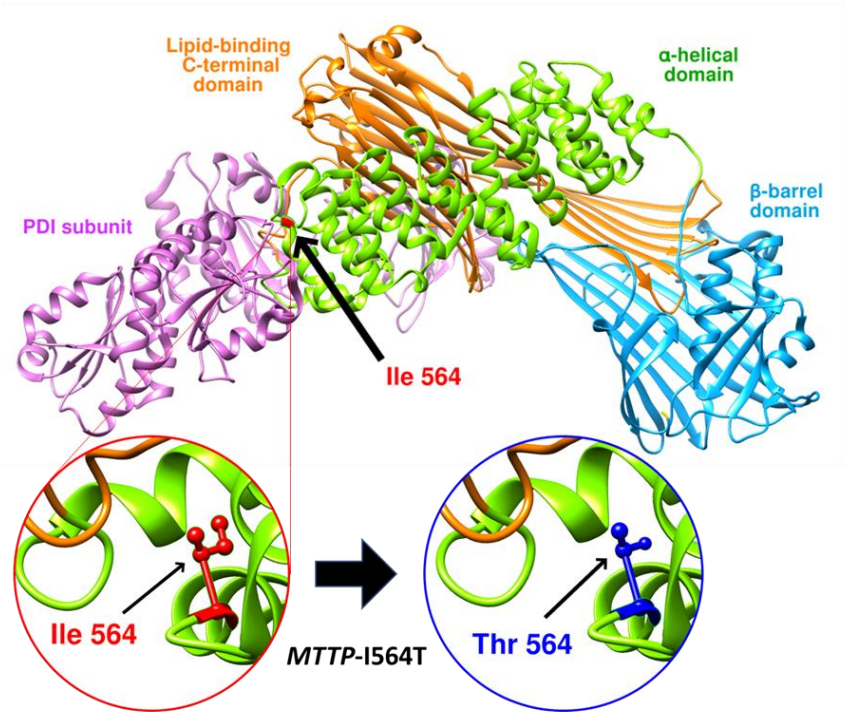
To obtain a basic insight of the potential mechanisms of action of this lipid transfer enzyme, it is essential to examine how the structure alteration may implicate in MTP functions. **Figure 1.8A** illustrate the structure of MTP-PDI protein complex, it is a heterodimer comprised of a unique large MTP α-subunit (~97kDa) and a multifunctional protein disulphide isomerase (PDI) β-subunit (~55kDa) [90]. The MTPα subunit comprises three distinctive domains including 1) N-terminal half β-barrel (amino acids (AA) 21 to 297), suggested to be involved in interactions with apoB [91]; 2) an α-helical domain (AA 298-603), interacts with PDI and apoB [91], [92]; and 3) a C-terminal domain (AA 604-884), the lipid-binding site is sandwiched between two β-sheets formed by A- and C-sheets [93]. The MTPα is responsible for the lipid-binding activity, the PDI subunit has an important role in oxidative protein folding in the ER [93].

DynaMut computational simulation allowed us to visualise the protein conformation and analyse the impact of mutations on protein dynamics, flexibility and stability; we have performed conformation simulation based on the PDB structure 617S (PDB accession number for MTP) [94]. The *MTTP*-p.I564T variant causes the original wildtype amino acid isoleucine (Ile) replaced by a threonine (Thr) at residue position 564 on the G chain, which is located in the α-helical domain within the MTPα subunit, which does not lie in the active lipid binding site or in the PDI functional region (**Figure 1.8A**). DynaMut simulation demonstrates that the T-C codon substitution possibly impacts on mRNA or protein stability/turnover and potentially alter the partner interaction with the PDI subunit, this could reduce the protein activity resulting a different phenotype to that of ABL (**Figure 1.8B**). Further analysis is required in order

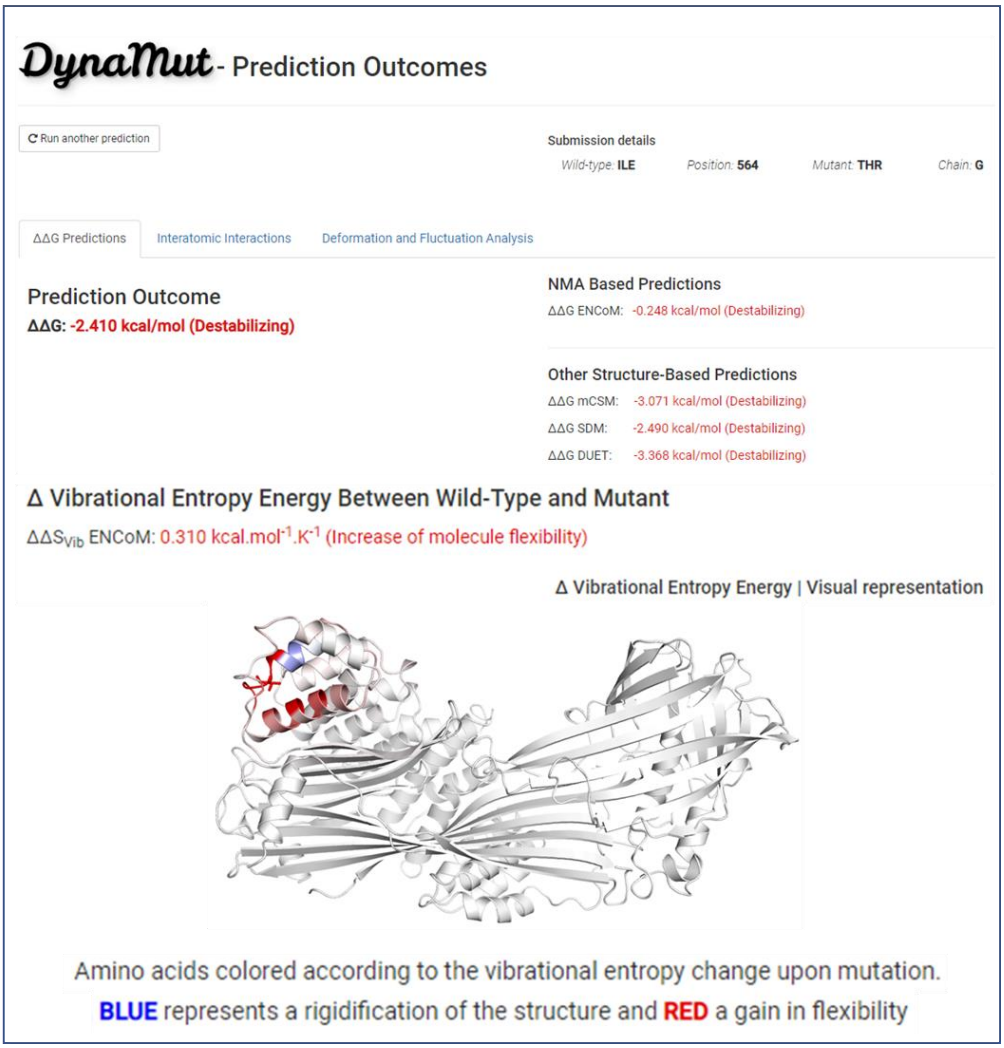
to understand how this rare *MTTP*-p.I564T differs from the other *MTTP* polymorphism. There is a need of using simplified stem cell-derived cell models to investigate how *MTTP*-p.I564T polymorphism can directly impact cellular behaviour and functionality on different cell types.

Figure 1.8 Impact of *MTTP*-p.I564T SNV upon MTP protein structure. (below) (A) Ribbon representation of the *MTTP*-p.I564T single nucleotide variation. Illustration shows the *MTTP*-p.I564T point mutation that causes a change in amino acid residue at position 564 from isoleucine (Ile) to threonine (Thr). This leads to a local structural change and affecting the overall MTPα-PDI complex stability. **(B)** Prediction outcome using the web-based server DynaMut to analyse the impact of *MTTP*-p.I564T on protein conformation, flexibility and stability. The replacement of Ile (WT) to Thr (VAR) at position 564 on chain G can destabilise the MTTP protein due to an increase of molecule flexibility.

A


Lipid-binding
C-terminal
domain
α-helical
domain
β-barrel
domain
PDI subunit
Ile 564
Ile 564
MTTP-I564T
Thr 564

B


DynaMut - Prediction Outcomes
Run another prediction
Submission details
Wild-type: ILE
Position: 564
Mutant: THR
Chain: G
ΔΔG Predictions
Interatomic Interactions
Deformation and Fluctuation Analysis
Prediction Outcome
ΔΔG: -2.410 kcal/mol (Destabilizing)
NMA Based Predictions
ΔΔG ENCoM: -0.248 kcal/mol (Destabilizing)
Other Structure-Based Predictions
ΔΔG mCSM: -3.071 kcal/mol (Destabilizing)
ΔΔG SDM: -2.490 kcal/mol (Destabilizing)
ΔΔG DUET: -3.368 kcal/mol (Destabilizing)
Δ Vibrational Entropy Energy Between Wild-Type and Mutant
ΔΔSVib ENCoM: 0.310 kcal.mol-1.K-1 (Increase of molecule flexibility)
Δ Vibrational Entropy Energy | Visual representation
Amino acids colored according to the vibrational entropy change upon mutation.
BLUE represents a rigidification of the structure and RED a gain in flexibility

1.4 Disease models for NAFLD

To further understand NAFLD phenotypes and its cellular and molecular mechanisms, several approaches have been undertaken to create disease models *in vitro* and *in vivo*, summary of the different approaches used to model NAFLD is presented in **Table 1.1**.

Animal models have played a vital role in elucidating the pathophysiological mechanisms of NAFLD in the past and continue to do so, mice and rats have been used most frequently in NAFLD modelling [64], [72], [95], [96]. In rodent models, steatosis is often induced through provision of excess energy substrates such as high-carbohydrate [70] Alternatively, by introducing gene modifications of genes that may be involved in lipid metabolism can help evaluate the role and influence toward NAFLD progression. Transgenic or knockout (KO) studies have been reported for modelling NAFLD and NASH, such as LDL receptor (KO) [97], circadian locomotor output cycles kaput (CLOCK) mutant ($Clk^{\Delta 19/\Delta 19}$) [98]; lysosomal Acid Lipase (KO) [99], *Fat-1* transgenic breeder mice [100]; they were shown to have an implication in the dysregulation of lipid metabolism and promote hepatic steatosis. However, it is vital to be aware that results obtained in an animal model may translate differently in human population and recapitulating all features is still lacking, which could have a major impact especially for the use of pre-clinical or clinical studies.

An example was the use of the phosphodiesterase-4 inhibitor ASP9831 to be tested in a clinical trial; it was shown to be able to lower alanine transaminase (ALT) levels, necroinflammation and fibrosis in both an acute hepatitis model and a methionine and choline deficient (MCD) diet NASH model, however, the compound failed to generate similar results in humans and failed in the subsequent clinical trial [101]. Other pharmacological compounds such as the hypolipidemic agent ezetimibe and the antioxidant resveratrol also have been very successful in preclinical studies, despite of elaborate pre-clinical investigations as a promising therapeutic target in animal models, only to fail in human clinical trials [102], [103]. It is therefore necessary to be critical choosing the best suited animal model relative to the matter

under investigation, as well as taking into account the species difference when interpreting animal-based research.

In addition to the nature of species difference, research using animal models also include a much higher cost and logistics compared to simple cell models. Ethical concerns over the use of research animals are often a controversy topic. Based on the type of animal models, various expertise may be needed to operate surgery and specific culture conditions. Due to the complexity of different animal models, it is also difficult to recapitulate disease states faithfully. Therefore, it is essential to develop a simplified disease model that can overcome these issues. Using human cell models *in vitro* allows us to have higher control over the culture conditions and to have direct comparison of the cell states to elucidate disease mechanism insights.

In vitro models such as primary cell cultures and immortalised cell lines have been widely employed in recent years [104]–[110], they utilise the culturing of isolated tissue components of an organ, while preserving many aspects of the *in vivo* environment by adjusting and manipulating the culture conditions. *In vitro* models can minimise experimental variables to effectively isolate various organ components or structures enabled research to be performed under well-controlled, reproducible, and easily assessed conditions. Primary human hepatocytes (PHHs) [104], [107], Kupffer cells [105], liver sinusoidal endothelial cells [105], and HSC [106] seem to be physiologically relevant model for NAFLD clinical conditions; however, limited number of primary samples and relatively difficult, labour-intensive isolation procedure make it extremely complicated to use primary cultures [111].

Dedifferentiation can also occur in PHHs, resulting in the loss of cellular phenotype in culture, this particularly hinders their utility in long-term *in vitro* studies; it has been shown that molecular lipid profile and lipid-metabolising enzyme expression of the dedifferentiating PHHs was massively altered during their prolonged culture [112], making it less reliable as a disease model. Moreover, heterologous expression of mammalian hepatic genes due to donor-to-donor variation may also generate biased

interpretation of the analysed results. Hepatic immortalised cell lines such as HepG2 are often obtained from resected tumour tissue; alternatively, artificially generated by the genetic modification of PHH via overexpress of viral oncogenes (e.g. SV40, HPV16) or human telomerase reverse transcriptase (hTERT) [113]. In contrast to primary cells, immortalised cell lines are readily available, with unlimited growth potential and high reproducibility [114]. Nevertheless, due to their malignant cancerous origin or the immortalisation procedure, certain metabolic functions including insulin signalling, glucose and lipid metabolism can be altered towards an aberrant phenotype and thus limit a direct comparison to the human situation [115], especially when studying NAFLD.

The emergence of human induced pluripotent stem cells (hiPSCs) can circumvent the ethical issue of animal models and it allows the derivation of patient-specific hiPSC line to produce hepatocyte-like cells (HLCs) and other lineage cell types, which resemblance the genotype and phenotype of NAFLD [116]–[119]. HiPSCs also pose as an unlimited source for large-scale expansion in many clinical and industrial applications, which can be beneficial by diminishing the variability in genetic profiles and quality between samples [118], [120], [121]. The capacity of hiPSCs for self-renewal and differentiation into almost any cell type provides a unique system for generating large quantities of autologous, disease-specific hepatocytes *in vitro*, which would be an optimal platform for modelling hepatic disorders, drug discovery and toxicity tests [122]; as well as a great source for regenerative medicine and cell therapy [123]–[126]. Patient-specific hiPSC-derived HLCs have been used previously to model drug-induced hepatotoxicity and for lipidomic profiling [127], [128].

Here we propose to develop donor-specific hiPSC-derived HLCs as a novel platform to model the inherent effect of *MTTP*-p.I564T genetic variation and exogenous influences of fatty acid-induced steatosis to evaluate the relationship between genetic predisposition and lipotoxicity in hiPSC-HLCs NAFLD model.

Table 1.1 Summary of advantages and challenges of different approaches for modelling NAFLD.

Disease model	Examples	Pros	Cons
Animal models	- Dietary-induced (*In vivo*) [70] - Genetically modified animals (*In vitro,* Transgenic/ gene knockout) [97]	- Genetically tractable. - Easily available cell and tissue samples - Enables study of whole organ (or organism)	- Species-differences (relative to human) - Time-consuming genetic manipulation - Cost and labour-intensive - Ethical issues
Isolated human primary cell cultures (monoculture/ co-culture/ 3D culture)	- Hepatocytes (from healthy and/or NAFLD patients) [104] - Kupffer cells and liver endothelial cells [105] - Hepatic stellate cells [106] - 3D hepatocyte spheroid [107]	- Physiologically relevant - Mimic *in vivo* settings and architecture - Important tools in cellular cross talk studies	- Isolation problems - Donor-to-donor variation - Limited culture time - Difficult to cultivate
Immortalized cell lines/ Hepatocellular carcinoma-derived cell lines	- Mouse macrophage RAW 264.7 cells [108] - Mouse hepatocytes AML-12 [129] - Mouse monocytes-macrophage J774A [109] - Human hepatocellular carcinoma-derived cell line HuH7, HepG2 [110]	- Continuous growth - Easy to culture - Stable phenotype	- Expression of several enzymes and nuclear factors alter according to the immortalization method - Diseased pre-existing condition
hPSC-derivatives (2D / 3D culture)	- hiPSC-HLCs [118], [130], [131] - hESC-HLCs [130], [132] - hPSC-HLCs, endothelial cells, stellate cells [133]	- Unlimited source - Species relevant - Genetic modification to correct or introduce specific mutation - Co-culture with different hPSC-derived cell types - Large-scale expansion - Prolonged experimentation (enables performing chronic studies)	- Immaturity - Immature phenotyping readouts - Differentiation protocol needs to be optimised

1.5 Hypothesis and aims

The central hypothesis of this thesis is that donor-derived hiPSC-HLCs can model hepatic steatosis in NAFLD *in vitro* and help us gain mechanistic insights for potential therapeutic targets and biomarker for a rare *MTTP*-p.I564T single nucleotide polymorphism (SNP).

To test the hypothesis, the following objectives will need to be achieved:

- Reprogramming donor-derived human dermal fibroblasts into hiPSCs.
- Optimisation of hepatocyte differentiation protocol to generate HLCs that are relatively more mature and phenotypically relevant to accurately model NAFLD.
- Generate an *in vitro* steatosis model by inducing lipid accumulation using extraneous fatty acid to mimic modern Western diet.
- Validate the utility of hiPSC-HLCs to model NAFLD *in vitro* and demonstrate their ability to recapitulate hallmarks of the disease.
- Identification of potential therapeutic targets and biomarkers using multi-omics profiling.

Chapter 2.

Materials and Methods

Chapter 2. Materials and Methods

2.1 Cell culture

All cell culture was carried out in a type II Biological Safety Cabinet. Cells were maintained at 37°C in a humidified atmosphere with 5% CO_2. Culture media and enzymes were warmed to 37°C in a water bath prior to use. All bright-field images of live and fixed cells were captured using a Nikon Eclipse TE2000-S inverted microscope, unless stated otherwise.

2.1.1 Media

All media, once prepared, were stored at 4°C for up to 2 weeks and warmed up to 37°C before being applied to the cells. Table 2.1 lists the composition of all the different media used in this thesis.

Table 2.1 Composition of culture media.

Medium and Use	Component	Supplier and Identifier	% (vol/vol) / Final conc.
HDF medium: Human dermal fibroblast growth medium.	DMEM (Basal medium)	Gibco, #21969-035	85%
	Antibiotic-Antimycotic (100X)	Gibco, #15240-062	2%
	Foetal bovine serum (FBS)	Gibco, #10270106	10%
	GlutaMAX™ Supplement	Gibco, #35050-038	1%
	Non-Essential Amino Acids (NEAA, 100X)	Gibco, #11140-050	1%
	Penicillin-Streptomycin (10,000 U/mL)	Gibco, #15140-122	1%
Commercial TeSR E7 medium: For reprogramming.	TeSR E7 (Basal medium)	Stem Cell Technologies, #05919	96%
	TeSR E7 (25X Supplement)	Stem Cell Technologies, #05915	4%
Commercial TeSR E8 medium: For hPSC culture.	TeSR E8 (Basal medium)	Stem Cell Technologies, #05991	96%
	TeSR E8 (25X Supplement)	Stem Cell Technologies, #05992	4%
HB E8 medium: Home-brew E8 medium for hPSC culture. (adapted from [134])	DMEM/F12 50/50 mix (Basal medium)	Corning, # 10-092-CM	99.85%
	L-ascorbic acid 2-phosphate tri sodium salt	Sigma-Aldrich, # 49752	64 µg/ml
	Heparin sodium salt	Sigma-Aldrich, #H3149	100 ng/ml

	Sodium selenite	Sigma-Aldrich, #S5261	14 ng/ml
	Transferrin	Sigma-Aldrich, #T3705	5 µg/ml
	Insulin (INS)	Sigma-Aldrich, #11376497001	20 µg/ml
	FGF2 (basic)	**Peprotech, #100-18B**	**100 ng/ml**
	TGF-β1	**Peprotech, #100-21**	**2 ng/ml**
CDM3 medium: Chemically defined medium, 3 components; for mesoderm induction (adapted from [135]).	RPMI 1640 (Basal medium)	Gibco, #21875034	98.6%
	Ascorbic acid-2-phosphate	Sigma-Aldrich, #A8960	213 µg/ml
	Albumin	Sigma-Aldrich, #A0237	500 µg/ml
	CHIR99021 (CMD3 Supplemented from day 0 to day 2 only)	**Tocris, #4423**	**4 µM**
	WntC59 (CMD3 Supplemented from day 2 to day 3 only)	**Abcam, #ab142216**	**2 µM**
NE medium: Medium for neuroectoderm induction (adapted from [136]).	RPMI 1640 (Basal medium)	Gibco, #21875034	97%
	B-27™ Supplement (50X)	Gibco, #17504044	2%
	NEAA (100X)	Gibco, #11140050	1%
	SB431542	**Tocris, #1614**	**10 µM**
	FGF2 (basic)	**R&D, #233-FB**	**12 ng/ml**
DE medium: Definitive endoderm differentiation medium. (adapted from [137])	RPMI 1640 (Basal medium)	Gibco, #21875034	96%
	B-27™ Supplement (50X)	Gibco, #17504044	2%
	NEAA (100X)	Gibco, #11140050	1%
	Pen-Strep (10,000 U/mL)	Gibco, #15140-122	1%
	Activin A	**Peprotech, #120-14P**	**100 ng/ml**
	Wnt-3a	**R&D, #5036-WN**	**50 ng/ml**
FG medium: Foregut differentiation medium. (adapted from [138])	RPMI 1640 (Basal medium)	Gibco, #21875034	96%
	B-27™ Supplement (50X)	Gibco, #17504044	2%
	NEAA (100X)	Gibco, #11140050	1%
	Pen-Strep (10,000 U/mL)	Gibco, #15140-122	1%
	Activin A	**Peprotech, #120-14P**	**50 ng/ml**
HE medium: Hepatic endoderm differentiation medium.	RPMI 1640 (Basal medium)	Gibco, #21875034	96%
	B-27™ Supplement (50X)	Gibco, #17504044	2%
	NEAA (100X)	Gibco, #11140050	1%
	Pen-Strep (10,000 U/mL)	Gibco, #15140-122	1%
	BMP4	**R&D, #314-BP**	**0-10 ng/ml (cell line dependent)**
	FGF10	**Peprotech, #100-26**	**20 ng/ml**
	SB431542	**Selleckchem, #S1067**	**10 µM**
OM (Old Maturation) medium: Hepatocyte maturation medium. (adapted from [139])	HepatoZYME-SFM (Basal medium)	Gibco, #17705021	93%
	Chemically Defined Lipid Concentrate	Gibco, #11905031	2%
	GlutaMAX™ Supplement	Gibco, #35050-038	1%
	NEAA (100X)	Gibco, #11140050	2%
	ITS Premix Supplement	Corning, #354352	1%

	Pen-Strep (10,000 U/mL)	Gibco, #15140-122	1%
	HGF	**Peprotech, #100-39H**	**50 ng/ml**
	Oncostatin-M (OSM)	**Peprotech, #300-10H**	**30 ng/ml**
NM (New Maturation) medium: Optimised hepatocyte maturation medium we developed.	HepatoZYME-SFM (Basal medium)	Gibco, #17705021	96%
	Chemically Defined Lipid Concentrate	Gibco, #11905031	1%
	GlutaMAX™ Supplement	Gibco, #35050-038	1%
	NEAA (100X)	Gibco, #11140050	1%
	Pen-Strep (10,000 U/mL)	Gibco, #15140-122	1%
	DKK-1	**Peprotech, #120-30**	**100 ng/ml**
	FGF10	**Peprotech, #100-26**	**200 ng/ml**
	FGF2 (basic)	**Peprotech, #100-18B**	**100 ng/ml**
	HGF	**Peprotech, #100-39H**	**10 ng/ml**
	Hydrocortisone (HC)	**Sigma-Aldrich, #H2270**	**10 µM**
	Insulin (INS)	**Sigma-Aldrich, #11376497001**	**10 µg/ml**
	Noggin	**Peprotech, #120-10C**	**100 ng/ml**
	Oncostatin-M (OSM)	**Peprotech, #300-10H**	**20 ng/ml**
HG medium: Hindgut differentiation medium.	RPMI 1640 (Basal medium)	Gibco, #21875034	96%
	B-27™ Supplement (50X)	Gibco, #17504044	2%
	NEAA (100X)	Gibco, #11140050	1%
	Pen-Strep (10,000 U/mL)	Gibco, #15140-122	1%
	CHIR99021	**Tocris, #4423**	**3 µM**
	Retinoic acid (RA)	**Sigma-Aldrich, #R2625**	**1 µM**
IO medium: Growth medium for 3D intestinal organoid differentiation. (adapted from [140], [141])	Advanced DMEM/F-12 (Basal medium)	Gibco, #12634010	93%
	B-27™ Supplement (50X)	Gibco, #17504044	2%
	GlutaMAX™ Supplement	Gibco, #35050-038	1%
	HEPES Buffer Solution	Gibco, #15630056	1%
	N-2 Supplement (100X)	Gibco, #17502001	1%
	N-Acetyl-L-cysteine (NAC)	Sigma-Aldrich, #A7250	1 mM
	Nicotinamide	Sigma-Aldrich, #N0636	10 µM
	Pen-Strep (10,000 U/mL)	Gibco, #15140-122	1%
	[Leu15]-Gastrin I human	**Tocris, #G9145**	**10 nM**
	A83-01	**Tocris, #2939**	**500 nM**
	CHIR99021	**Tocris, #4423**	**6 µM**
	EGF	**Peprotech, #AF-100-15**	**100 ng/ml**
	Noggin	**Peprotech, #120-10C**	**100 ng/ml**
	R-Spondin-1	**Peprotech, #120-38**	**100 ng/ml**
	SB202190	**Tocris, #1264**	**10 µM**

2.1.2 Isolation and derivation of human fibroblasts from human dermal tissue

Participants were recruited to the study at Queens Medical Centre, Nottingham University Hospitals between 1/11/2016 and 1/6/2017. The meal-response study was approved by the Health Research Authority after review by National Research Ethics Service Committee North-East (Ref 16/NE/0251) and was sponsored by Nottingham University Hospitals NHS Trust. The Genetics of Rare Inherited Disorders (GRID) study was approved by the Health Research Authority after review by National Research Ethics Service East Midlands Northampton Committee (Ref 12/EM/0262). The study was conducted according to the Declaration of Helsinki (Hong Kong Amendment) and Good Clinical Practice (European guidelines). All participants provided written informed consent. Skin biopsy material was collected into culture media and immediately processed for growth. Three 2-mm human skin punch biopsy samples were received from the Nottingham Digestive Diseases Centre obtained from three different donors with informed consent. These biopsy samples were from a male healthy donor (GF06), and two different family members (both female) with either a homozygous (GF10) or heterozygous (GF11) genetic variation of the microsomal triglyceride-transfer-protein (*MTTP*) gene respectively. In addition, GF10 donor also underwent a liver transplant prior to the skin biopsy collection.

Each biopsy sample was processed in a class 2 safety cabinet as soon as it arrived in the laboratory. The biopsy was dissected into 12 evenly sized pieces using a scalpel, each of the dissected skin biopsy pieces was transferred and plated into uncoated 6-well tissue culture plates. To ensure tissue attachment and cell outgrowth, a coverslip is placed on top of each piece and cultured in human dermal fibroblast (HDF, Table 2.1) medium at 37°C with 5% CO_2. HDF medium was replaced every 2-3 days and once fibroblasts were confluent in each well to the point where they reached the edges of the coverslip, HDFs were then trypsinised using 0.25% Trypsin-EDTA (Gibco, #25200072) for 3 min at 37°C and passaged into a T75 flask (passage 0) including the tissue pieces. Each HDF cell line were further expanded and routinely passaged in a ratio of 1:3-1:6; while a portion of cells was cryopreserved in heat-inactivated foetal

bovine serum (HI FBS; Gibco, #10500064) containing 10% dimethyl sulfoxide (DMSO; Sigma-Aldrich, #D2650) for future use. All cell lines were tested negative for mycoplasma contamination using the EZ-PCR Mycoplasma Test Kit (Biological Industries, #20-700-20) prior to reprogramming or for other experiments.

2.1.3 Generation of hiPSC in feeder-free condition

REBLPAT hiPSC line was reprogrammed from human dermal fibroblasts (HDFs) using Sendai virus (SeV) vector performed by Dr Gary Duncan at the University of Nottingham. CytoTune™-iPS 2.0 Sendai Reprogramming Kit (Invitrogen, #A16517) containing three Sendai virus (SeV) vectors (polycistronic Klf4–Oct3/4–Sox2; cMyc; and Klf4) was used to reprogram three patient-derived HDF lines (GF06, GF10 and GF11) according to the manufacturer's protocol with minor adjustments (Figure 2.1). Briefly, approximately 20,000 HDFs were seeded per well in a 6-well plate a day prior to transduction. 24h later, HDFs were transduced with SeV vectors in HDF medium (Table 2.1, without antibiotic) at a multiplicity of infection (MOI) of 5:5:3 (hKOS: hc-Myc: hKlf4). One day after transduction, the medium was replaced with fresh HDF medium. Transduced cells were cultured in HDF medium for 3-7 days of expansion. Once cells reached 80-90% confluency, they were dissociated using 0.05% Trypsin (Gibco, #25300062), resuspended in TeSR-E7 medium (Table 2.1) and transferred to Matrigel™ coated 6-well plates at a split ratio of 1:3. After passaging, the medium was replaced daily with TeSR-E7 medium to support the formation of hiPSCs. Once hiPSC colonies arose (usually between day 13-22 post transduction), culture medium was replaced with TeSR-E8 (Table 2.1) daily allowing the colonies to grow in size. From day 13-45 after reprogramming, hiPSC colonies were picked for expansion and characterisation using either 0.5 mM EDTA (Invitrogen, #15575020), or ReLeSR™ (STEMCELL Technologies, #05872).

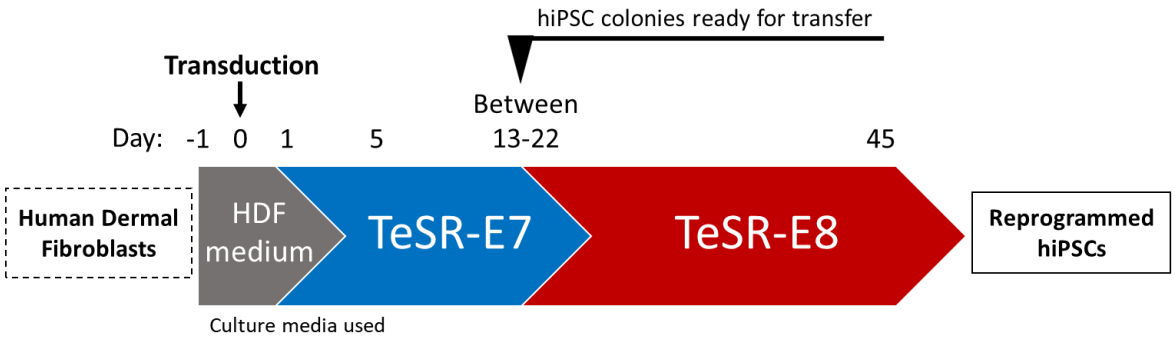


Figure 2.1 Schematic timeline of the protocol used to obtain iPSCs by the transduction of sendai virus vectors.

2.1.4 Colony isolation using EDTA or ReLeSR

When hiPSC colonies grew to approximately 500-1000 µm in diameter (10X) within the 6-well plate, they were ready to be isolated using EDTA or ReLeSR™. To isolate colonies using the EDTA method, cells were washed once with Dulbecco's Phosphate-Buffered Saline (DPBS; Gibco, #14190094), then incubated with 1 ml of 0.5 mM EDTA (0.5M EDTA stock diluted in DPBS) at 37°C for 3 min. EDTA solution was aspirated and replaced with TeSR-E8 medium, ready for picking.

Alternatively, 1ml of ReLeSR™ was added to the cells and aspirated within 1 min to allow colonies exposed to a thin film of liquid. Colonies were picked after 7-9 min incubation at room temperature (RT) according to manufacturer's instructions.
Using a microscope inside a sterile biological safety cabinet, each colony was picked using a P200 pipette and then transferred to a Matrigel™-coated 48-well plate containing 200 µl warm TeSR-E8 medium supplemented with 10 µM of Y27632 ROCK inhibitor (ROCKi; Tocris, #1254). Once transferred, colonies were mechanically triturated using the pipette to ensure even attachment of cells within the well. Thereafter, plated colonies were placed in the incubator and TeSR-E8 medium was changed daily.

2.1.5 Human induced pluripotent stem cell (hiPSC) culture and maintenance

Essential 8 (E8) medium was used to culture human induced pluripotent stem cells (hiPSCs). E8 medium used in this thesis was either a commercially available TeSR™-E8™ medium (Stem Cell Technologies, #05990), or an in-house manufactured E8 (HB E8, Table 2.1) following the previously described formulation, with an addition of 100 ng/ml heparin sodium salt [142]. For routine culture, all hiPSCs including REBLPAT and patient-derived cell lines (LOPCK from GF06, MOPIK from GF10 and HETIK from GF11) were maintained in either HB E8 or TeSR-E8 medium on Matrigel™ (Corning, #354230)-coated Nunc™ plasticware (Thermo-Fisher) in a 37°C incubator. Matrigel was diluted in cold Dulbecco's Modified Eagle Medium (DMEM; Gibco, #21969-035) at a density of 34.7µg/cm^2 and coated onto the plastic surface, it was left to polymerise for at least 1 hour to overnight at 37°C to ensure even coating.

HiPSCs were passaged every 3-4 days (75-90% confluent) by washing once with Ca2+/ Mg2+-free Dulbecco's phosphate-buffered saline (DPBS, Gibco #14190169), followed by incubation with TrypLE™ Express (Gibco, #12604021) for 3-5 mins at RT until cells have visibly detached. After gently dislodging the cells, TrypLE™ was quenched by washing cells in HB E8 or TeSR-E8 medium to obtain single cell suspension. Cells were then centrifuged at 200 x g for 3 min and resuspended in E8 supplemented with 10µM ROCKi and seeded at a split ratio of 1:10-1:20 (cell line dependent) at approximately 20,000 cells/cm^2. Cells were maintained in ROCKi-supplemented medium for the first 24 hours only, E8 medium was changed daily after passaged.

2.1.6 Differentiation of hiPSCs

All hiPSCs were manually counted using a haemocytometer and seeded at the desired density in the presence of 10 µM ROCKi for the first 24 hours as previously described.

Formation of mesodermal and ectodermal progenitor cells

Mesoderm progenitor cells were generated according to the differentiation method described by Burridge et al. (2014). HiPSCs were dissociated using TrypLE as described

(**section 2.1.5**) and seeded at 20,000 cells/cm^2 on Matrigel™-coated 48-well plate. 72h after seeded, E8 medium was replaced to CDM3 medium and changed every 48h (**Table 2.1**). 4 µM of CHIR99021 was supplemented in CDM3 medium from differentiation D0 to D2 only; after D2 CDM3 was supplemented with 2 µM of WntC59 instead. On D3, differentiated cells were fixed and used for immunocytochemistry.

Induction to neuroectoderm lineage was adapted from the protocol described in Vallier et al. (2009), hiPSCs plated onto Matrigel™-coated 48-well plate at a density of 50,000 cells/cm^2. 24h after seeding, E8 medium was replaced with NE medium (**Table 2.1**) and cultured for 7 days (medium replaced daily). Cells were fixed at D7 and immunostained for neuroectoderm markers.

Formation of definitive endoderm, foregut, hepatic endoderm, and hepatocyte-like cells (HLCs)

Undifferentiated hiPSCs were dissociated into single cells using TrypLE™ Select Enzyme, they were then resuspended in E8/TeSR-E8 medium supplemented with 10µM Y27632 and plated at a density of 15,000-20,000 cells/cm^2 (cell line dependent) onto Matrigel™-coated vessel with a minimum of two biological replicates. Seeding densities were optimised for individual hiPSC line based on their growth rate.

Definitive endoderm (DE) differentiation was initiated 48h after seeding (D0) when cells were approximately 50% confluent, hiPSCs were cultured in DE medium (**Table 2.1**; adapted from Hay et al. (2008a) for 3 days (D0-D3). To generate foregut (FG) population, DE medium was replaced after 72h to FG medium (**Table 2.1**) for 2 days (D3-D5) as previously described by Hannan et al. (2013). Hepatic endoderm (HE) specification (D5-D9) was achieved using the HE medium (**Table 2.1**) for 4 days, BMP4 concentration was optimised to each hiPSC line. To induced hepatocyte-like cells (HLCs) maturation (D9-D19), HE medium was replaced to the NM medium (**Table 2.1**) we developed for 10 days. HLCs cultured in NM medium (**Table 2.1**) were harvested or fixed on D19 for qPCR and immunostaining, in comparison to HLCs generated by OM medium. **Figure 2.2** illustrates the timeline of the complete hepatic

differentiation procedure; medium was changed daily from DE to HE stages, whereas during HLC maturation stage medium was changed every 48h.

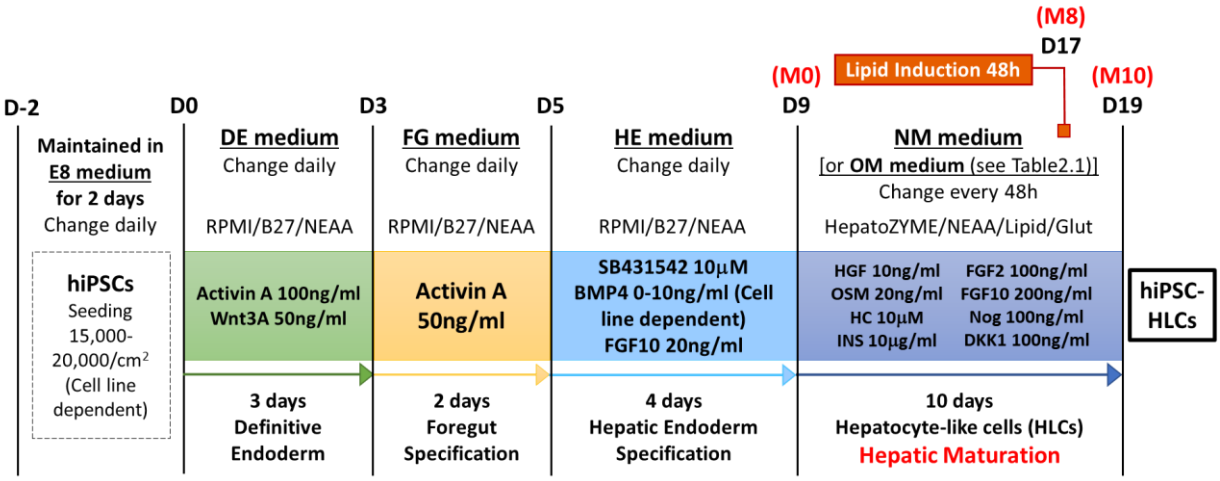


Figure 2.2 Schematic diagram of the four-stage stepwise strategy to induce hiPSC differentiation into HLCs, which takes total of 21 days (from seeding D-2).

Optimisation of hepatocyte maturation using small molecules

Three small molecule (SM) candidates PNU-74654 (PNU; TOCRIS, #3534), IWP-4 (TOCRIS, #5214) and LDN-193189 (LDN; TOCRIS, #6053) were used in replacement of the recombinant proteins Dickkopf-related protein 1 (DKK-1) and Noggin in NM medium (Table 2.1) mentioned in **section 2.1.6**. A dose response experiment was conducted to determine toxicity, DKK-1 was substituted by PNU or IWP-4 at a concentration ranging from 0.05µm to 1µm; Noggin was substituted by LDN between 0.1µM to 1µM. After hepatocyte maturation, HLCs were harvested and their gene expression were analysed by qPCR. To determine the combine effect of the two selected SM candidates (0.25µM of PNU and 1µM of LDN), a time-course experiment was conducted in comparison to the single SMs and the original recombinant protein-based NM medium, differentiating cells were harvested every 5 days from maturation day 0 (M0, equivalent to differentiation D9) up to day 25 (M25 = diff D36) for qPCR analysis.

Formation of hindgut and intestinal organoids

After differentiation into definitive endoderm [section 0, D0-D3], hindgut (HG) induction was achieved by replacing DE medium to HG medium (**Table 2.1**) for 7 days

(D3-D9), medium was changed daily. At differentiation D9, 2D culture was transitioned into 3D culture to promote spontaneous rearrangement of cells into intestinal organoids (IOs) (adapted from Fair et al., 2018; Spence et al., 2011). Briefly, 2D monolayer of HG cells were washed once with cold DPBS and scraped off into fragments using a 5ml stripette. Fragmented cells were collected and centrifuged at 400 x g for 1 min. Supernatant was carefully aspirated and the pellet was resuspended in IO medium (**Table 2.1**, supplemented with 10 µM ROCKi) mixed with phenol-red free Matrigel™ (Corning, #356231); IO medium-to-Matrigel™ ratio is 1:2. Fragmented cells were embedded in Matrigel™ and dispensed as droplets (30-40µl per droplet) into each well of a pre-warmed 48-well plate. The plate was placed in 37°C incubator for 10-15 min to allow the Matrigel™ polymerisation; once the Matrigel™ was solidified, IO medium (with 10 µM ROCKi) was overlaid and replaced every 3-4 days (without ROCKi). To expand the culture, organoids were split every 4-10 days (depending on growth rate) in a 1:4-1:6 ratio using mechanical dissociation, but with the addition of multiple ice-cold DPBS washes (400 x g, 1 min) to break up the organoids dome and remove excess Matrigel™. After at least 40 days of maturation, IOs (at D53) were treated with palmitic acid (PA; 0 µm or 300 µM) for 48h, spent media were collected (at D55) to measure apolipoprotein B-100 (ApoB-100) levels in comparison to that of PA-treated HLCs.

2.1.7 Fatty acid (FA) preparation and treatment

Linoleic acid (LA; #L1376), oleic acid (OA; #O1008) and palmitic acid (PA; #P0500) were all purchased from Sigma-Aldrich.

Preparation of 24% (w/v) fatty-acid-free bovine serum albumin (BSA) for fatty acid binding

6g of fatty-acid-free bovine serum albumin (BSA; Sigma-Aldrich, #A6003) was dissolved in 17.5ml of 150mM sodium chloride (NaCl) at RT. Once dissolved, the pH was adjusted to 7.4 with 5M sodium hydroxide (NaOH) and the final total volume was increased to 25ml with 150mM NaCl. The solution was then filtered through a 0.45 µm filter and stored at -20°C until use.

Preparation of 10mM BSA-conjugated palmitic acid stock solution

To prepare a 10mM PA stock solution, 36mg of PA powder was first dissolved in 7ml of 150mM NaCl on a stirrer hot plate (~40-50°C) for approximately 5 min. The dissolved solution was then added to 7ml of 24% (w/v) BSA solution with 48µl of 5M NaOH to balance the pH, the mixture was gently heated and stirred until a solution/emulsion was formed.

FA treatment to hiPSC-HLCs or hiPSC-IOs

Fatty acids (FAs) were supplemented to hepatocyte maturation media (OM or NM, see **Table 2.1**) or intestinal organoids medium (IO, **Table 2.1**); either on their own or as a mixture to hiPSC-HLCs or hiPSC-IOs to increase fatty acid flux.

Initially, FAs were used as a mixture at 1:2:2 ratio of LA to OA to PA (40 µM-80 µM-80 µM, respectively; total final concentration = 200 µM). HiPSC-HLCs were exposed to FA mixture from hepatic maturation day 8 (M8 = D17, Figure 2.2) to maturation day 10 (M10 = D19) for 48h.

In a separate dose-response experiment, HiPSC-HLCs were treated with OA during hepatocyte maturation for 5 days from M0 [differentiation D9, section 0] to M5 (D14) at a final concentration of 0 µM, 25 µM, 50 µM and 100 µM. OA-treated HLCs were harvested at M5 (D14) for qPCR analysis.

A similar dose-response experiment was conducted, PA was added to hiPSC-HLCs from M8 (D17, Figure 2.2) to M10 (D19) at 0 µM, 300 µM and 600 µM.

To simulate steatosis *in vitro*, hiPSC-HLCs or hiPSC-IOs were treated PA (0 µM or 300 µM) and incubated for 48h from M8 (D17) to M10 (D19). PA-treated cells were used for functional evaluation.

2.2 CRISPR/Cas9 knockout (KO) strategy for gene editing

2.2.1 CRISPR/Cas9 guide RNA (gRNA) and targeting construct

Single guide RNA/Cas9 strategy was used to introduce a homology directed repair (HDR) mediated knockout (KO) of the *MTTP* gene in LOPCK hiPSC ($MTTP^{WT/WT}$) cell line as an isogenic *MTTP* negative control. A commercially available MTTP Human Gene Knockout Kit was purchased from Origene (#KN213699), which includes the

DNA donor template targeting construct and guide RNAs (gRNAs) vectors. Oligonucleotides corresponding to two gRNAs targeting the sequence 5'-AAAGGGGAGGGGTTTATGCG-3' or 5'- GGGGTCTGGAGTTAGTGTTT-3', respectively, in *MTTP* were annealed and cloned into the pCas-Guide vector by the manufacturer (total size ~8kb). The pCas-Guide vector comprised of a U6 vector backbone with CMV-driven human codon-optimised Streptococcus pyogenes Cas9 nuclease bearing the D10A mutation, the vector also contained BamH I and BsmB I restriction sites. The ~7kb targeting construct donor template from the kit comprised of pUC backbone with a GFP-puromycin functional cassette, which is flanked by left and right locus specific homologous arms (~600bp each side). The puromycin resistance cassette is driven by a PGK promoter.

2.2.2 Transformation and plasmid DNA preparation

To generate large amounts of plasmid DNA, transformation of E. coli was first performed in One Shot™ TOP10 competent E. coli (Invitrogen, #C404010). Targeting donor template vector, pCas-Guide RNA 1 and 2 vectors were each incubated on ice with the E. coli for 30 min before a 30 sec heat-shock at 42°C in a water bath. Plasmid DNA and E. coli mixture was cooled on ice for 2 min, it was then allowed to grow in super optimal broth with catabolite repression (SOC) medium in a shaking incubator at 37°C for 1 hr. Thereafter, 20-200µl from each transformation vial was plated out onto lysogeny broth (LB) agar plates with 100µg/ml ampicillin. The LB agar plates were incubated at 37°C overnight, viable colonies were selected. Plasmid DNA were extracted using NucleoBond® Xtra Midi kit (Macherey-Nagel, #740420) according to manufacturer's instructions. Purified plasmid DNA were eluted in endotoxin-free water and concentrations were obtained using a NanoDrop-1000 spectrophotometer (Thermo-Fisher).

2.2.3 Transfection of hiPSCs and antibiotic selection

Lipid-based transfection of hiPSCs was achieved using Lipofectamine™ 2000 Transfection Reagent (Stock concentration is 1mg/ml; Invitrogen, #11668030). A day prior to transfection, 500,000 cells (or ~50,000 cells/cm^2) were seeded onto a

matrigel™-coated 6-well plate. Cells should be approximately 60-90% confluent on the day of transfection. Two transfection mixtures were prepared on the day – mixtures A (lipofectamine™ + Opti-MEM™) and B (plasmid DNA + Opti-MEM™). Transfection reagent optimisation was performed by using three different amounts of lipofectamine™ reagent (Mixture A – 0µl, 6µl, 9µl, 12µl); to transfect for a single well of a 6-well plate each was diluted in separate vials of 150µl sterile-filtered Opti-MEM™ (Invitrogen, #31985070). 2µg of GFP-expressing plasmid DNA was added to 700µl of Opti-MEM to make up mixture B (equivalent to 0.5µg of DNA for a single well of 6-well plate). Mixture A and B were then combined in a 1:1 ratio (150µl of A + 150µl of B) and incubated for 5 min at RT to form a DNA-lipid complex. Each well of seeded cells was replaced from E8 medium to 700µl of Opti-mem basal medium, the combined DNA-lipid complex (300µl/well) was subsequently added dropwise to the seeded cells (total volume 1ml/well) and placed in a 37°C incubator. The next day, Opti-MEM was replaced to E8 medium and cells were cultured as usual.

Nucleofection of hiPSCs was achieved using an Amaxa™ 4D-Nucleofector™ and P3 primary cell kit (Lonza, #V4XP-3024). The following conditions were used for nucleofection of hiPSCs to be seeded onto a single well of a 6-well plate. On the day of nucleofection, hiPSCs were dissociated using TrypLE and resuspended in E8 medium for cell counting. The required number of cells (1,000,000 cells/well) were centrifuged at 115 x g for 3 min, then resuspended in 100µl P3 solution and co-transfected with 1µg of each sterile DNA (donor template DNA, with either pCas-Guide RNA vector 1 or 2; max. 10% of final sample volume). The mixture was transferred into a Nucleocuvette™ vessel and placed in the 4D-Nucleofector™ X unit, appropriate nucleofection programme (DN-100) was selected to start the nucleofection. Cells were left to recover for 5 minutes in a 37°C incubator before being carefully added dropwise to a matrigel™-coated 6-well plate with the standard volume of E8 medium (+ 10 µM ROCKi, without Pen/Strep). Transfected ells were cultured in E8 as usual and passaged 72hr post-transfection at a ratio of 1:3. On day 5 post-transfection, cells were selected with 0.3-0.8µg/ml of puromycin dihydrochloride (Gibco, #A1113802) for another 6-10 days until defined colonies

were visible. Viable colonies were isolated following to the method described (section 2.1.4), individual clones were expanded and cryopreserved for further PCR genotyping.

Transfected cells were visualised with a fluorescence microscope to observe GFP. Alternatively, transfection efficiency was determined by imaging transfected cells using the Operetta™ high content image analyser (PerkinElmer), followed by automated estimation of GFP positive cells normalized to total cells based on signal area using the Columbus™ software.

2.2.4 DNA extraction from cultured mammalian cells

Genomic DNA from cultured mammalian cells was extracted using the DNeasy Blood & Tissue Kit (Qiagen, #69504) according to manufacturer's instructions, DNA was eluted in nuclease-free water (NFW). Alternatively, cell pellets were lysed with DirectPCR® DNA Lysis Reagents (PEQLAB, #31-302-C) supplemented with 4% (v/v; final concentration 0.8mg/ml) proteinase K (Qiagen, #19131) and incubated in a 55°C shaking incubator for 5-16 hours. Proteinase K was inactivated by incubating the lysates in an 85°C water bath for 45 min. The resulting cell lysates were diluted 1:10 with NFW before being used for PCR genotyping (0.5-1µl diluted lysate was used per 50µl PCR reaction).

2.2.5 Polymerase chain reaction (PCR) genotyping, gel electrophoresis and purification

Genotyping of clones was performed by PCR using 100-200ng of genomic DNA (gDNA), or 0.5-1µl diluted cell lysate with standard Taq DNA polymerase (NEB, #M0267) following manufacturer's instructions; **Table 2.2** detailed the standard PCR components and volumes used. Primers used for genotyping are listed in

Table 2.3. PCR thermocycling parameters were: Initial denaturation at 95°C for 5 min (1 cycle); 95°C for 30 sec, 60°C (55-65°C for gradient PCR) for 30 sec and 72°C for 1 min/kb (40 cycles); final extension at 72°C for 10 min (1 cycle); hold at ; hold at 4°C.

Amplified DNA were thereafter loaded in between 1-2% (w/v) agarose (Sigma-Aldrich, #A7431) gels stained with 0.004% (v/v) ethidium bromide (EtBr; Sigma-Aldrich, #E1510). Depending on the desired DNA band size, gel electrophoresis was carried out in 1X TAE buffer at 100V for 60-90 min unless stated otherwise. Gels were visualised in a LAS-4000 imaging system (Fujifilm Life Science). PCR products were isolated from gels using QIAquick Gel Extraction Kit (Qiagen, #28706) and were sent externally to Source BioScience for Sanger sequencing service.

Table 2.2 Standard PCR reaction mix.

Component	Volume (µl) per 50 µl reaction
10X Standard *Taq* Reaction Buffer	5
10 mM dNTPs	1
10 µM Forward Primer	2.5
10 µM Reverse Primer	2.5
Template DNA	0.5-1µl lysate / 100-200ng gDNA
Taq DNA Polymerase	0.25
Nuclease-free water	Up to 50

Table 2.3 Sequence of primers used for genotyping the genome-edited hiPSC clones.

Primer Name & Screening Location	Forward (F) or Reverse (R) Sequence (5' → 3')	
Primer 1 (3' Screen); Outside MTTP RHA to Resistance casette	F	CTCCCTCAGCTACTCTTTGCC
	R	TAGGTCCCTCGAAGAGGTTCA
Primer 2 (5' Screen); Outside MTTP LHA to Resistance casette	F	CCTCGGGCTCTCTACATTTCA
	R	GGTGCTCTTCATCTTGTTGGTC
Primer 3 (5' Screen); Outside MTTP LHA to Inside MTTP RHA	F	TGTGGGGTTCATTCGCAGAC
	R	TAGGAGCCTTTCTTCGTTGTTTTG

Note: LHA, left homology arm; RHA, right homology arm. Primer locations please refer to **Figure 3.11A**.

2.3 Molecular biology

2.3.1 RNA extraction and cDNA synthesis

Total RNA was isolated from cells using RNeasy Mini kit (Qiagen) according to manufacturer's protocol. Reverse transcription (RT) reaction was carried out after determining the concentration and purity of extracted RNA using NanoDrop-1000

spectrophotometer (Thermo-Fisher), cDNA was synthesized by reverse transcribing 500ng of total RNA. Briefly each RT reaction contained dNTP (Promega, #U1511) and random primers (Promega, 430 #C1181) and were incubated at 65°C for 5 min and then snap cooled on ice. Subsequently, RT master mix was made with total reaction volume of 20µl consisting of first strand buffer (5x), 0.1M DTT, RNase out (Invitrogen, 18054071) and Superscirpt II (Invitrogen, #18064071). Master mix was added to each RNA sample and the RT was performed using thermocycler settings of 25°C for 10min, followed by 50min incubation at 42°C, and finally 15min at 70°C.

2.3.2 Real-time quantitative polymerase chain reaction (qPCR)

Real-time PCR (qPCR) was carried out after cDNA samples were diluted to a final volume of 600µl with nuclease free water. QPCR reactions were run using cDNA samples (from initial 500ng of reverse-transcribed RNA, diluted 1:30); 5µM forward and reverse primers; and SensiMix™ SYBR® & Fluorescein Kit (Bioline, #QT525-20). QPCR amplification was performed on an Applied Biosystems® 7500 Fast Real-Time PCR Systems using a three-step cycling programme of 40 cycles consisting of incubation at 95°C (15sec), 60°C (30sec) and 72°C (30sec). All samples were run with three technical replicates. Fold changes in expression of differentiating cells over undifferentiated hiPSCs were calculated using comparative ΔΔCt method standardised against the housekeeping gene porphobilinogen deaminase (*PBGD*, also known as hydroxymethylbilane synthase, *HMBS*). *PBGD* has been shown to provide stable expressions in liver, intestinal, blood, and hepatocellular carcinoma tissues, which helps to normalise other influences throughout differentiation and varying conditions [143]–[146]. Table 2.4 shows a list of primer sequences used for qPCR gene expression studies. QPCR data were as the mean of Ct values ± standard error of mean (SEM) unless stated otherwise.

Table 2.4 Primer sequences used for qPCR.

Gene	Forward (5' → 3')	Reverse (5' → 3')
A1AT	ACTTAGCCCCTGTTTGCTCC	CGGCATTGTCGATTCACTGTC
AADAC	ACATTTGTGGAGCTCCTGGG	ACTTAGAGCAGCACTTCCCAC
ADH1	TCTGGGAAAAGTATGCGTACCATT	TGAAGACTGCCACAAGGGAA

ADH6	TGGAAAATGTATCCGCTGTATCCT	GGAGGCTGATCCTTGGTGAC
AFP	AAACTATTGGCCTGTGGCGA	TTTTGTCCCTCTTCAGCAAAGC
ALB	CTCGGCTTATTCCAGGGGTG	AAAGGCAATCAACACCAAGGC
ALDH2	GGAAGATGTGGACAAGGCAGT	GGATTAC GCGGCCAATCTCA
AMPK	CTGAGAAGCAGAAGCACGAC	TCCATCTCTTCAACCCGTCC
APOB	TGAACTGGTGGCAAAACCCT	GCTCTAATCTGGTGTCCCCG
APOC3	CAGGGTTACATGAAGCACGC	GCAGGTGGACTTGGGGTATT
ATF-4	GTTCTCCAGCGACAAGGCTA	ATCCTGCTTGCTGTTGTTGG
ATF-6	CCTGTCCTACAAAGTAC CATGAG	CCTTTAATCTCGCCTCTAACCC
BIP	TGTTCAAC CAATTATCAGCAAACTC	TTCTGCTGTATCCTCTTCACCAGT
COL1	GGCCAAGACGAAGACATCCC	AGTAGCACCATCATTTCCACGA
COL3	CGCCCTCCTAATGGTCAAGG	CATCGAAGCCTCTGTGTCCT
CXCR4	CACCGCATCTGGAGAACCA	GCCCATTTCCTCGGTGTAGTT
CYP2A6	TCCATCGGAAAGCGGAACTG	TCTTAGCTGCGCCCCTCT
CYP2B6	TCTGTATTCGGCCAGCTGTT	ATGTGGGCCAATCACCTGTT
CYP2C8	ACCCAGAGGTCACAGCTAAAG	AGGTGATAGCAGATCGGCAG
CYP2D6	TACTGCTTCGACCAGTTGCG	ACTGCTCCAGCGACTTCTTG
CYP3A4	AAAGAAACACAGATCCCCCTGA	CCACGCCAACAGTGATTACA
CYP3A5	AGCCTGGTGCTCCTCTATCT	ACTGGGCCTAAAGACCTTCG
CYP3A7	TACCCAATAAGGCACCACCC	CAGGCTCCACTTACGGTCTC
CYP7A1	AATTAGGAGAAGGCAAACGGGT	TCCATCCATCGGGTCAATGC
EDEM	CAAGTGTGGGTACGCCACG	AAAGAAGCTCTCCATCCGGTC
FMO3	AAGGTTACCATGGGGAAGAAAGT	CCTCCTCTGCATGGTCTGAAA
FOXA1	CCAGGATGTTAGGAACTGTGA	GAGTAGGCCTCCTGCGTG
FOXA2	GGGAGCGGTGAAGATGGA	TCATGTTGCTCACGGAGGAGTA
FOXA3	GTGTCCCGGCTATAAAGCGT	GCGAGTAGACCTCGCCC
GATA4	TCCCTCTTCCCTCCTCAAAT	TCAGCGTGTAAAGGCATCTG
GATA6	GAGCGCTGTTTGTTTAGGGC	GCTGACGTCTAGCTCCTCGG
GRP78	CTGCCATGGTTCTCACTAAAATG	TTAGGCCAGCAATAGTTCCAG
GRP94	GAAACGGATGCCTGGTGG	GCCCCTTCTTCCTGGGTC
GSTpi	AGTCCAATACCATCCTGCGTC	CCCGCCTCATAGTTGGTG
HHEX	TGCATAAAAGGAAAGGCGGC	TTGCTTTGAGGGTTCTCCTGT
HNF4A	ACTCTCCAAAACCCTCGTCG	CCCTTGGCATCTGGGTCAAA
IDO2	CCGGATCTTTCTCTCTGGATGG	TTCAGGGGCTCTTGGGAAAC
IL18	AAAACCTGGAATCAGATTACTTT	GTCCGGGGTGCATTATCTCT
IL1B	CCAGCTACGAATCTCCGACC	AGAACACCACTTGTTGCTCCA
IL23	GACAACAGTCAGTTCTGCTTGC	TGGAGGCTGCGAAGGATTTT
IL8	CTGTGTGAAGGTGCAGTTTTGC	CAACCCTCTGCACCCAGTTT
IRE1	GCGAACAGAATACACCATCAC	ACCAGCCCATCACGATTG
LIPA	TGTCCTTGTTCATTTTCACCC	TCGCCCTGCCTATATTAACC
LIPC	AGGAGAAACCCAGCAAAGAATG	TTTATGAGAGTGAAACATACCCCC
MIA2	GACCTGACTGCCGATACCTG	TTCCTTTACTTCCTGCCCACA
MTTP	GCTACATAGAACGTAGTCCCCG	TGAGGGGCAAACACCACTTT
NANOG	CATGAGTGTGGATCCAGCTTG	CCTGAATAAGCAGATCCATGG
NFKB	CAACAGATGGCCCATACCTTC	GCTCTTTTTCCCGATCTCCCA
NKX2.1	GCTGCCTAAAAC CTGGC GCCG	ATGAAGCGGGAGATGGCGGGGAA
OCT4 (POU5F1)	AGTGAGAGGCAACCTGGAGA	ACACTCGGACCACATCCTTC

PBGD	GGAGCCATGTCTGGTAACGG	CCACGCGAATCACTCTCATCT
PDX1	GATTGGC GTTGTTTGTGGCT	GCCGGCTTCTCTAAACAGGT
PNPLA3	AAGTTCCTCCGACAGGGTCT	TCCATCCACATATCGCACGC
PROX1	ACGTCATCATTCCGAACCCC	TTCCTGCATTGCACTTCCCG
SOX17	CGCACGGAATTTGAACAGTA	GGATCAGGGACCTGTCACAC
SOX2	TGGACAGTTACGCGCACAT	CGAGTAGGACATGCTGTAGGT
sXBP1	CTGAGTCCGAATCAGGTGCAG	ATCCATGGGGAGATGTTCTGG
TAT	CCTCCCCTCAATTCTGGACG	GGATAGGAAGCCGATGGATGG
TBX3	AGTCGGGAAGGCGAATGTTT	AGCGTGATCACTTGGGAAGG
TDO2	ATGGGAACTACCTGCATTTGGA	GTCCAAGGCTGTCATCGTCT
TGF-β	CAGAAATACAGCAACAATTCCTGG	TTGCAGTGTGTTATCCCTGCTGTC
TLR1	CAGAGTGAATGGTGCCATTATGAAC	CCTTGGGC CATTCCAAATAAGTC
TLR2	GAAAGCTC CCAGCAGGAACATC	GAATGAAGTC CC GCTTATGAAGACA
TLR3	GGACTTTGAGGCGGGTGTT	TGTTGAACTGCATGATGTACCTTGA
TLR4	AAGC CGAAAGGTGATTGTTG	CTGAGCAGGGTCTTCTCCAC
TLR5	GGAGTAGAAGGCACAGGTTATG	GGTGGAAGATGAGGCTAAAGAG
TM6SF2	CTCTATGCTGTCTTCGCTGTCT	TGGTGGCTGGTGGAAGAATG
TNF-α	GCTGCACTTTGGAGTGATCG	GCTTGAGGGTTTGCTACAACA
TTR	ACCGGTGAATCCAAGTGTCC	GGTTTTCCCAGAGGCAAATGG
tXBP1	TGGCCGGGTCTGCTGAGTCCG	ATCCATGGGGAGATGTTCTGG
usXBP1	CAGCACTCAGACTACGTGCA	ATCCATGGGGAGATGTTCTGG
VLDLR	CAGAACAGTGCCGCAATATAACA	CCCATCACATCGCCACTTCT

2.3.3 Allele- specific PCR (ASPCR), restriction digestion and band densitometry

An allele-specific PCR was used to detect single nucleotide polymorphism of *MTTP* - *p.I564T* (rs745447480) in hiPSC samples. Allele-specific primers were designed using NEBcutter V2.0 website to permit the PCR amplification only if the nucleotide at the 3'-end of the primer complemented the base at the wild-type or variant-type DNA sample. The primers were then searched for uniqueness using the Basic Local Alignment Search Tool search engine. Allele-specific PCR was achieved by using 500 ng DNA; 10 mM dNTPs; 10 µM of forward (TCTTAACGGCCTCAGCCTAG) and reverse (CAGAGTTACCAGTCATGGACTC) primers; 10X ThermoPol reaction buffer (NEB, #B9004S) with standard Taq DNA polymerase (NEB, #M0267) following manufacturer's instructions. The thermocycling parameters included initial denaturation at 95°C for 5 min; 95°C for 30 sec, 51°C for 30 sec and 68°C for 1 min for 40 cycles; final extension was at 68°C for 10 min and held at 4°C. Amplified DNA were

then incubated with 10X ThermoPol Buffer (NEB, #B9004S) and Hpy166II (NEB, #R0616S) restriction enzyme for digestion at 37°C for 1 hour, enzyme was inactivated afterward by 15 min incubation at 65°C. Undigested DNA was used as a control. DNA fragments were then loaded into a 1.8% agarose gel, run for 2 hr at 80V, followed by image acquisition using EtBr. Band densitometry analysis was performed using Image Studio™ Lite version 5.2 software (LI-COR, NE, USA) according to manufacturer's guide.

2.3.4 Karyotype assessment of hiPSCs

hiPSCs were karyotyped as previously described [147]. Each hiPSC line was passaged to two T25 flasks as previously described to allow culture grow into log phase. After 48 hours, sub-confluent cells were then treated with 100ng/ml of KaryoMAX® Colcemid™ solution (Gibco, #15212012) in culture medium for 1 hour, at 37°C. KaryoMAX-containing medium with any floating cells were collected in a 30ml universal tube. The attached cells were harvested using TrypLE passaging and were added to the same 30ml universal tube. Cell suspension was centrifuged at 160 x g for 4 min; the cell pellet was resuspended dropwise in 8-10ml fresh hypotonic solution (0.6% sodium citrate in distilled water; Fisher Chemical, #S/3320/53) and incubated at RT for 20 min. Cell suspension was then centrifuged at 300 x g for 5 min; the cell pellet was resuspended dropwise in 8-10ml fixative consisting 16.7% glacial acetic acid (Fisher Chemical, #A/0400/PB17) in methanol. After two further washes with the fixative, the cell pellet was resuspended in 0.5-1ml fixative and stored at -20°C until ready for Giemsa-banding (G-banding) analysis. This was performed by Mr Nigel Smith or Ms Katherine Yates as a service provided by the Cytogenetics Department of Nottingham City Hospital, G-banding analysis was in accordance with the International System for Human Cytogenetic Nomenclature (ISCN) International Guidelines [148]. 30 metaphase spreads were analysed for each sample.

2.3.5 Immunocytochemistry (ICC) and Image acquisition

Cells were fixed in 4% paraformaldehyde (PFA) for 20 min at 4°C, followed by 30 min blocking and membrane permeabilization using PBST (0.1% Triton X-100 in PBS)

containing 10% foetal bovine serum (FBS) to prevent unspecific antibody binding. Subsequently, fixed cells were incubated overnight at 4°C in PBST with 1% FBS containing primary antibodies (1° Ab) with the dilutions highlighted in **Table 2.5**. Cells were then washed three times in PBST-1% FBS and incubated with the appropriate secondary antibodies (2° Ab; **Table 2.5**) diluted in PBST-1% FBS for 1 hour at RT. Unbound antibodies were removed by PBST-1% FBS wash (5 min x 3 times), followed by 5 min (at RT) nuclei counterstaining using 0.5µg/ml DAPI (Sigma, #D9542) diluted in PBST-1% FBS. Samples were subsequently washed and stored at 4°C in PBS until image acquisition. Automated Operetta™ high content image analyser (PerkinElmer) was used for image acquisition; captured images were then analysed using Columbus™ software (PerkinElmer), fluorescence intensity of specific channel was determined with the developed algorithms in the software.

Table 2.5 Primary and secondary antibodies used.

Primary Antibody (1° Ab) Target Protein	1° Ab Host Species	Supplier & Identifier	1° Ab dilution	Secondary antibody (2° Ab)	Supplier & Identifier	2° Ab dilution
GATA-4	Goat	R&D, #AF2606	1:200	Donkey Anti-Goat AF 647	Invitrogen, #A21447	1:400
NANOG	Goat	R&D, #AF1997	1:200			
AFP	Mouse	Abcam, #ab3969	1:200	Donkey Anti-Mouse AF 488	Invitrogen, #A21202	1:400
ALB	Mouse	R&D, #MAB1455	1:100			
CYP2A6	Mouse	OriGene, #TA503832	1:100			
Ki-67	Mouse	Santa Cruz, #sc-23900	1:50			
Nestin	Mouse	Merck, #MAB5326	1:100			
NFkB p65	Mouse	ThermoFisher, #710048	1:100			
OCT3/4	Mouse	Santa Cruz, #sc-5279	1:200			
TLR4	Mouse	Santa Cruz, #sc-293072	1:50			
A1AT	Rabbit	Abcam, #ab179443	1:100	Donkey Anti-Rabbit AF 647	Invitrogen, #A31573	1:400
GST-π	Rabbit	Enzo, #ADI-MSA-102-E	1:500			
HNF-4α	Rabbit	Santa Cruz, #sc-8987	1:100			
MESP1	Rabbit	Abcam, #ab129387	1:100			
MTTP	Rabbit	R&D, #ab63467	1:100			
SOX2	Rabbit	Novus, #NB110-37235	1:500			

2.4 Lipid detection and quantification

2.4.1 Oil Red O (ORO) staining

Oil Red O (ORO) staining was used to visualise the distribution of lipid droplets within HLCs after 48 h of PA treatment (0 µM or 300 µM) under brightfield microscope. ORO working solution was prepared by diluting ORO stock solution (Sigma-Aldrich, #O1391) in distilled water (dH_2O) in 3:2 ratio. The solution was left for 20 min at RT and then filtered through a 0.22 µm syringe filter right before use. After cells were fixed (4% PFA for 20 min at 4°C), the fixative solution was removed and washed twice with PBS. PBS was removed and the multi-well plate was air dried before adding ORO. ORO working solution was added to each well and incubated at RT for 15 min. After removing the ORO solution from each well, the cells were rinsed with dH_2O 2-4 times until the solution became clear. Stained cells were examined under a light microscope using 10X and 20X objectives, the red oil droplet staining in the cells indicate lipid accumulation.

2.4.2 Nile Red Assay

Nile Red (NR; Invitrogen, #N1142) stock solution was prepared at 30mM in methanol, stock solution was aliquoted and stored at -20°C until needed. For each experiment, NR working solution was made freshly by adding NR stock solution in methanol to give a final concentration of 30 µM. HLCs were fixed after 48 h of palmitic acid treatment (0 µM or 300 µM) and ready for NR staining. Fixed cells were washed twice with PBS, followed by 15 min incubation at RT in the dark. After two times of PBS washes, fluorescence of stained cells was examined by the Operetta™ high content image analysis system (PerkinElmer). The excitation and emission wavelengths of 535 and 595 nm were selected, respectively. Fluorescence intensity was quantified by the Columbus software, statistical significance between cell lines and treatment conditions were calculated.

2.5 Lipoprotein separation via ultracentrifugation

During the meal-response study visit fasting and postprandial blood samples were taken and immediately processed to obtain plasma and serum for biomarker and metabolite analyses. Lipoprotein fractions were prepared within 12 h and other samples were stored at -80°C and analysed within 6 months, without freeze/thaw cycles, at the University of Nottingham Metabolic Analysis Facility to quantify insulin, glucose, cholesterol, triglycerides, and free fatty acids. Lipoprotein separation was performed by collaborator Professor Andrew Salter from the School of Biosciences in the University of Nottingham. Lipoproteins were separated by preparative ultracentrifugation by established techniques based on those originally described by Havel et al. (1955). Briefly, chylomicron and very low-density lipoproteins (VLDL) were obtained from donors' plasma (up to 3ml) and separated within 72 h of collection by sequential non-equilibrium density-gradient ultracentrifugation. The chylomicron and VLDL samples isolated from GF03 (*MTTP*$^{VAR/VAR}$, without liver transplantation), GF06 (*MTTP*$^{WT/WT}$, LOPCK derivative) and GF10 (*MTTP*$^{VAR/VAR}$, MOPIK derivative; with liver transplantation) donors were used to compare their apolipoprotein B-100 (ApoB-100) levels using an ELISA kit.

2.6 Measurement of ApoB-100 levels by sandwich ELISA

Cell culture supernatants of LOPCK- and MOPIK-derived HLCs and intestinal organoids were collected after 48h of PA treatment (0 µM or 300 µM); hepatocyte maturation media and intestinal organoid media were used as negative controls. Human APOB/ Apolipoprotein B-100 ELISA kit (Sigma-Aldrich, #RAB0610) was used to provide a quantitative colorimetric measurement of ApoB-100 in cell culture supernatants according to manufacturer's instructions. In brief, reconstituted APOB protein standards and diluted supernatant samples were added to human APOB antibody-coated ELISA plate. After overnight incubation at 4°C, the plate was thoroughly washed. Wash buffer was completely removed from each well before a 1-hour incubation with the Biotinylated Detection Antibody at RT. After the plate was washed, Streptavidin was added and incubated for 45-min at RT. Finally, colour development was initiated by 30-min incubation of the ELISA colorimetric TMB

Reagent and terminated by adding Stop solution to each well. Measurement of the absorbance was performed on a microplate reader within 10 min at 450 nm. Each sample was tested in duplicate. The mean absorbance for each set of duplicate standards, controls, and samples were calculated. To reduce the interference from a non-specific signal, the average of blank measurements was subtracted from mean value of each well. Normalised values of the standards were plotted into a standard curve using GraphPad Prism 8.3.0 software in order to interpolate the ApoB-100 concentration of each sample. The fold change was obtained by comparing PA-treated samples with the MTTP wildtype LOPCK-derived HLCs PA-untreated control (indicated as a value of 1).

2.7 Detection and Quantification of mitochondrial content and Reactive Oxygen Species (ROS) in live cells

To visualise the mitochondria content after 48h of PA treatment (0 µM vs 300 µM), hiPSC-HLCs were stained using 100nM MitoTracker green FM (Invitrogen, #M7514) or MitoTracker deep red FM (Invitrogen, #M22426). Intracellular reactive oxygen species (ROS) and mitochondrial superoxide production by hiPSC-HLCs were investigated by staining with 2.5µM CellROX green (Invitrogen, #C10444) or 2.5µM MitoSox Red (Invitrogen, #M36008) respectively. To make up the staining solution, dyes were diluted in Ca2+/Mg2+ rich HBSS (Gibco, #14025) to their final concentration, 5µg/ml of Hoechst 33342 (Invitrogen, cat# H1399) was also added to allow nuclei cell count. Live cells were incubated with the dyes for 30 minutes at 37°C and 5% CO2, followed by two times of DPBS (without Ca2+/Mg2+) wash. Cells were then replaced with warm HepatoZYME basal media for live cell imaging using the Operetta™ high content image analysis system (PerkinElmer). The spectra were collected at three excitation wavelengths: 445nm for Hoechst 33342; 525nm for CellROX green and MitoTracker green; 705nm for MitoSOX Red and MitoTracker deep red. Data was analysed using Columbus™ software (PerkinElmer) to quantify the mean ± SD and total fluorescence intensity of each channel from each well (with multiple image acquisition fields). Statistical significance was determined by two-way

ANOVA with Sidak correction; *, P⩽0.05; **, P⩽0.01; ***, P⩽0.001; ****, P⩽0.0001.

2.8 Measurement of mitochondrial respiration using Seahorse analyser

The Seahorse XF96 extracellular flux analyser was used to assess mitochondrial respiration by measuring the oxygen consumption rate (OCR), following manufacturer's instructions. The Seahorse XF96 plates (Agilent, #101085-004) were pre-treated with phenol-red growth factor reduced (GFR) Matrigel™ (Corning, #354230). At differentiation day 14 (D14; hepatocyte maturation day 4, M4), HLCs were dissociated by incubating them in TrypLE™ Express enzyme (Gibco, #12604021) at 37°C with 5%CO_2 for 45-90 min until became single cells, they were then re-seeded onto Matrigel™-coated XF96 plate with a density of 25,000-50,000 cells per XF96 well. HLCs were maintained for further 6 days, at D18 (M8) cells were treated with palmitic acid (PA, 0 µM or 300 µM) for 48 h and the Seahorse MitoStress test was performed on D20 (M10). On the day of the assay, culture medium was exchanged for Seahorse XF base medium (Agilent Technologies, #102353-100), supplemented with 10mM glucose (Sigma, #G7528), 1mM sodium pyruvate (Sigma, #S8636) and 2mM L-glutamine (Life Technologies, #25030-081). Cells were then placed in a 37 °C non-CO_2 incubator 1 h prior to the assay. Selective inhibitors (all from Agilent Technologies) were injected sequentially during the rate measurements to achieve final concentrations of oligomycin (1.5µM), FCCP (0.4µM) and rotenone (1µM). Agilent Seahorse Wave software was used to measure the oxygen consumption rates (OCR), these values were recorded and reported as pmol/min after each compound injection. OCR values were further normalised to the number of cells present in each well, quantified by the Hoechst staining (5ng/ml Hoechst 33342 [Invitrogen, cat# H1399] diluted in Ca2+/Mg2+ HBSS [Gibco, #14025]) using fluorescence at 355 nm excitation and 460 nm emission in an automated imaging platform (CellaVista, Synentec).

2.9 Transcriptomic analysis

2.9.1 rRNA removal and mRNA library preparation

Total RNA from human adult liver tissues (received from the Nottingham Digestive Diseases Centre), hiPSCs and hiPSC-HLCs were purified using RNeasy Mini Kit (Qiagen, #74106) according to manufacturer's instructions. Human foetal liver total RNA was purchased from Cell Applications, Inc (Cat#1F21-50, Lot# 1394-2). The RNA yields were quantified by a Qubit® Fluorometer (Invitrogen, #Q32857) with the Qubit® RNA BR Assay Kits (Thermo-Fisher, #Q10210). 4200 TapeStation System (Agilent Technologies, #G2991AA) was used to evaluate qualities of RNA and DNA using their specific ScreenTapes. RNA was assessed for quality control parameters of minimum concentration and integrity number (RIN) using Agilent RNA ScreenTape Assay kit (#5067-5576,5577,5578). All sequenced samples had a RIN ≥ 9.8 (except RNA obtained from human adult, RIN 5.0; and foetal liver, RIN 7.2). To enrich mRNAs from total RNA samples, NEBNext® rRNA Depletion Kit (NEB, #E6310) was used to remove ribosomal RNAs (rRNAs). To evaluate RNA concentration and degradation, depleted RNA sample was assessed using Agilent High Sensitivity RNA ScreenTape Assay Kit (#5067-5579, 5580, 5581) (RIN ranges 1.0-5.4). mRNA-sequencing (mRNA-seq) cDNA libraries were constructed using NEBNext® Ultra™ II Directional RNA Library Prep Kit for Illumina® (NEB, #E7760, set 1 and 2 indexes) following the manufacturer's protocol. Generated library DNA concentration and size was measured using Agilent High Sensitivity D1000 ScreenTape Assay Kit (#5064-5584, 5585, 5587).

2.9.2 mRNA sequencing and bioinformatics data analysis

mRNA-Seq and bioinformatics analysis were performed at the Babraham Institute by Ms Kristina Tabbada and Dr Simon Andrews as a service. Library samples were multiplexed into each lane and sequenced on the Illumina HiSeq Sequencing system to yield targeted number of single-end 100bp reads to a depth of 30 million per sample. Reads were mapped to the GRCh38.p10 Ensembl human genome.

2.10 Proteome profiler antibody array analysis

Human NFκB Pathway Array Kit (#ARY029), Human Phospho-Kinase Array Kit (#ARY003B) and Human XL Cytokine Array Kit (#ARY022B) were purchased from R&D Systems and used as followed by the manufacturer's instructions. These arrays were used to examine the differences in proteome and secretome between LOPCK- and MOPIK-derived HLCs under normal (0 µM) and PA-treated (300 µM) condition after 48 hours. Cell protein lysates were collected to be analysed for the NFκB and Phospho-kinase array kits; cell culture supernate was collected to be analysed for the XL Cytokine array kit. Protein expression was semi-quantitatively analysed, comparing HLCs derived from LOPCK and MOPIK hiPSC lines after 48 hours with or without palmitic acid (300 µM) treatment. NFκB signalling proteins, phosphorylated proteins and extracellular cytokines were detected using different proteome profiler array kits according to manufacturer's instructions. Total protein concentration was quantified by NanoDrop-1000 spectrophotometer (Thermo-Fisher); 400ug and 2000µg of total protein were used to incubate each NFκB and phosphor-kinase array membrane, respectively. To detect the secreted protein levels of spent medium, 1.5ml of cell culture supernate from each culture condition was used to incubate on each XL cytokine array. In brief, control and specific capture antibodies used in different array kits have been spotted in duplicate on nitrocellulose membranes, protein sample was incubated with each array at 4°C overnight on a rocking platform shaker. The arrays were then washed to remove any unbound proteins, followed by incubation with a cocktail of biotinylated detection antibodies. Detection of proteins was visualised by adding Streptavidin-HRP and chemiluminescent detection reagents to the arrays; images were then taken using ImageQuant LAS-4000 (Fujitsu Life Sciences). Signal produced from each capture spot correspond to the amount of protein bound, the pixel intensity score of each duplicated array spot was measured using Image Studio™ Lite Software (version 5.2), and the averaged intensity was calculated by subtracting the averaged background signal before comparisons of protein expression was made. The fold change was obtained by comparing with the LOPCK-HLCs without PA treatment (control, indicated as a value of 1).

2.11 Metabolomic analysis

Sample preparation and analytical techniques were following the methodologies described in Surrati et al. (2016).

2.11.1 Metabolite extraction

For extracellular metabolites extraction, 1ml of the spent medium from each hiPSC-HLC culture condition (LOPCK and MOPIK cell lines, PA 0 µM or 300 µM treated) was collected at hepatocyte maturation day 10 (differentiation D19, Figure 2.2). Collected media were centrifuged at 7378 x g for 5 min and 250µl of the supernatant was transferred to a new pre-cooled eppendorf tube for extraction. Protein precipitation was achieved by adding 750µl of cold methanol (MeOH) solvent to 250µl of supernatant at a ratio of 1:3 (supernatant: MeOH), the mixture was vortexed vigorously for 1 min then incubated at -20°C for 20 min. After the incubation, samples were vortexed for 15 sec before centrifuging at 13,200 x g for 10 min at 4°C. The final supernatant products were transferred to pre-cooled eppendorf tubes and stored at -80°C until Liquid chromatography (LC)-mass spectrometry (MS) analysis. Samples of fresh hepatocyte maturation media (NM, see **Table 2.1**; with additional 0 µM or 300 µM PA) were processed in parallel as no-cells media blank controls. All samples were prepared as six biological replicates. An equal mix of all samples was prepared as quality control (QC) for instrument performance assessment.

2.11.2 Mass spectrometry, metabolites identification and data interpretation

Metabolite profiling of spent culture media was achieved using LC-MS-based analytical approach, both the LC-MS and data analysis were performed by Mr Salah Abdelrazig as a service at the Centre for Analytical Bioscience (University of Nottingam). LC-MS was executed on an Accela system coupled to an Exactive MS (Thermo Fisher Scientific, Hemel Hempstead, UK). LC-MS data was processed using IDEOM excel template and SIMCA-P version 13.0.2 (Umetrics AB, Umea, Sweden) as described in Surrati et al. (2016).

2.12 Statistical analysis

Values presented in text and figures are as mean ± standard error of the mean (mean ± SEM, unless stated otherwise). Statistical analysis was performed by using Graph Pad Prism version 8 (La Jolla, CA, USA) software. Statistical significance was determined using the most relevant statistical test, indicated as followed: * $p < 0.05$; ** $p < 0.01$; *** $p < 0.001$; **** $p < 0.0001$; where P-value > 0.05 was classified as not significant. In general, one-way analysis of variance (ANOVA) followed by Dunnett's multiple comparison test was used to compare data from multiple samples grouped by a single factor. Two-way ANOVA followed by Sidak's post hoc test was used to compare data grouped by two factors.

Chapter 3.

Generation and characterisation of hiPSCs from donor-derived dermal fibroblasts

Chapter 3. Generation and characterisation of hiPSCs from donor-derived dermal fibroblasts

3.1 Introduction

In addition to lifestyle and environmental factors, genetic predispositions related to lipid metabolism can often contribute to the susceptibility and severity of NAFLD. We have access to a unique patient cohort comprised of a family that has multiple members with a rare *MTTP*-p.I564T (c.1691T>C) SNV, causing a missense point mutation changing from a T to C nucleotide resulting a replacement of isoleucine (Ile) to threonine (Thr) at residue position 564 on the G chain of MTTP protein. This mutation offers the opportunity to develop a model of NAFLD using hiPSCs and differentiation strategies to generate hepatic-like cells from the resulting hiPSCs.

This chapter seeks to outline the generation of hiPSC lines derived from human dermal fibroblasts with different sets of the same single nucleotide variation (SNV) in the *MTTP* gene (rs745447480). This would enable us to use these hiPSC lines for downstream experiments including directed differentiation to different lineages, as well as phenotypic characterisation relating to the donors' genotypes, in order to help us elucidate the underlying mechanisms that lead to NAFLD. This chapter concludes the generation and characterisation of hiPSCs after reprogramming, to validate that they were suitable for further investigation as NAFLD disease model.

3.1.1 Implication of rare MTTP-p.I564T in NAFLD pathophysiology

Microsomal triglyceride transfer protein (MTTP) is a product of the *MTTP* gene, which is fundamental for the transport of dietary and endogenous fat by assisting the assembly and secretion of triglyceride-rich apolipoprotein B (apoB)-containing lipoproteins between the endoplasmic reticulum (ER) membranes (Hussain et al., 2003). A rare autosomal recessive disorder called abetalipoproteinemia (ABL, also known as Bassen-Kornzweig syndrome, OMIM 200100) is estimated to affect less

than 1 per million worldwide, characterised by the absence of plasma apoB-containing lipoproteins including chylomicrons, very-low-density lipoproteins (VLDLs) and low-density lipoproteins (LDLs), which can lead to vitamin E deficiency and fat malabsorption by the intestines and liver [151]–[153]. To date there are over 30 mutations of *MTTP* pathogenic variants as biallelic homozygous or compound heterozygous that have reported to cause ABL due to defective or missing MTTP function. Mutations in the *MTTP* gene could lead to defect in assembly and secretion of apolipoprotein B (apoB)-containing lipoproteins including chylomicron or very-low-density lipoprotein (VLDL), causing a malabsorption of dietary fat and deficiency of fat-soluble vitamins, particularly vitamin E, by the intestine and liver, consequently results in steatorrhea and abdominal distension [84], [152], [154].

Hepatic steatosis can be observed in patients suffered in abetalipoproteinemia as well as NAFLD, both can be caused by mutations in the *MTTP* gene, however disease progressions could be drastically different depending on the type of genetic variants found in these patients [85], [86]. Hence, there is a need to create a specific human disease model to further investigate the underlying mechanisms on how *MTTP-P.I564T*SNV drives toward NAFLD instead of abetalipoproteinemia.

3.1.2 HiPSC reprogramming strategies

Since the first successful reprogramming from murine adult somatic cells to induced pluripotent stem cells (iPSCs) reported using retroviral transduction by Yamanaka back in 2006 [155], a lot of work have been done in the last decade to increase reprogramming efficiencies as well as minimising transgenes integration into the donor cell genome. The original method to reprogram human adult somatic fibroblasts developed by Takahashi and Yamanaka in 2017 utilised retroviral transduction of four human transcription factors *OCT3/4 (POU5F1), SOX2, KLF4,* and *c-MYC* (OKSM, a.k.a. Yamanaka factors) into human dermal fibroblasts (HDFs) [156]. Several exogenous transcription factors are commonly used in reprogramming that are important in embryonic development, proliferation and cell cycle, such as *OCT4,*

SOX2, NANOG, LIN28, c-Myc, KLF4, and *SV40LT*, but the reprogramming efficiency is greatly influenced by the combination of these transcriptions factors, as well as the transduction methods [157], [158].

To improve reprogramming efficiency and the quality of hiPSC derivation, various integrating, non-integrating transfer systems either by viral and non-viral based vectors have been developed from different groups of scientists using different sources of somatic cells as Figure 3.1 illustrated [159]–[164]. Each of these reprogramming strategies has its own advantages and disadvantages.

Retroviral vectors were one of the first integrative viral vectors used to generate hiPSCs without severe effects on cell viability [156], the expression of integrated gene could effectively become silenced towards the later stage of reprogramming due to epigenetic modifications on gene regulation [165], [166]. However, integrative viral-based reprogramming has been shown to cause multiple and random transgene integration into genomic DNA, which may cause reactivation of silenced exogenous oncogenes such as *KLF4* and *c-MYC* with an increased risk of virally induced tumorigenicity [167]. Adenovirus is an alternative viral vector that is non-integrative to the genome DNA, but the reprogramming efficiency can be as extremely low as 0.0002% in human cells [168], [169]. Non-viral transposon gene delivery systems such as PigyBac is relatively safer for therapeutic applications, however it poses the same issue of poor efficiency (0.02-0.05%) and potential difficulty in excising the vector from the reprogrammed human hiPSCs [170], [171].

Due to these limitations, that had led to the technical development of non-integrative approaches aiming to improve reprogramming efficiency. Non-integrative and non-viral based vectors such as episomal plasmids and RNAs (mRNA or miRNA) transfection would allow for the generation of footprint-free hiPSCs, however transient transfection with the standard plasmid or RNA vector may not result in expression for a long enough period of time to fully reprogram cells, often it would require repeated transfections and therefore is labour intensive [172], [173]. Delivery

of transcription factors as protein eliminates genome manipulation and DNA transfection, but synthesising large amounts of bioactive proteins that can cross the plasma membrane has been proven to be technical challenging [174].

Sendai virus (SeV) is an RNA virus that is non-integrative to genome DNA, it has been shown to be quite successful in reprogramming from fibroblasts and peripheral blood cells with good cell survival efficiency [175], [176]. There are many commercially available Sendai-based reprogramming kits to generate hiPSCs and only require a single transduction event as compared to other methods [177], [178]. In this thesis, we have chosen Sendai-based reprogramming vectors to induce hiPSCs from human dermal fibroblasts.

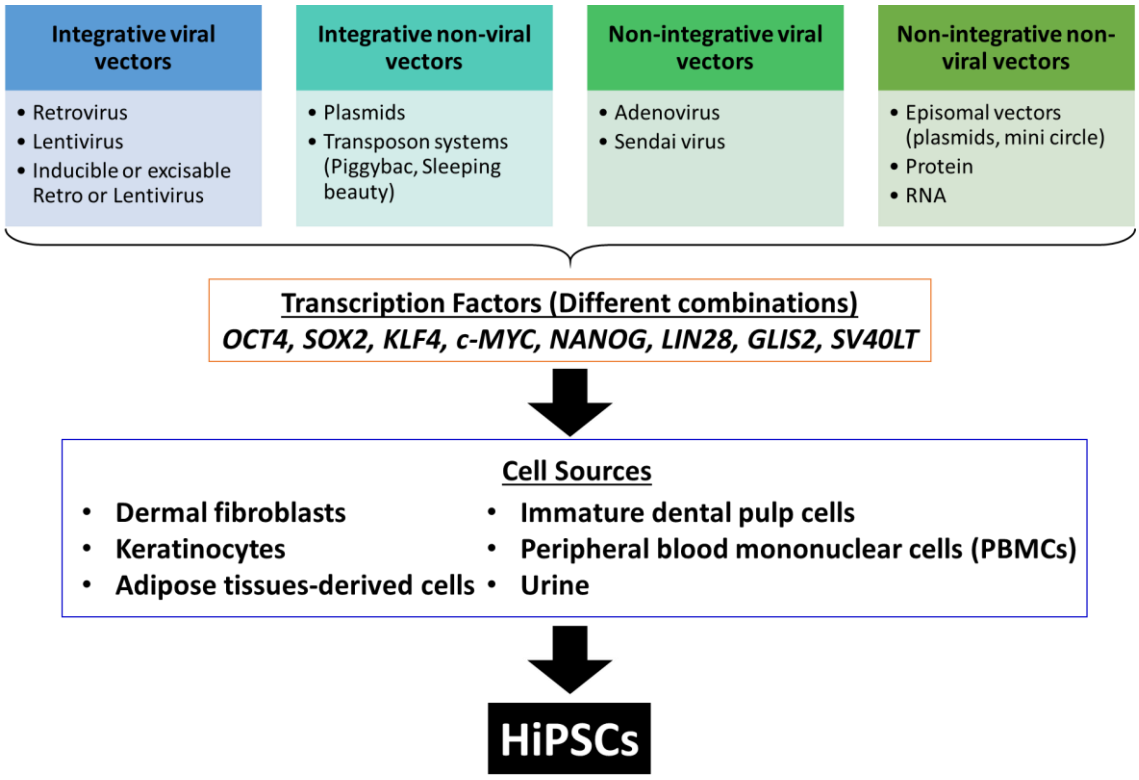


Figure 3.1 Overview of common hiPSC reprogramming approaches. Defined transcription factors can be induced to various cell sources using different types of integrative or non-integrative vectors to generate hiPSCs. (Figure adapted from [179]).

3.1.3 Genetic manipulations of patient-derived hiPSCs

One of the advantages of using hiPSCs model is their ability for genetic modification, this allow researchers to establish the creation of patient-specific isogenic controls for drug screening for personalised medicine, or to do knockout studies to investigate specific genetic mutations as causative factors of NAFLD. There are three major genome editing techniques commonly used: zinc finger nucleases (ZFNs) [180], transcription activator-like effector nucleases (TALENs) [181] and clustered regularly interspaced short palindromic repeats (CRISPR)-associated protein 9 (Cas9) [182].

CRISPR/Cas9 system is currently the most commonly used gene editing tool and is relatively more efficient compared to ZFNs or TALENs [183], the conventional CRISPR/Cas9 system is based on the bacterial and archaea adaptive immunity response to phage infection [184], this editing system requires the delivery of Cas9 endonuclease and single guide RNA (sgRNA, 20-nucleotide sequence) into hPSCs genomic DNA [185]. The Cas9 endonuclease stimulates site-specific double-stranded breaks (DSBs) at a target genomic locus guided by the sgRNA, the target locus typically undergoes either the canonical nonhomologous end joining (NHEJ) or the more accurate homology-directed repair (HDR) pathway in mammalian cells [185]. In the absence of a template, DSBs are re-ligated through the NHEJ process, which could instigate a scar in the form of insertion/deletion (indel mutations) leading to frameshift mutations, this approach could be used to mediate gene knockouts. Unlike NHEJ, HDR generally occurs only in dividing cells; with the presence of an exogenously introduced repair template [185]. The delivery of CRISPR/Cas9 components to the host cell can be achieved using various types of transfection strategies such as lipid-based transfection [186], electroporation and nucleofection [187], which we will be exploring in this chapter.

3.2 Chapter aims and objectives

In this chapter, the generation and characterisation of hiPSCs derived from a healthy volunteer and NAFLD patients that are from the same family with different *MTTP*-p.I564T (rs745447480) genotypes is described. CRISPR/Cas9 technology would also

be explored to create *MTTP* knockout (*MTTP-/-*) hiPSC line as a control in comparison to other derived-cell lines.

3.3 Results

3.3.1 Derivation of human dermal fibroblasts from skin punch biopsy

Skin punch biopsies were obtained from three individuals that contained different genetic variations of the missense I564T (rs745447480, *MTTP*-p.I564T) T>C single nucleotide variation (SNV) in the microsomal triglyceride transfer protein (*MTTP*) gene, encoding the Isoleucine (Ile) to Threonine (Thr) variant at protein position 564 (I564T) in exon 13. Healthy volunteer (patient number GF06, Male, 73 year old; T/T wildtype alleles, amino acid residues at MTP 564: Ile/Ile , termed $MTTP^{WT/WT}$) carries two T alleles of the *MTTP*-p.I564T SNV. **Figure 3.2A** displays the 4-generation pedigree of the investigated family. Family member J with a homozygous variation (GF10, Female, 57 year old; C/C, amino acid residues Thr/Thr, $MTTP^{VAR/VAR}$) contains two C alleles. She was diagnosed with cirrhosis at age 50 and hepatocellular carcinoma at age 54, she then undergone a liver transplant at age 56 and she is now recovered. Family member K only carries one T allele (GF11, 55 year old; T/C, amino acid residues Ile/Thr, $MTTP^{WT/VAR}$). She was diagnosed with NASH at age 48 and after making dietary and lifestyle changes, she is now recovered. Both family members had no sign of abetalipoproteinemia. We only have access to obtain skin punch biopsies from family member J and K; therefore, their samples were used to derive dermal fibroblasts for downstream experiments.

To derive a human dermal fibroblast (HDF) culture from each biopsy, each biopsy sample was dissected to remove subcutaneous fat to remove subcutaneous fat and cultured in HDF media over time (approximately 10-24 days) to allow fibroblasts outgrowth (**Figure 3.2B**). Keratinocytes started migrating out from the biopsy pieces after 7-10 days in culture, they are rounded to columnar in shape, forming a thick layer of cells that are tightly packed. After another 7-10 days, dermal fibroblasts

started to appear after the first outgrowth of keratinocytes (day 14-20), they appeared with a uniform spindle-like morphology that is typical of fibroblasts. To help isolate HDFs from the heterogeneous population, cells were trypsinised and transferred from 6-well plates to a T75 flask (day 22-30). Fibroblasts began forming a monolayer and were then passaged (1:2 ratio) to two T175 flasks once they reached at least 80% confluency. These fibroblasts were expanded further for cryopreservation or reprogrammed into hiPSCs. In total, three fibroblast cell lines were derived, including GF06 (*MTTP*$^{WT/WT}$) healthy control, GF10 (*MTTP*$^{VAR/VAR}$) homozygous variant and GF11 (*MTTP*$^{WT/MUT}$) heterozygous variant.

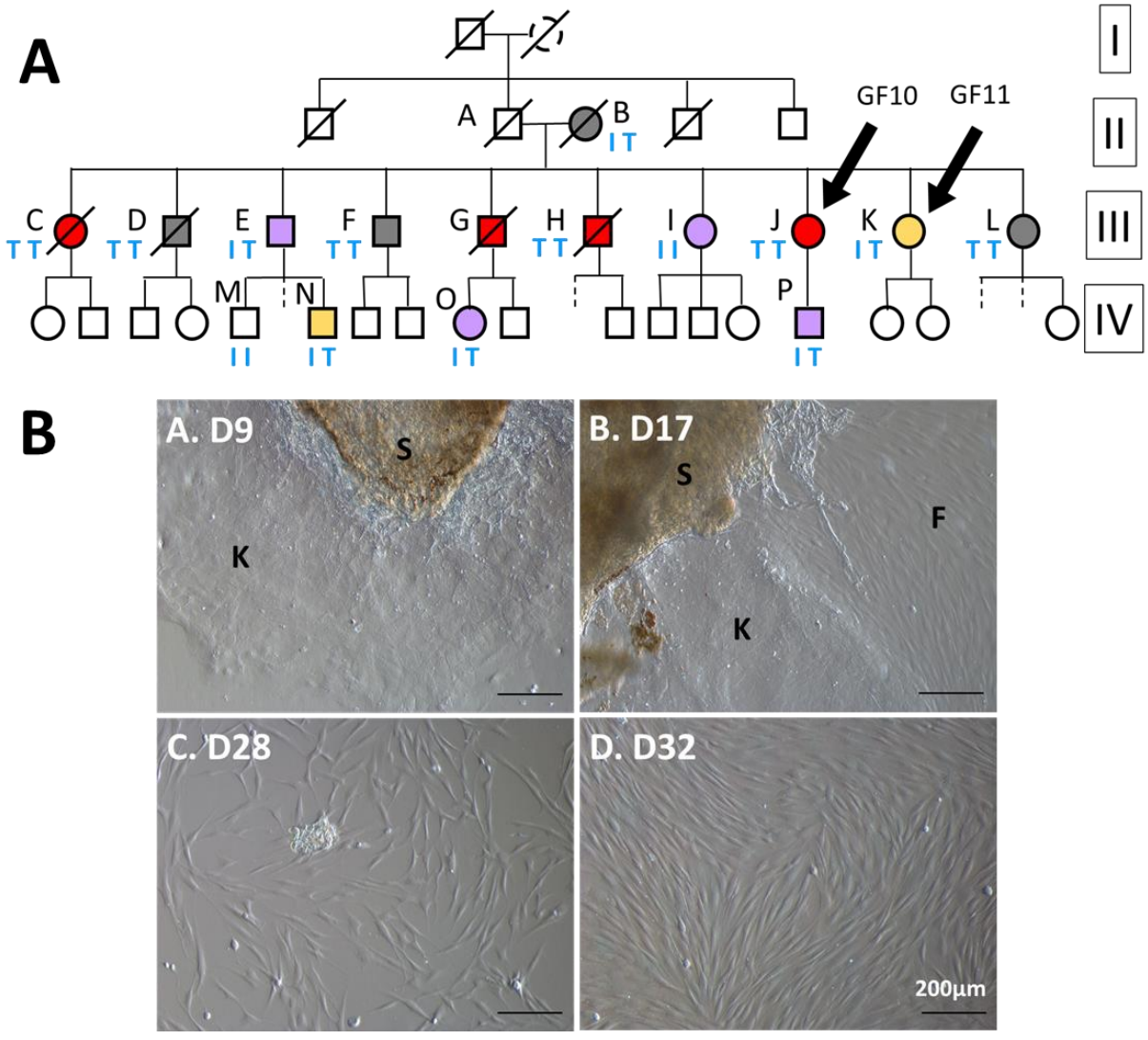


Figure 3.2 Isolation of human dermal fibroblasts from skin biopsy. (A) Pedigree of the investigated family. Square: male; circle: female; slashed: deceased. Red symbols indicate diagnosis of hepatocellular carcinoma (HCC); dark grey: cirrhosis; yellow: non-alcoholic steatohepatitis (NASH); lilac: fatty liver; dashed lines indicate that person was not

investigated. Disease status is not shown for all people in generation IV; they are aged 19-46. Skin biopsies samples (arrowed) were obtained only from family member J (GF10) and K (GF11). Blue letters indicate amino acid 564 in MTP encoded by the genotype, Wildtype I: Isoleucine; variant T: Threonine. **(B)** Representative images of the derivation of HDFs after the skin (S) biopsy has been dissected into pieces and transferred into 6-well plates. **A.** Keratinocytes (K) appeared after 7-10 days after processing (at day 9 = D9). **B.** Fibroblasts (F) were observed around D14-20 in culture (image taken on D17). **C.** Fibroblasts were isolated from mixed cell population by transferring the outgrown cells from 6-well plate to T75 flask approximately 8-12 days after their first appearance (D28). **D.** Once fibroblasts reached 80-90% confluency they are then passaged to T175 flasks for expansion to be cryopreserved later (D32). Scale bars = 200µm.

3.3.2 HiPSC reprogramming using Sendai-virus based vectors

All fibroblast cell lines were expanded and then reprogrammed into hiPSCs between passage 3-7 using non-integrating Sendai viral vectors (Figure 3.3**A**). Each HDF line was transduced with CytoTune-iPS 2.0 Sendai reprogramming vectors containing the human transcription factors *OCT3/4, SOX2, KLF4* and *c-MYC* (OSKM, Yamanaka factors). Fibroblasts were seeded at a density of 2 x 10^5 cells per well in an uncoated 6-well plate 24 hours prior to Sendai virus (SeV) transduction (day -1), viral transduction was performed the next day when cells reached 40-60% confluency (day 0). Approximately 5-10 days post SeV transduction, cells were undergoing morphological changes converting from the elongated fibroblast structure to a more polygonal shape and small colonies started to emerge (between 7-14 days). Depending on the cell line, at around day 13-32 colonies exhibited representative hESC-like morphology, the dense cell colonies were tightly packed with distinctive borders with a high nuclear-cytoplasmic (N:C) ratio. At this point, putative hiPSC colonies were ready to be isolated from the heterogenous population using either EDTA or ReLeSR for colony picking. Previous attempts of isolating hiPSC colonies by manual dissection had failed due to poor dissociation of cells upon transfer, mechanical disaggregation also caused cell death. To overcome these issues, we utilised EDTA and ReLeSR, which are enzyme-free reagents that have chelating properties to bind ions; both allowed selective detachment of hiPSC colonies using a pipette without complicated manipulation.

Overall, 36-96 clones were picked from each hiPSC line (GF06: 36, GF10: 48, GF11: 96), depending on the growth rate sub-populations of each cell line were expanded for further characterisation and the rest were cryopreserved. Different number of hiPSC lines were established approximately 40 days post-transduction, two lines were derived from GF06-HDF, four lines were derived from GF10-HDF and only one line was derived from GF11- HDF. We have chosen an hiPSC cell line from each donor (Figure 3.3**B**), they were named LOPCK (GF06-HDF derived, *MTTP*$^{WT/WT}$), MOPIK (GF10-HDF derived, *MTTP*$^{VAR/VAR}$) and HETIK (GF11-HDF derived, *MTTP*$^{WT/VAR}$).

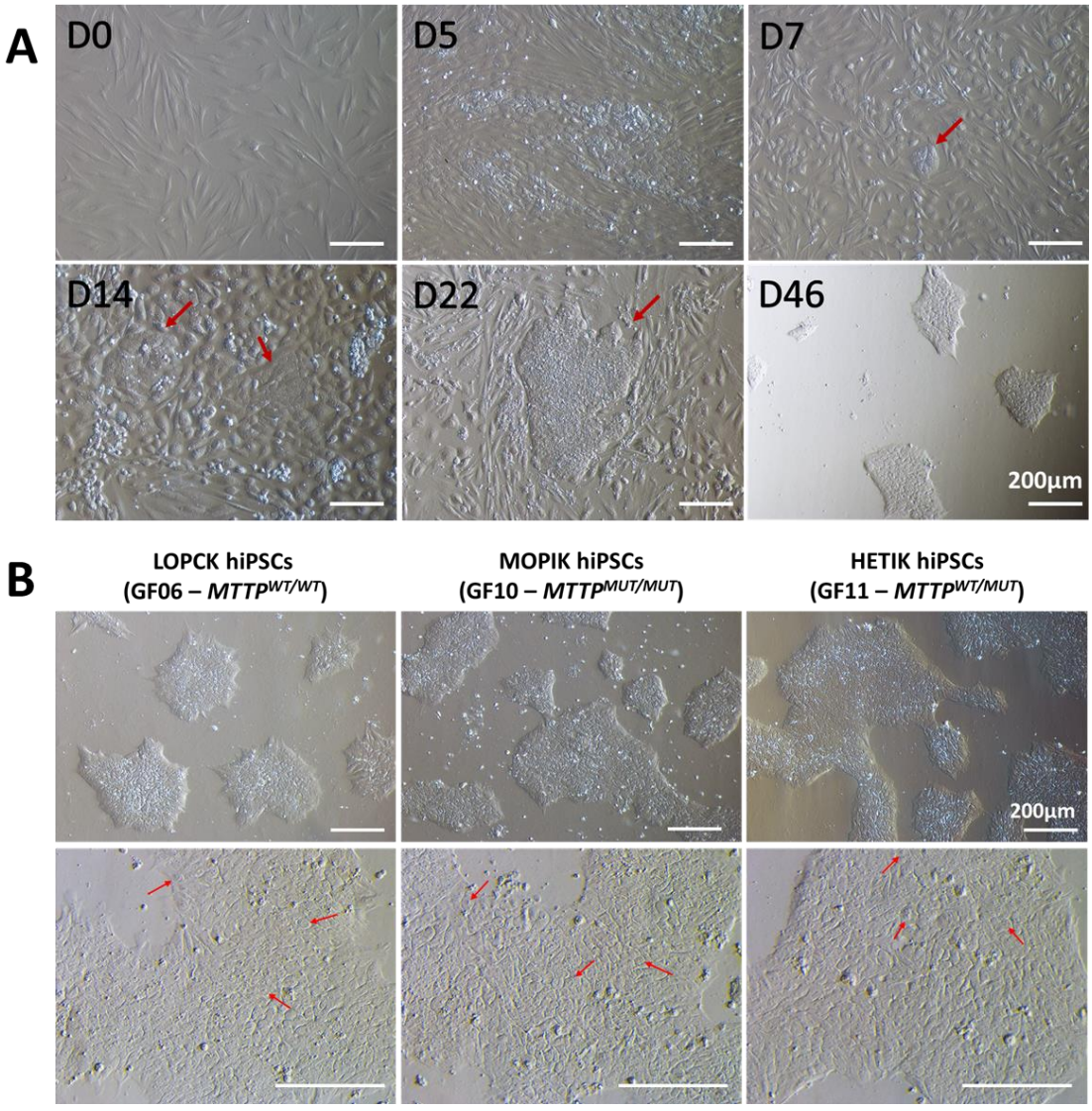


Figure 3.3 Derivation of hiPSCs from dermal fibroblasts. (A) Representative images of the reprogramming of hiPSCs from HDFs. Small colonies of potential hiPSCs start to emerge (red arrow) between 7-22 days. **(B)** Representative light microscopy of the three established cell lines, images were taken between passage 4 to 7. HiPSCs grown under feeder free conditions exhibiting typical flat colony, a tight edge, and a high nuclear to cytoplasmic ratio, with prominent nucleoli (red arrow). Scale bars = 200µm.

3.3.3 Characterisation of reprogrammed hiPSC lines

All generated hiPSCs have been passaged 2-5 times for cells expansion and cryopreservation. Characterisation was performed after somatic cell reprogramming to ensure all hiPSC lines fulfilled the criteria for being pluripotent and suitable to use for downstream experiments.

Chromosome analysis

Genomic stability of reprogrammed hiPSCs assessment was achieved following standard cytogenetic G-banding procedures. Karyotypes of LOPCK, MOPIK and HETIK hiPSC lines are all proven to be normal (Figure 3.4). All the reprogrammed cell lines display genomic integrity, the loss of chromosome 20 in LOPCK hiPSC line is most likely a random loss due to overexposure of hypotonic solution during the technical preparation of slides [188], this is not seen in subsequent routine karyotyping of LOPCK.

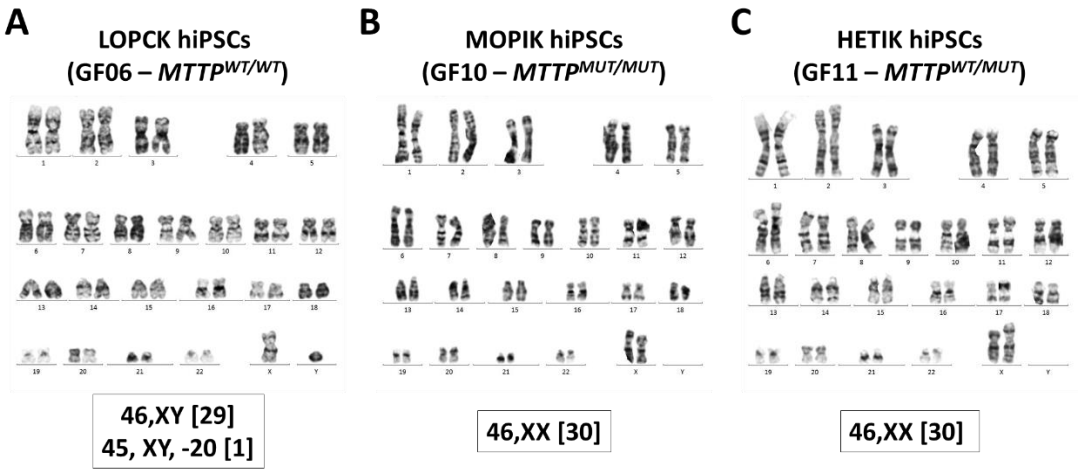


Figure 3.4 Karyotype of reprogrammed hiPSC lines. Representative karyotypes of **(A)** LOPCK hiPSC line derived from wild-type *MTTP-p.I564T* donor, **(B)** MOPIK hiPSCs reprogrammed from homozygous $MTTP^{VAR/VAR}$ fibroblasts, and **(C)** HETIK hiPSCs derived from heterozygous $MTTP^{WT/VAR}$ fibroblasts. Karyotyping service was performed by Nigel Smith (Cytogenetics Department, Nottingham City Hospital).

Stable pluripotency throughout cell culture media transition

A defined commercially available essential 8 (E8) medium produced by Stem Cell Technology (named TeSR-E8) was used during the reprogramming process to derive hiPSC colonies in feeder-free condition. To reduce the cost of overall culture

maintenance we have utilised a sequential adaption approach to transition the culture media from TeSR-E8 to an in-house made "homebrew (HB)" E8. This was implemented by serial passaging and increased the percentage of HB E8 by 25% in each passage (i.e. media composition of passage 1 would be 25% HB E8 with 75% TeSR-E8; passage 2 would be 50% HB E8 with 50% TeSR-E8; and so forth).

No major morphological changes were observed in all three hiPSC lines (**Figure 3.5A**) when compared to two other reference hPSC lines, including REBLPAT hiPSCs and H9 hESCs (**Figure 3.5B**). All reprogrammed hiPSC lines displayed the typical embryonic stem cell round shape colony morphology with small, tightly packed cells. Though the N:C ratio remained high in LOPCK hiPSCs, the colonies observed to be slightly more spread out in the 100% HB E8 medium, which resembled more like the H9 hESCs morphology comprised of small round cells with large nuclei, notable nucleoli, and larger space in between cells. In contrast, the two *MTTP*-p.I564T variant cell lines MOPIK and HETIK had relatively unnoticeable morphological changes during the adaptation and their growth rates remained similar, both looked a lot like the REBLPAT hiPSC line forming tight colonies with defined borders.

Despite the subtle differences in cell morphology, qPCR data revealed that pluripotency transcription factors *OCT4, NANOG* and *SOX2* gene expression in all three hiPSC lines were at comparable levels throughout the transition, REBLPAT hiPSCs were used as the reference cell line (**Figure 3.5C**). Interestingly, a global trend of *MTTP* downregulation was observed in all 3 hiPSC lines, but these were not statistically significant. Whether the genetic variation *MTTP*-p.I564T would remain intact post-reprogramming will be assessed later prior to further downstream experiments.

Statistically significant differences ($p<0.05$) were observed in some of the transcription factors expression in LOPCK and MOPIK cell lines between different passages. Morphological changes were relatively more blatant in LOPCK hiPSCs, the sizes of LOPCK hiPSCs began to enlarge gradually after each passage, this fluctuation

reflected on the change in gene expression (*OCT4*, 50% HB: 75% HB, p = 0.0472; *NANOG*, 25% HB: 75% HB, p = 0.0122; *SOX2*, 75% HB: 100% HB, p = 0.0368). In comparison, MOPIK hiPSC sizes also increased morphologically but at a much lower degree. Notwithstanding, qPCR also showed statistically significant differences between early and late stage of the transition (*OCT4*, 25% HB:1005% HB, p = 0.0114; 50% HB:1005% HB, p = 0.0457).

Though qPCR data has shown similar gene expression levels of pluripotency markers *OCT4, NANOG* and *SOX2,* it is also important to consider the potential arise of detecting pseudogenes. Pseudogenes are genomic DNA sequences that resemble to normal genes but have been mutated into defunct forms of functional genes [189], [190]. Two types of pseudogenes are identified according to their precise mode of origin: non-processed pseudogenes derive from gene duplication which may possess introns and flanking sequences, located on the same chromosome as the parental gene from which they are derived; processed pseudogenes originate by retrotransposition of functional mRNA which do not contains introns, and are located on different chromosomes than the genes from which they originate, this type of pseudogene can cause qPCR artifacts if the DNase digestion before cDNA synthesis is incomplete, generating false-positive results [190], [191].

It is known that the human *OCT4* gene can generate at least three different transcripts by alternative splicing including *OCT4A*, *OCT4B*, and *OCT4B1* [192]. OCT4A is the main isoform responsible for the stemness property of embryonic stem cells; at least six processed *OCT4* pseudogenes have been identified with high homology to *OCT4A* [193], [194]; *NANOG* has at least ten processed pseudogenes in the human genome [195], [196]. To mitigate pseudogene amplification bias and to verify whether the derived hiPSCs are indeed pluripotent, protein expression of pluripotency markers will also be evaluated in the next section.

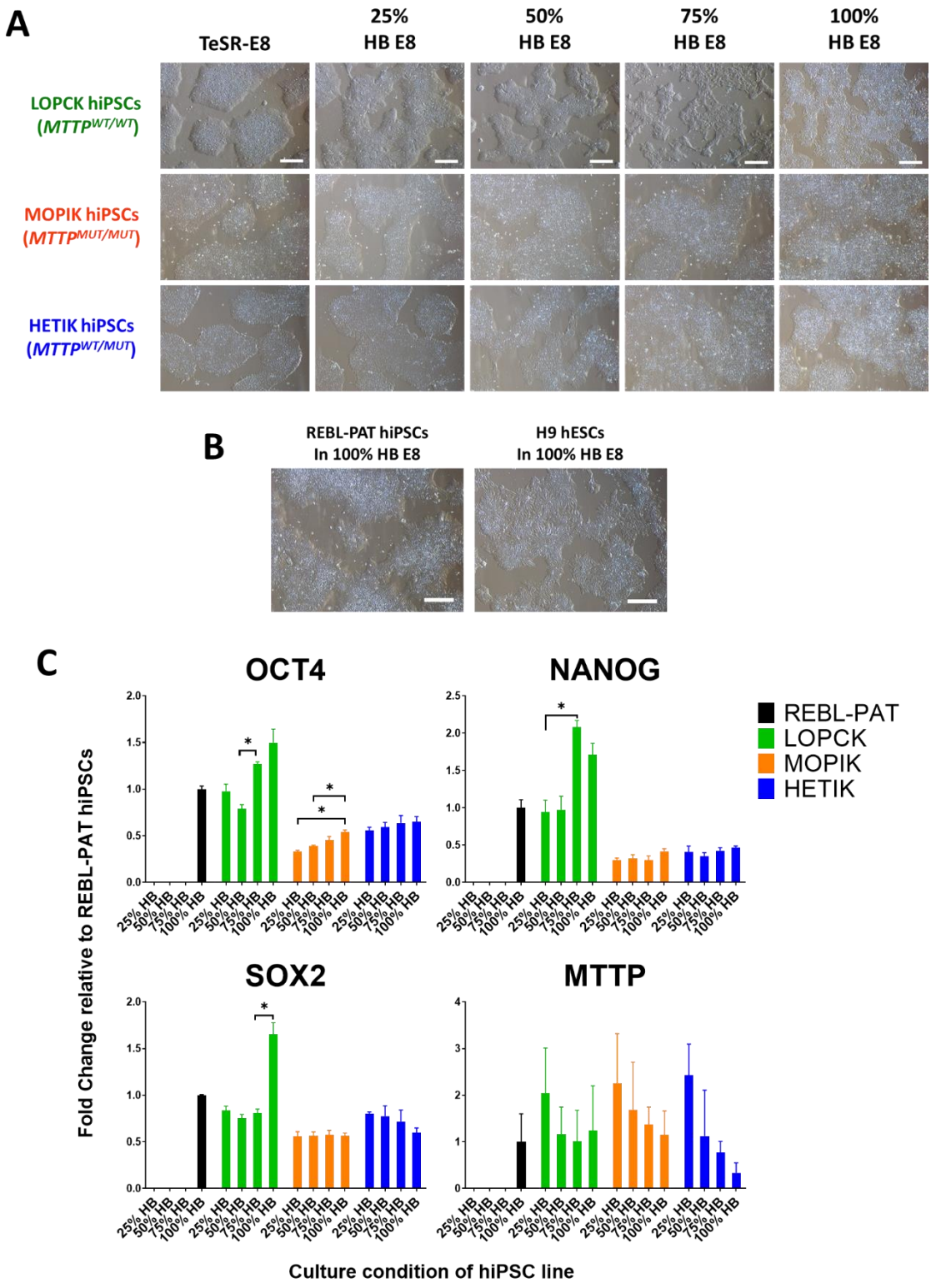


Figure 3.5 Sequential adaptation of media transition from TeSR-E8 to HB E8. (below) (A) Representation brightfield images of hiPSCs at different passages. Cells were maintained in media composited of 25% increment of HB E8 along with 25% reduction of TeSR-E8 after each split. **(B)** REBLPAT hiPSCs and H9 hESCs were used as controls for morphology assessment against new reprogrammed hiPSC lines. **(C)** Gene expression analysis of pluripotency markers and *MTTP* using qPCR (Statistical significance *p<0.05). Scale bars =200 µm.

Assessment of pluripotency markers and trilineage differentiation

To confirm the pluripotency status of these hiPSC lines, HDF-derived hiPSCs were expanded on Matrigel™-coated plates and tested for the presence of pluripotency markers by immunocytochemistry (**Figure 3.6A**). Indeed, both OCT4 and NANOG were detected within the nuclei of undifferentiated LOPCK, MOPIK, and HETIK hiPSCs.

After that, trilineage differentiation was performed to validate the ability of established hiPSC lines (**Figure 3.6B**). LOPCK, MOPIK and HETIK hiPSCs were differentiated toward the three embryonic germ layers including endoderm, mesoderm, and ectoderm using directed *in vitro* assays to demonstrate that they are fully pluripotent. All three cell lines underwent drastic morphological changes with extensive cellular migration and proliferation, by D3 of the endodermal differentiation cells displayed a classic petal/cobblestone like morphology which is indicative of definitive endoderm. HiPSCs undergoing mesodermal differentiation became more rounded after D1 and cells started to migrate out similarly in all three cell lines. During neuroectodermal differentiation, though all three hiPSC lines began to form flatter cell population, MOPIK and HETIK seemed to retain some stem-cell like colonies compared to LOPCK cell line. Further examination using immunocytochemistry was performed to identify the presence of lineage-specific protein markers.

The resulting cells were immunophenotyped for markers characterised for each germ layer. Fluorescence microscopy was used rather than flow cytometry because it can help us determine the differential expression, localisation, and subcellular distribution of proteins of interest. HiPSCs were first differentiated to hepatic progenitor using our developed protocol, hepatic progenitors derived from all 3 cell lines were expressing markers specific to liver buds. Positive cytoplasmic expression of alpha foetal protein (AFP) was detected and hepatocyte nuclear factor 4 alpha (HNF4A) was localised within the nuclei of differentiated cells (**Figure 3.6C**).

Following differentiation into cardiomyocyte progenitor using the protocol described by Burridge et al. (2014), cells were probed on differentiation day 3 for the expression of mesoderm posterior protein 1 (MESP1) and early cardiomyocyte/ mesendoderm marker GATA binding protein 4 (GATA4), although differentiation efficiency varies depending on the cell line, these markers were all presented within the nuclei (**Figure 3.6D**).

Finally, we used an adapted version of the protocol described in 2009 by Vallier et al. Differentiated cells were immunostained on day 7 for the detection of neuroectodermal markers including SRY-box 2 (SOX2) and Nestin. SOX2 was positively expressed in all 3 cell lines within the nuclei, cytoplasmic expression of Nestin was also detected while the pluripotency marker NANOG was not detected (**Figure 3.6E**).

Immunofluorescence results demonstrate that reprogrammed hiPSC lines are truly pluripotent. It should be noted that the *in vitro* directed mesoderm and ectoderm differentiation protocols were not optimized for the generation of cells for downstream differentiation or other applications, they were mainly utilised to prove the potential of derived hiPSCs to differentiate into any of the three germ layers.

The next stage of the experiment would be to examine whether the genetic variation *MTTP*-p.I564T would remain intact post-reprogramming prior to further downstream experiments.

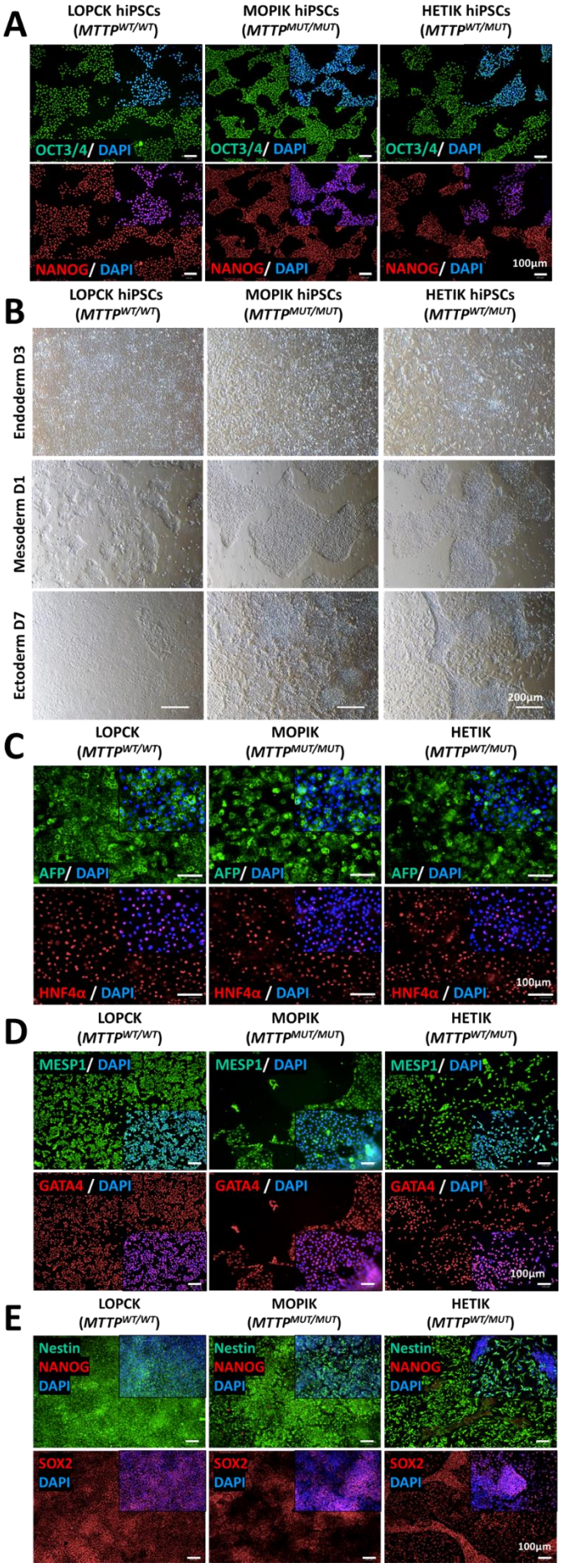


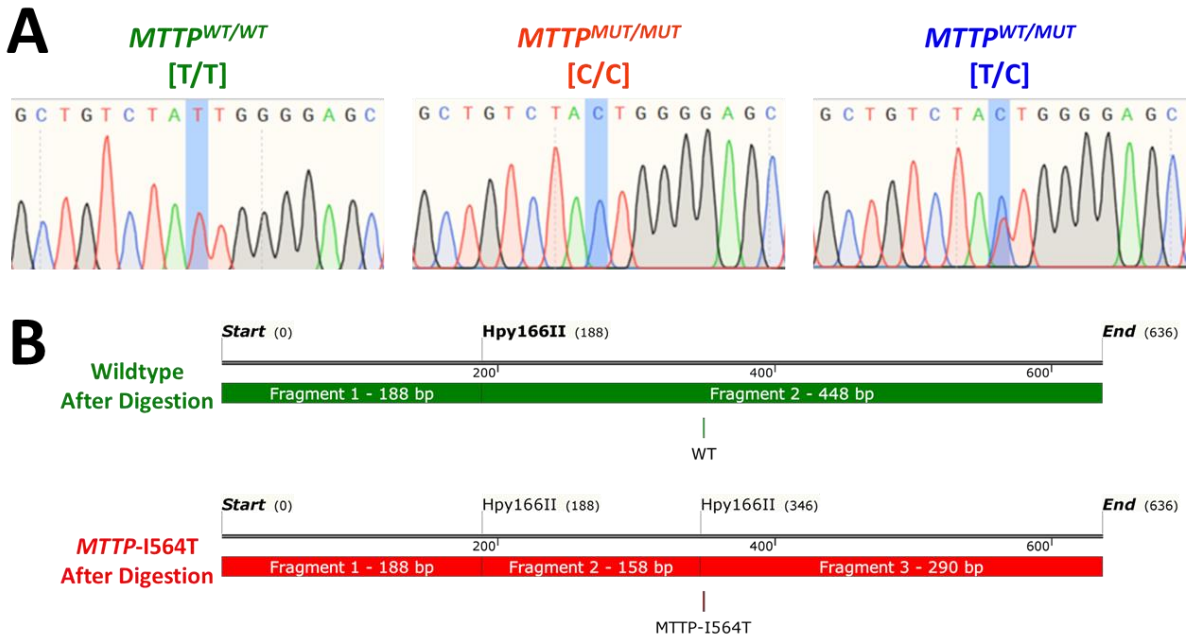
Figure 3.6 Fibroblast-derived hiPSCs are pluripotent. (A) Detection of pluripotency-associated markers. OCT3/4 and NANOG are detected in the nuclei of LOPCK, MOPIK, and HETIK hiPSCs. **(B)** Trilineage differentiation. Representative images of differentiating hiPSCs taken during endoderm differentiation day 3; mesoderm day 1; and ectoderm day 7. Scale bars = 200 µm. **(C)** Hepatic progenitors expressed liver-specific markers AFP in the cytoplasm and HNF4A within the nuclei. **(D)** Mesodermal marker MESP1 and GATA4 are detected within the nuclei in all 3 cell lines with variable differentiation efficiencies. **(E)** Neuroectodermal markers SOX2 and Nestin are both expressed while stem cell marker NANOG is absent. SOX2 is detected within the nuclei, whereas Nestin is localized to the intermediate filaments in the cytoplasm. Insets for **(B-E)** (either top right or bottom right in each image) show the combined staining with DAPI to display where nuclei are located. Scale bars **(B-E)** = 100 µm

Validation of pre-existing MTTP SNVs remain intact post-reprogramming

To ensure that the pre-existing *MTTP*-p.I564T SNVs remain intact even after reprogramming, genomic PCR and gel electrophoresis were used to confirm the presence of this genetic variation. It is fundamental that the reprogrammed hiPSC genome remained faithful to the genetic copy of the dermal fibroblasts which they were derived, in order to help us understand the underlying driving mechanisms causing NAFLD. PCR amplification was done using DNA extracted from donors' blood samples, Sanger sequencing alignment revealed that WT genotype would have 2 T alleles, whereas the *MTTP*-p.I564T variants would be replaced with a C allele instead (**Figure 3.7A**, courtesy of Dr Jane Grove, collaborator).

Genotypes of the reprogrammed hiPSC lines was determined by doing a restriction enzyme digestion using Hpy166II, the PCR product of WT hiPSCs should produce 2 fragments (188 bp and 448 bp) and mutant hiPSCs would generate 3 fragments (188 bp, 158 bp and 290 bp) after Hpy166II-digestion (**Figure 3.7B**). Allele-specific expression can be determined with further band densitometry analysis of the gel electrophoresis image. **Figure 3.7C** shows that Hpy166II-digested PCR product of LOPCK hiPSCs only produced 2 fragments with the lack of band size 290 bp. Both MOPIK and HETIK hiPSC lines generated 3 fragmented PCR products, the signal intensity of homozygote MOPIK hiPSCs was at 290 bp, which is approximately 50% more of that from the heterozygote HETIK line. This validated that both the MOPIK and HETIK hiPSC lines remained their *MTTP*-p.I564T biallelic and monoallelic genotypes after reprogramming.

Figure 3.7 Allele-specific expression of the *MTTP* gene. (below) (A) DNA extracted from donors' blood samples were PCR amplified with specific primers. Sanger sequencing alignment of the PCR products at the region of *MTTP*-p.I564T, where the T allele (wildtype) changes to C allele, causing a replacement of the amino acid isoleucine to threonine. WT = T/T; Homozygote = C/C; Heterozygote = T/C. **(B)** Hpy166II digestion is used to digest distinguish between WT and mutant alleles, WT produces 2 fragments, whereas the mutant alleles would produce 3 fragments. **(C)** Before Hpy166II digestion, size of the complete PCR product is 636 bp. After digestion, LOPCK hiPSCs (WT) resulted in 2 fragments (188bp and 448bp), MOPIK ($MTTP^{VAR/VAR}$) and HETIK ($MTTP^{WT/VAR}$) hiPSCs both generated 3 fragments (188bp, 155bp, 290bp). Band densitometry analysis shows that the signal intensity produced by MOPIK with both the C alleles is the highest, followed by HETIK (heterozygote line), LOPCK with the wildtype T alleles has the lowest signal. Analysed bands are highted in yellow boxes, normalisation is done by subtracting the background signal.


A
MTTPWT/WT
[T/T]
MTTPMUT/MUT
[C/C]
MTTPWT/MUT
[T/C]
B
Wildtype
After Digestion
Start (0)
Hpy166II (188)
End (636)
200
400
600
Fragment 1 - 188 bp
Fragment 2 - 448 bp
WT
MTTP-I564T
After Digestion
Start (0)
Hpy166II (188)
Hpy166II (346)
End (636)
Fragment 1 - 188 bp
Fragment 2 - 158 bp
Fragment 3 - 290 bp
MTTP-I564T
C
LOPCK
WT/WT
MOPIK
MUT/MUT
HETIK
WT/MUT
Hpy166II
1517
1200
1000
900
800
700
600
500/517
400
300
200
100
Uncut
636bp
Wildtype
448bp
188bp
MTTP-I564T
mutants
290bp
188bp
158bp
Signal Intensity
200000
150000
100000
50000
0
LOPCK
MOPIK
HETIK
Signal
0
182100
92100

3.3.4 Using CRISPR/Cas9 approach to create MTTP knockout hiPSCs as a NAFLD positive control

After we characterised all three reprogrammed hiPSC lines, we decided to focus on LOPCK (*MTTP*$^{WT/WT}$) and MOPIK (*MTTP*$^{VAR/VAR}$) cell lines as the models moving forward to investigate the pathological mechanisms of *MTTP*-p.I564T in NAFLD susceptibility and pathogenesis. These two cell lines consist of the two extreme genotype spectra, which would enable us to decipher the implications of this variation compared to that of the heterozygote cell line HETIK (*MTTP*$^{WT/VAR}$). In addition to the patient-derived cell lines, we have utilised CRISPR/Cas9 technology to create a positive isogenic control to the LOPCK cell line by knocking out the *MTTP* gene completely using a commercially available kit.

Determination and optimisation of transfection agent for high efficiency CRISPR/Cas9 targeting

Transfection efficiency into hiPSCs was first tested using GFP plasmids with a lipid-based Lipofectamine™ 2000 transfection agent at various concentrations (0 µg, 6 µg, 9 µg and 12 µg). It has reported that analysis of flow cytometry tends to measure higher percentage transfection and fluorescence intensity compared to fluorescence microscopy, the discrepancy could be due to additional preparation of a sample due to cell dissociation and centrifugation causing partial cell lost [197]. To increase cell viability and avoid potential contamination of the transfected cells, fluorescence microscopy was used to give the most direct observation for both quantification and visualisation without additional preparation of samples. Live imaging also allows us to determine the optimal time after transfection for analysis of results, GFP expression should be detectable 24 to 48 h post-transfection.

LOPCK hiPSCs were seeded 500,000 cells per well on a Matrigel-coated 6-well plate (equivalent to ~50,000 cells/cm^2) and the transient expression of GFP plasmids after 24 and 48 hours were used to assess the transfection efficiency (**Figure 3.8A**). Bright-field images revealed that cells had good recovery 24 h post-transfection using lipofectamine overall compared to the negative control (0 µg lipofectamine), GFP

expression was also observed using an inverted microscope incorporated with fluorescence lasers.

To determine whether greater transfection efficiencies could be achieved, an electroporation-based nucleofection method was performed utilising the Amaxa™ 4D device with the program setting as DN-100 (**Figure 3.8B**). LOPCK hiPSCs were also seeded at the same density and transfected with the same amount of GFP plasmids similar to the lipid-based method. Bright-field images showed that there were relatively less cells attached 24 h post-transfection compared to that using lipofectamine, however cells quickly recover and grew back after 48 h. Moreover, fluorescence images showed that relatively more cells were expressing GFP as well as having a much stronger expression.

Quantification of GFP fluorescence intensity was performed in order to evaluate the transfection efficiency using these two methods (**Figure 3.8C**). Fluorescence intensity values were measured using Image J software and plotted. Nucleofection using the DN-100 program outperformed the results obtained by using lipofectamine as the transfection reagent regardless of the concentration. Overall, GFP fluorescence intensity was statistically significantly higher under nucleofection condition and achieved approximately 1.5-fold higher GFP expression compared to lipid-based methods. As a result, Amaxa™ 4D nucleofection was chosen as the preferred method for doing CRISPR/Cas9 targeting of LOPCK hiPSCs.

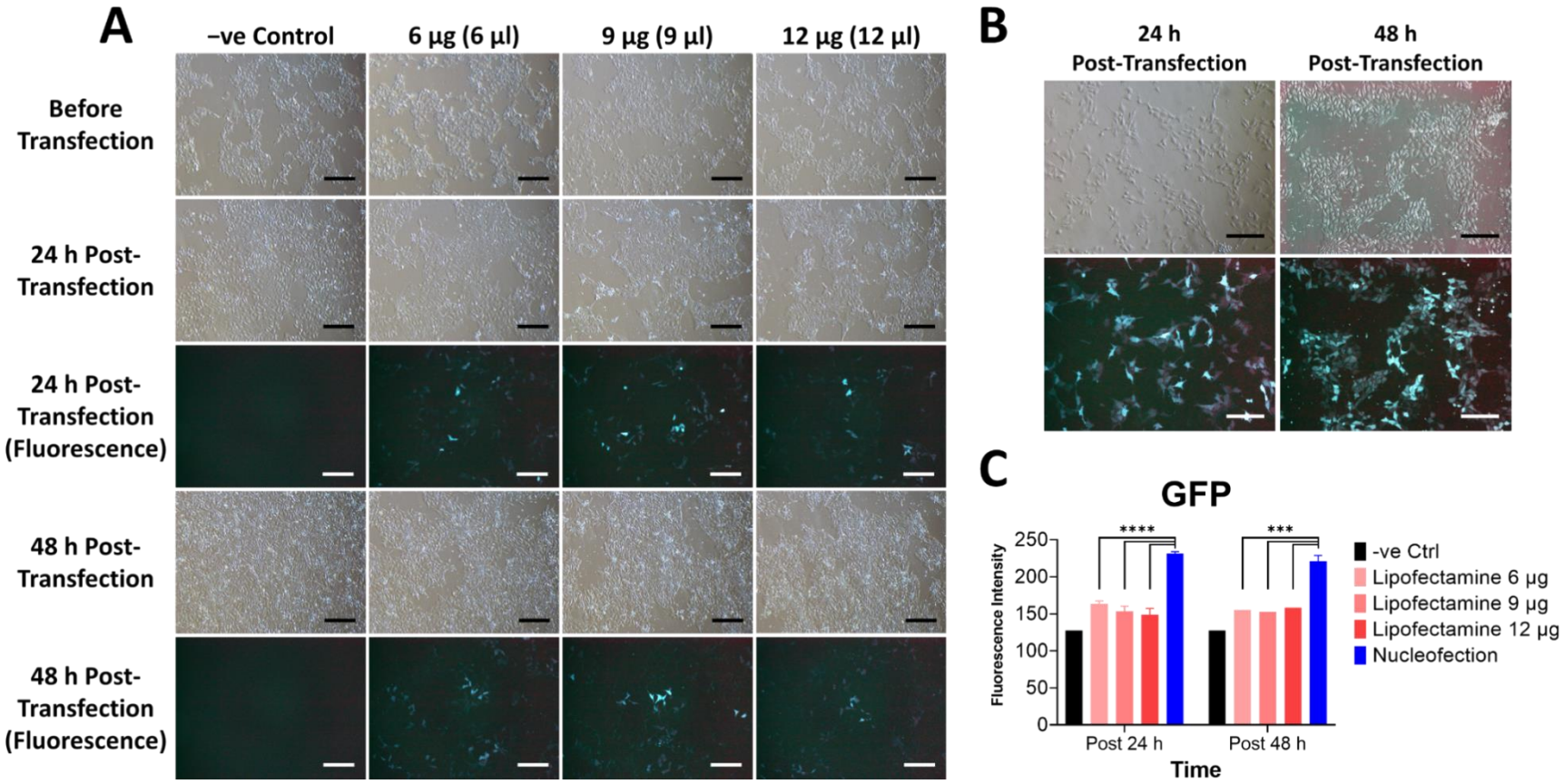


Figure 3.8 Transfection efficiency comparison between lipofectamine and Amaxa™ 4D nucleofection using GFP plasmid on LOPCK hiPSCs. (A) Live images (bright-field and fluorescence) of LOPCK hiPSCs before and after transfection using lipofectamine at various dosages along with 2µg of GFP plasmid. 0 µg of lipofectamine is used in negative (–ve) control. **(B)** Representative images after nucleofection using the Amaxa™ 4D with the program setting as DN-100, 2 µg of GFP plasmid is used. **(C)** Comparison of GFP fluorescence intensities between lipofectamine-based and nucleofection post-transfection. Mean ± SD (n = 3). Scale bars = 200 µm.

Determination of optimal dosage for colony antibiotic selection

After choosing the preferred transfection approach, the next critical step was to determine the optimal antibiotic concentration for selecting stable targeted cell colonies. A puromycin dose-response kill curve experiment was performed to determine the minimum antibiotic concentration to select successfully targeted clones (Figure 3.9). Operetta™ high content image analysis system combined with Columbus™ software were used to assess the cell confluence percentage (%) during antibiotic treatment over the course of 72 hours, this approach enabled us to identify the minimum required puromycin dosage to kill untargeted hiPSCs (Figure 3.9**A-D**). The software was trained to recognise areas with and without cells, in order to calculate the overall % of cells presented (**Figure 3.9E**), this was done by dividing cell population area over the total area and multiplied by 100.

*% Confluency = (**Cell population area** / (**Cell population area** + **No cells area**)) * 100*

54 fields of view were captured for each condition and the mean confluence % values were calculated, which were then plotted to generate a kill curve graph (**Figure 3.9F**). Most cells were killed at 0.4 µg/ml of puromycin after 24 h with approximately 8.4% confluence, by 72 h the confluence % was significantly reduced to 0.74% using 0.4 µg/ml compared to other dosages. 0.3 µg/ml of puromycin eradicated the majority of cells with a confluence of 2.18%, but that only happened after 48h. Based on these results, 0.4 µg/ml was selected as the working concentration to enrich targeted cells.

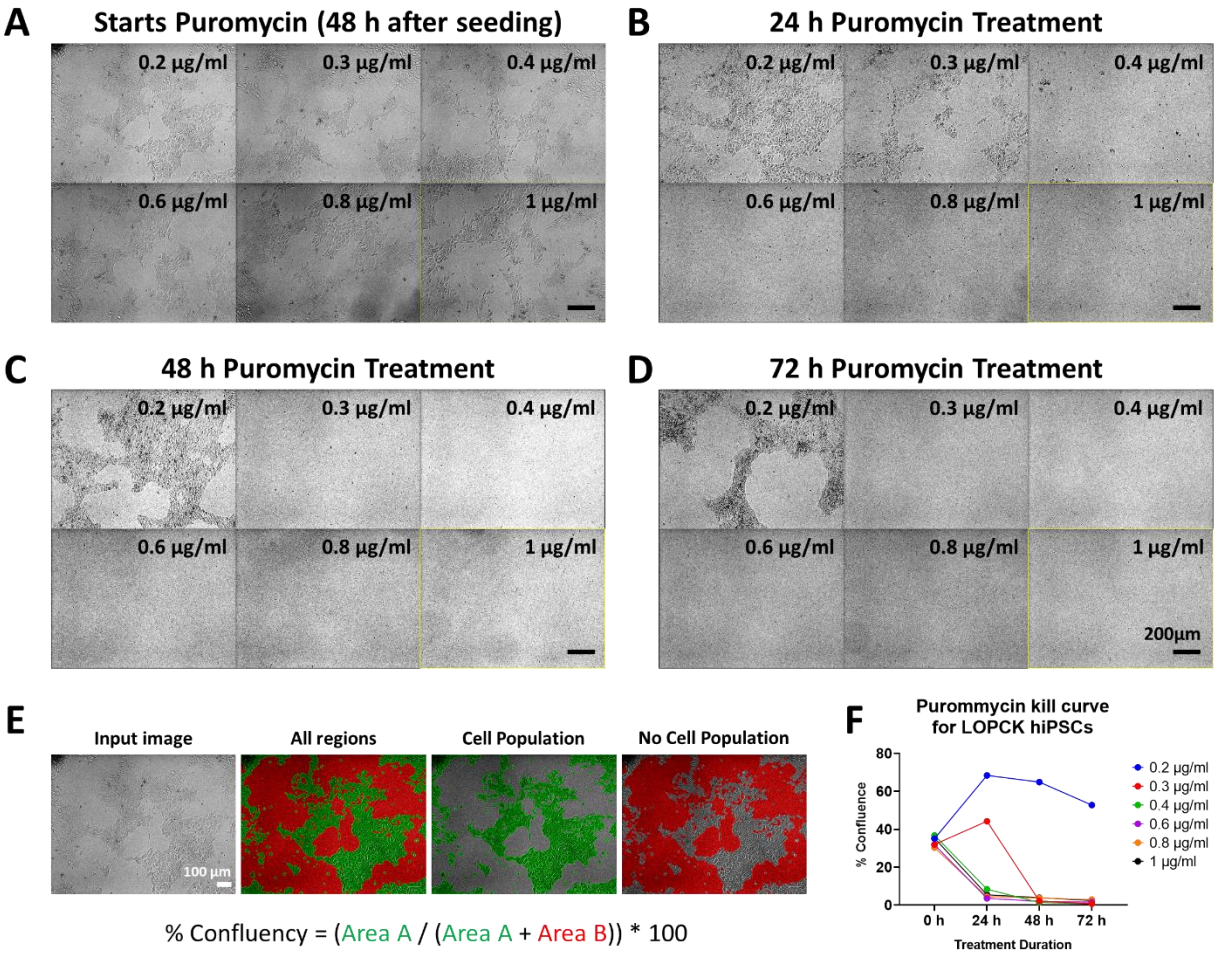


Figure 3.9 Puromycin titration on LOPCK hiPSCs to determine optimal selection concentration. Representative bright-field images are taken over 72 h by the Operetta™ high content image analysis system. **(A)** Puromycin treatment starts 48 h after seeding (20,000 cells/cm2). Live cell images are taken **(B)** 24 h, **(C)** 48 h and **(D)** 72 h of puromycin treatment at various concentrations. Scale bars (A-D) = 200 µm. **(E)** Live cells images are taken by the Operetta™ system and image analysis to calculate the percentage (%) of confluence using the Columbus™ system incorporated. By selecting different programs, the software is trained to identify areas to distinguish between cell (area A in green) and no cell (area B in red) within the whole image. Scale bar = 100 µm. **(F)** % confluency of each time point at different puromycin concentrations is plotted as the mean values out of 54 fields (for each condition) in a kill curve graph, the minimal puromycin concentration of which cells are killed is at 0.4 µg/ml at 24 h.

MTTP KO in LOPCK hiPSCs using CRISPR/Cas9 technology and genotypic characterisation of targeted clones

Once the optimal transfection and selection conditions were determined, the next step was to transfect different plasmid vectors to the LOPCK hiPSCs using nucleofection in order to introduce a knockout (KO) in the *MTTP* gene, followed by

positive colony selection (**Figure 3.10**). The commercially available CRISPR/Cas9-based *MTTP* knockout kit from Origene contained an all-in-one pCAS-Guide vectors that already has Streptococcus pyogenes Cas9 endonuclease, along with 2 different guide RNA (gRNA) scaffolds incorporated within the vectors. A pCas-Scramble was used as a negative control. In addition to these, a separate plasmid contained the donor DNA template targeting the *MTTP* homology arms with a GFP-puromycin resistance cassette for positive selection. Following nucleofection of these plasmids, hiPSCs were selected by puromycin treatment for 7-12 days until clearly defined colonies were visible. These colonies were then individually picked using either EDTA or ReLeSR, which were further expanded for genotyping and cryopreservation.

Genotypic characterisation of targeted clones using PCR

To screen for colonies that have been successfully knockout of the *MTTP* gene, PCR genotyping was utilised. Different sets of primers were used to depict the correct PCR product sizes, genomic DNA were extracted from puromycin-resistant clones and assessed (**Figure 3.11A**). Primer sets 1 and 2 were aimed at left and right homology arms respectively, and the PCR reactions were only successful in positive clones, in contrast to untargeted hiPSCs. Primer set 3 was designed to amplify both alleles and sequencing of the amplified product enabled confirmation of the heterozygous versus homozygous genotype of positive colonies detected.

Out of 53 puromycin-selected clones, only one clone (0.4 µg/ml puromycin) was able to generate a PCR product (size 954 bp) corresponded to the 3' integration from outside the right homology arm into the resistance cassette using primer set 1; allele that has not been inserted with the donor template would not produce a product at all (**Figure 3.11B**). The positive colony was targeted by gRNA 1 and it was clone number 33, hence named as g1#33. Using the same principle, we validated that g1#33 was able to generate a PCR product (size 864 bp) with a successful 5' integration from outside the left homology arm into the cassette (**Figure 3.11C**).

To validate whether g1#33 was successfully edited on both alleles, primer 3 was used to elucidate the targeting event (**Figure 3.11D**). A homozygous *MTTP* KO clone should not be expressing a band at 2048 bp as it represents the PCR product without a cassette integration, instead, a band at 4544 bp would be generated with the resistance cassette incorporated. There was a faint band at 2048 bp observed from g1#33 genomic DNA, which implied that the targeting was monoallelic. Notably, the expected 4544 bp band was not found from g1#33 either. No bi-allelic targeting events were found using the commercial *MTTP* CRISPR KO kit. Out of the 53 screened clones, only 1 clone was targeted mono-allelically (**Figure 3.11E**). A directed differentiation towards hepatic fate was performed on g1#33 clone to see if GFP expression can be detected at all, but no GFP expression was observed throughout the whole differentiation at different stages (**Figure 3.11F**).

In summary, the mono-allelic targeted g1#33 clone (originated from LOPCK hiPSCs) was not used as a control for the downstream experiments because it would not serve as a subjective reference to be compared with the *MTTP*-p.I564T homozygote MOPIK cell line.

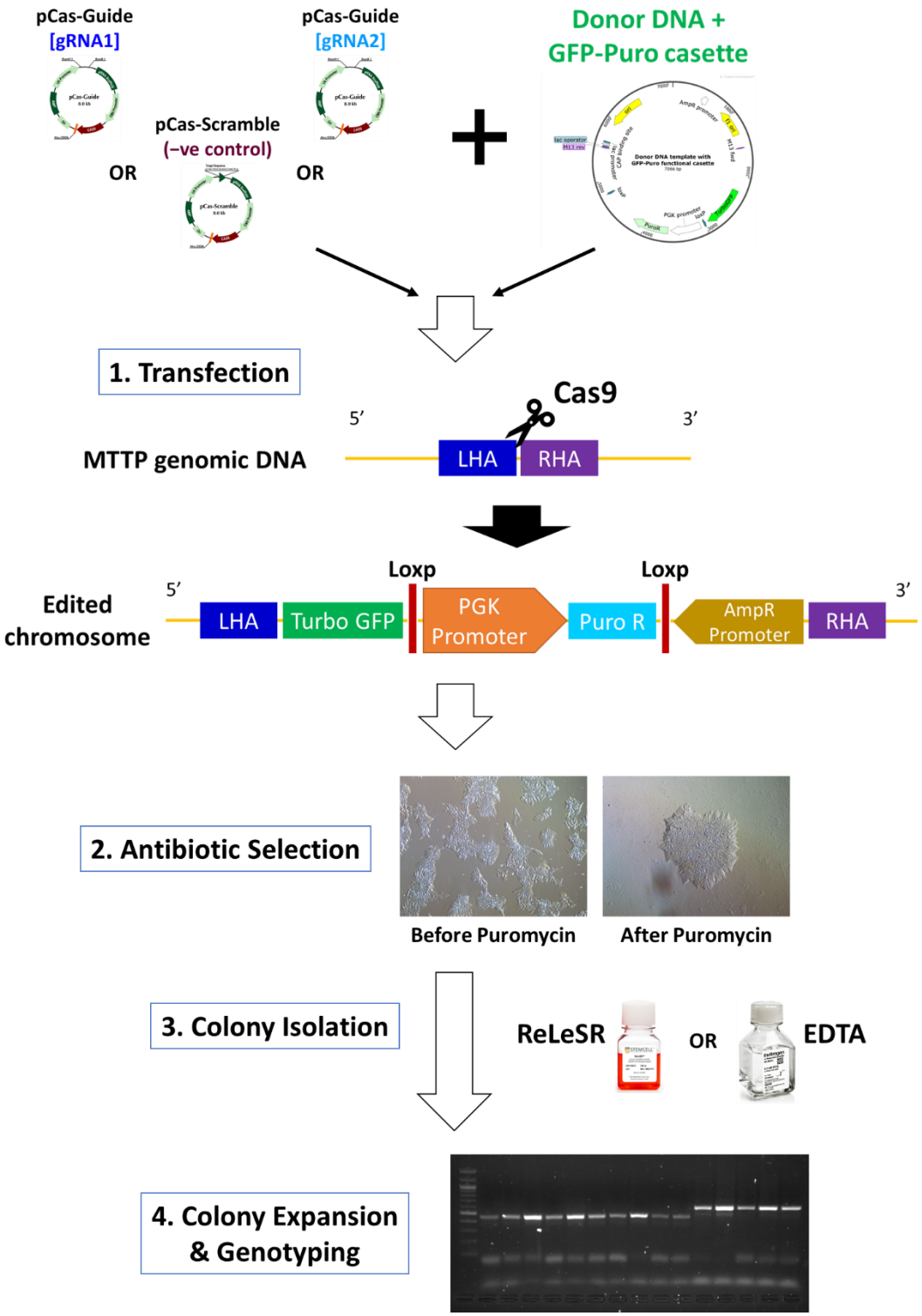
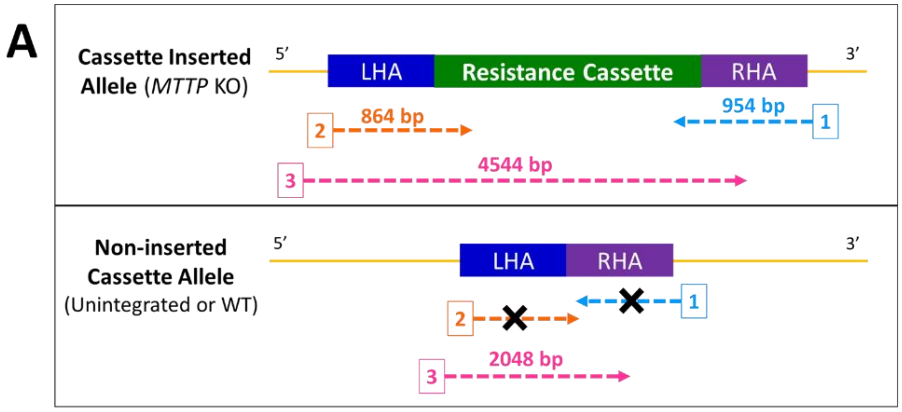
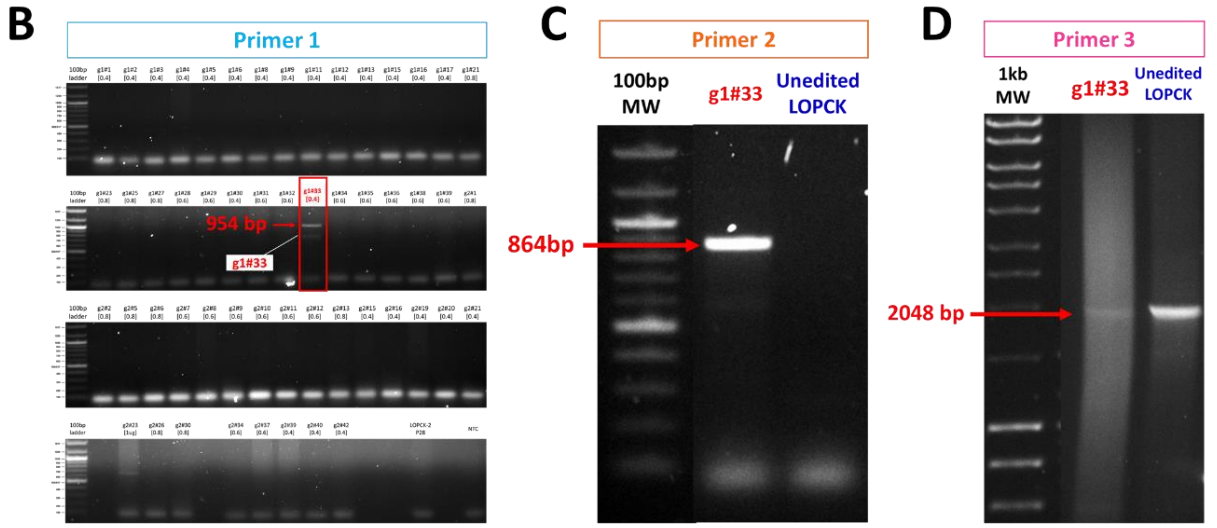


Figure 3.10 Overview of CRISPR/Cas9 KO targeting workflow. (1) pCas-Guide vectors containing gRNAs, pCas scamble (negative control) and donor DNA template (containing GFP-puromycin resistance cassette) are transfected into hiPSCs to initiate KO targeting. (2) Transfected cells are then enriched by antibiotic selection using puromycin. (3) Viable colonies would be isolated using either ReLeSR or EDTA. (4) Colonies are expanded and cryopreserved for downstream genotyping.



E

Edited cell line	LOPCK hiPSCs
Puromycin-Resistant Colonies	53
Positive Colonies with 3' Integration	1
Mono-allelic Colonies	1
Bi-allelic Colonies	0



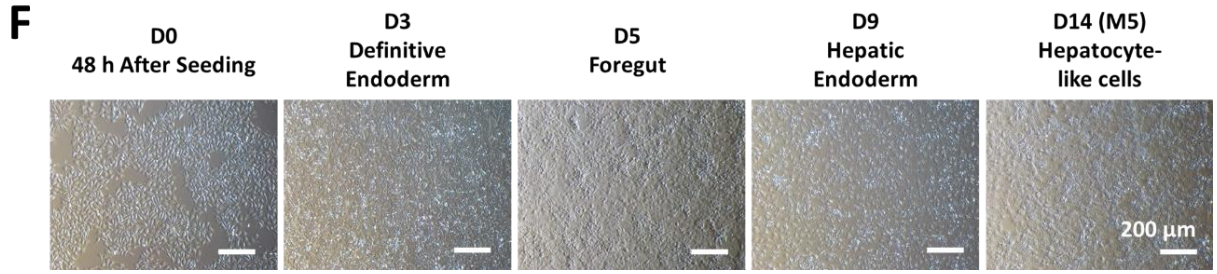


Figure 3.11 PCR genotypic characterisation of genome-edited LOPCK hiPSCs. Schematic diagram of the expected PCR products generated from successfully KO colonies, as well as the non-edited clones. A cross indicates no PCR product is generated. **(B)** DNA electrophoresis gels showing the results of the PCR amplification of primer 1, which indicates successful 3' integration from outside the right homology arm (cassette allele), non-inserted cassette allele would not generate a product, 53 colonies were screened. Colony g1#33 produced the corresponding product (band size 954 bp). Unedited LOPCK hiPSC DNA is used as a negative control in all PCRs. MW – Molecular weight marker; NTC- non template control. **(C)** Primer 2 is specific for generating product that is integrated from outside the 5' left homology arm up until the resistance cassette, colony g1#33 generated the expected band at 864 bp. **(D)** Primer 3 amplifies PCR products on both the cassette and non-integrated alleles but with different product sizes. Colony that is homozygous *MTTP* KO should only produce a band at 4544 bp, whereas a band size at 2048 bp indicates a monoallelic editing is achieved. A faint band can be seen at 2048 bp from g1#33 DNA, indicating that a

heterozygous genotype is detected. **(E)** Number of positively-selected colonies, only 1 clone is edited mono-allelically. **(F)** G1#33 clone was differentiated to HLCs for checking potential GFP expression, no GFP expression is observed throughout the different stages (fluorescence images not shown as they are all black). Scale bar = 200 µm.

3.4 Discussion

In this chapter, hiPSCs have been reprogrammed from donor-derived dermal fibroblasts using SeV-based reprogramming method. Generated hiPSCs were characterised using karyotyping, qPCR and immunocytochemistry to ensure that they are truly pluripotent for downstream applications. CRISPR/Cas9 technology was also utilised in attempt of creating a *MTTP* knockout cell line as a control in comparison to the donor-derived hiPSC lines.

We have been able to isolate and culture human fibroblasts from three donors by dissecting skin biopsy samples and seeding them onto tissue culture plates. Alternatively, isolation of human fibroblasts can also be achieved using enzymatic treatments such as dispase, however it can take up to 20 hours and may experience over-digestion, which can reduce cell viability and subsequent attachment of cells when not handles properly [198]. Therefore, we have decided to manual dissect the obtained skin biopsy samples instead of enzymatic digestion when deriving dermal fibroblasts. This method is a lot quicker (15-45 mins) compared to using enzymatic treatment and relatively pure fibroblast population can be obtained this way, the reproducibility of this method allowed us to derive all the fibroblast lines from previous patient tissue samples [199]. Fibroblasts were observed around 7-10 days growing from the skin biopsy explant, cells demonstrated the morphological features of elongated, spindle-like cell bodies, round to oval cell nuclei, they grew aligned and in bundles when confluent [199].

Derivation of HDF was done in a quarantine laboratory before conducting a mycoplasma test, due to the nature of limited time culture, distinction between keratinocytes and fibroblasts were only done based on qualitative observation.

Molecular techniques such as staining should be utilised if we wish to generate new cell lines in the future, this will help to confirm the cell type identity. For example, positive expression of vimentin surface marker CD90/Thy1 can be used to stain for fibroblast[200], whereas Keratin 5 or 14 can be used for distinguishing basal undifferentiated keratinocytes [201].

Dermal fibroblast was used as the preferred cell source over other cell types such as blood cells for reprogramming, not only because dermal cells can be relatively easier to acquire due to its abundance, also due to the expertise we have in our group on using dermal fibroblast for reprogramming in the past. We could expand the number of fibroblasts and cryopreserve them for the future, whereas blood cells would be more difficult to store long term.

All fibroblast cell lines were reprogrammed with the same multiplicity of infection (MOI) ratio of 5:5:3 (KOS: hc-MYC: hKlf4) SeV vectors and seeding densities, however the success rate of hiPSC line establishment varied a lot between these three cell lines during induction. LOPCK hiPSCs were the first cell line reprogrammed from GF06 (Male, 73 y; $MTTP^{WT/WT}$), followed by MOPIK (Female, 57 y; GF10, $MTTP^{VAR/VAR}$) and HETIK hiPSCs (Female, 55 y; GF11 $MTTP^{WT/VAR}$). LOPCK (survival rate: 2 out of 36 clones*100 = 5.55%) and MOPIK (survival rate: 4 out of 48 clones*100 = 8.33%) hiPSCs were very easy to maintain and expand in culture after reprogramming, whereas HETIK (survival rate: 1 out of 96 clones*100 = 1.04%) was having difficulties to proliferate (reprogramming experiment was conducted twice), as well as generating heterogeneous cell population during trilineage differentiation stages. Based on the literature, although age could play a role in iPSC reprogramming efficiency [202], the fact that LOPCK and MOPIK are derived from older donors without having cell proliferation issues, the reason could be due to the underlying genetic variations [203].

A study done by Zhang's group [204] depicted that the genome could be undergoing changes at the single nucleotide level during iPSC induction, as they have shown that

in 22 generated hiPSC lines an average of five protein-coding point mutations were found in the regions they sampled (an estimated six protein-coding point mutations per exome). The origin of genetic variations could be 1. Pre-existing variations in parental somatic cells, 2. Reprogramming-induced, or 3. Passage-induced, certain point mutations present in the somatic population of origin may not favour the reprogramming process, altogether with these changes could possibly impact functional consequences of generated hiPSCs for downstream applications as well [203]–[206].

Based on the karyotyping results, no chromosomal abnormalities were observed in all three hiPSC lines, pluripotency markers including OCT4 and NANOG were also expressed in all cell lines. After derivation, hiPSCs were transitioned from commercial TeSR-E8 to in-house made "homebrew" E8 to reduce the cost of culture maintenance. Gene expression of pluripotency markers remained relatively similar in all cell lines during the media transition for each passage, no major morphological changes were observed in MOPIK and HETIK hiPSCs, however LOPCK hiPSCs showed subtle changes in morphological parameters with lower N:C ratio, as well as slightly fewer compact colonies. This could be cell line dependent due to the difference in growth rates between these three hiPSC lines. Nevertheless, the observed morphological variation did not seem to affect the pluripotency gene expression; however, differentiation efficiencies varied when derived cells were directed to differentiate into three germ layer lineages, optimisation of culture condition (concentration of growth factor/ small molecules) is required to achieve higher yields for each cell line.

The composition information of TeSR-E8 medium is not available for us to directly compared with our homebrew E8 components, the recipe we adapted is from Thomson group developed in 2011 [142], we have substituted sodium bicarbonate ($NaHCO_3$) to heparin sodium salt instead. At high cell density medium acidosis can occur and it can alter cell cycle and cellular metabolism, $NaHCO_3$ is often included in stem cell medium as a non-toxic natural buffer to supress medium acidosis to increase stem cell survival, derivation, maintenance and differentiation [207]. The

use of heparin sodium salt instead of $NaHCO_3$ is to increase the stability of fibroblast growth factor (FGF) and supports the binding of to its receptor, FGF2 is one of the E8 components that is known to have short half-life with an average of 7.6 hours and is important in maintaining pluripotency [208]. It has been shown that the addition of heparin can improve FGF2 signalling and extend the half-life of FGF2 to regulate stem cell pluripotency [209], [210].

Initially, we would like to investigate the effect of *MTTP*-p.I564T SNV contribute to the susceptibility and progression of NAFLD by using all three reprogrammed hiPSC lines. However, after experiencing slow proliferation rate, inconsistent differentiation efficiency and heterogeneous population in HETIK cell line while performing tri-lineage differentiation, we decided to focus on LOPCK and MOPIK hiPSC lines moving forward. Also, by comparing LOPCK ($MTTP^{WT/WT}$) and MOPIK ($MTTP^{VAR/VAR}$) in parallel, we can observe greater effects of how the genotype may influence cellular response. Since we only had a single piece of skin biopsy from each patient and they were collected at different time, the quality of the biopsy may affect the subsequent fibroblast derivation and eventually to hiPSC reprogramming. Due to that circumstance, we need to take into consideration of how good the quality of the biopsy origins were, that could be one of the reasons why the HETIK cell line did not perform as well as the other two. It has also been shown that lipid metabolism (particularly in lipogenesis) could play a role during reprogramming [211]. We noticed that the genotype of the heterozygous *MTTP*-p.I564T donor also had another heterozygous variation in the *MTTP* gene (rs1800592, TG), whereas the other two donors were both homozygous (TT) for the effect allele, there could be a negative synergy effect when two heterozygous mutations combined in these lipid metabolism related genes, there could be other predisposed mutations within the heterozygous donor's genome. To probe the issue of genome integrity in HETIK cell line further, performing RNA sequencing in the future may allow us to pinpoint what genetic variations have possibly caused these irregular cell behaviours. This is however beyond the scope of current study.

After successful hiPSC derivation, by using PCR and restriction enzyme digestion we validated that the pre-existing *MTTP*-p.I564T SNV still remained intact post-reprogramming in all three hiPSC lines. This can reassure that any phenotypic presentation observed in downstream investigation should correlates to the genotype-phenotype relationship. In addition to the existing genotype variable cell lines we have, we wanted to examine the effect and role of the *MTTP* gene in cellular behaviours under steatosis scenario, therefore we attempted to create a *MTTP* knockout (KO) cell line on the wildtype LOPCK hiPSC line using a commercial CRISPR/Cas9 KO kit due to time constraint.

The kit utilised homology-directed repair approach using a donor template that contains GFP and puromycin-resistance cassette for colony identification and selection. Based on the transfection efficiency results, we have chosen nucleofection to transfect the guide RNAs (gRNAs) and the donor template to LOPCK hiPSCs. Optimal puromycin concentration of 0.4 μg/ml was determined by doing a kill curve experiment. According to a study done by Niwa group in 2013, they investigated the importance of choosing appropriate drug resistance gene, as well as considering their dose-dependent characters in mouse embryonic stem cells [212]. The study found that by increasing puromycin dose from 4 μg/ml to 6 μg/ml during selection process resulted in 100% efficiency of the homozygous mutant selection, whereas the majority survived at 4μg/ml were heterozygotes [212]. To maximise the selection of bi-allelic colony, we used not only 0.4 μg/ml but to also culture the transfected cells at higher doses of puromycin at 0.6, 0.8 and 1 μg/ml in parallel to compare their transfection efficiencies. Unfortunately, we achieved very low targeting efficiency as the majority of clones did not display 3' integration throughout the PCR screens regardless of what puromycin dosage was used, only 1 clone was integrated with the cassette properly but it was later found to be a heterozygote mutant after further screening.

The commercial CRISPR KO kit uses the traditional RNA-guided Cas9 nuclease to generate double-strand breaks (DSBs) at targeted sites in the genome, however

literatures have shown that this approach has significant off-target effects [213]–[215]. The Cas9 nuclease is sensitive to the number, position and distribution of mismatches between gRNA and target DNA [214], often we need to take into account between activity and specificity, as study shows that the shorter, less-active gRNA is usually more specific than a longer, more active gRNA [215]. There are a lot of restrictions when using a commercial kit, making it difficult to identify what might have compromise the targeting and to then further optimise the procedure from it. If time were not a limiting factor, we would opt for designing the gRNA ourselves and perhaps choosing a different targeting strategy. The use of paired Cas9 nickases have been proven to drastically reduce off-target effects because both nickases must function together to make a DSB, though the efficiency may be lower the specificity is increased [216].

In summary, this chapter reports the successful generation of hiPSCs from donor-derived dermal fibroblasts which contain different *MTTP*-p.I564T genotypes. The underlying genotypes could influence the cellular phenotype in terms of proliferation rate, morphology, and gene expression. Genotype-phenotype relationship should be taken into account on how the cells may behave undergoing directed differentiation, the impact of growth rate and sizes of cells could have a massive effect on the yield of differentiated cells. Therefore, moving on to the next chapter, we will be focussing on optimising the hepatic differentiation platform in order to generate suitable and reproducible hepatic disease model for NAFLD, which would be used later for phenotypical comparison and various functionality tests.

Chapter 4.

Development and Optimisation of differentiation method towards hepatocyte fate

Chapter 4. Development and Optimisation of differentiation method towards hepatocyte fate

4.1 Introduction

With the advent of iPSC technology, it is now possible to generate many different cell types, this has led to major breakthrough in the fields of human biology, bioengineering and disease modelling in the past decade. However, one of the biggest challenges to date remains to cultivate hiPSCs and differentiate them towards desired cell populations that are mature; currently functionally and phenotypically immature HLCs remain an issue for downstream applications. Numerous *in vitro* models endeavour to differentiate hiPSCs into functionally relevant HLCs by mimicking the macro and microenvironment using various approaches, such as changing the type of biomaterial used to support cell growth [217]; 2D or 3D scaffold or suspension system [139], [218], [219]; co-culture with endothelial cells [220]; the use of micro-RNAs [221] and small-molecule cocktails [222]. There are many different approaches and aspects to consider when direct differentiating hiPSCs into desired cell lineage, as Figure 4.1 illustrates some of the main criteria to consider including the use of culture media, supplements, and the types of culture system; some studies have also explored the use of co-culture with endothelial cells or fibroblasts to improve hepatocyte maturity [220], [223], [224].

4.1.1 Manipulation of cell signalling using culture media and supplements

Numerous researchers endeavour to mimic the signalling pathways of human liver development to generate HLCs from hiPSCs, this is often achieved by modifying the exogenous factors such as media composition and the addition of supplements during the differentiation. Different studies have investigate liver development via transcriptomics [225], [226], proteomics [227], and metabolomics [228], [229] *in vivo* and *in vitro* using animal or cell models, in order to better understand the underlying mechanisms and signalling pathways that are important. In general, hepatic

differentiation protocols of stem cells are optimised based on soluble chemical signals driving towards specific signalling pathways, this could be induced using recombinant protein growth factors or small molecules present in the culture medium and supplements [222], [230], [231]. It is well documented that fibroblast growth factor (FGF) and bone morphogenetic protein (BMP) signals are particularly important during liver specification [232]–[234]. Several essential transcription factors (TFs) are commonly found to be expressed during hepatogenesis by the use of immunohistochemistry and transcriptomics in animal and cell models, these include TBX3, HNF4A, FOXA and GATA [235]–[238]; some studies have performed overexpression of microRNAs (miRNAs) such as miRNA-375 and miRNA-122 to induced the upregulation of these genes, hiPSCs were differentiated into functional HLCs without growth factors [239]. Although the use of miRNAs may be a good way to reduce the cost of using multiple supplements for the hiPSC differentiation, certain miRNAs including miRNA-122, miRNA-33 and miRNA-34a were reported to play a major role in NAFLD and its progression towards more severe stages of the disease [240], therefore they should be avoided for the use of creating NAFLD disease model to prevent any potential influence on the phenotyping characterisation sequentially. Other studies have utilised the approach of co-culture with different cell types such as mesenchymal stem cells [241], fibroblast [224], and endothelial cells in order to improve the maturity of differentiating HLCs [220], [223], [241], [242]. Co-culture differentiation would be a great approach for a holistic study investigating the cell-cell interaction between different cell types and how they may affect the signalling pathways, this approach however, is not ideal for the investigation of NAFLD disease modelling because certain genetic predisposition of the individuals may have an impact on the derived hiPSCs and other differentiated cell types. In addition, it may be difficult to separate the generated hepatocytes from the mixture of cells for downstream applications. Taking these factors into consideration, optimisation of hepatic differentiation for creating NAFLD disease model should focussed on the composition of media and supplements in this study.

4.1.2 2D vs 3D culture system

Traditional methods for cell growth and expansion rely on two-dimensional (2D) coating on plastic culture plates, it is commonly used in many studies for hepatic differentiation due to its simplicity and low cost, hence 2D culture still remains a popular option for many researchers [217], [231], [243]. More and more recent studies are utilising three-dimensional (3D) approach to mimic the *in vivo* environment generating HLCs; hiPSCs can be cultured in either scaffold-free environment in a suspension, forming aggregates as spheroids [244], or using bioreactors to scale-up the production [245]; alternatively, cells can be seeded onto scaffolds [246], encapsulated in an extracellular matrix (ECM) biomaterial such as Matrigel and self-assemble into organoids [247].

A study done by Meier *et al* in 2017 was comparing two 3D methods, including a scaffold-free micro-spheroid culture system and a 3D hollow-fibre perfusion bioreactor, in comparison to 2D cultivation; they found that cell differentiating under 3D conditions were relatively more mature, as the expression of α-fetoprotein was lower, while the drug metabolising enzymes CYP1A2 or CYP3A4 activities were higher [248]. Indeed, 3D environment can facilitate cell-to-cell contacts; the interaction between cells via adherence junctions, desmosomes, tight junctions and gap junctions allow the development of liver-specific functionality and thus enhance the maturity of HLCs [249]. The scaffolds serve as synthetic ECM and support the embedded cells organised into a 3D architecture, providing stimuli for cell growth and maturation. A huge drawback relates to 3D scaffold or static bioreactor cultivation is that cells often yield a low seeding density and efficiency due to the lack of perfusion, nutrients may not be able to distribute sufficiently through diffusion in stagnate medium [250]. With the addition of perfusion techniques, cells can be seeded more uniformly in a dynamic environment; oxygen and nutrients can also be transported to the cells more effectively, coupled with waste removal [251]–[254]. Nevertheless, the cost of bioreactor implementation can be quite high, the lack of standardisation can also limit widescale utilisation; various bioreactor systems such as spinner flask and rotational bioreactor are designed to simply move fluid across

the exterior of the scaffold, therefore interior chemo-transportation is not guaranteed and it has been reported to potentially cause a decline in core cell density over time [255]. 3D cultivation methods could potentially improve hepatocyte maturity in general, but they could also be very costly and labour intensive [256]. Moreover, scaffold-free 3D method utilising organoid culture could potentially experience more cell death and low cell yield due to mechanical or enzymatic dissociation of organoids from the matrix, it may also be difficult to seed cells for downstream applications because cells are organised as aggregates [257]. Considering the overall cost and the ease of cell manipulation for sequential characterisation and applications, 2D culture approach is being used in this study.

In chapter 3, we have generated hiPSC lines that express different *MTTP*-I564T genotypes. This chapter explores different aspects of *in vitro* hepatic differentiation optimisation in order to create disease model that can recapitulate and reflect NAFLD manifestations more accurately. During my MSc project, we have developed a differentiation platform that could improve maturity of HLCs. This was achieved by screening different activators and inhibitors of key signalling pathways which are important in embryogenesis. We have successfully identified various single- and multiple-growth factor combination that facilitate directed differentiation from hiPSCs to HLCs, moving forward, we will be investigating various optimisation approaches based on the protocol we have previously developed.

4.2 Chapter Aims and Objectives

In the previous chapter, three hiPSC lines were generated from patient-derived dermal fibroblasts using Sendai-virus based reprogramming. The aim of this chapter is to focus on further optimising the hepatic differentiation protocol I have developed from my MSc project, in order to generate hepatocyte-like cells (HLCs) that are more phenotypically and functionally suitable for modelling NAFLD in the next chapter. We will be looking into different aspects during directed differentiation to determine the optimal culture conditions for each hiPSC line.

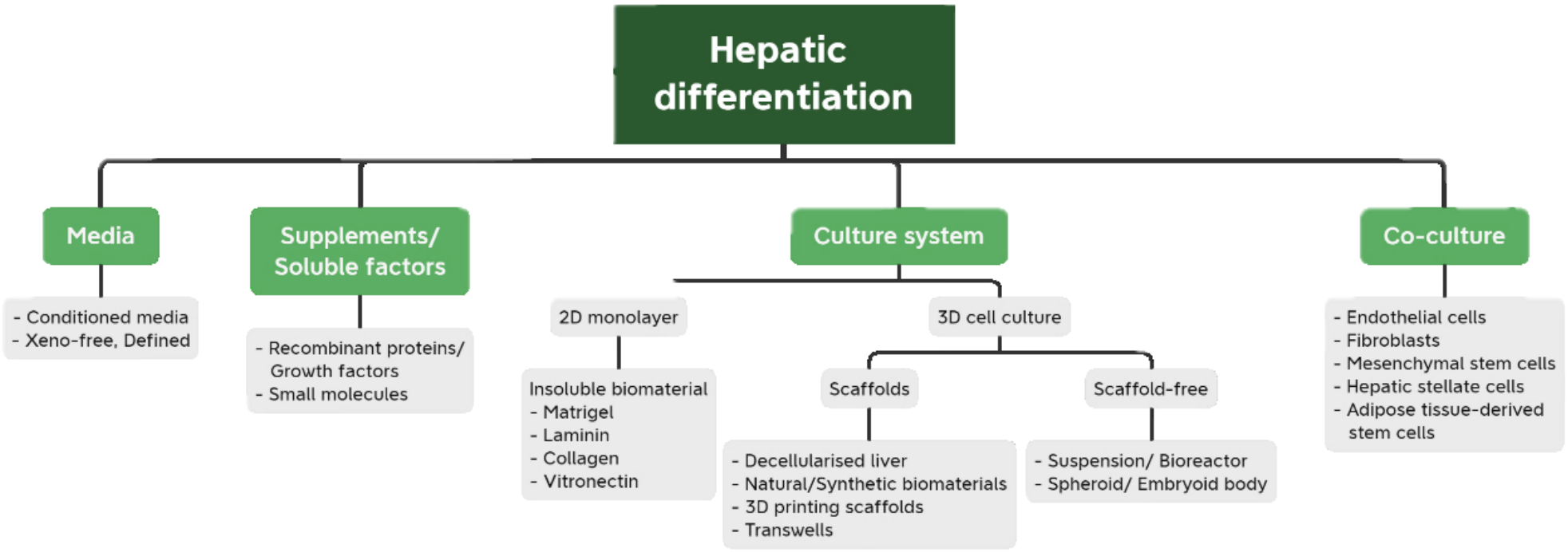


Figure 4.1 Overview of different aspects to consider for direct differentiation toward hepatocyte-like cells.

4.3 Results

4.3.1 48 hours induction is sufficient to generate anterior foregut (FG) endoderm population

To generate hepatic lineage populations homogeneously and effectively, we have investigated foregut optimisation, which allows us to produce proliferative foregut (FG) cells in the shortest time. Definitive endoderm (DE) population was treated with Activin A for different duration to generate anterior foregut cells and harvested for qPCR analysis. As **Figure 4.2A** is shown, at 0-hour definitive endoderm grew into a monolayer of petal/cobblestoned-shaped cells. Morphology started to change after 24-hour culture, the monolayer of cells remained on the plasticware, however they became rounder and looser; we have also observed floating cells in the spent media, suggesting cell detachment occurred during the transition into foregut population.

Primitive gut marker *HNF4A* expression significantly increased statistically since 48-hour of foregut induction up to 96-hour; *GATA4* is also upregulated significantly at 96-hour timepoint (**Figure 4.2B**). As the primitive gut markers gene expression are raised, DE markers such as *SOX17* begin to decrease significantly as the differentiation continues; the level of *FOXA2* is quite stable throughout the whole course. Anterior foregut marker *HHEX* expressed similar levels from 0 to 72-hr, however at 96-hour cells *HHEX* expression starts to drop. A downward trend is also observed in the liver bud marker *TBX*3; however, the fold changes are very low overall regardless to the timepoint.

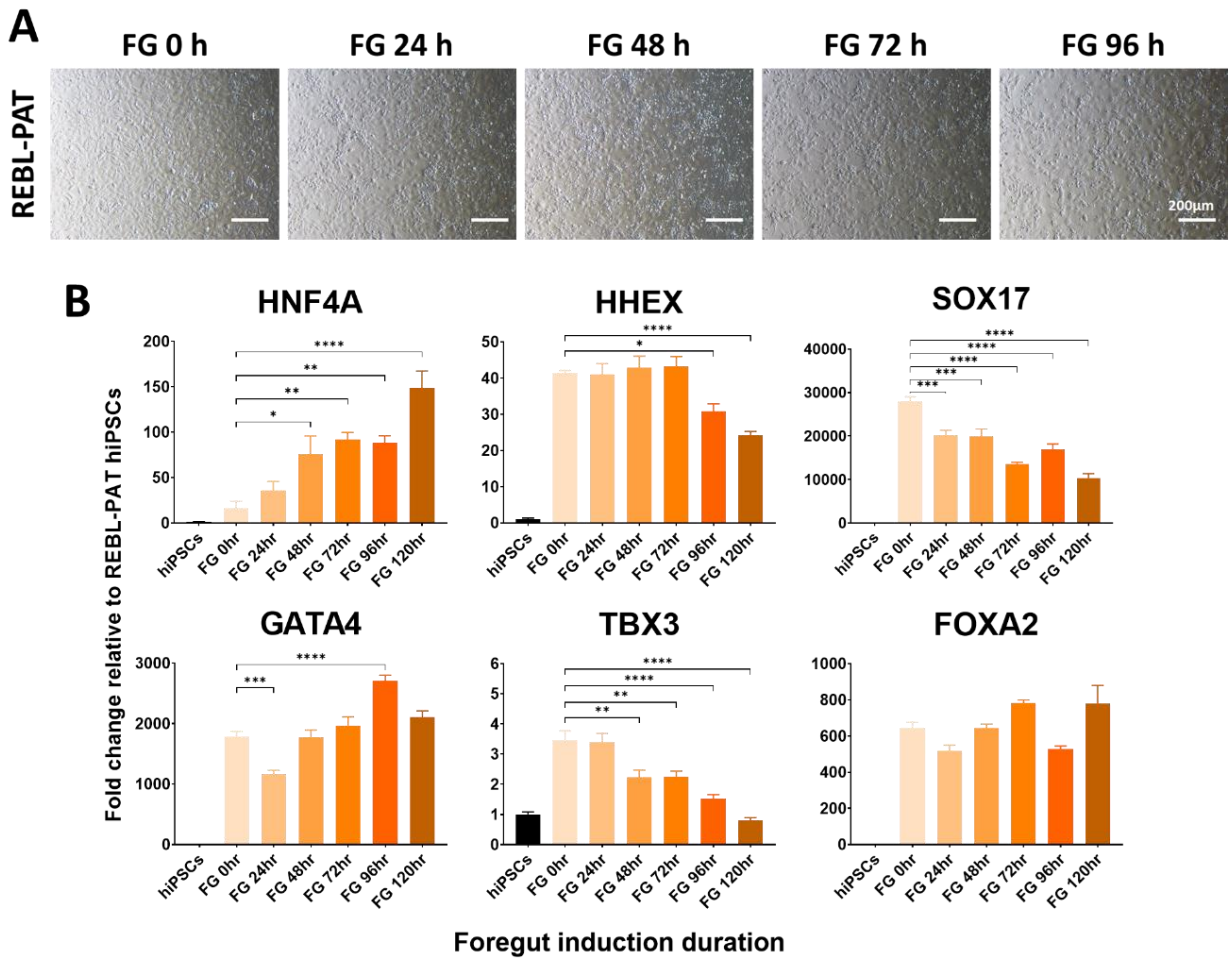


Figure 4.2 Foregut endoderm markers are upregulated after 48 h induction. (A) Representative images of REBLPAT hiPSCs differentiation to anterior foregut (FG) population. Scale bar = 200µm. **(B)** Cells were harvested at different timepoint for qPCR to assess gene expression differences. qPCR analysis of cells harvested every five days from maturation stage day 0 (M0, equivalent to differentiation D9) to endpoint day 20 (M20, equivalent to D29) of small molecule- (SM, blue) and recombinant protein- (RP, orange) based culture media against undifferentiated REBLPAT hiPSCs control. Statistical significance is analysed between SM versus RP at each time point: *P ⩽ 0.05, **P ⩽ 0.01, ***P ⩽ 0.001, ****P ⩽ 0.0001.

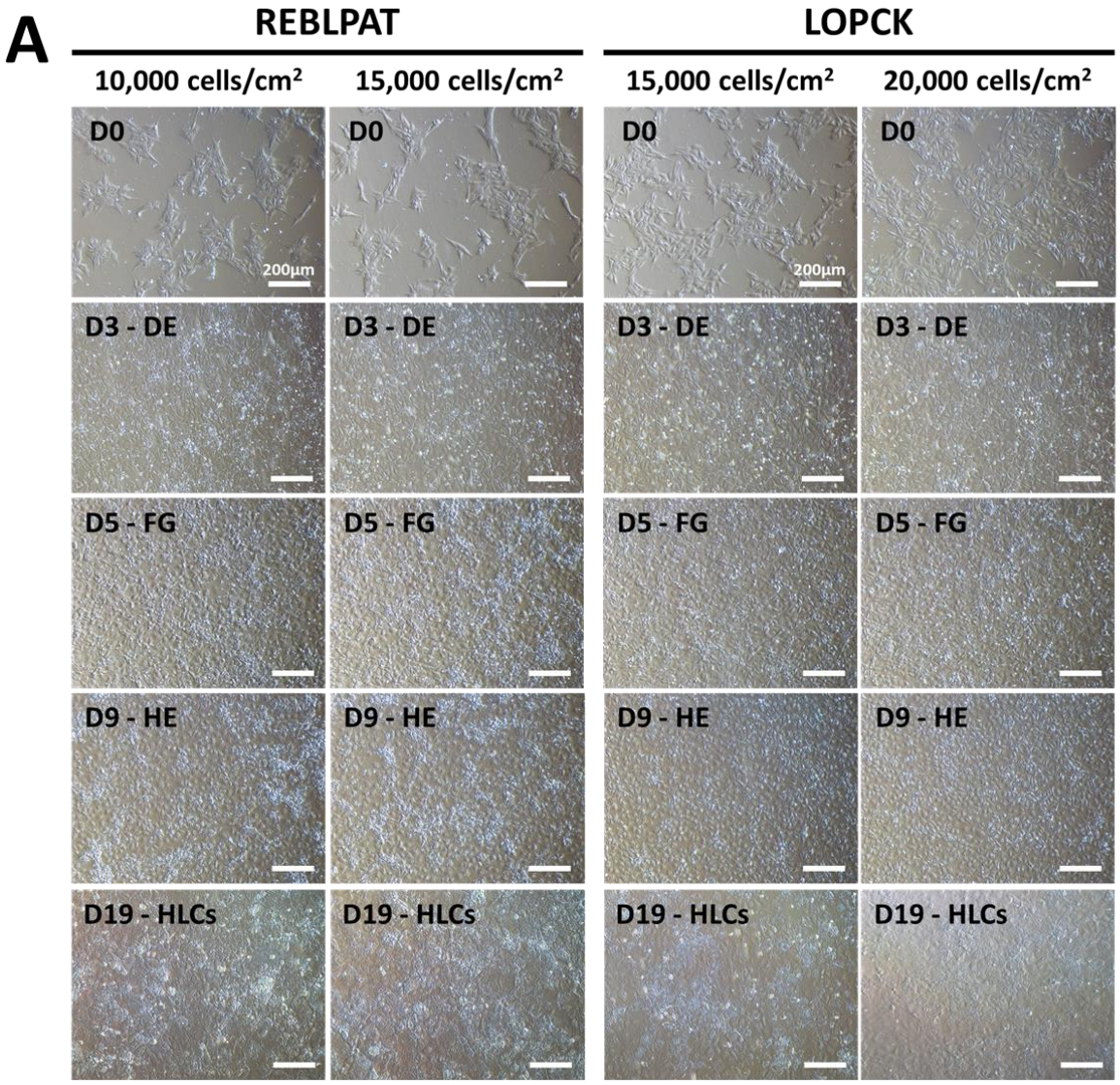
4.3.2 Cell line optimisation

In chapter 3, derivation of hiPSCs was described and we have reported that different cell lines would have variations in basal protein and gene expression levels related to pluripotency. Different hiPSCs would have their unique differentiation propensity depending on their intrinsic properties, therefore it is important to optimise each derived cell line in order to produce HLCs that are comparable, and most importantly, that can resemble bona fide hepatocytes as closely as possible for the downstream NAFLD modelling.

Seeding density

Some of the key observations we described in chapter 3 about the derived hiPSC lines was the differences in cell morphology and proliferation rate, these can influence the size and growth rate of cells during differentiation. The density of cells therefore has a huge impact in regulating cell fate and yield, so the first step would be to determine optimal seeding density for individual hiPSC line. From the previous chapter, we observed that LOPCK hiPSC colonies were relatively less compact compared to REBLPAT and MOPIK hiPSC lines, it also had a relatively slower growth rate. Hence, we decided to mainly focus on LOPCK and REBLPAT cell lines to investigate the suitable seeding density, REBLPAT is used as the reference cell line since it has similar morphology and proliferation rate as MOPIK hiPSCs. We tested 10,000/cm^2 and 15,000/cm^2 for REBLPAT; for LOPCK hiPSC line we tested 15,000/cm^2 and 20,000/cm^2, they were differentiated to day 19 (M10), cells were then harvested for gene expression study. There was not any major difference in terms of cell morphology, except that the monolayer of HLCs starting from higher sending density were more compact and potentially resulting in higher cell yield (**Figure 4.3A**).

Cells differentiated from higher density had higher mRNA transcripts of liver-related markers, *HNF4A* and *AFP* were found to have statistically significant differences in REBLPAT hiPSCs (**Figure 4.3B**). No statistical significance was found in LOPCK cell line; however, the overall gene expressions are higher at 20,000/cm^2. In conclusion, 15,000/cm^2 would be the seeding density for REBLPAT and MOPIK hiPSC lines, whereas LOPCK cell line would be seeded at 20,000/cm^2 instead.


A
REBLPAT
LOPCK
10,000 cells/cm²
15,000 cells/cm²
15,000 cells/cm²
20,000 cells/cm²
D0
D3 - DE
D5 - FG
D9 - HE
D19 - HLCs
200µm

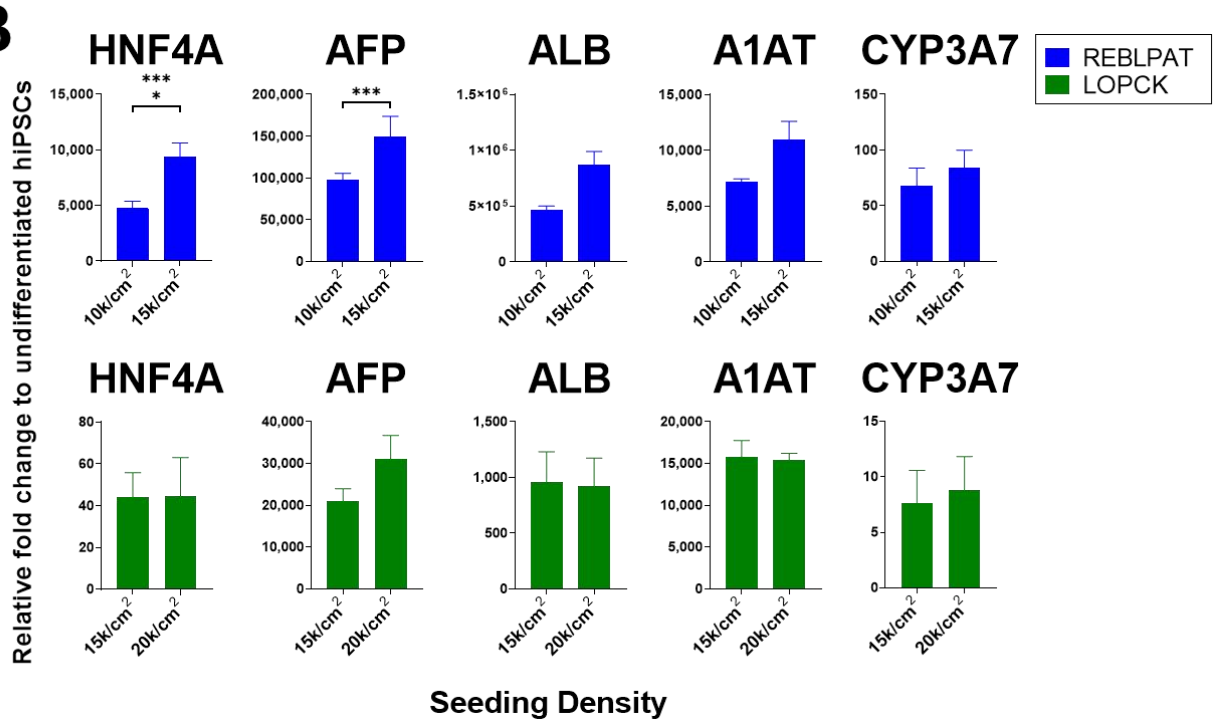

B
HNF4A
AFP
ALB
A1AT
CYP3A7
REBLPAT
LOPCK
Relative fold change to undifferentiated hiPSCs
10k/cm²
15k/cm²
20k/cm²
Seeding Density

Figure 4.3 Different cell lines require different seeding densities. (below) **(A)** Representation images of REBLPAT and LOPCK hiPSCs captured at various stages of hepatic differentiation. DE = definitive endoderm; FG = foregut; HE = hepatic endoderm; and HLCs = hepatocyte-likes cells, scale bar = 200 µm. **(B)** REBLPAT and LOPCK hiPSCs are seeded at different densities and harvested at differentiation D19 (equivalent to maturation day 10, M10) to be analysed by qPCR. Fold change in expression of differentiating cells over their respective undifferentiated hiPSC line calculated using comparative ΔΔCt method standardised against the housekeeping gene *PBGD*. Statistical significance: *P ⩽ 0.05, **P ⩽ 0.01, ***P ⩽ 0.001, ****P ⩽ 0.0001.

BMP4 concentration is cell-line specific during hepatic specification stage

Bone morphogenetic protein (BMP) signalling is essential for the induction of hepatic specification, the basal level of BMP signals differ from each cell line and it is important to identify the optimal concentration. REBLPAT, LOPCK and MOPIK hiPSCs were seeded at their desired densities, they were then treated with an escalating concentration of BMP4 or 100 ng/ml of Noggin (NOG; inhibitor of BMP signalling) for 4 days of hepatic specification, cells were then harvested at day 9 to be analysed by qPCR (**Figure 4.4**). Gene expression of liver progenitor markers HNF4A; AFP; TBX3; GATA4; TTR; and FOXA2 were examined (**Figure 4.4A**). All liver markers were downregulated when treated with 100 ng/ml NOG, indicating that BMP signal is fundamental for the specification of hepatic progenitor. AFP was highly upregulated in REBLPAT cells at 0 ng/ml of BMP4, TTR and FOXA2 was also shown to be statistically significant without any addition of BMP4. For LOPCK cells, 15 and 20 ng/ml of BMP4 were found to significantly increase HNF4A expression, however TBX3 level was peaked at 5 ng/ml. Since the liver markers were upregulated at two ends of the dosage spectrum, we decided to select 10 ng/ml of BMP4 as the final concentration, this is because TTR expression was highest at 10 ng/ml. When we looked at the overall liver-related gene expression in MOPIK line, though cells treated at 20 ng/ml of BMP4 was found to be statistically significant (adjusted p-value: 0.0276), no statistical significance was found in all the other genes such as AFP and TTR. Since we will be mainly using LOPCK and MOPIK hiPSC lines to create NAFLD disease model, we thought it would be best to keep the BMP4 concentration the same in both cell lines, using BMP4 at 10 ng/ml during hepatic specification. **Figure 4.4B** demonstrates

the effect of BMP4 concentration in differentiating cell morphology, inhibition of BMP signal using NOG has a great impact on cellular structure and causing cell detachment, heterogenous populations were also observed. When each cell line was treated with the suitable BMP4 dosage, we could see that all three cell lines generated an even monolayer of homogenous population, cells started to form individual border and have the early polygonal form of hepatocyte-like structure.

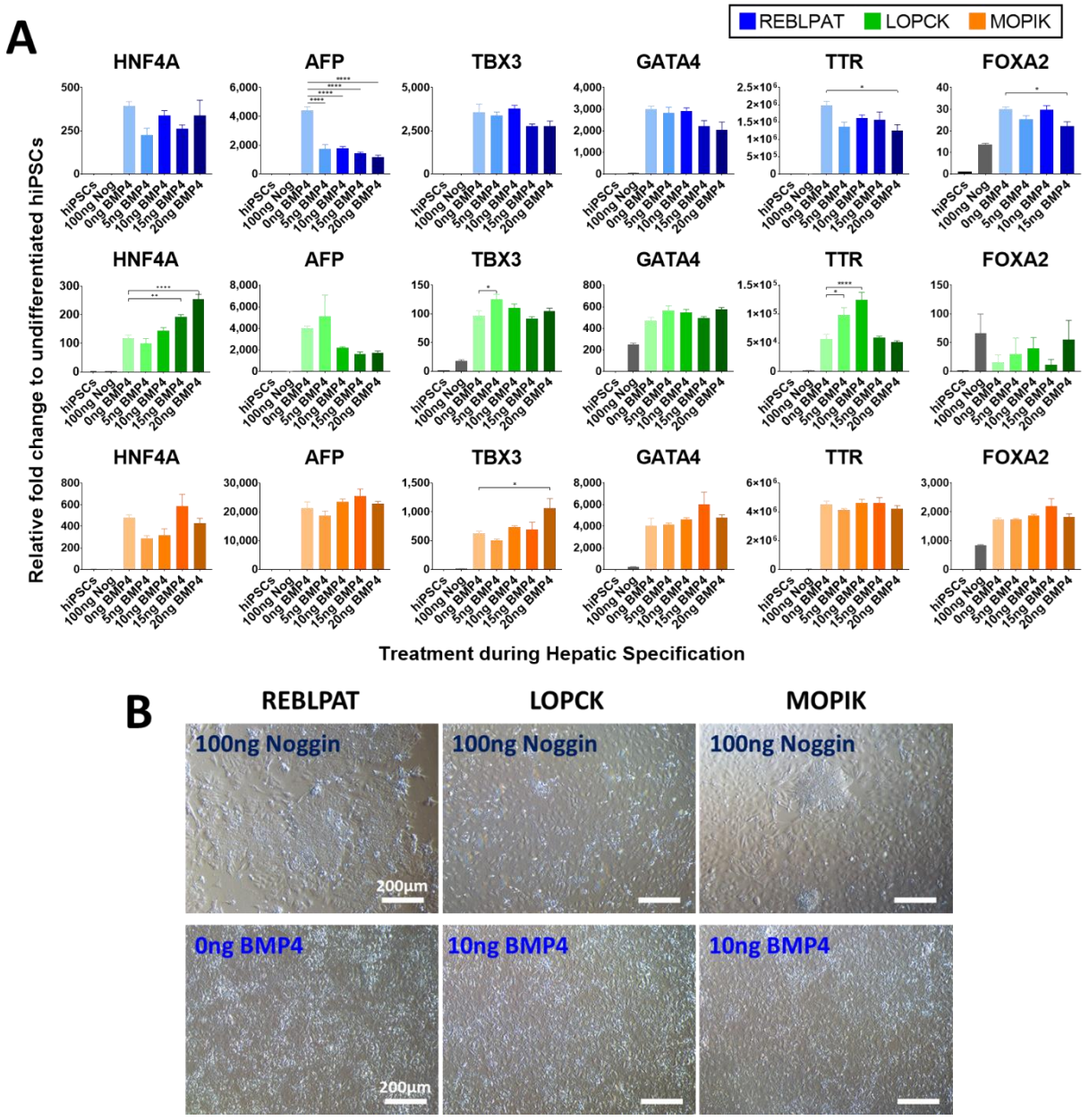


Figure 4.4 Different hiPSC lines require different dosage of BMP4 during hepatic specification. **(A)** qPCR reveals the different gene expression related to liver-bud development in three hiPSC lines: REBLPAT (in blue), LOPCK (in green) and MOPIK (in orange). Fold change in expression of differentiating cells harvested at D9 over their respective undifferentiated hiPSCs, calculated using comparative ΔΔCt method standardised against the housekeeping gene *PBGD*. Statistical significance was analysed between various dosage: *P

⩽ 0.05, **P ⩽ 0.01, ***P ⩽ 0.001, ****P ⩽ 0.0001. **(B)** Representative images of hepatic differentiation of three hiPSC lines, captured at D9 after four days of hepatic endoderm development, cells were treated with varying dosage of BMP4 and its inhibitor, noggin. Different hiPSC lines require different dosage of BMP4 as that can influence the cell morphology, in comparison, treatment of noggin can disrupt the structure of differentiating cells to varied degrees. Scale bar = 200 µm.

4.3.3 Explore the use of small molecule-based directed hepatic differentiation approach

Small molecule candidates screening for the optimisation of hepatic differentiation

During my MSc project, we have developed a differentiation platform to generate HLCs that can recapitulate liver development. Our approach was based on screening various activators and inhibitors of different signalling pathway that are important in embryonic development, from that we have found a combinations of growth factors that facilitate the directed differentiation at different stages. Noggin (BMP inhibitor) and Dickkopf-related protein 1 (DKK, Wnt/β-catenin inhibitor) are two of the most expensive components in our developed culture medium, to reduce the cost we wanted to replace these two growth factors with cheaper small molecule candidates. We have first tested the recombinant protein alternatives including PNU-74654 (PNU), inhibitor of WNT Production-4 (IWP-4) and LDN-193189 (LDN) with a dose response experiment using the recommended dosages to examine any toxicity and the optimal concentration for the maturation media. REBLPAT hiPSCs were seeded at the same density and direct differentiated toward HLCs, morphology of HLCs was observed throughout the entire differentiation progress (**Figure 4.5A**). After 10 days of maturation, HLCs were harvested and their gene expression were analysed by qPCR (**Figure 4.5B**).

We observed that as PNU concentration increased, morphology of the differentiating cells started to flatten, and the cell borders became less obvious at 1 µM of treatment. In contrast, an upward trend of gene expression was found in liver-bud markers including *HNF4A*, *AFP, TTR*, as well as mature markers *ALB* and *A1AT*; the increase of

HNF4A and *TTR* gene expressions were statistically significant. Interestingly, for IWP-4 the differentiating cells displayed the normal polygonal shape of HLCs at 0.05 µM and 0.5 µM, but when cells were cultured under 0.1 µM and 0.25 µM, adverse effect was observed as the cells seemed to have lost their structure. Nonetheless, the qPCR data showed a relatively consistent trend of either upregulation or downregulation of gene expression in a dose-dependent manner. The level of *AFP* gene expression increased as the concentration of IWP-4 increased, however the liver bud marker *TTR* and mature marker *ALB* were both downregulated. LDN-treated differentiating cells displayed a different phenomenon as the dosage increased, liver markers such as *HNF4A* and *AFP* are upregulated and relatively high in cells treated with lower dosage (0.1-0.5 µM), however these cells do not retain the polygonal morphology as well as cells treated with 1 µM LDN. Though the expression of mature marker *ALB* is relatively lower at 1 µM, *A1AT* and liver bud marker *TTR* are highly upregulated in comparison.

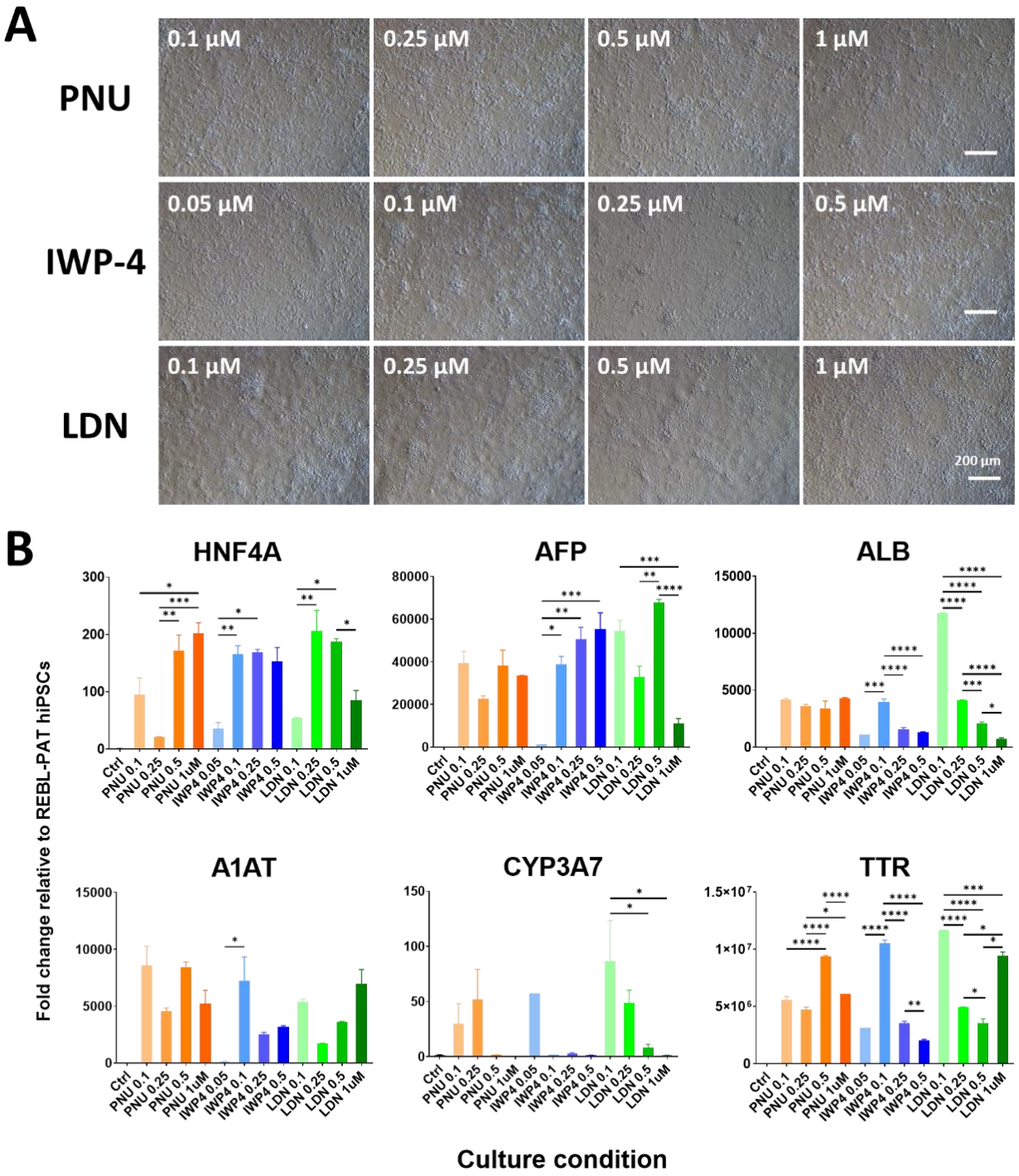


Figure 4.5 Initial dose response screening of the small molecule candidates. (A) Bright-field images of HLCs treated with small molecules at different doses after 10 days of maturation. PNU = PNU-74654, LDN = LDN-193189. Scale bar = 200µm. **(B)** qPCR expression analysis of genes encoding hepatic progenitor markers *HNF4A*, *AFP* and *TTR*; mature hepatocyte markers *ALB* and *A1AT*; and foetal liver detoxication gene *CYP3A7*. Gene expression in HLCs quantified as fold difference over levels in undifferentiated REBLPAT hiPSCs. Statistical significance symbols: *P ⩽ 0.05, **P ⩽ 0.01, ***P ⩽ 0.001, ****P ⩽ 0.0001 versus undifferentiated REBLPAT hiPSCs (Ctrl).

Hepatic differentiation efficiency comparison using small molecule cocktail and recombinant growth factors

Based on the dose response experiment done previously, we have selected two small molecule (SM) candidates (0.25 µM of PNU and 1µM of LDN) to be tested for their synergetic effect on hepatocyte maturation. A time-course experiment was conducted to compare with the original recombinant protein (RP)-based medium D, differentiating cells were harvested every 5 days from maturation day 0 (M0, day 9) up to day 20 (M20, d29) for qPCR analysis. Differentiating cells have very similar morphology at M5, exhibiting the same polygonal shape with multinucleated cells that are compact and organised (**Figure 4.6A**). Cell presentations begin to variate starting at M10, SM- treated cells remain quite small similar to that at M5, whereas RP-treated cells are growing relatively larger than before and there are several denser areas with more prominent cells. At M15 and M20, SM-treated cells begin to detach from the culture plasticware and lose their structure. In the opposite, RP-treated cells remain attached and retained their structure.

Indeed, qPCR data reflect on the morphological changes we observed (**Figure 4.6B**). Foetal marker *AFP* is expressed at peak on M10, then the gene expression declines as the cell mature. Reversely, mature markers such as *ALB, A1AT* and *ADH1* were upregulated at the later stage of maturation, however gene expressions of these genes remained lower when the cells were treated with SM. As the liver bud markers *HNF4A* and *TTR* expressed less as the maturation continues, drug metabolising enzyme *CYP3A7* expression starts to increase in both SM and RP culture conditions; nonetheless, RP-treated cells expressed relatively higher levels of *CYP3A7* throughout the maturation.

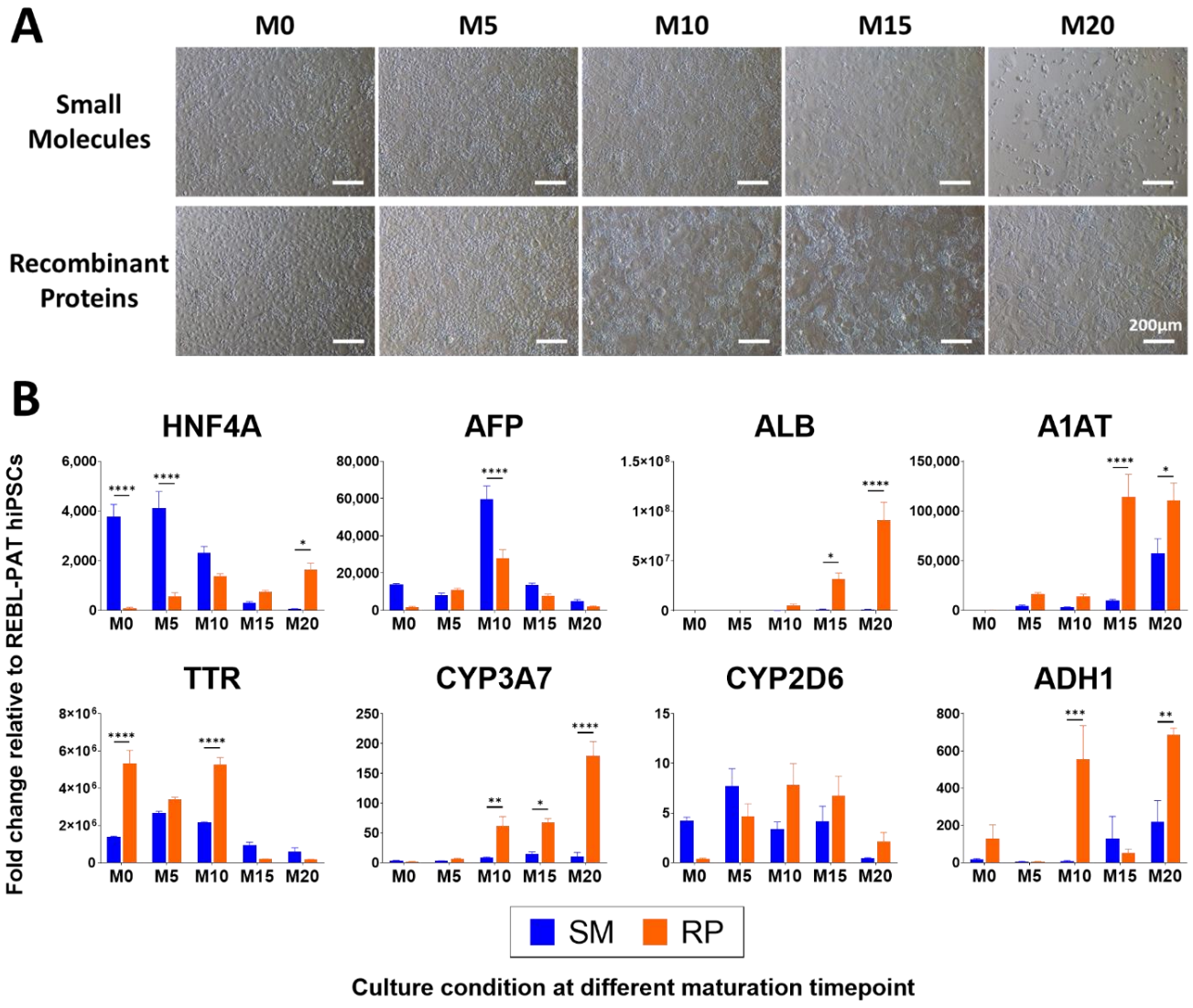


Figure 4.6 20-day maturation time course to assess developmental trajectory of small molecule versus recombinant protein approach. (A) Bright field images of maturating hepatocytes. Small molecules = 0.25µM PNU-74654 and 1µM LDN-193189, recombinant proteins = 100ng/µl DKK-1 and 100ng/µl Noggin. Scale bar = 200µm. **(B)** qPCR analysis of cells harvested every five days from maturation stage day 0 (M0, equivalent to differentiation D9) to endpoint day 20 (M20, equivalent to D29) of small molecule- (SM, blue) and recombinant protein- (RP, orange) based culture media against undifferentiated REBLPAT hiPSCs control. Statistical significance is analysed between SM versus RP at each time point: *P ⩽ 0.05, **P ⩽ 0.01, ***P ⩽ 0.001, ****P ⩽ 0.0001.

4.3.4 New developed platform produces HLCs with a relatively more mature phenotype compared to old differentiation approach

To validate that our newly developed recombinant protein-based protocol can indeed generate HLCs that are functionally and phenotypically more mature than the old approach, we have compared the differentiated HLCs using multiple parameters including transcriptomic, protein expression, as well as metabolomic analyses. REBLPAT-hiPSCs were seeded and differentiated to hepatic endoderm (day 9, maturation day 0, M0), half of the cell population was cultured in Old maturation media and the other half with New maturation media. HLCs were then harvested at day 29 (equivalent to M20) for downstream analyses.

Cell morphology

REBLPAT hiPSCs were differentiated and cultured in the same condition up till day 9 (M0), after the hepatic specification differentiating cells were then cultured in either Old or New maturation media **Figure 4.7**. demonstrates the sequential morphological changes of the differentiating cells at different stages transitioning from undifferentiated hiPSCs to definitive endoderm (DE), foregut (FG), hepatic endoderm (HE) and hepatocyte maturation (M0-M20). At M0, cells were fully grown into a monolayer of homogenous population, the foregut cell clusters have flatten and spread out evenly as individual cells, cells began to look rounder and resemble the early phase of HLCs, nuclei were becoming more prominent. Distinct morphological changes started to occur from around M5, cells grown in Old maturation medium remained relatively flat compared to New medium and were less proliferative, New medium-treated cells are more compact and the clusters formed were more three dimensional, canaliculi-like structure. By the end at M20, both New and Old media generated polygonal, multinucleated HLCs, but we observed higher number of cells in New medium condition.

Protein expression profile

In addition to morphology observation, immunocytochemistry (ICC) was utilised to confirm the protein expression of differentiating cells during maturation day 10 (M10, **Figure 4.8A**) and 20 (M20, **Figure 4.8B**) for both Old and New maturation conditions. Mature markers ALB, A1AT and CYP2A6 were detected at M10 for both conditions and at M20 higher expression of these proteins were found. ALB was detected with relatively higher level in New medium-treated HLCs compared to the Old medium particularly. In parallel to the rising levels of mature markers, foetal markers including AFP and HNF4A were reduced from M10 to M20 transition. Interestingly, another immature marker, Glutathione S-transferase Pi (GSTpi) followed the opposite trend, and their protein expression were found slightly increased at M20 in both conditions, Old medium-treated cells however detected relatively higher level of GSTpi, indicating that HLCs generated using Old maturation medium are less mature than New condition based on the ICC data.

Gene expression profile

Evidently, qPCR data presented a similar progression supporting our ICC findings (**Figure 4.8C**). *ALB* gene expression was upregulated from M10 to M20 that is statistically significant, a broader increase was found in Old medium-treated cells (p-value = 0.0004) compared to New condition (p-value = 0.0018). Again, in accordance with the immunostaining data, we found that levels of *AFP* and *HNF4A* decreased at M20 reversely in both culture conditions, indicating that the differentiating cells were becoming more mature. No statistical significance was found in *A1AT, CYP2A6* and *GSTpi* between M10 and M20 regardless of the maturation media used, but overall, their gene expressions were elevated slightly.

To further investigate the effect of Old and New media on hepatic maturation, we have repeated the experiment and conducted further qPCR testing with extensive liver markers to evaluate the maturity of the generated HLCs at M10, M15 and M20 (**Figure 4.9**). Mature markers ALB, A1AT were again upregulated in both culture conditions as the differentiation continued, statistically significant elevation of A1AT

at M15 and M20 were identified in New medium-treated cells in particular. We have examined gene expression profile of phase 1 cytochrome P450 (CYP450) drug metabolising enzymes such as *CYP3A7, CYP3A4, CYP2A6, and CYP2D6*; phase 2 transferase GSTpi; arylacetamide deacetylase (*AADAC*) esterase; as well as a heme enzyme called Tryptophan 2,3-Dioxygenase (*TDO2*). A global escalating trend was observed in most of these genes, except for the foetal marker GSTpi with similar levels throughout the maturation in both culture conditions, New condition-cells did have relatively lower expression of GSTpi compared to that of the Old medium. Noticeably, expression of *CYP2D6* and *AADAC* both peaked at M15 in New condition-HLCs and reduced at M20; this progression, however, is not found in Old condition-HLCs.

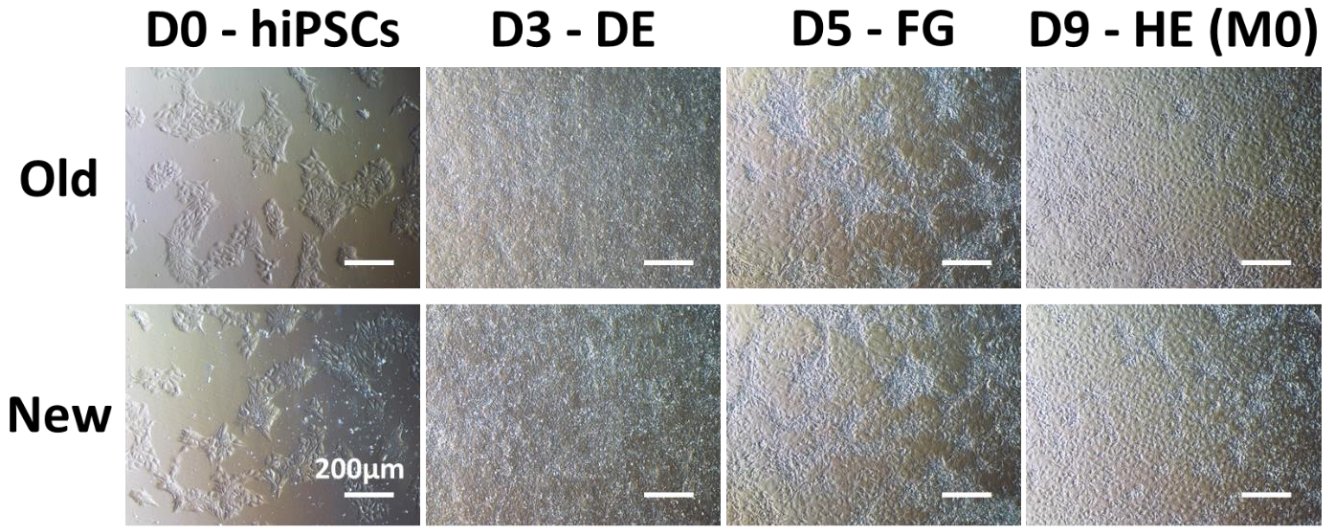


Figure 4.7 Morphological changes of cells cultured under Old and New formulated media during hepatocyte maturation stage. (left) REBLPAT hiPSCs were seeded at 15,000 cells/cm^2 at day -2 (D-2), directed differentiation started 48 hours after seeding at day 0 (D0) to definitive endoderm (DE); foregut (FG); hepatic endoderm (HE) under the same condition. At day 9, which is equivalent to maturation (M) day 0 (M0), HLCs were cultured under either Old or New maturation media for 20 days till D29 (M20). Scale bar = 200 µm.

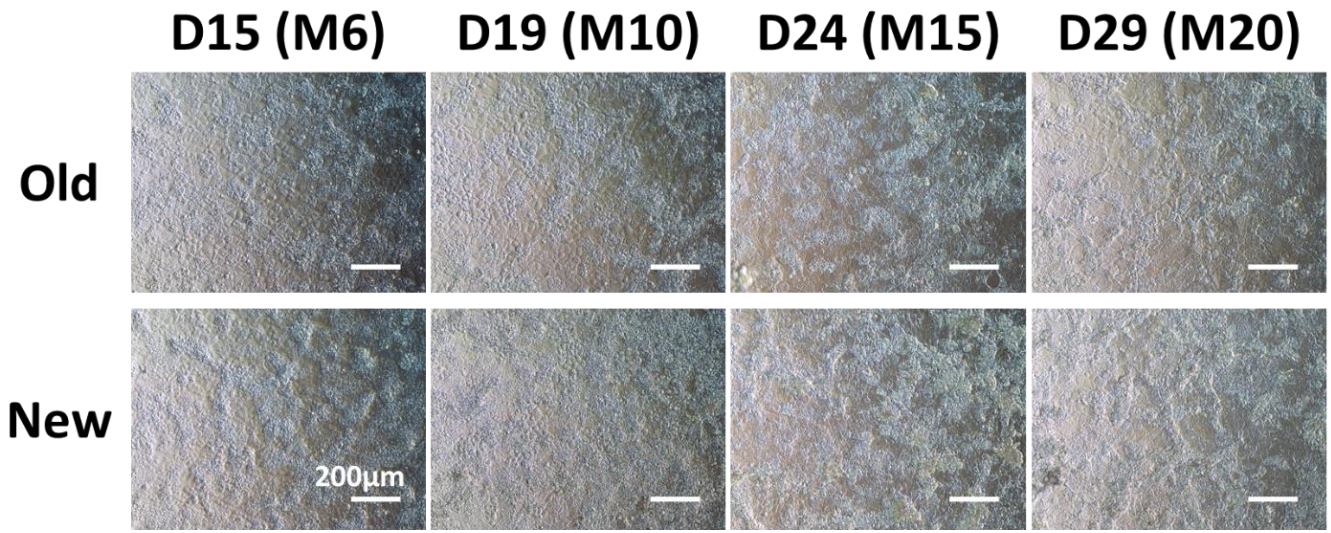
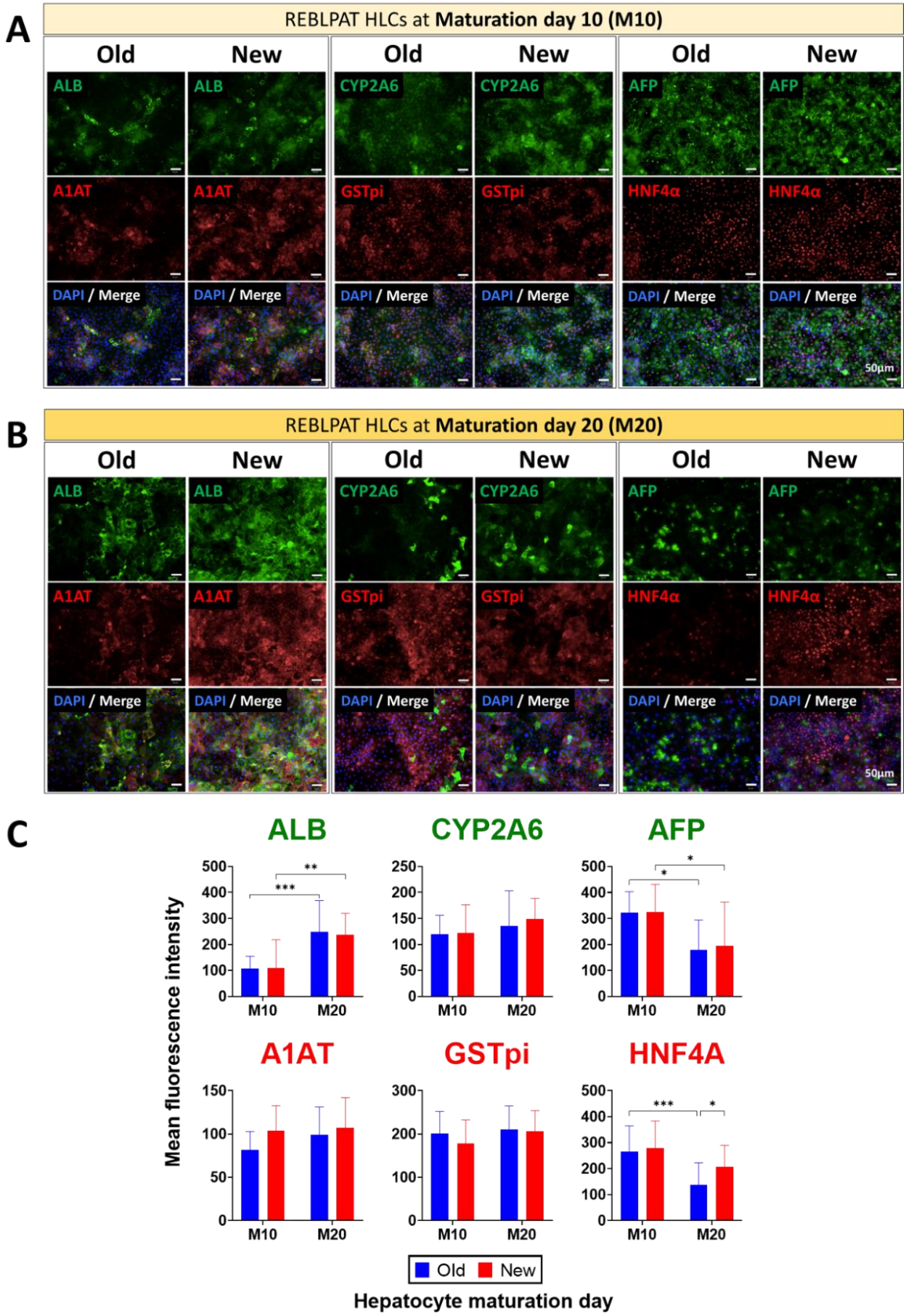


Figure 4.8 HLCs generated using New maturation media expressed higher levels of mature markers. (below) Protein expression of REBLPAT-derived HLCs were assessed at **(A)** maturation day 10 (M10 = D19) and **(B)** 20 (M20 = D29), scale bar = 50 µm. **(C)** Mean fluorescence intensity for liver-related markers was quantified using the Columbus software. Statistical significance: *P ⩽ 0.05, **P ⩽ 0.01, ***P ⩽ 0.001, ****P ⩽ 0.0001.


A
REBLPAT HLCs at Maturation day 10 (M10)
Old
New
ALB
CYP2A6
AFP
A1AT
GSTpi
HNF4α
DAPI / Merge
50μm
B
REBLPAT HLCs at Maturation day 20 (M20)
C
ALB
CYP2A6
AFP
A1AT
GSTpi
HNF4A
Mean fluorescence intensity
M10
M20
Old
New
Hepatocyte maturation day

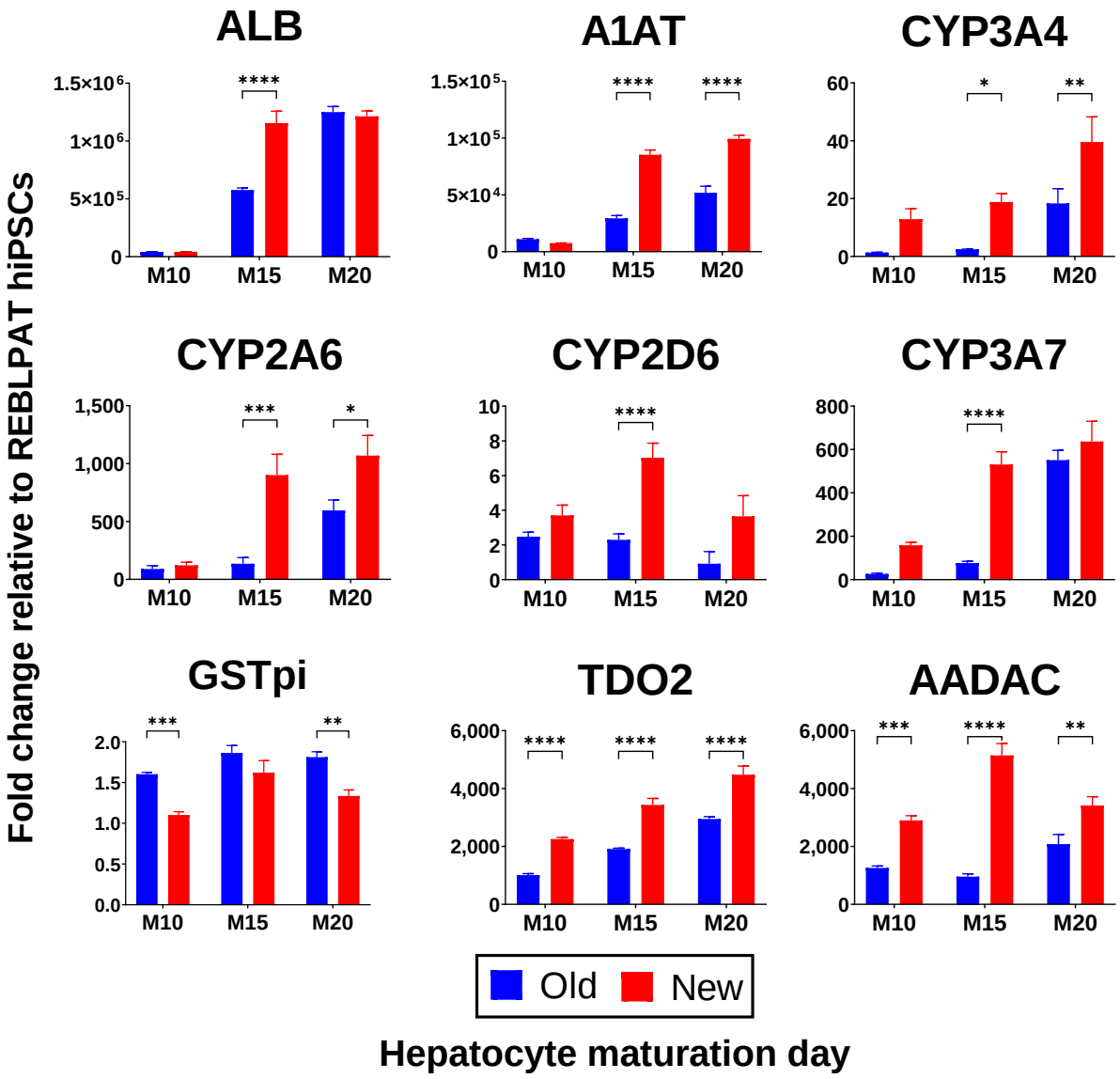


Figure 4.9 Mature liver-related genes are relatively more upregulated in New media-cultured HLCs. Gene expression of an array of liver-related, metabolic and several cytochrome P450 drug metabolising genes were tested using qPCR. In contrast, glutathione S-transferase Pi (GST_{pi}) is used to measure as a foetal liver marker, its level tend to decrease in hepatocytes with maturity and remained low. Statistical significance is analysed between Old and New maturation media at different time point: *P ⩽ 0.05, **P ⩽ 0.01, ***P ⩽ 0.001, ****P ⩽ 0.0001.

mRNA sequencing – Correlation tree

In order to dive deeper and obtain a more comprehensive transcriptomic profiling of the HLCs produced from both Old and New maturation media at M20, mRNA sequencing was performed to identify differentially expressed genes, in comparison to REBLPAT hiPSCs, as well as foetal and adult liver samples. Dimensionality reduction techniques were used to evaluate the overall relatedness of the different sample sets, sample similarity is presented as correlation tree as well as matrix form (**Figure 4.10A**), which shows that the sample replicates all cluster together, but the different cell types were distinguished separately as three major groups of primary liver samples, undifferentiated hiPSCs and hiPSC-derived HLCs. The Old and New maturation media samples are more closely related to each other, they are relatively closer to undifferentiated cells other than the foetal and adult liver samples; the relationship between the two liver samples is much closer than that to any of the HLCs in comparison. From the correlation matrix, we can see that New-HLCs shared higher similarity to the liver samples compared to the Old-HLCs numerically (ranged between 0.93-0.97); moreover, New-HLCs are farther away from undifferentiated hiPSC samples comparatively.

To see the global pattern of the differentially expressed genes, heatmaps are created for upregulated (**Figure 4.10B**) and downregulated genes (**Figure 4.10C**) that expressed with a log2 fold change above -2 and a false discovery rate (FDR) of less than 0.05, when comparing Old and New media conditions on the effect of HLCs. From the upregulated gene sets, we can see that the expression profile of New-HLCs share more similarities to both the foetal and adult liver samples, whereas Old-HLCs and REBLPAT hiPSCs are clustered together in a separate group (**Figure 4.10B**). Similar observation is found in the downregulated gene sets, withal in this gene set the New-HLCs and Old-HLCs are more closely related together, separating the sample sets into three main clusters of HLCs, hiPSCs and liver samples (**Figure 4.10C**).

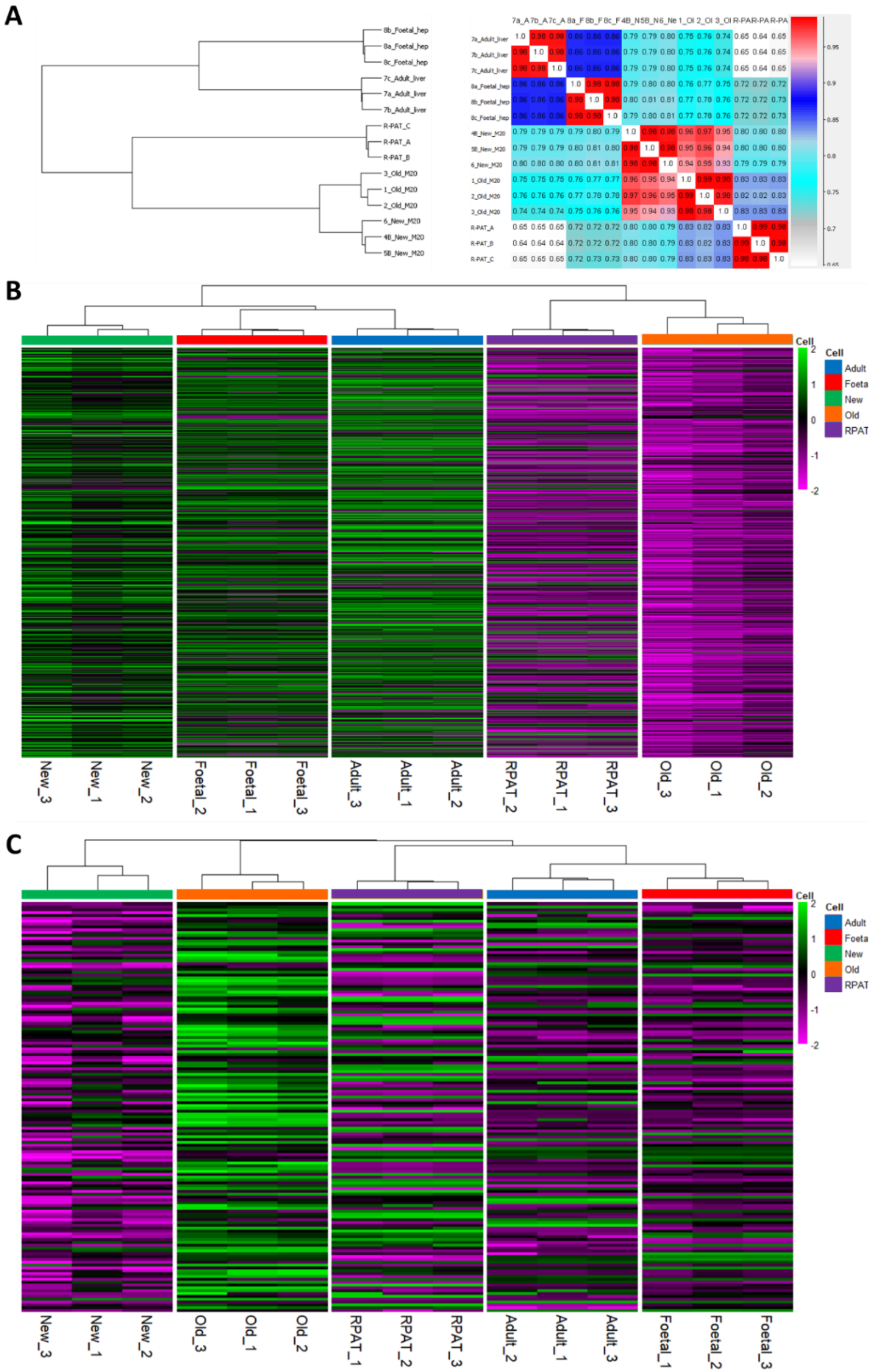

A
8b_Foetal_hep
8a_Foetal_hep
8c_Foetal_hep
7c_Adult_liver
7a_Adult_liver
7b_Adult_liver
R-PAT_C
R-PAT_A
R-PAT_B
3_Old_M20
1_Old_M20
2_Old_M20
6_New_M20
4B_New_M20
5B_New_M20
B
Cell
Adult
Foeta
New
Old
RPAT
New_3
New_1
New_2
Foetal_2
Foetal_1
Foetal_3
Adult_3
Adult_1
Adult_2
RPAT_2
RPAT_1
RPAT_3
Old_3
Old_1
Old_2
C
Cell
Adult
Foeta
New
Old
RPAT
New_3
New_1
New_2
Old_3
Old_1
Old_2
RPAT_1
RPAT_2
RPAT_3
Adult_2
Adult_1
Adult_3
Foetal_1
Foetal_2
Foetal_3

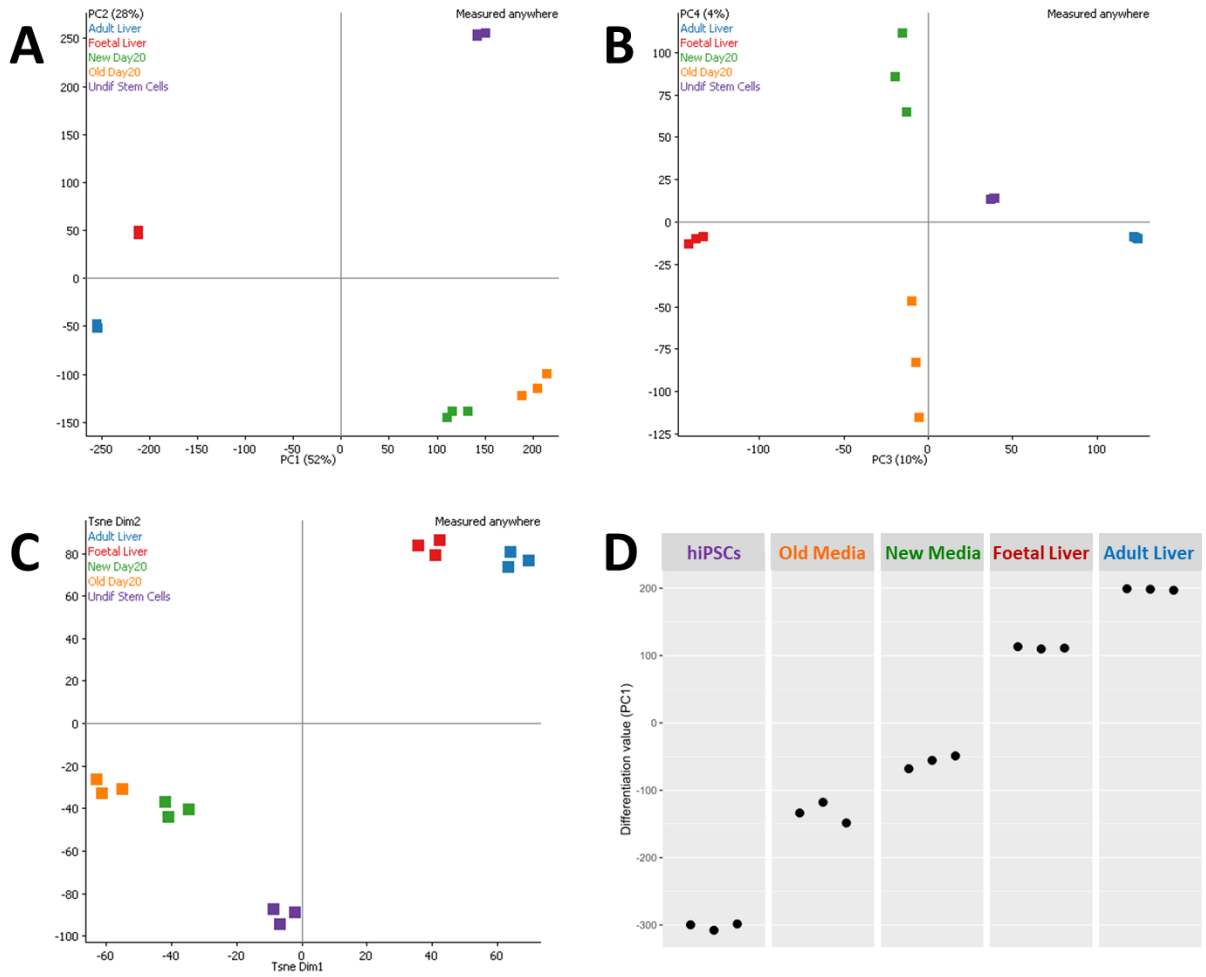
Figure 4.10 Overall similarity of differentially expressed genes between REBLPAT hiPSCs, Old-, New-maturation generated HLCs, foetal and adult liver samples. (above) (A) Correlation tree and matrix showed that sample replicates can be split into different clusters; Old and New media samples are more related to each other, they are closer to the undifferentiated cells than that or the liver samples. Gene expression profile of **(B)** upregulated and **(C)** downregulated genes in New medium samples were analysed by DESeq2 differential expression analysis, upregulated gene list remsembles more toward foetal and adult liver samples in comparison to that of the Old medium samples.

mRNA sequencing – Multi-dimensional analysis

Principal component analysis (PCA) and t-Distributed Stochastic Neighbour Embedding (t-SNE) algorithm were utilised to explore the relationships between the different sample groups a little deeper. By applying non-linear dimensionality reduction, multivariate data table can be transformed into a smaller set of variables to observe trends, jump, clusters and outliers. **Figure 4.11A-B** demonstrate how the sample sets correlate to each other as PCA plots, again, supporting the previous results that samples sets fall into 3 main categories, New- and Old-HLCs are highly associated, notwithstanding, New-HLCs are relatively closer to the liver samples than that of Old-HLCs. The t-SNE model in **Figure 4.11C** illustrates the same pattern we have described. To further define a differentiation value of all sample groups, we have developed a linear scale running from REBLPAT undifferentiated hiPSCs, through to foetal and fully mature liver samples, which enabled us to position the HLC samples cultured from Old and New maturation media (**Figure 4.11D**). Indeed, New-HLCs resembled more toward primary foetal and adult hepatocytes than the Old medium.

Figure 4.11 Multi-dimensional PCA and t-SNE analyses of similaities between sample groups. (below) mRNA sequencing reveals that the gene expression profile of HLCs cultured in New maturation media are relatively similar to primary foetal and adult liver samples, whereas Old media-HLCs are relatively closer to REBLPAT hiPSCs compared to liver samples. Overall relatedness of the different samples are illustrated as PCA plots, **(A)** PC1/2 and **(B)** PC3/4 classes of variance between REBLPAT hiPSCs, HLCs cultured in Old and New media, as well as foetal and adult liver samples. **(C)** t-SNE is analysed to explore high-dimentional data

showing the samples categorised in different clusters. **(D)** Principal component (PC) score is plotted to illustrate the differentiation scale when compared to hiPSCs for each sample group.

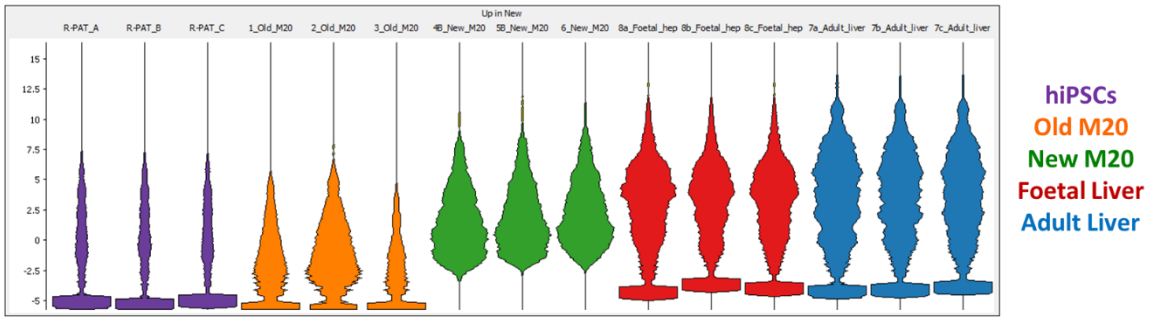


mRNA sequencing – Gene expression distribution

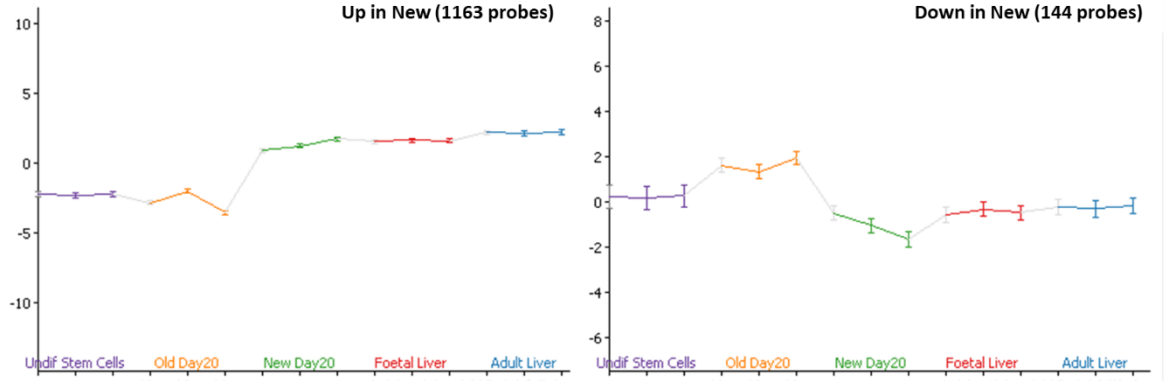
Figure 4.12A shows the global structure and expression distribution of the gene hits, a large proportion of these of these genes are on an obvious shift from low expression in undifferentiated hiPSCs through to high expression in liver samples, whereas the expression of both the Old- and New-HLCs are intermediate. Substantial proportion of the genes expressed in New-HLCs are much close to the foetal and adult liver samples. To conflate the different absolute levels of expression for each replicate from the sample sets, we applied per-gene normalisation to examine the overall trend of the upregulated and downregulated gene expression (**Figure 4.12B**). The means of per-gene normalised expression distributions are calculated and delineated, and once again, New-HLCs follow more closely to the liver samples, whereas Old-

HLCs are relatively more relevant to the undifferentiated hiPSCs. Gene set enrichment was performed on the upregulated genes from the New-HLCs sample, gProfiler search tool was used to determine the relevant gene ontology (GO) terms and pathways that were enriched. The filter was set at FDR<0.0001 with the term size less than 100 to obtain more specific results, the top hits were analysed using enrichR and they were compared to the Human Cell Atlas cell type defining genes (**Figure 4.12C**). We found that enriched upregulated gene set is highly related to liver and foetal liver compared to other tissue types, reinforcing that the New medium can indeed facilitate the maturation of HLCs more efficiently compared to Old medium.

A



B



C

Index	Name	P-value	Adjusted p-value	Odds Ratio	Combined score
1	Liver	7.588e-98	6.374e-96	5.59	1250.78
2	Fetalliver	1.423e-41	5.976e-40	8.33	783.04
3	Kidney	1.779e-13	4.982e-12	4.24	124.44
4	small_intestine	1.436e-9	3.015e-8	2.97	60.48
5	Pancreas	1.130e-7	0.000001582	3.76	60.17
6	colon	4.079e-8	6.852e-7	2.60	44.23
7	PancreaticIslet	0.00008780	0.001054	2.66	24.81
8	Trachea	0.002826	0.02968	2.63	15.42
9	Leukemialymphoblastic(MOLT-4)	0.003496	0.03263	2.19	12.36
10	Adipocyte	0.004391	0.03689	1.90	10.31

Figure 4.12 Gene expression profile of HLCs generated by New maturation medium is more closely related to liver cell type. **(A)** Global distribution trend of differentially expressed

genes. **(B)** Per-gene normalised expression distribution for each of the replicates of the upregulated and downregulated gene lists. **(C)** Upregulated genes of New maturation medium are compared to the Human Cell Atlas cell type defining genes using Enrichr, the analysed genes are mostly contributed to the liver.

mRNA sequencing – Liver-related genes

Originally 38171 of transcripts were found and 24004 genes were left after removing unmeasured genes, differential expression analysis was performed using DESeq2 package on R programme for pairwise comparison between HLCs cultured in Old and New media. 7020 genes were found to be significantly different between these two conditions, we have then set the filter for genes that expressed above -2 with minimum 4-fold change and FDR <0.05 (after Benjamimi and Hochberg correction); total 1307 genes were identified fitting this category. Within the 1307 genes, 1163 were upregulated and 144 genes downregulated, from the upregulated gene set we have selected some liver-related genes and presented in a heatmap (**Figure 4.13**). According to the correlation tree, two main clusters were identified and New-HLCs are grouped together with the foetal and adult liver samples based on the liver-relevant genes. Conversely, Old-HLCs resembles more closely to REBLPAT hiPSCs with a lot of the genes downregulated. Genes that are related to lipid metabolism such as lipase C (*LIPC*); Apolipoprotein A1 (*APOA1*); Apolipoprotein A2 (*APOA2*), Apolipoprotein A4 (*APOA4*); Apolipoprotein C3 (*APOC3*) and microsomal triglyceride transfer protein (*MTTP*) were detected at relatively higher levels in New-HLCs compared Old-HLCs, which correlate more to that of the liver sample sets. Similar pattern is also found in drug metabolising cytochrome P450 genes including *CYP7A1*, *CYP2C8* and *CYP3A4*, these were found to be downregulated in Old-HLCs and hiPSCs.

In conclusion, correlation tree (**Figure 4.10**) and multi-dimensional PCA analyses (**Figure 4.11**) indicated that HLCs cultured in New medium are more closely related to primary adult liver and foetal samples in comparison to that of Old-HLCs. Cells differentiated using Old media were relatively closer to undifferentiated hiPSCs. Moreover, gene set enrichment results showed that upregulated genes of New-HLCs are more closely related to liver cell type (**Figure 4.12**). Based on the analysed

transcriptomic data, New maturation medium would be more suitable to use as the culture medium during hepatocyte maturation.

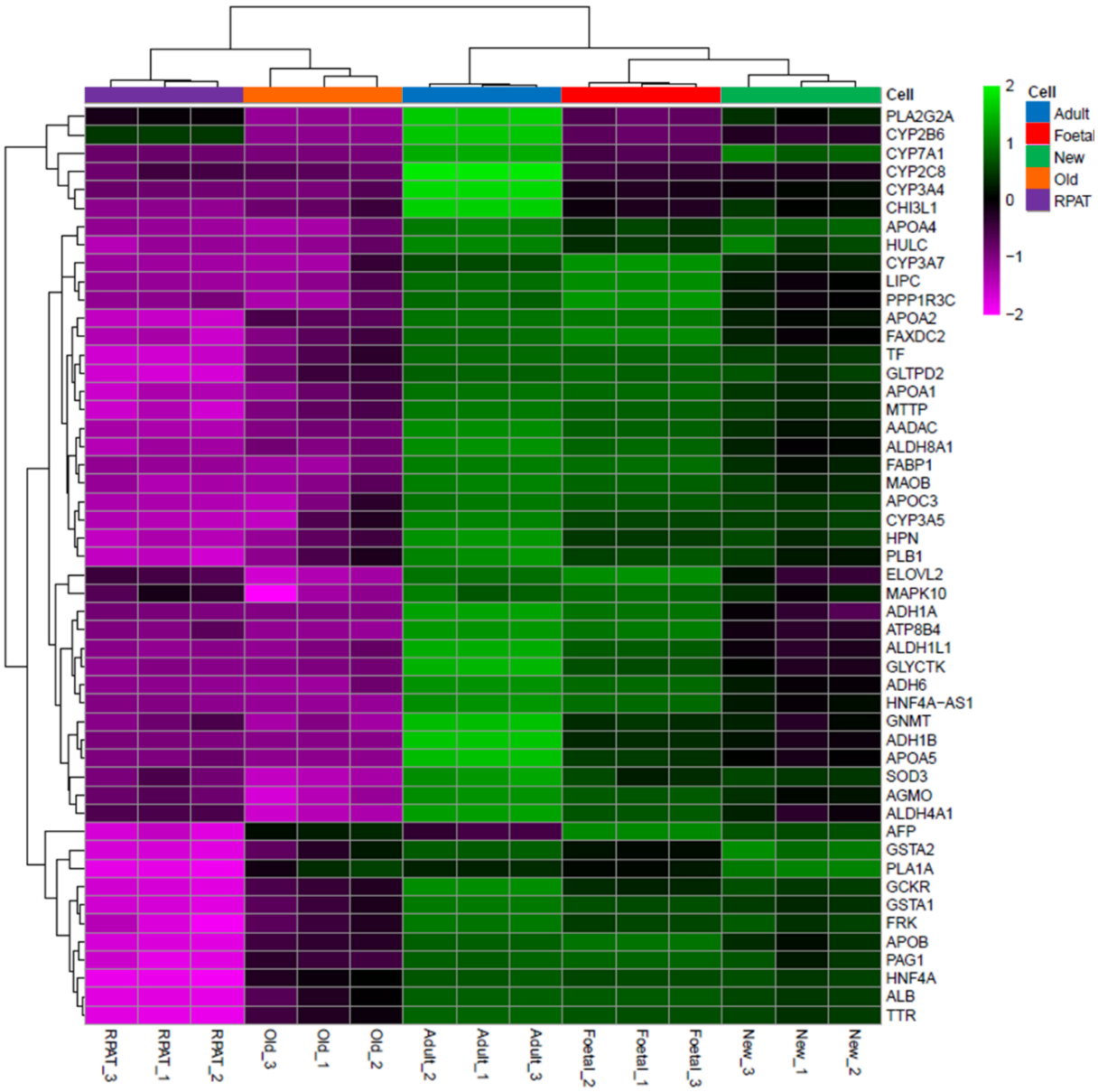


Figure 4.13 Expression profile of liver-related genes that are upregulated in New medium samples. A list of 50 genes are selected from the upregulated genes expressed in New medium samples compared to other sample sets based on DEseq2 data, values have been normalised to log2.

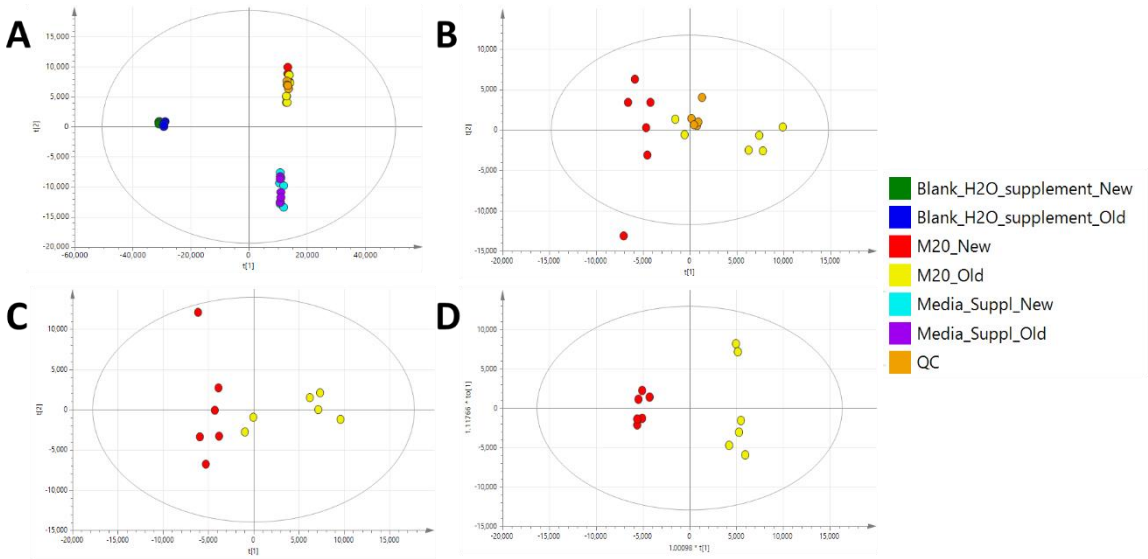
Metabolomic profiling for Old and New maturation media culture

To further characterise and understand the influence of Old and New media during hepatic maturation, liquid chromatography-mass spectrometry (LC-MS) based analytical approach was used to assess their secretome components. REBLPAT hiPSCs were differentiated for the complete 29 days, spent culture media were collected at maturation day 20 (M20, equivalent to D29) with six biological replicates from each condition, LC-MS analysis was then executed (**Figure 4.14**). Control sets for LC-MS include Old and New media blanks without cells; water with media supplements only; methanol blanks; and quality control (QC) samples with a small quantity mix of the actual cell culture samples, standards were also tested to help predict and determine the tested molecules. Multivariate analyses were performed to evaluate how closely the sample groups are related, PCA and Orthogonal Projections to Latent Structures Discriminant Analysis (OPLS-DA) approaches were utilised. First, the QC and media samples are shown to be normal with no outlier sample (**Figure 4.14A**). Old and New media samples were then examined regarding to their relatedness and similarity as depicted in **Figure 4.14B-D**, there is a distinct disparity between the two maturation media based on OPLA-DA analysis.

We have performed further statistical analysis and identified a list of metabolites that were present in both culture conditions with statistically significant differences (Figure 4.14**E**), in which they must fit the filter criteria of q-value (p-value adjusted for the FDR) less than 0.05 with a variable's important (VIP) score more than 1. Some of the molecules detected such as Tromethamine is commonly used as biological buffer substances, it is measured relatively higher in New spent medium, which helps to control levels of specific ions in solution. A lot of the metabolites detected are amino acids (AA), these include Asp-Lys-Thr-Thr; Ile-Met-Thr-Thr; Lys-Phe-Trp; and Lys-Ala-Gln, however they were only found in New spent medium and absent in Old spent medium. The level of AA has a crucial role in metabolism as well as CYP450 functions in hepatocytes, undetectable level of AA in Old spent medium may suggest that HLCs cultured in Old condition are not functionally mature enough to secrete such metabolites. In addition to that, we also found that glycerol and uridine were

detected at much higher levels in New spent medium compared to Old ones. Glycerol is metabolised predominantly in liver; it is also a precursor for the synthesis of triglycerides and phospholipid in liver and adipose tissue; this proposes that New-HLCs were metabolically more active and therefore were able to secrete glycerol more efficiently than that of Old-HLCs. Uridine is a pyrimidine nucleoside and the biosynthesis of it is regulated by the liver and adipose tissues, it is important in liver protein glycosylation which consequently can affect liver energy metabolism; higher secretion of uridine in New-HLCs implied that the endogenous level is relatively high and thereby can protect the generated cells against lipid accumulation. These data suggest that New-HLCs are evidently more mature than Old-HLCs, their metabolic efficiency is relatively higher.

To summarise the main biological functions and roles of the metabolites detected, a pie chart showing the classification of 621 metabolites is generated (Figure 4.14**F**). Majority of the metabolites are involved or related to amino acid, lipid, and carbohydrate metabolism, which are all crucial in energy production in the liver. The LC-MS data gave us a good indication that HLCs differentiated in both maturation media are functioning, nevertheless, New-HLCs are proven to be relatively more mature based on their metabolomics profile. New maturation medium is therefore more suitable for the direct differentiation towards hepatic lineage for downstream application.



E

Mass	RT (min)	Formula	Putative metabolite
147.0352	9.90	C5H9NO2S	Thiomorpholine 3-carboxylate
121.0738	11.18	C4H11NO3	Tromethamine
444.2145	4.28	C25H32O7	[FA methyl,oxo(5:0/5:0)] methyl 4R,12S-diacetoxy-9-oxo-5Z,7E,10Z,13Z,17Z-prostapentaenoate-cyclo[8,12]
83.0370	10.03	C4H7NO2	1-Aminocyclopropane-1-carboxylate
462.2252	4.28	C25H34O8	[ST trihydroxy(2:0)] 11beta,17alpha,21-trihydroxypregn-4-ene-3,20-dione 21-succinate
463.2285	4.28	C18H33N5O9	Asp-Lys-Thr-Thr
462.2251	4.30	C25H34O8	[ST trihydroxy(2:0)] 11beta,17alpha,21-trihydroxypregn-4-ene-3,20-dione 21-succinate
463.2284	4.29	C18H33N5O9	Asp-Lys-Thr-Thr
332.1986	5.09	C20H28O4	Gibberellin A12
464.2313	4.29	C19H36N4O7S	Ile-Met-Thr-Thr
358.0764	4.32	C11H12N4O7	Inosine-5'-carboxylate
332.1988	4.27	C20H28O4	Gibberellin A14 aldehyde
122.0771	11.19	C23H30N2O2	fumigaclavine C
484.2070	4.31	C22H26N6O4	Trp-Pro-His
363.2119	5.12	C14H26N4O6	Leu-Gln-Ser
92.0472	8.58	C3H8O3	Glycerol
479.2517	4.37	C26H33N5O4	Lys-Phe-Trp
345.2017	4.47	C14H27N5O5	Lys-Ala-Gln
362.2087	5.11	C21H30O5	[ST trihydroxy(2:0)] 11beta,17,21-trihydroxypregn-4-ene-3,20-dione
244.0694	8.83	C9H12N2O6	Uridine
375.1639	8.45	C15H25N3O8	Glu-Asp-Ile
344.1983	4.45	C21H28O4	[ST hydroxy(3:0)] 21-hydroxy-pregn-4-ene-3,11,20-trione
330.1829	5.10	C20H26O4	Gibberellin A15
409.1482	8.32	C18H23N3O8	Glu-Asp-Phe

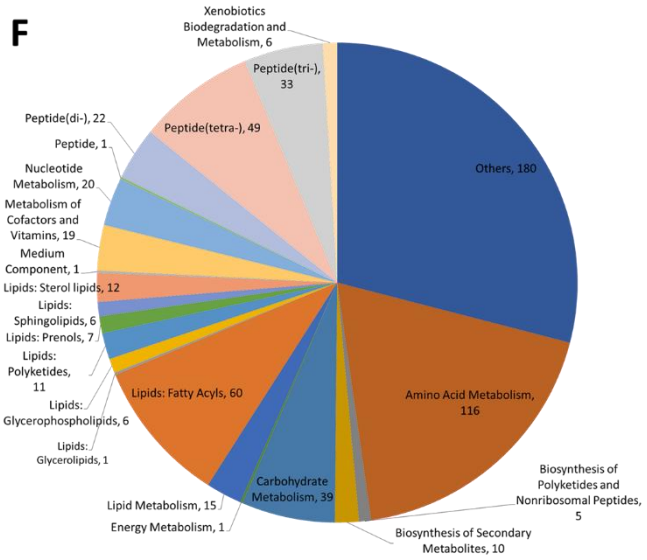


Figure 4.14 Extracellular metabolite profiling between Old and New maturation media using LC-MS-based method. Spent medium samples of HLCs were harvested after 20 days of maturation in Old and New culture media to identify what extracellular metabolites were secreted. PCA and OPLS discriminant analysis (OPLS-DA) score plots were analysed against standards and their corresponding medium-only blanks. **(A)** Combined standards, Old and New medium samples and their corresponding medium-only blanks (coloured according to class in M1, R2 = 0.961, Q2 = 0.933) **(B)** Standards, Old and New medium samples only. (class in M2, R2 = 0.549, Q2 = 0.162) **(C)** Old and New medium samples (class in M3, R2 = 0.507, Q2 = 0.14) **(D)** OPLS-DA score plot of Old and New medium samples, scaled proportionally to R2X (class in M4, R2X = 0.431, R2Y = 0.991, Q2 = 0.858). **(E)** A list of metabolites that are found between Old and New maturation media culture to be most siginificantly different, data is analysed by OPLS-DA and one-way ANOVA. **(F)** Functional categorisation of the nutrients and metabolites produced by HLCs in Old and New media, 621 metabolites are categorised based on their biological function.

4.4 Discussion

In this chapter, we focussed on optimising hepatic differentiation for individual hiPSC lines that will be used in the next chapter to model NAFLD, this ensures that the generated HLCs can recapitulate the phenotypes caused by the genetic variations as accurately as possible. We have explored ways to optimise the directed differentiation protocol in various aspects, including seeding density, BMP4 concentration, as well as the potentials of replacing recombinant growth factor proteins to small molecules to reduce the overall cost (**Figure 4.15**).

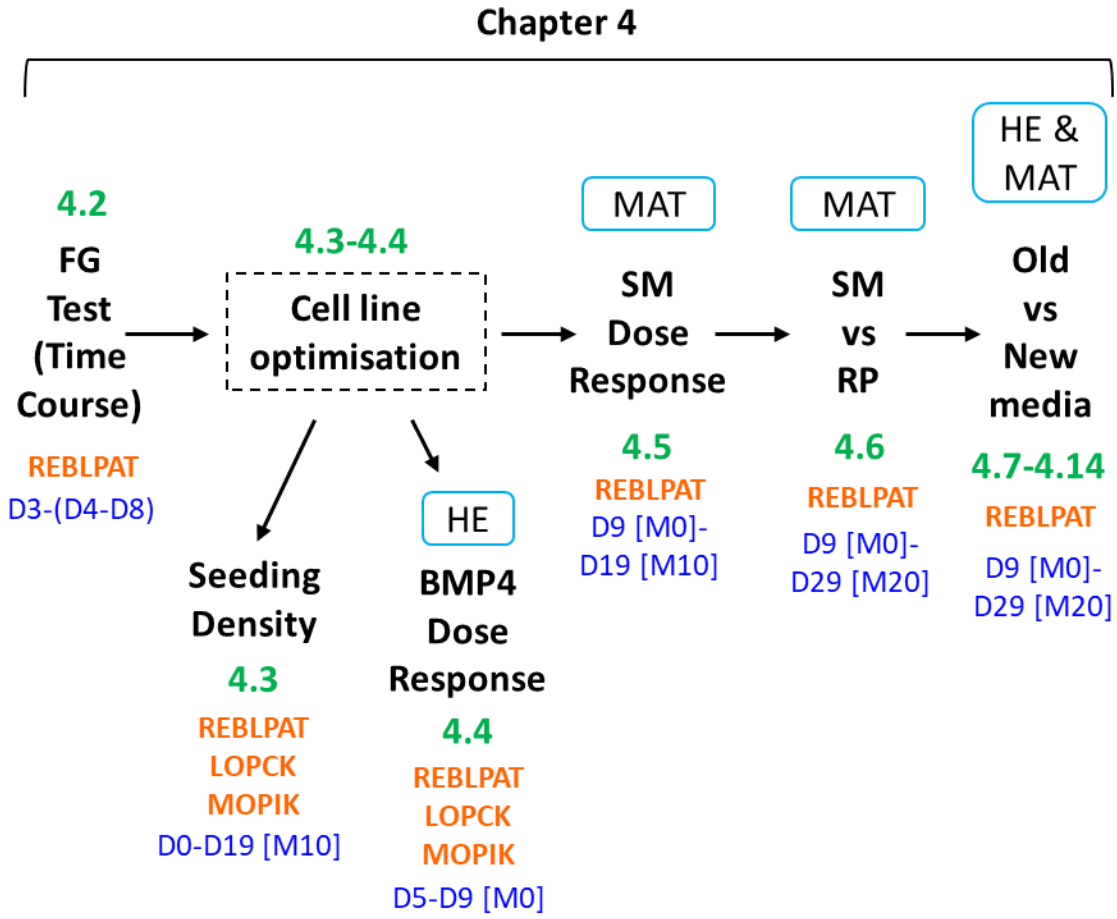


Figure 4.15 Schematic illustration of the experimental timeline of chapter 4. Experiments conducted are stated in black letters. Green letters represent the result figures related to that particular experiment. Orange letters represent the cell lines that are used in those experiments. Blue letters represent the specific period of hepatic differentiation that are tested. Blue boxes represent the differentiation stages that are of interest. Key: FG, foregut; HE, hepatic endoderm; MAT, maturation; SM, small molecule; RP, recombinant protein; BMP4, Bone Morphogenetic Protein 4.

We began to perform all the standardised optimisation experiments on the REBLPAT cell line because it is a well-established cell line within our laboratory, this had been used to generate many different cell types and we were more familiar with their cell behaviours. Once the main differentiation aspects were fulfilled, we could then adjust the modification to suit the specific hiPSC lines that were newly derived.

According to some of the well-known hepatic differentiation protocols, the usual timeframe would be between 20-30 days to produce HLCs *in vitro* [219], [231], [243], [258]. We decide to focus the time on hepatocyte maturation, so we investigated the possibility of reducing days in culture during anterior foregut formation. It was reported that 50 ng/ml Activin A alone can induce the expression of foregut markers such as *HNF4A*, *HHEX*, *SOX17* and *GATA4* to a comparable level of when using 200 ng/ml [138], we therefore used the same concentration of 50 ng/ml Act A. REBLPAT was seeded at the same density and underwent differentiation as usual, but the duration of foregut stage varied from 0 h to 120 h. We observed that cell population retained the petal-shape morphology, but as the time increased, the differentiating cells began to spread out more and less compact from around 72 h. Based on the qPCR data, liver-bud markers *HNF4A* and *TBX3* were upregulated statistically significant starting from 48 h of FG induction. Taking into consider that prolonged FG induction could reduce the cell yield, we established that 48 h of Activin A treatment would be sufficient to generate FG cells.

To further enhance the differentiation efficiency and to produce comparable HLCs, we also optimise the seeding density for each hiPSC line. We observed different proliferation rate and cell appearance of HDF-derived hiPSCs in chapter 3, these differences can influence the size and growth during differentiation. The seeding density therefore has a huge impact in regulating cell fate and yield. It was determined that LOPCK hiPSC colonies had a relatively slower growth rate compared to REBLPAT and MOPIK hiPSC lines. As expected, cell morphology and qPCR data also proven that LOPCK hiPSC line required lower seeding density of 15,000/cm^2 compared to REBLPAT and MOPIK hiPSCs using 20,000/cm^2 (**Figure 4.3)**

There are several signalling pathways that are particularly crucial in liver development; endodermal cells that possess hepatic competence can give rise to hepatoblasts by inducing FGF, BMP, TGF-β and Wnt signals in a concentration-dependant manner [234], [238], [259], [260]. Hence, during the early hepatic specification we have supplemented foregut cells generated from different hiPSC lines with an optimised concentrations of FGF10, BMP4 and SB431542 (SB, a TGF-β inhibitor) for four days; then later during hepatocyte maturation we adjusted the supplement combinations to higher concentration of FGF2, FGF10, DKK and Noggin, with the removal of BMP4 and SB to recapitulate the embryonic development [234], [259].

Via the animal studies on both *Xenopus* and mouse, literature shows that suppression of Wnt signalling using an inhibitor encoding *secreted frizzled- related protein 5 gene (sFRP5)* allows cardiac development, the Wnt antagonists might have an indirect role in hepatic induction by the nascent cardiac mesoderm [261], [262]; DKK has the similar effect during maturation stage. BMP signal was essential during the early stage of hepatic induction, it is particularly important in maintenance of the hepato-pancreatobiliary boundary patterning , which is achieved by indirectly repress SOX9 in the hepatic endoderm [11], [263]; once the hepatic endoderm is established, we then used the BMP antagonist Noggin to regulate the signal to an appropriate level of activity. In conclusion, it is fundamental to closely monitor the morphological changes, as well as gene and protein expression of the differentiating cells; concentration of growth factors need to be adjusted according to the stage of differentiation and cell lines used.

After optimisation of seeding densities and BMP4 concentration during hepatic endoderm differentiation, we decided to look into ways that can reduce the overall cost of differentiation to allow potential scale-up for future applications, such as high throughput drug screening. REBLPAT hiPSC line was used to validation the protocol we have previously developed during my MSc project, we first investigated whether

the small molecule candidates could replace several of the medium components that were costly.

The growth factor DKK and NOG were used during hepatic maturation stage, they played an important role of inhibiting Wnt/β-catenin and BMP signalling at the later stage of HLC development. The alternative small molecules we tested as a replacement for DKK are PNU and IWP-4; and LDN for BMP inhibition. QPCR data showed that liver-related markers were expressed in all of the SM conditions, however, the concentration of the compounds had a massive impact on cell morphology. PNU-treated cells looked similar in terms of morphology, notwithstanding, we could see that at 0.25 μM cells were relatively more compact and with higher cell yield. No statistical significance was found in *ALB* level regardless of the PNU dosage, PNU at 0.25 μM could induce liver-related gene expression overall, *CYP3A7* was also measured the highest at this concentration, hence it was selected for the next stage of combination testing.

IWP-4 was able to induce liver-related genes across the different concentrations, significant upregulation was seen in *HNF4A, AFP, ALB, A2AT* and *TTR* expressions. This trend, however, is not reflected on their cell morphology, IWP-4 treated cells generally look less defined and relatively flat in comparison to PNU-treated cells regardless of the dosage. Due to this reason, we decided not to use IWP-4 as an alternative of DKK during hepatocyte maturation, instead we only used PNU as the only SM candidate. PNU inhibits the Wnt/β-catenin signalling between β-catenin and T-cell factor (TCF), blocking the canonical pathway [264]; whereas IWP-4 acts differently and preventing both canonical and non-canonical signalling by inhibiting Wnt family member 5a directly [265], [266].

The SM alternative for NOG we used was LDN, it is a potent selective BMP type I receptor inhibitor which inhibits activin receptor-like kinase-1 (ALK1) to ALK3, as well as ALK4 to ALK6 with a weaker effect [267]. Expressions of liver-specific genes did not follow a particular pattern as the concentration escalate, so we determined the final

concentration to use mainly based on morphology. Cells treated with 1 µM LDN retained their structure and clear cell borders were observed, whereas lower doses did not seem to provide sufficient nutrients to support their architecture, therefore we selected 1 µM as the dosage moving forward.

After determining the optimal concentration of separate SM candidates, we wanted to further maximise differentiation efficiency by combining them together to create a synergetic effect. During the maturation stage, we tested SM-based culture medium against RP-based medium and observed a distinct difference between the two conditions. Initially, SM-treated cells were behaving similarly to that of RP-treated cell in terms of proliferation rate and cell architecture up until M10; *HNF4A* was highly upregulated at M0 and M5 but started to decrease at M10 in SM condition, indicating that SM combination is not as efficient in facilitating HLC maturation long term.

There have been other protocols reported to use only SMs for the complete hepatic differentiation and they stated that pure SM-cocktails were highly efficient in inducing hepatocyte maturation [222], hiPSCs were undergoing several stages of differentiation using SMs to produce definitive endoderm, hepatic endoderm and further hepatocyte maturation using three to five SM components; whereas their growth factor-induced protocol only involved two stages of differentiation using Activin A (100ng/ml) only during DE stage, then two recombinant proteins of BMP4 (10ng/ml) and FGF4 (10ng/ml) during hepatic specification stage. This has given greater advantages to cells that were treated under SM condition with the abundance of nutrients. In contrast, our approach was to differentiate hiPSCs exactly the same way towards hepatic endoderm and only replacing the two growth factors DKK and NOG during hepatic maturation, this can reduce the discrepancy between the two culture conditions and allowed us to monitor the direct effects of the replaced SMs. In our culture model, it is evident that even just by replacing two growth factors into SMs can greatly reduce the differentiation efficiency and

downregulate mature related gene expression in differentiating cells, therefore we will be using RP-based medium moving forward to minimise these effects.

After finalising our newly developed differentiation protocol, we wanted to certify that the new platform can indeed generate HLCs that are more phenotypically mature. REBLPAT hiPSCs were differentiated to DE, FG, and HE according to the protocol we described. During hepatocyte maturation, we tested the same population using two maturation medium formulas from day 9 (M0) onwards; the "Old" medium utilised the medium recipe from the protocol reported by Vallier group [139], the other half population was cultured in the "New" growth factor-based medium we have developed. Generated HLCs from the two maturation media were evaluated systemically in terms of their morphology, protein expression, transcriptomics, and metabolomics. There are key features that define mature hepatocytes structurally and functionally (**Table 4.1**), these hepatocyte characteristics should be taken into consideration during the generation and maturation of human HLCs. We have taken some of these measurement parameters and performed cell morphology examination, qPCR, immunofluorescence, mRNA sequencing, and mass spectrometry to evaluate the maturity of differentiated cells.

Table 4.1 Characteristics and measurement parameters of mature human hepatocytes. Adapted from [268]

Measurement parameter	Characteristic	Description
Morphology	Epithelial morphology	Polygonal in shape; microvilli on cell surface
	Polyploidization	Presence of 2 or more nuclei in fraction of the cells
Gene expression	Serum proteins	*ALB, TF, TTR*
	Hepatocytic transcription factors	*HNF4A, HNF1A, CEBPA/B*
	Drug metabolism enzymes	*CYP3A4, CYP7A1, CYP2A6, CYP2D6, CYP2B6, CYP2C8, CYP2C9, CYP1A2*
	Clinically relevant hepatic enzymes	*A1AT, G6Pase*
	Absence of biliary markers	*HNF1B, CK7, SOX9*
	Absence of stem cell markers	*LGR5, OCT4*
	Absence of hepatic immature markers	*AFP, CYP3A7*

In vitro testing	Phase 1 CYP activities	Metabolism of phenacetin (CYP1A2), bupropion (CYP2B6), tolbutamide (CYP2C9) diclofenac (CYP2G9), diclofenac (CYP3A4)
	Phase 2 transferase activities	Metabolism of bilirubin (UGT1A1), dopamine (SULT1A1), p-aminobenzoic acid (NAT1), 1-chloro-2,4-dinitrobenzene (GSTs)
	Phase 3 transporter activities	Transport of indocyanine green (OATP1B1), rhodamine 123 (MDR1), 5(6)-carboxy-2,070-dichlorofluorescein (MRP2)
	Bile acid synthesis	Formation of cholic acid and chenodeoxycholic acid (CYP8A1, AKR1D1, AKR1C4) Periodic
	Glycogen storage	Periodic acid–Schiff staining for glycogen
	Serum protein synthesis	Secretion of albumin, α–1 antitrypsin, fibronectin, transferrin, apoprotein, transthyretin, complement factors, coagulation factors
	Cholesterol metabolism	Formation of 7α-hydroxycholesterol (CYP7A1)
	Lipid uptake	Transport of low-density lipoprotein
	Urea metabolism	Synthesis of urea in cell extract
	Coagulation factors	Factors II, V, VII, IX, X

Overall assessments depicted that New-HLCs are relatively closer to primary foetal and adult liver samples' transcriptomic profiles compared to that of Old-HLCs by mRNA sequencing. We have also tested a set of mature markers such as *CYP2D6, CYP3A4* and *AADAC* using qPCR, a similar trend of upregulation of these genes as reported in [269], suggesting that the New medium could facilitate HLC maturation more effectively in terms of gene expression. Immunostaining also showed that higher levels of mature markers including ALB and A1AT were found in New-HLCs, as well as the drug metabolising enzymes CYP2A6.

When examining the metabolomic profiles between the two culture conditions, we found that New-HLCs were relatively more mature, this is based on the biological classification of the metabolites found in the spent medium. New-HLCs secreted quite a lot of compounds that OLD-HLCs lacked, or alternatively, with higher levels of the metabolites detected in New-HLCs. We have found compounds such as glycerol, uridine and multiple of amino acids present in the New-HLCs spent medium but with

low to absence levels in Old-HLCs, these are compounds metabolised predominantly in the liver and have different roles in the synthesis of triglycerides and phospholipids [270]; liver protein glycosylation; insulin signalling [271]; as well as amino acid and energy metabolism [272]. Detection of these metabolites indicate that New-HLCs were metabolically more active; higher secretion of these compounds also implied that the endogenous levels are relatively high compared to Old-HLCs, thereby the New-HLCs are more effective in protecting the generated cells against potential lipid accumulation. [271], [273].

Notwithstanding, to fully study the functionality of these cells *in vitro*, further functional assays such as albumin production, ureagenesis ability, bile acid production and assays for testing cytochrome P450 activity should be assessed using commercially available ELISA kits to prove that cells are functionally mature. However, due to time constrains to setting up the differentiation platform, we decided to move forward to the next stage of the project and focus on phenotyping the generated NAFLD models from different cell lines. Study on the functional maturity of cells under different culture conditions will be fully investigated in the future.

To drive hiPSCs toward hepatic cell fate, common components such as the hepatotrophic hormone insulin; as well as growth factors including hepatocyte growth factor (HGF) and oncostatin M (OSM) were routinely added to maturation media, they can directly affect hepatocyte proliferation, phenotype and metabolism [137], [231], [243], [274], [275]. Studies showed that insulin can enhance hepatocyte differentiation by activating the phosphoinositide-3-kinase/ AKT PI3K/AKT pathway and it has a prominent role in regulating glucose uptake [276], [277]. HGF can initiate the primary differentiation of hiPSCs into hepatoblasts, it is also a potent mitogen for differentiating cells; addition of OSM can inhibit their proliferation and promote maturation instead via signal transducer and activator of transcription 3 (STAT3) signalling pathway [278]–[280]. Both HGF and OSM can direct differentiating cells into hepatic lineage while suppressing the development into bile duct [279], [280]. In the new maturation medium recipe, we have added hydrocortisone; DKK; NOG;

fibroblast growth factor 2 (FGF2) and FGF10. HC is a glucocorticoid that acts synergistically with different essential growth factors and potentially influence the synthesis of extracellular matrix (ECM) ground substance [281]; it has been shown that specific concentration of insulin and hydrocortisone can maintain hepatic phenotype of adult human primary hepatocytes for around 15 days [282].

In summary, we have investigated different aspects of the differentiation protocol including seeding density, choice of supplements, and the adjustment of growth factor concentrations in order to optimise each cell line to generate HLC population that is phenotypically more relevant for downstream application of disease modelling, which we will be exploring in the next chapter.

Chapter 5.

Validation and phenotyping of hiPSC-HLCs as NAFLD disease model

Chapter 5. Validation and phenotyping of hiPSC-HLCs as NAFLD disease model

5.1 Introduction

Steatosis is the hepatic manifestation and main clinical feature of NAFLD, where excess triglyceride (TG) accumulation occurs in the form of lipid droplets within the hepatocytes. HiPSC-derived HLCs are a valuable tool for studying NAFLD disease pathophysiology, drug discovery and personalised regenerative medicine. Scientists have utilised different approaches to simulating hepatic steatosis *in vitro* in 2D or 3D culture with the addition of substances. These could be steatosis drugs such as valproate, doxycycline, amiodarone and tamoxifen [283], [284]; endotoxin such as lipopolysaccharides (LPS) [285], [286]; environmental pollutant such as bisphenol-A (BPA) [287], [288]; culture supplementation of fructose [289] and glucose [290]. Recent studies showed that a more popular agent to induce hepatic steatosis would be using fatty acid (FA) [107], [118], [131], [291]–[295], they are the main consistent of both dietary fat and of triglycerides, which can be found in vegetable oils (linoleic acid, LA); nuts, seeds and fruits (oleic acid, OA); as well as meat (palmitic acid, PA) [296].

Fatty acids are relatively cheap and there are a variety options can be chosen from, they are the functional components found in food, **Figure 5.1** shows how fatty acid (FAs) can be classified under their structural properties. Fatty acids are carbon chains with a methyl group at one end of the molecule (–CH3; designated as omega, ω) and a carboxyl group (–COOH) at the other end [297]. Based on the number of double bonds (C=C) and the location of the double bond closest to the methyl end (ω, or alternatively as the letter *n*); FAs can then be categorised into saturated fatty acid (SFA, with no double bonds) or unsaturated fatty acid (USFA, with one or more double bonds and can have either *cis* or *trans* isoforms configuration) [297]. Furthermore, USFA can be sub-categorised into monounsaturated FA (MUFA) and polyunsaturated FA (PUFA)[298]. USFAs are generally healthier than SFAs as they are relatively easier

to break down and stay in liquid or less solid form at room temperature, this is because of the increase of double bonds in USFA can reduce their melting points compared to SFAs [298]. It is therefore important to take into consideration the choice of fatty acid used to induce hepatic steatosis *in vitro*.

Some of the most commonly used free FAs to induce lipid accumulation in cell-based models include linoleic acid (LA; a type of PUMA) [95], [299], oleic acid (OA; MUFA) [107], [291], [294] and palmitic acid (PA; SFA) [118], [292], [300]. These FAs are found naturally in food; they can be used on their own or in combination at different concentrations or with other substrates to mimic the different types of dietary supplementations, this allow us to study how cellular behaviours and functionalities are influenced. In this chapter, we will be investigating the intrinsic roles of different *MTTP*-p.I564T variants act on healthy LOPCK ($MTTP^{WT/WT}$) and diseased MOPIK ($MTTP^{VAR/VAR}$), as well as the extrinsic influence in response to the exposure of FA treatments. To study the complex biological processes holistically in our model, it is imperative to take an integrative systemic approach by combining multi-omics analytical methods, which would allow us to highlight the interrelationships involved in a more global and objective manner to identify potential biomarker discovery and therapeutic targets.

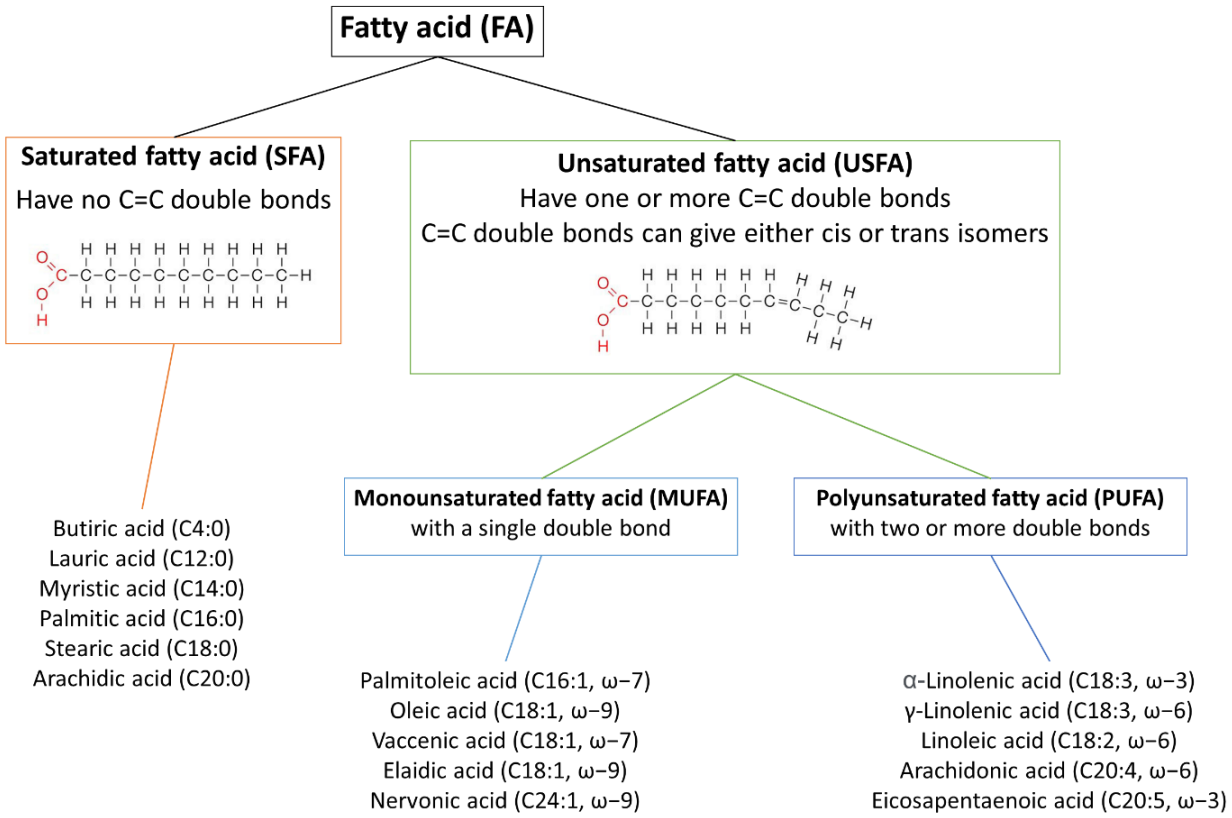


Figure 5.1 Classification of fatty acids according to their degree of saturation and unsaturation. Examples were listed under each category with their lipid number (total number of carbon atoms of the fatty acid: number of double bonds in it), the last carbon in the chain and counts of the carbons from that end is labelled as "ω−x", ω = omega.

5.2 Chapter aims and objectives

In the previous chapters, we have optimised hepatic differentiation for each patient-derived hiPSC lines to generate HLCs. We will be using these cell lines in this chapter to create an *in vitro* NAFLD disease model. This chapter will be investigating the influence of genetic predisposition by the *MTTP*-p.I564T single nucleotide variation in hiPSC-HLCs derived from both healthy individual and NAFLD patient, as well as their cellular response to external fatty acid addition. With the use of functionality testing, transcriptomics, proteomics and metabolomics profiling, these can help us to understand the underlying mechanism causing NAFLD, which can potentially help us to identify biomarker for disease diagnosis and prognosis.

5.3 Results

5.3.1 In vitro screening of fatty acid candidates for steatosis induction

Simulation of Western diet using fatty acid (FA) cocktail in vitro

It is essential to first evaluate if hepatic lipid accumulation can occur in differentiated HLCs after an influx of fatty acid (FA) to simulate the postprandial state *in vitro*. To do that, we first utilised a FA cocktail which is composed of polyunsaturated FA (PUFA); monosaturated FA(MUFA); and saturated FA (SFA) to mimic a common composition of western diet.

The FA cocktail contains 40 µM linoleic acid (LA), 80 µM oleic acid (OA) and 80 µM palmitic acid (PA), making up of a total final concentration of 200 µM FA combination. We first tested the effect of FA cocktail for 48-hour treatment in HLCs derived from the hiPSC line REBLPAT, which does not have the *MTTP*-p.I564T variation. This would help us evaluate how normal Differentiated HLCs were harvested at maturation day 10 (M10, equivalent to differentiation D19) for further analysis (**Figure 5.2**).

REBLPAT-HLCs treated with FA cocktail showed a relatively more compact morphology compared to untreated cells (**Figure 5.2A**), oil red O (ORO) staining demonstrated the presence of neutral triglycerides and lipids is relatively more abundant in FA-treated HLCs, indicating that FA can induce intracellular lipid accumulation in differentiating cells. QPCR showed that addition of FA to differentiating cells elevated mature hepatocyte gene markers significantly such as albumin (*ALB*), alpha-1 antitrypsin (*A1AT*), arylacetamide deacetylase (*AADAC*) and tryptophan 2,3-dioxygenase (*TDO2*); several of the cytochrome P450 (CYP) enzymes including *CYP3A7* and *CYP3A5* were also upregulated. Interestingly, genes that are related to inflammatory or fibrotic pathways are downregulated with FA treatment, statistically significant reduction of transforming growth factor beta (*TGFβ*) and pro-inflammatory interleukin 8 (*IL8*) were found; other genes such as indoleamine 2,3-

dioxygenase 2 (*IDO2*), tumour necrosis factor alpha (*TNFα*), collagen type I (*COL1*) and III (*COL3*) were also downregulated under FA treatment (**Figure 5.2B**).

Potential beneficial effects of oleic acid (OA) in hepatocyte maturation

Although differentiating REBLPAT-HLCs exhibited intracellular lipid accumulation with the use of FA cocktail, pro-inflammatory and fibrotic related gene expression were decreased overall, whereas the adult hepatocyte markers were increased based on the qPCR results (**Figure 5.2B**). We hypothesised that the addition of monounsaturated FA oleic acid (OA) could potentially improve hepatocyte maturity, a dose response experiment was therefore conducted on LOPCK ($MTTP^{WT/WT}$) cell line to investigate the potential beneficial effects to enhance hepatocyte maturation.

Oleic acid was added as a medium supplement during the hepatic maturation stage, differentiating cells were treated with various dosages of OA every 48 hours from maturation day 0 (M0) to day 5 (M5), samples were then harvested for qPCR analysis. We want to determine whether 5 days of OA treatment can upregulate hepatic markers drastically compared to M10 OA-untreated HLCs. OA-treated cells were harvested at M5 for qPCR analysis, gene expression fold change was measured against undifferentiated REBLPAT hiPSCs. We observed low level of lipid accumulation within cells starting at the lowest dosage of 25 µM (**Figure 5.3A**), deposition of lipid droplets became worsen as the OA concentration increased (50 µM and 100 µM).

We detected statistically significant higher level of *ALB,* microsomal triglyceride transfer protein (*MTTP*), *TDO2, AADAC* and *CYP3A5* in HLCs treated with 25 µM OA compared to all the other conditions (**Figure 5.3B**). In the contrary, the inflammatory modulator *TGF-β* gene expression reduced as OA concentration increased, indicating that addition of OA could possibly improve hepatocyte maturity, nevertheless, OA may not be the ideal fatty acid candidate to simulate hepatic steatosis *in vitro* due to its anti-inflammatory properties.

Palmitic acid (PA) is the ideal fatty acid candidate to simulate hepatic steatosis

Due to the potential anti-inflammatory quality of oleic acid, we then decided to investigate the use of saturated palmitic acid (PA) alone to model hepatic steatosis *in vitro*. REBLPAT and LOPCK (*MTTP*$^{WT/WT}$) hiPSCs were differentiated to maturation day 8 (M8, equivalent to differentiation D17), then treated with different concentrations of PA (0 µM, 300 µM and 600 µM) for 48 hours, HLCs were harvested at maturation day 10 (M10). **Figure 5.4A** (REBLPAT) and **Figure 5.4B** (LOPCK) displayed similar morphology with a monolayer of polygonal-shaped cells at 300 µM PA conditions between REBLPAT- and LOPCK-HLCs, though there is a subtle difference in the compactness of space probably due to the different seeding density and growth rate between cell lines overall. REBLPAT-HLCs retained the hepatocyte-like architecture as PA dosage increase, additionally cells became more compact with the addition of PA than compared to untreated condition, tiny lipid droplets were observed in both 300 µM and 600 µM PA. When PA was added at relatively lower dosage at 300 µM to LOPCK-HLCs, it seemed to have aided cell proliferation and a homogenous layer of cells was formed, however, when added at 600 µM PA cells began to detach resulting in lower yield; lipid droplets were observed in both PA-treated conditions in LOPCK-HLCs as well.

Indeed, an upregulation of pro-inflammatory factor *TNFα* was observed in both cell lines as PA concentration increased, similarly, *IL8* gene expression also increased and particularly higher at 600 µM (**Figure 5.4C**). Interestingly, *TGFβ* as the key regulator of extracellular matrix (ECM) assembly and remodelling had a reduction of expression in both REBLPAT- and LOPCK-HLCs, downregulation of this gene may have an implication of the negative regulation of fibrotic gene *COL1*. Palmitic acid seemed to have induced inflammatory genes but no signs of developing fibrosis within 48 hours treatment. Adult markers including *ALB* and *A1AT* were both upregulated and peaked at 300 µM PA particularly in LOPCK-HLCs, levels of these genes decreased at 600 µM; no statistical significance was found between different PA treatments in REBLPAT cell line. Although inflammatory gene expressions were relatively higher at 600 µM, it

had a huge impact on cellular architecture, take into consideration of cell proliferation rate and morphological changes, 300 µM PA would be the ideal fatty acid candidate to model hepatic steatosis.

To validate whether 300 µM PA is able to induce lipid accumulation while maintaining cellular structures, LOPCK (*MTTP*$^{WT/WT}$) and MOPIK (*MTTP*$^{var/var}$) HLCs undergone the same treatment using 300 µM PA, in comparison to their untreated condition (**Figure 5.5).** Culture conditions for differentiating each cell line was optimised with the optimal seeding densities (LOPCK: 20,000/cm^2, MOPIK: 15,000/cm^2) and BMP4 concentration (both at 10 ng/ml) as we have described in the last chapter, which helped to produce hepatocyte-cell like populations that were comparable. LOPCK- and MOPIK-HLCs looked very similar in untreated condition based on light microscopy examination, both cell lines formed a compact monolayer of polygonal shaped HLCs, nonetheless, faint yellow deposition of lipid droplets were seen in MOPIK (*MTTP*$^{var/var}$)-HLCs even without the addition of palmitic acid, suggested that this cell line could be more likely to store fat intrinsically or maybe due to insufficient lipid export, in comparison to healthy LOPCK cell line (**Figure 5.5A**). When treated with 300 µM of PA for 48 hours, both cell lines presented lipid droplets confirmed by ORO staining, notwithstanding, higher degree of lipid accumulation was detected in MOPIK-HLCs treated with PA. Additionally, PA-treated MOPIK cells were forming small aggregates of potential microvesicular steatosis caused by excess lipid accumulated in vesicles that displaced the cytoplasm. Indeed, Nile Red (NR) staining (**Figure 5.5B**) and fluorescence quantification (**Figure 5.5C**) demonstrated the same phenomenon, the level of lipid accumulation is highest at MOPIK-HLCs treated with 300 µM PA, followed by untreated MOPIK cells, then PA-treated LOPCK-HLCs, untreated LOPCK cells remained the lowest. Based on these results, we concluded that 300 µM PA is sufficient to induce hepatic steatosis *in vitro* while maintaining the cellular architecture without excessive cell death. The next stage would be the phenotypic validation of generated HLCs under untreated and PA-treated conditions and how the genotypic variation may have influence cell behaviours due to underlying mechanisms, which we will be investigating in this chapter.

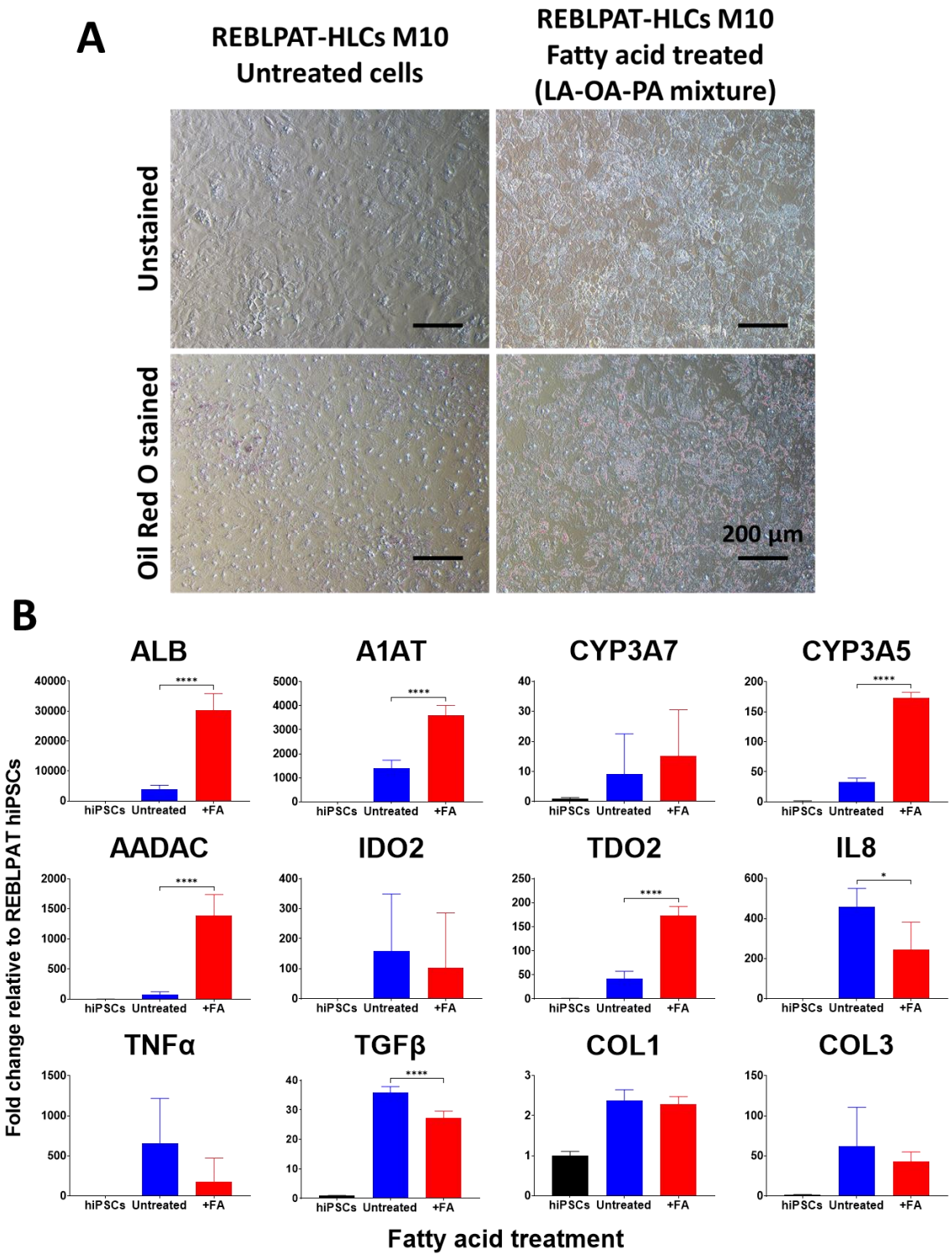


Figure 5.2 Simulation of Western diet using fatty acid (FA) cocktail in REBLPAT-HLCs. FAs were used as a mixture at 1:2:2 ratio of linoleic acid (LA, 40 µM); oleic acid (OA, 80 µM) and palmitic acid (PA, 80 µM) respectively for 48 hours (total final concentration = 200 µM). **(A)** Representative picture of HLCs before and after oil red O (ORO) staining at maturation day 10 (M10, equivalent to differentiation D19), with or without FA treatment. **(B)** qPCR expression analysis of genes encoding mature hepatic marker such as *ALB*, *AADAC*, *CYP3A5*; inflammatory related gene *TGF-β*, *TNF-α, IL8* and fibrotic gene *COL1, COL3*. Gene expression in HLCs quantified as fold change over levels in undifferentiated REBLPAT hiPSCs. Statistical significance symbols: *P ⩽ 0.05, **P ⩽ 0.01, ***P ⩽ 0.001, ****P ⩽ 0.0001.

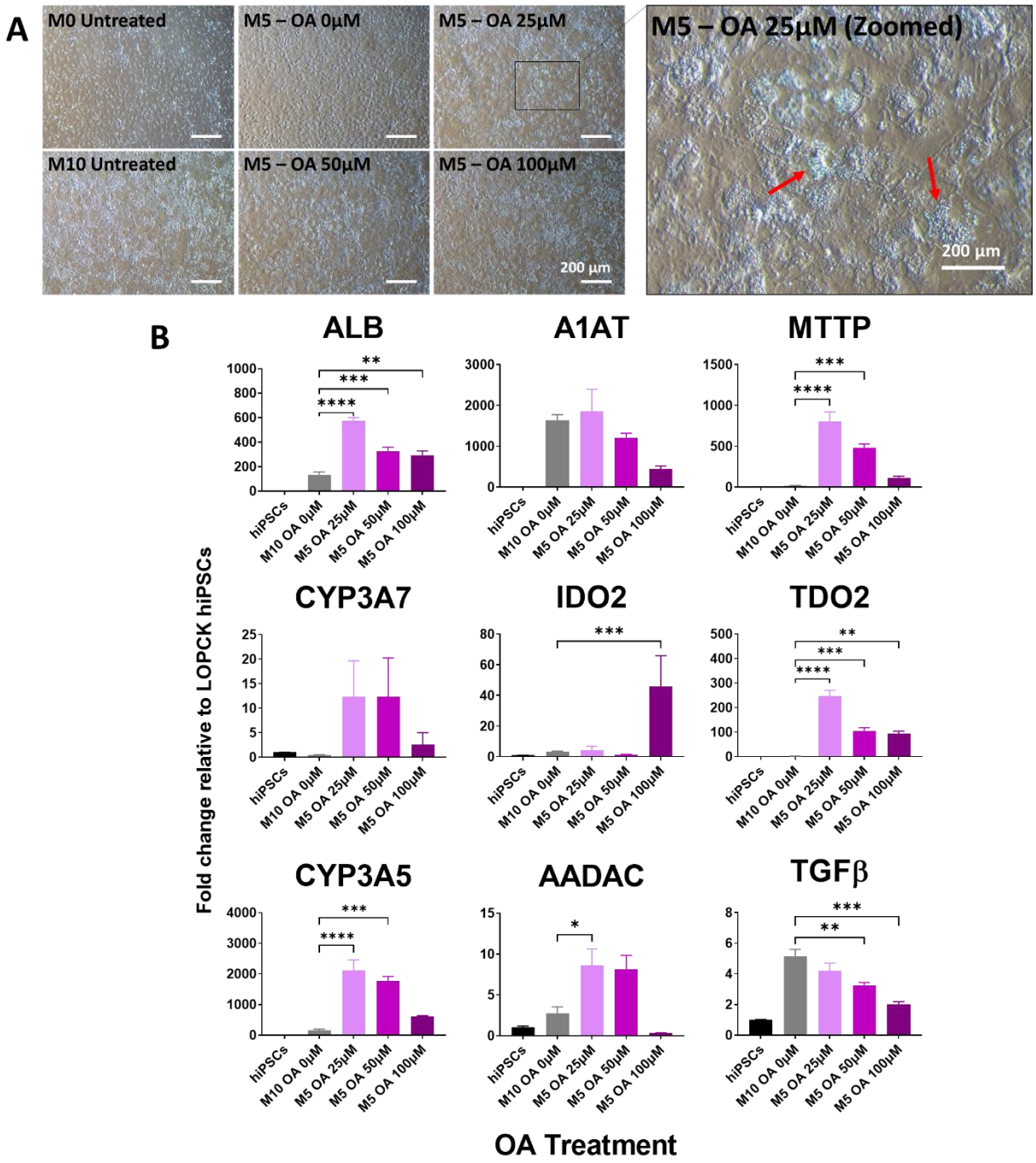
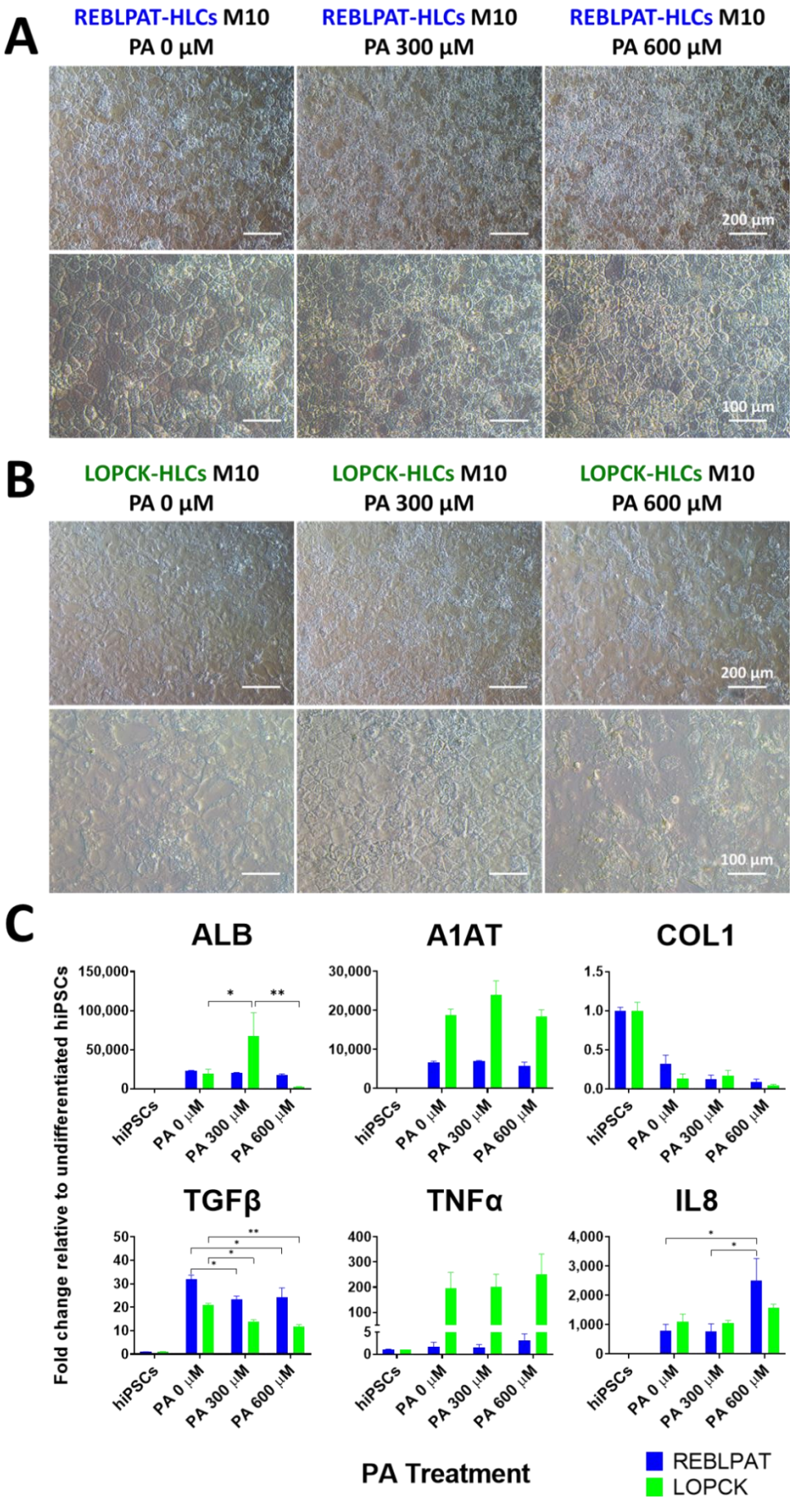


Figure 5.3 Effects of OA treatment at different dosages on LOPCK-HLCs. LOPCK ($MTTP^{WT/WT}$) hiPSCs were differentiated towards HLCs, from maturation day 0 (M0, equivalent to differentiation D9) cells were additionally supplemented with OA every 48 hours. **(A)** Light microscopy images of differentiating cells treated with various concentrations of OA, in comparison to M0 and M10 untreated HLCs. Lipid droplets (red arrow) were observed starting from the lowest dosage at 25 μM OA. **(B)** Gene expression profile of OA-treated HLCs harvested at M5 in comparison to hiPSCs and M10-untreated HLCs. Fold change measurement is relative to undifferentiated LOPCK-hiPSCs. Statistical significance symbols: *P ⩽ 0.05, **P ⩽ 0.01, ***P ⩽ 0.001, ****P ⩽ 0.0001.


A
REBLPAT-HLCs M10
PA 0 µM
REBLPAT-HLCs M10
PA 300 µM
REBLPAT-HLCs M10
PA 600 µM
200 µm
100 µm
B
LOPCK-HLCs M10
PA 0 µM
LOPCK-HLCs M10
PA 300 µM
LOPCK-HLCs M10
PA 600 µM
200 µm
100 µm
C
ALB
A1AT
COL1
TGFβ
TNFα
IL8
Fold change relative to undifferentiated hiPSCs
hiPSCs
PA 0 µM
PA 300 µM
PA 600 µM
PA Treatment
REBLPAT
LOPCK

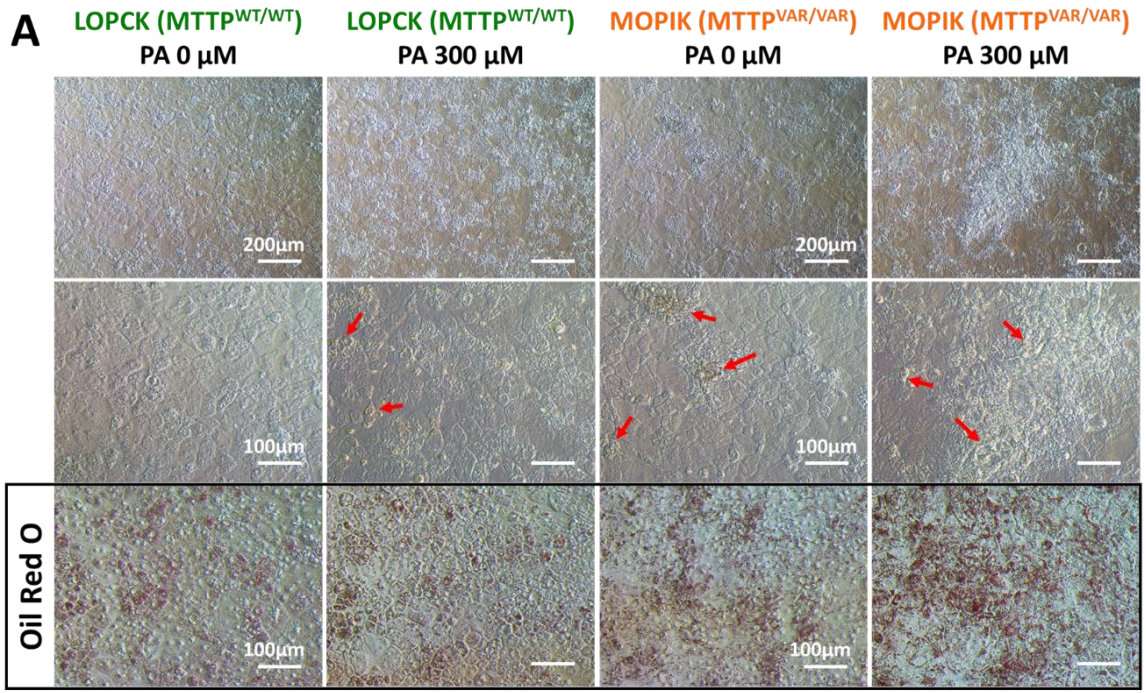


Figure 5.4 Effects of 48-hour PA treatment at different dosages on HLCs lipid induction. (above) REBLPAT and LOPCK ($MTTP^{WT/WT}$) hiPSCs were differentiated towards HLCs, cells were analysed at maturation day 10 (M10, equivalent to differentiation D19). Light microscopy images of **(A)** REBLPAT and **(B)** LOPCK differentiating cells treated with various concentrations of PA. (C) Gene expression profile of untreated and PA-treated HLCs harvested at. Fold change measurement is relative to undifferentiated REBLPAT- or LOPCK-hiPSCs. Statistical significance symbols: *P ⩽ 0.05, **P ⩽ 0.01, ***P ⩽ 0.001, ****P ⩽ 0.0001.

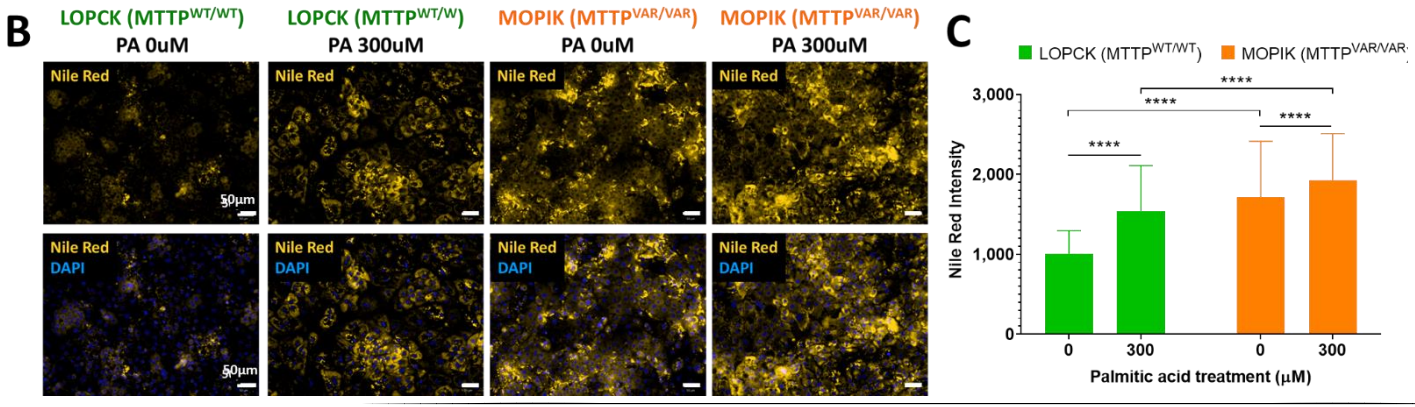


Figure 5.5 48-hour Palmitic acid treatment can induce lipid accumulation in hiPSC-derived HLCs at 300 µM while maintaining cellular architecture. (left) **(A)** Light microscopy images of LOPCK (*$MTTP^{WT/WT}$*)- and MOPIK(*$MTTP^{VAR/VAR}$*)-HLCs at maturation day 10 (M10, equivalent to differentiation day 19) with or without 300 µM PA treatment. Yellow depositions (red arrow) of potential lipid droplets appear in certain areas. HLCs are stained with Oil Red O (ORO) to visualise lipid accumulation. **(B)** HLCs are also stained with Nile Red (NR) and visualised using the Operetta high content imaging system, (C) fluorescence intensity is quantified and compared between LOPCK and MOPIK cell lines. Statistical significance symbols: *P ⩽ 0.05, **P ⩽ 0.01, ***P ⩽ 0.001, ****P ⩽ 0.0001.

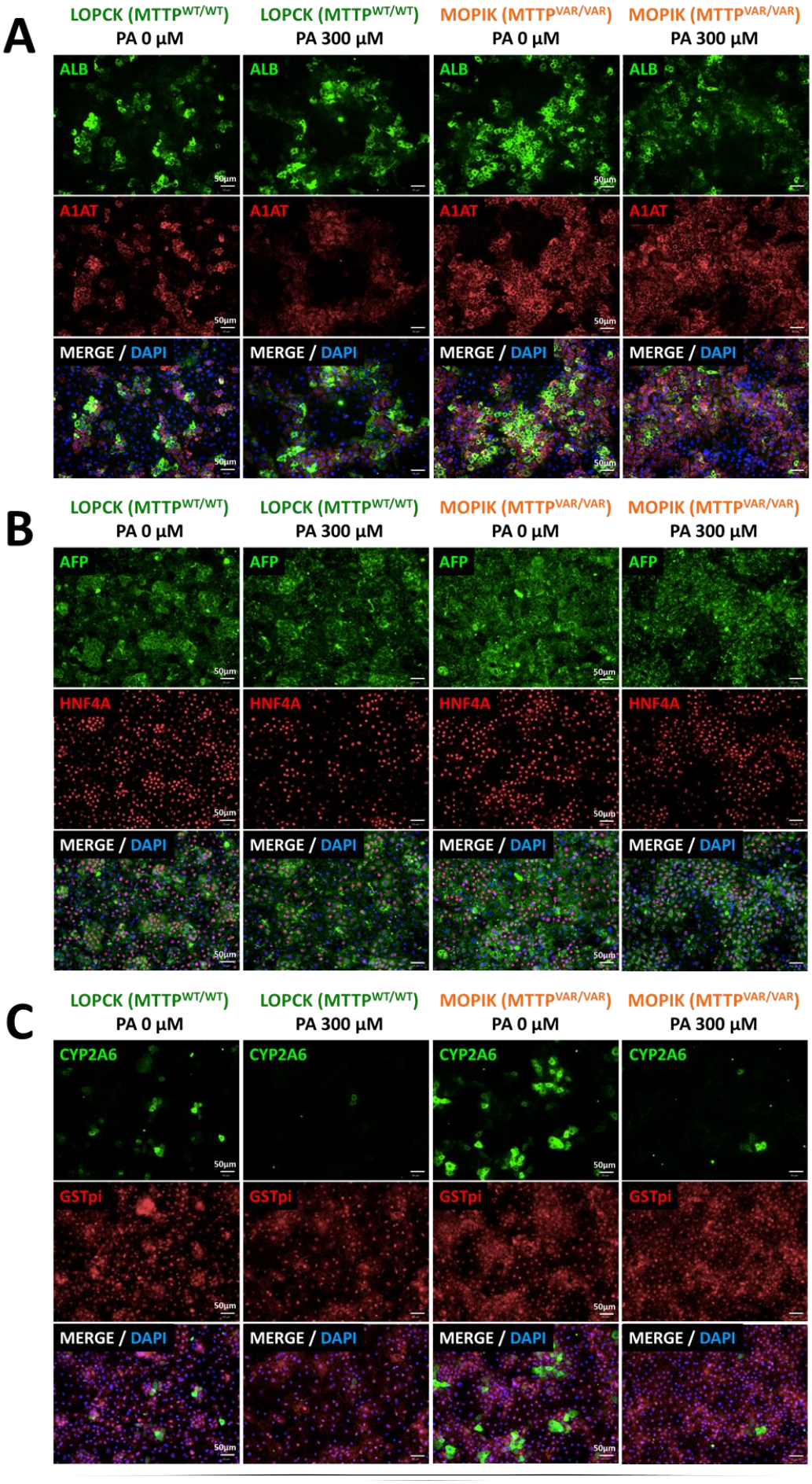
5.3.2 Phenotype validation of LOPCK (*MTTP*$^{WT/WT}$) and MOPIK (*MTTP*$^{VAR/VAR}$) as NAFLD disease models

In this section, we will be focussing on the *in vitro* NAFLD disease models which we have created in two ways; first by assessing the intrinsic influence of the *MTTP*-p.I564T genetic variation has on differentiated hiPSC-derived HLCs, secondly, to evaluate how external lipid influx may cause different cellular behaviours or changes in transcriptomic, proteomics and metabolomics overall. LOPCK (*MTTP*$^{WT/WT}$) and MOPIK (*MTTP*$^{VAR/VAR}$) hiPSCs were differentiated to maturation day 8 (M8, equivalent to differentiation D17) using our optimised differentiation protocol and treated either with 0 µM or 300 µM palmitic acid for 48 hours to induce hepatocellular lipid accumulation, cells were then harvested for further phenotypic screening.

LOPCK and MOPIK HLCs expressed liver-related proteins at comparable levels

Mature liver markers ALB and A1AT (**Figure 5.6A**) were expressed in both LOPCK and MOPIK HLCs, nevertheless, foetal markers AFP and HNF4A (**Figure 5.6B**) were also presented, which is a common phenomenon in differentiated HLCs. Adult cytochrome P4502A6 enzyme CYP2A6 was double stained with glutathione S-transferase Pi (GST_{Pi}), to distinguish between adult-like population (CYP2A6 positive) from their foetal counterparts (**Figure 5.6C**). An interesting observation is that addition of PA did not seem to increase CYP2A6 protein expression compared to untreated HLCs, an alteration in liver protein abundance of drug-metabolising enzyme in an abnormal state may compromise ability of metabolising external substrates and potentially exacerbate the adverse effects caused by it.

Figure 5.6 LOPCK and MOPIK HLCs expressed liver markers at similar levels. (below) Immunocytochemistry staining of **(A)** mature hepatocyte markers ALB and A1AT; **(B)** liver bud markers AFP and HNF4A; **(C)** adult cytochrome P4502A6 enzyme CYP2A6 and foetal liver marker GSTpi; all counterstained with nuclei DAPI staining.


A
LOPCK (MTTP^WT/WT) PA 0 µM
LOPCK (MTTP^WT/WT) PA 300 µM
MOPIK (MTTP^VAR/VAR) PA 0 µM
MOPIK (MTTP^VAR/VAR) PA 300 µM
ALB
A1AT
MERGE / DAPI
B
AFP
HNF4A
C
CYP2A6
GSTpi
50µm

Detection of MTTP gene transcript and protein level

The genetic variation *MTTP*-p.I564T causes a replacement of amino acid from isoleucine (I, WT) to threonine (T, VAR), which consequently could impact on gene and protein expression. Hence, we utilised immunostaining and qPCR to evaluate MTTP protein abundance and mRNA transcript level (**Figure 5.7**). Based on immunofluorescence results, there is overall statistically significant reduction of MTTP protein levels in MOPIK cell line in comparison to LOPCK-HLCs under both untreated and PA-treated conditions (**Figure 5.7A**), this is verified by fluorescence quantification using the Columbus analytic software (**Figure 5.7B**). Notwithstanding, MTTP proteins increased slightly more in PA-treated condition compared to untreated HLCs in both cell lines. This is however, reversed in *MTTP* gene expression, where untreated MOPIK-HLCs had relatively higher mRNA transcripts than LOPCK-HLCs with statistical significance, less MTTP proteins were translated (**Figure 5.7C**). In healthy LOPCK cell line, there is a positive correlation between *MTTP* gene transcript and MTTP protein expression, whereas MOPIK ($MTTP^{VAR/VAR}$) HLCs had a negative correlative correlation with higher levels of gene transcript but translation of protein was decreased.

Since MTTP is a key player in the assembly and secretion of hepatic very-low-density-lipoproteins (VLDL) and secretion in the form of apolipoprotein B-100 (apoB-100), genetic variation of *MTTP*-p.I564T could have an impact on level of apoB-100 secretion. Therefore, the next step would be to measure the level of apoB-100 in hiPSC-derived HLCs to assess the influence of *MTTP*-p.I564T on the ability of VLDL export via apoB-100 secretion.

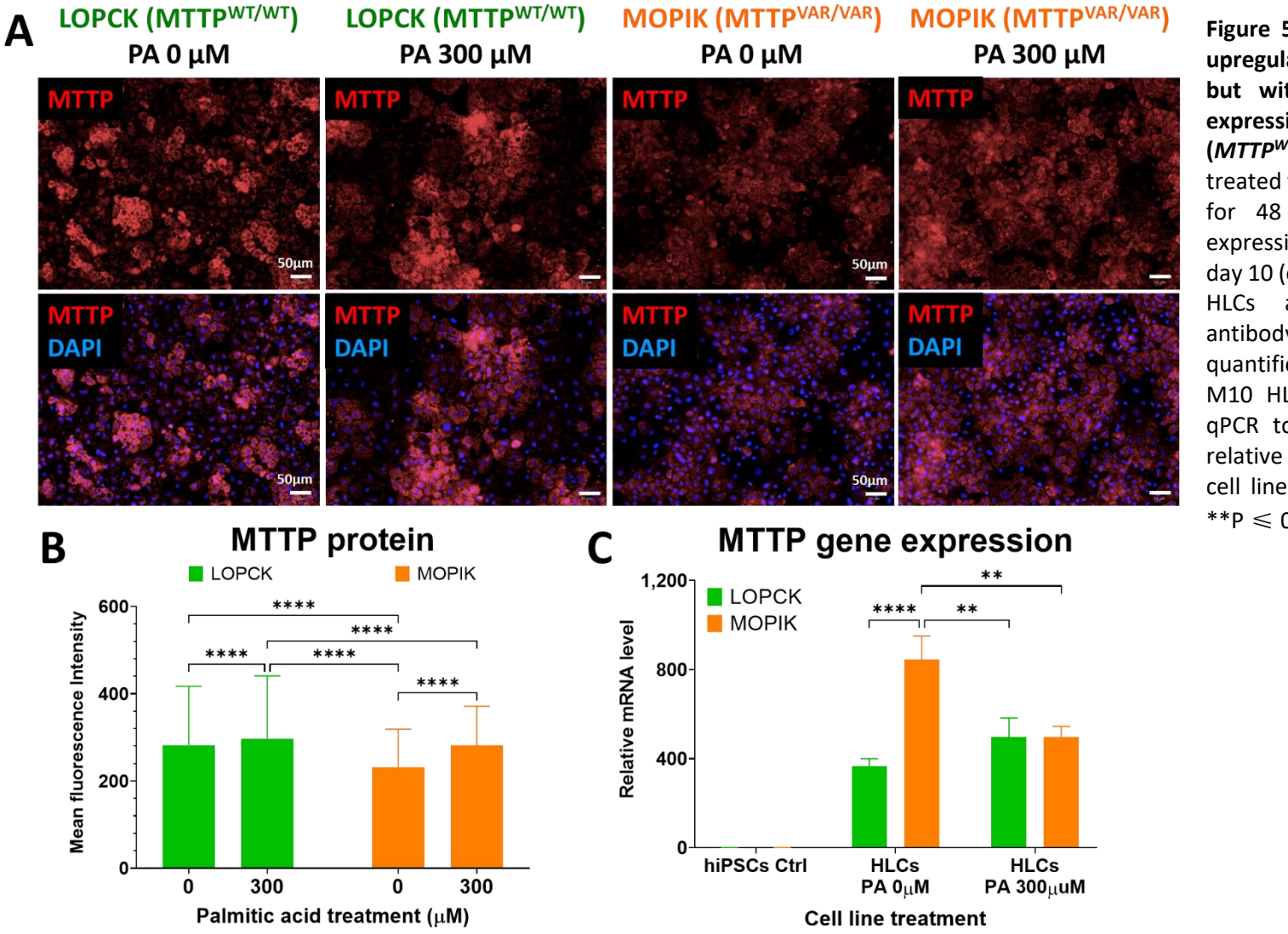


Figure 5.7 *MTTP* gene expression is highly upregulated in MOPIK (*MTTP*$^{VAR/VAR}$) HLCs but with relatively lower MTTP protein expression compared to that of LOPCK (*MTTP*$^{WT/WT}$) HLCs. Differentiating cells are treated with 0 or 300 µM of palmitic acid (PA) for 48 hours, MTTP protein and gene expression are then measured at maturation day 10 (equivalent to differentiation D19). **(A)** HLCs are immunostained with MTTP antibody, **(B)** fluorescence intensity is then quantified using the Columbus software. **(C)** M10 HLCs are harvested and analysed by qPCR to check for *MTTP* gene expression relative to undifferentiated hiPSCs from each cell line. Statistical significance: *P ⩽ 0.05, **P ⩽ 0.01, ***P ⩽ 0.001, ****P ⩽ 0.0001.

Validation of apolipoprotein B-100 levels in HLCs compared to hiPSC-derived intestinal organoids and patient plasma serum

To assess whether *MTTP*-p.I564T SNV would affect the level of apolipoprotein B-100 (apoB-100) secreted into the serum from the liver via VLDL, Human Apolipoprotein B-100 (apoB-100) ELISA kit was used to measure secreted apoB-100 levels from HLCs and intestinal organoids (IOs) differentiated from LOPCK and MOPIK hiPSCs (**Figure 5.8**). In addition, pre- (at fasting state) and post-prandial (180 mins after) plasma serum samples, as well as fractionated VLDL samples were collected from GF06 healthy individual and GF10 (NAFLD patient with $MTTP^{VAR/VAR}$ genotype). LOPCK and MOPIK HLC culture supernatants were collected 48 hours post-PA treatment or without, supplemented media without cells were used as a blank control. Each sample was tested in duplicate, and normalization was achieved by subtracting the average of blank controls from each measurement.

As expected, supernatants of hiPSC-derived intestinal organoids detected very low levels of apoB-100 compared to that of hiPSC-derived HLCs, since apoB-100 is enriched in the liver. Instead of secreting apoB-100, the intestine chylomicrons would be secreting the alternative form of lipoprotein as apolipoprotein B-48 (apoB-48), hence, we detected barely any apoB-100 in supernatants from both LOPCK and MOPIK intestinal organoids. There was a slight increase (1.27 times) of apoB-100 with PA treatment relative to untreated MOPIK-HLCs. In opposite to this observation, LOPCK-HLCs secreted less apoB-100 (1.42 times less) in the supernatant after 48 h of 300 µM treatment relative to its untreated control. Despite this contrasting trend, higher levels of apoB-100 were still detected overall in LOPCK-HLCs compared MOPIK-HLCs in both untreated and PA-treated culture.

There is an increasing trend of apoB-100 concentration postprandial in all serum and VLDL samples compared to their fasting states, the differences are particularly apparent in both healthy GF06 serum and VLDL samples compared to that of GF10. Regardless of the sample type, healthy individual's serum, VLDLs (GF06) and its derivative cell line (LOPCK) all have relatively higher levels of apoB-100 in comparison

to the NAFLD/NASH patient's serum, VLDLs (GF10) and its derivative MOPIK cell line overall. There is a larger difference (16 times higher) of apoB-100 between the fasting (26,513 ng/ml) and postprandial (428,196 ng/ml) in GF10 VLDL samples, relative to 1.8 times higher between the fasting (456,838 ng/ml) and postprandial (850,799 ng/ml) in GF06 VLDL samples. However, the differences between fasting and postprandial serum samples in GF06 (1.06 times) and GF10 (1.03 times) are a lot less compared to the fractionated VLDL samples, suggesting that apoB-100 were indeed secreted in the serum but not in the form as VLDL. This is an indication that the assembly and packaging of apoB-100 into VLDL via the MTTP enzyme is ineffective, which could be due to the *MTTP*-p.I564T genetic variation.

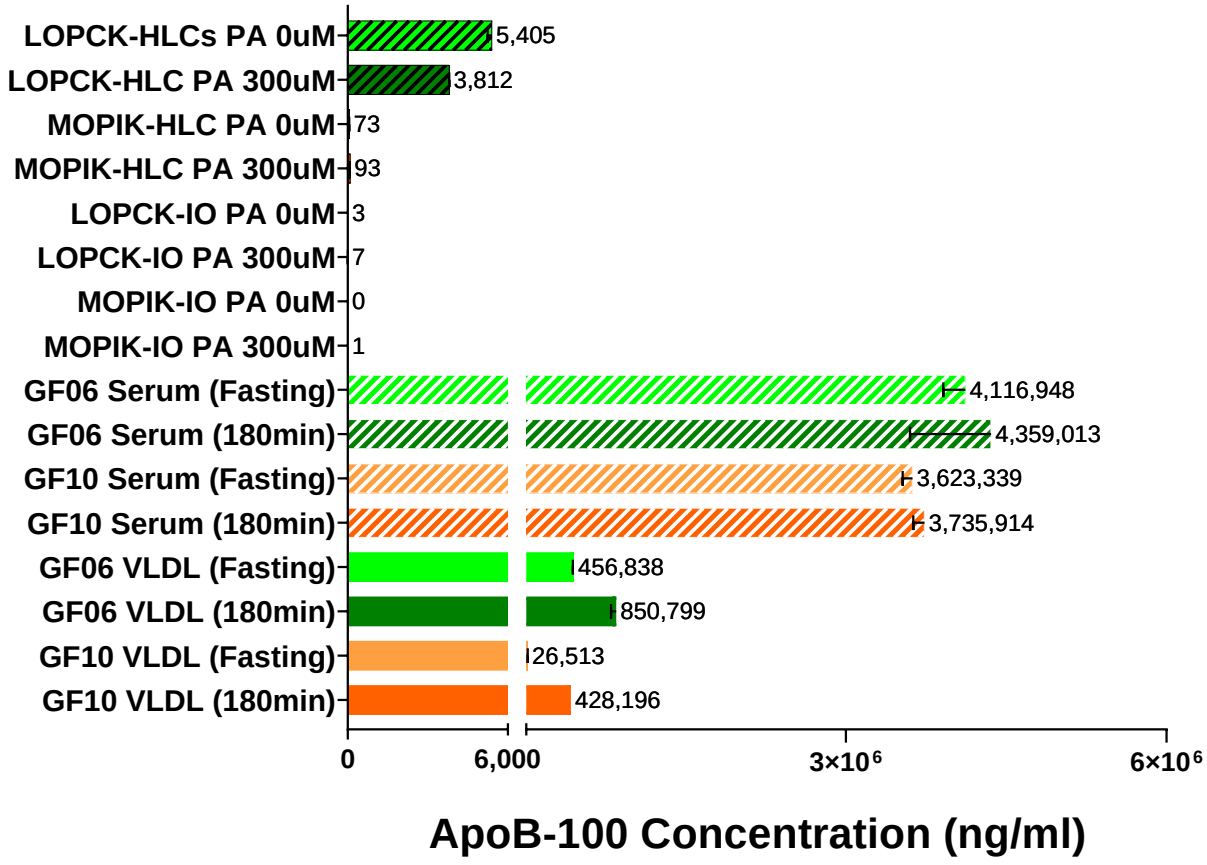


Figure 5.8 ApolipoproteinB-100 (ApoB-100) quantification by ELISA. Cell culture media are collected from LOPCK- and MOPIK-HLCs, as well as intestinal organoids generated from these cell lines to compare the levels of ApoB-100 with and without palmitic acid (PA) treatment. Patient serum and isolated very-low-density-lipoprotein (VLDL) were used in parallel to verify the trend of ApoB-100. LOPCK hiPSCs was derived from GF06 individual with wildtype *MTTP* $^{WT/WT}$ genotype, whereas MOPIK hiPSCs was derived from GF10 NAFLD patient with variant *MTTP*$^{VAR/VAR}$ genotype. Actual concentration of ApoB-100 was calculated based on the extrapolated values using GraphPad Prism.

MOPIK (MTTP$^{VAR/VAR}$)-HLCs have lower lipid metabolising efficiency and accumulate intracellular lipid inherently

To further understand the cause of reduction of apoB-100 in MOPIK-HLCs from the ELISA data, qPCR was performed to examine the gene expression discrepancy between healthy LOPCK (*MTTP*$^{WT/WT}$) and diseased MOPIK (*MTTP*$^{VAR/VAR}$) cell lines. We first verify the gene expression levels of liver-specific markers *ALB* and *AFP*; primary foetal and adult liver RNAs were used as references in comparison to hiPSC-derived HLCs (**Figure 5.9A**). Intriguingly, MOPIK-HLCs expressed *ALB* significantly higher compared to LOPCK-HLCs in both untreated and PA-treated conditions, at the same time foetal marker *AFP* was downregulated in MOPIK-HLCs with the similar trend as the primary liver samples, though they were not as low as the adult liver sample. This founding is aligned with our immunostaining results of the ALB protein level.

Genes related to lipid metabolism were also tested (**Figure 5.9B**), we found that expression of apolipoprotein B (*APOB*) gene was peaked in untreated MOPIK-HLCs, which is opposite to the trend we observed in secreted apoB-100 level; increased gene expression did not seem facilitate greater rate of apoB-100 secretion, which could be due to the *MTTP*-p.I564T genotype. Detection of the very-low-density-lipoprotein receptor (*VLDLR*) showed that although untreated HLCs had slightly higher levels of *VLDLR*, no statistical significance was found, suggesting that there could be a lack of VLDL protein rather than the lack of VLDL ligand binding and transport by the VLDL receptor. This indicates that there is an insufficient export of packaged lipoproteins from HLCs to the culture media supernatant.

Divergence transcript levels of lipase A (*LIPA*) and lipase C (*LIPC*) were detected. Lipases perform essential roles in digestion, transport, and processing of dietary lipids such as triglycerides, fat and oils. Lipophagy is a process that occurs during autophagic degradation of intracellular lipid droplets, neutral lipids such as cholesteryl esters and TG in the lipid droplets are partially sequestered in autophagosomes and transported to lysosomes [301]. Lysosomal acid lipase (LAL),

which is encoded by *LIPA,* it functions in the lysosome to hydrolyse these neutral lipids to generate free fatty acids (FFA) and cholesterol in the cell during lipophagy. High lipid accumulation within MOPIK-HLCs in both untreated and PA-treated conditions may require higher demand of lipophagy, hence *LIPA* expression was upregulated and relatively higher than that of LOPCK-HLCs with statistical significances.

Hepatic lipase (encoded by *LIPC*) is predominantly found in the liver, it hydrolyses TG and phospholipids present in circulating plasma lipoprotein, including chylomicrons, intermediate density lipoproteins (IDL), low density lipoproteins (LDL) and high density lipoproteins (HLD); releasing FFA and smaller lipoprotein particles [302]. Interestingly, reduction of *LIPC* expression was found in MOPIK-HLCs compared to that of LOPCK-HLCs, particularly even lower after PA treatment. Nevertheless, *LIPC* expression (between 30,000-230,000 folds) of all HLC samples were a lot higher than those of *LIPA* expression (~3-11 folds), suggesting that although *LIPC* level was lower in MOPIK-HLCs, cells were still actively going through lipolysis to overcome the influx of palmitic acid.

Patatin like phospholipase domain containing 3 (*PNPLA3*, also called adiponutrin) is greatly expressed in adipocytes and hepatocytes, it is important in the regulation lipogenesis as acetyl-CoA-independent transacylase A and lipolysis as a TG hydrolase, it is tightly controlled by changes in nutritional status [303]. *PNPLA3* level was noticeably higher in LOPCK-HLCs compared to that of MOPIK-HLCs, suggesting that the healthy LOPCK ($MTTP^{WT/WT}$) cell line could be inducing its hydrolase property more actively compared to diseased MOPIK ($MTTP^{VAR/VAR}$) cell line. On the contrary, the fat metabolism regulator transmembrane 6 superfamily member 2 (*TM6SF2*) was significantly low in PA-treated MOPIK-HLCs relative to PA-treated LOPCK-HLCs; it has been shown that inhibition of *TM6SF2* could be associated with reduced secretion of TG-rich lipoproteins and increased cellular TG concentration [304], downregulation of *TM6SF2* in PA-treated MOPIK-HLCs may suggests that TG were not able to be

secreted in the form as apoB, which correlates to the ELISA results with decreased apoB-100 detected in MOPIK-HLCs supernatant.

Melanoma inhibitory activity protein 2 (*MIA*2) is a receptor in the endoplasmic reticulum (ER), which plays a role in the export of pre-chylomicrons and pre-VLDLs [305]. *MIA2* expressions were comparable between LOPCK and MOIK HLCs in untreated condition; after PA treatment LOPCK-HLCs was upregulated whereas MOPIK-HLCs had the opposite effect of downregulation, suggesting that healthy LOPCK ($MTTP^{WT/WT}$) cell line had a higher rate of lipid export. In addition, we tested the expression of apolipoprotein C-III (*APOC3*), which is a VLDL component that functions to inhibit lipoprotein lipase and hepatic lipase [306]. Intriguingly, we found untreated MOPIK-HLCs expressing relatively high level of *APOC3* in comparison to LOPCK-HLCs, as well as its PA-treated condition, suggesting a potential inhibition of lipase activity could be caused by the upregulation of *APOC3*, contributing to reduction in lipolysis and lipid export.

Overall qPCR data of lipid metabolism related markers suggests that there is a demand of lipoprotein packaging and lipid export in MOPIK-HLCs compared to LOPCK-HLCs (*APOB* ↑, *VLDLR* ↑). At the same time lipolysis (*LIPC* ↓) is potentially inhibited by the increase of *APOC3* resulting in higher lipid accumulation within MOPIK-HLCs.

MOPIK ($MTTP^{VAR/VAR}$)-HLCs sustained higher degree of ER stress

Endoplasmic reticulum (ER) stress can stimulate the degradation of intracellular lipid droplets in liver; it is a condition when there is an accumulation of unfolded or misfolded proteins in the ER, which induces a cellular stress response called the unfolded protein response (UPR). UPR is a regulatory mechanism that instigates transcriptional and translational response to readjust the ER folding capacity to restore protein homeostasis. We have measured several important genes related to UPR pathway (**Figure 5.10A)**.

Expression of UPR pathway sensors inositol requiring enzyme 1 (*IRE1*) and activating transcription factor 6 (*ATF6*) were significantly upregulated and relatively higher in MOPIK-HLCs compared to that of LOPCK-HLCs, untreated condition also had slightly higher gene expression than with PA treatment. When IRE1 pathway is stimulated, its downstream target UPR regulator X-box binding protein 1 (*XBP1*; unspliced *usXBP1*, spliced *sXBP1*, total *tXBP1*) would undergo splicing. *XBP1 (usXBP1*, *sXBP1* and *tXBP1*) gene expressions were significantly higher in the diseased cell line MOPIK overall, suggesting UPR pathway was more activated.

Activating transcription factor 4 (*ATF4*) is the downstream mediator of the third ER stress sensor: protein kinase r-like er kinase (PERK); *ATF4* mRNA level was also raised in MOPIK-HLCs upon phosphorylation of eukaryotic initiation factor 2 alpha (eIF2a), consequently may induce genes responsible for the antioxidant response, amino acid metabolism, and apoptosis.

One of the most abundant proteins within the ER lumen is the Hsp70-type chaperone: binding immunoglobulin protein (*BIP,* a.k.a *GRP78*); statistically significant upregulation was measured in both untreated and PA-treated MOPIK-HLCs relative to LOPCK. Interestingly, we found a downregulation in another Hsp90-type chaperone: glucose-regulated protein 94 (*GRP94*), its mRNA level was relatively higher in the healthy LOPCK ($MTTP^{WT/WT}$) cell line instead; MOPIK's *GRP94* expressions were comparable to undifferentiated hiPSCs. Terminally misfolded or mutated proteins in the ER can be targeted to the ER–associated degradation (ERAD) pathway by the recognition of ER degradation-enhancing mannosidase-like protein (*EDEM*), which subsequently degraded by the ubiquitin-proteasome system. No statistical significance was observed in *EDEM* expression between both healthy LOPCK and diseased MOPIK cell lines, suggesting that ERAD activities were similar in both cell lines to process misfolded proteins.

Overall upregulation of UPR activators and mediators in MOPIK-HLCs indicated that although ERAD degradation was working efficiently, there was a greater stimulation

of UPR activity and ER stress, which consequently could lead to activation of inflammatory signalling pathways.

NFκB inflammatory pathway is activated in MOPIK (MTTP$^{VAR/VAR}$)-HLCs

We detected statistically significant upregulation of the pro-inflammatory chemokine interleukin-8 (*IL-8*) gene expression after 48 hours of PA treatment in MOPIK-HLCs, whereas *IL8* level remained similar at PA 0 µM and 300 µM in LOPCK-HLCs (**Figure 5.10B**). Although the level of *IL-8* was slightly lower in MOPIK-HLCs compared to LOPCK-HLCs in untreated condition, its downstream transcription factor NFκB was activated and the levels of *NFκB* were significantly higher in MOPIK-HLCs compared to LOPCK-HLCs in both PA-treated and untreated conditions.

Transforming growth factor beta (*TGF-β*) is a pleiotropic cytokine involved in cell survival, proliferation, differentiation, fibrosis, and wound healing by activating Smad- and TGF-β-activated kinase 1 (TAK1)-dependent signalling [307]. Expression of *TGF-β* in MOPIK-HLCs were significantly higher statistically compared to LOPCK-HLCs, indicating there may be a need for cell proliferation, tissue repair and survival, alternatively, upregulation of *TGF-β* could be an indication of promoting fibrosis by enhancing type I collagen (*COL1*). Indeed, mRNA level of *COL1* was also upregulated in MOPIK-HLCs relative to LOPCK-HLCs in both untreated and PA-treated conditions, whereas PA-treated LOPCK-HLCs had a downregulation of *COL1* instead; this may suggest an activation of extracellular matrix (ECM) protein synthesis in MOPIK-HLCs for structural remodelling.

Tumour necrosis factor alpha (*TNF-α*) is an inflammatory cytokine released by Kupffer cells (liver macrophages), which is also a crucial signal that initiate regeneration and restoration of liver function [308]. It is however found that the concentration of TNF-α could determine its functions to whether being pro-inflammatory or exerting a

protective effect, this also depends on the cause of hepatic injury [309]. Low TNF-α could promote Yap1 nuclear translocation triggering hepatic proliferation; whereas high TNF-α could promote cell death by triggering phosphorylation, inactivating Yap1 and preventing its nuclear import [309]. This may explain why untreated LOPCK-HLCs were detected with significantly high level of *TNF-α*, notwithstanding the upregulation of *NFκB*, indicating that either the canonical or non-canonical NFκB pathway was activated, but perhaps activation was caused by other stimuli such as reactive oxygen species (ROS), interleukin 1-beta (IL1β), or bacterial lipopolysaccharides (LPS).

Pattern recognition receptors such as toll-like receptors (*TLR*) 1-5 gene expressions were also measured to detect any potential stimulation of immune response. We found that *TLR4* was highly upregulated (> 100 folds) particularly in MOPIK-HLCs in comparison to LOPCK-HLCs, with a slight reduction after PA treatment. Interestingly, though *TLR1* was also upregulated in a relatively low level, it had the opposite trend where LOPCK-HLCs expressed higher *TLR1* relative to that of MOPIK-HLCs, additionally, PA-treated MOPIK-HLCs had significantly low expression, almost to none. Significant increase of *TLR4* gene expression in both untreated and PA-treated MOPIK-HLCs compared to LOPCK-HLCs indicating that there may be an activation of damage-associated molecular pattern molecules (DAMPs) caused by endogenous intracellular triggers such as cytokines. Secretion of cytokine and phosphorylated protein will be examined later on in proteomics profiling to determine whether they are related to the activation of DAMP.

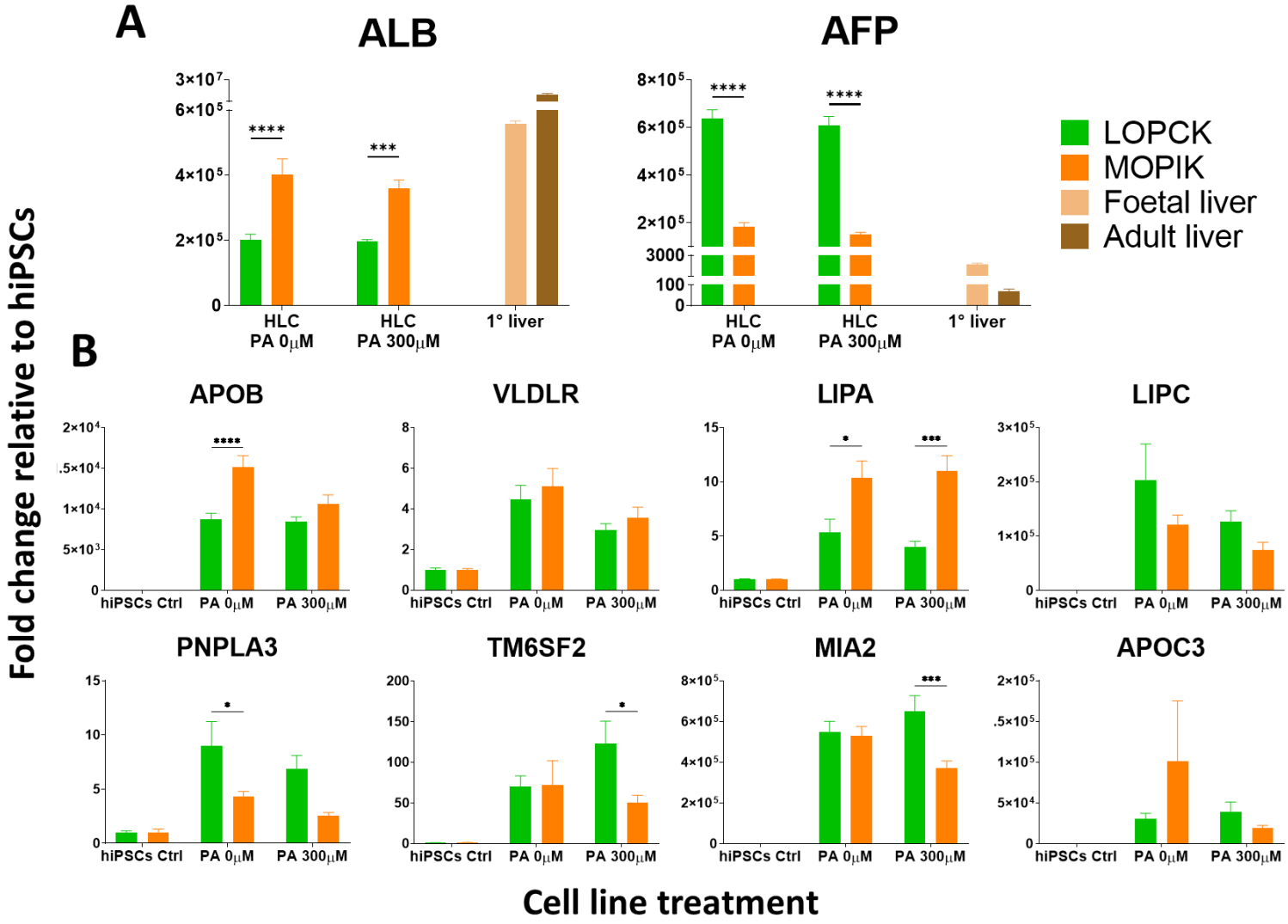


Figure 5.9 MOPIK (*MTTP*$^{VAR/VAR}$) HLCs are relatively more mature than LOPCK(*MTTP*$^{WT/WT}$) HLCs, with various expression levels of genes related to lipid metabolism. **(A)** LOPCK- and MOPIK-HLCs are treated without or without PA (300 μM) and harvested at maturation day 10 (M10, equivalent to differentiation D19) for qPCR analysis. Fold change is relative to undifferentiated hiPSCs from each cell line. Primary foetal and adult liver RNAs are used as references in comparison to hiPSC-derived HLCs. Gene expression of mature marker *ALB* and foetal marker *AFP* are measured. **(B)** Transcript profile of genes related to lipid metabolism, including genes encode for apolipoprotein-B (*APOB*); apolipoprotein C3 (*APOC3*); very-low-density-lipoprotein receptor (*VLDLR*); lipase A (*LIPA*); lipase C (*LIPC*); patatin-like phospholipase domain-containing protein 3 (*PNPLA3*); transmembrane 6 superfamily 2 (*TM6SF2*) and melanoma inhibitory activity protein 2 (*MIA2*). Statistical significance: *P ⩽ 0.05, **P ⩽ 0.01, ***P ⩽ 0.001, ****P ⩽ 0.0001.

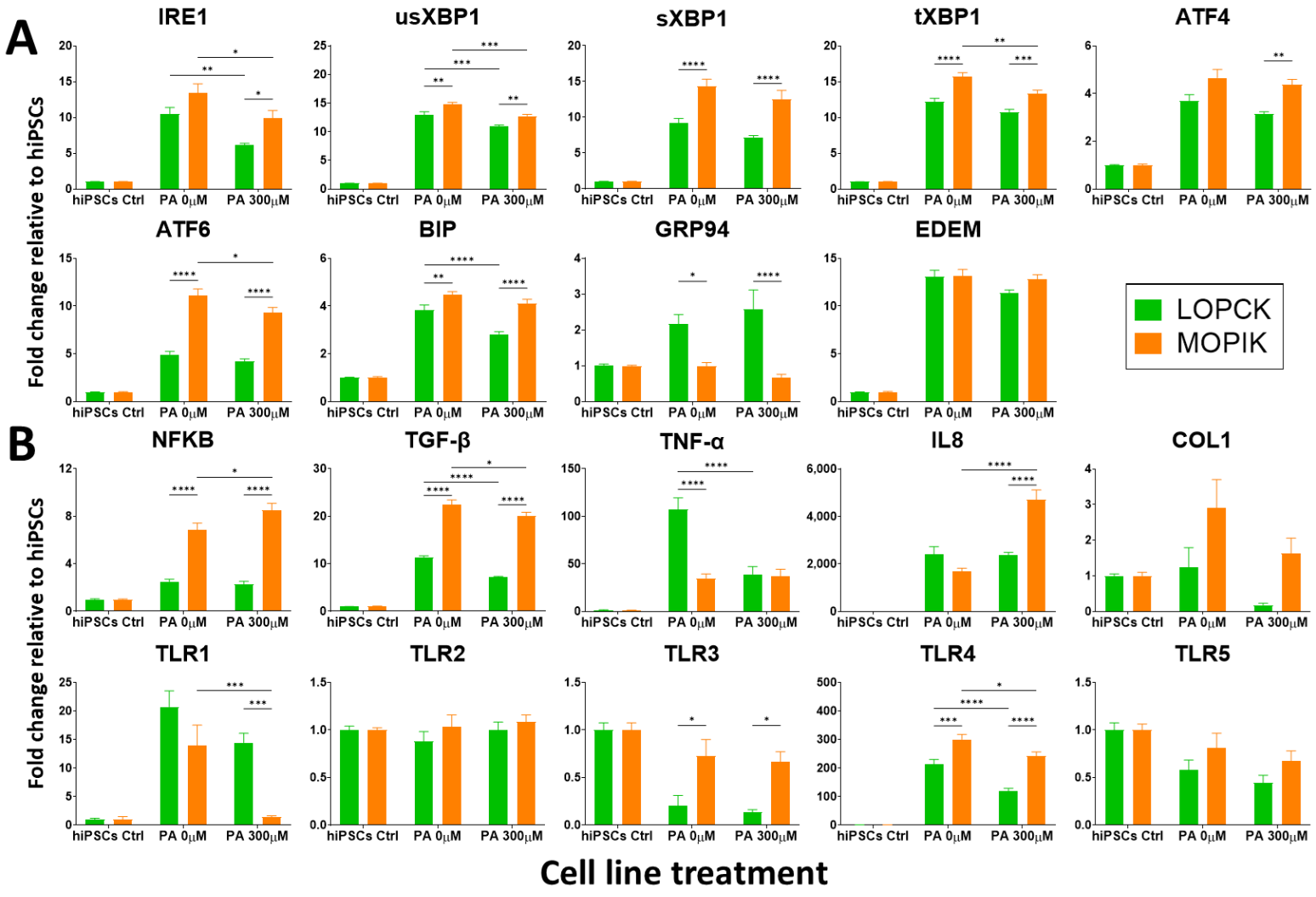


Figure 5.10 MOPIK (MTTP$^{VAR/VAR}$) HLCs show a relatively higher degree of inflammatory gene upregulation and activated unfolded protein response (UPR). (A) Transcript profile of gene regulatory network formed by UPR genes, including inositol-requiring 1 (*IRE1*), activating transcription factor 6 (*ATF6*), binding immunoglobulin protein (*BIP*), X-box binding protein 1 (*XBP1*; unspliced fom, u; spliced, s; total, t), ATF4, glucose-regulated protein 94 (*GRP94*) and ER degradation-enhancing mannosidase-like protein (EDEM). **(B)** LOPCK- and MOPIK-HLCs are treated without or without PA (300 μM) and harvested at maturation day 10 (M10) for qPCR analysis. Expression of inflammatory genes including Nuclear factor-κB (*NFκB*); transforming growth factor beta (*TGF-β*); tumour necrosis factor alpha or (*TNF-α*); interleukin 8 (*IL8*); toll like receptor 1 to 5 (*TLR1-5*) and fibrotic gene collagen type I alpha 1 (*COL1*). Statistical significance: *P ⩽ 0.05, **P ⩽ 0.01, ***P ⩽ 0.001, ****P ⩽ 0.0001.

Increased cellular and mitochondrial ROS production in MOPIK (MTTP$^{VAR/VAR}$)-HLCs

We found that UPR and pro-inflammatory related genes were upregulated in diseased MOPIK-HLCs based on qPCR results. To validate whether NFκB signalling pathway was activated due to UPR-mediated ROS production, we performed live staining using CellROX (**Figure 5.11A**) and MitoSOX (**Figure 5.11B**) to identify any cellular and mitochondrial ROS generation, MitoTracker was also used to help identify where mitochondria were within the cells. We observed a much higher autofluorescence signal from the MitoTracker Green dye compared to MitoTracker Red. It should be noted that MitoTracker dyes are rather expensive and have a limited shelf life. Due to that reason the MitoTracker Green dye stock solution was opened several times and the signal might have weakened overtime, leading to the presence of non-specific signals as seen in **Figure 5.11B**. Fresh MitoTracker Red dye was used, it was stained well and clear in comparison (**Figure 5.11A**).

We noticed that CellROX dye was mainly deposited within the cytoplasm in PA-treated LOPCK-HLCs (**Figure 5.11A**, blue arrows). However, with the use of Hoechst to counterstain the nuclei, we noticed that CellROX were also localised at the nuclear level within untreated LOPCK-HLCs and PA-treated MOPIK-HLCs, this condition was most severe in untreated MOPIK-HLCs where almost all the nuclei were infiltrated with CellROX (**Figure 5.11A**, pink arrows), demonstrating a higher level of ROS production in MOPIK-HLCs inherently even without the addition of PA. Quantification of CellROX (**Figure 5.11C**) also showed that mean fluorescence intensity was at the highest in untreated MOPIK-HLCs compared to all other conditions. Strikingly, we detected relatively a lot more MitoSOX within MOPIK-HLCs than LOPCK-HLCs overall (**Figure 5.11B**), notwithstanding, MitoSOX superoxide production was also at the most in untreated MOPIK-HLCs based on fluorescence quantification data (**Figure 5.11D**). Consistent with the qPCR results, increased ROS production may be caused by the UPR activation in diseased cell line.

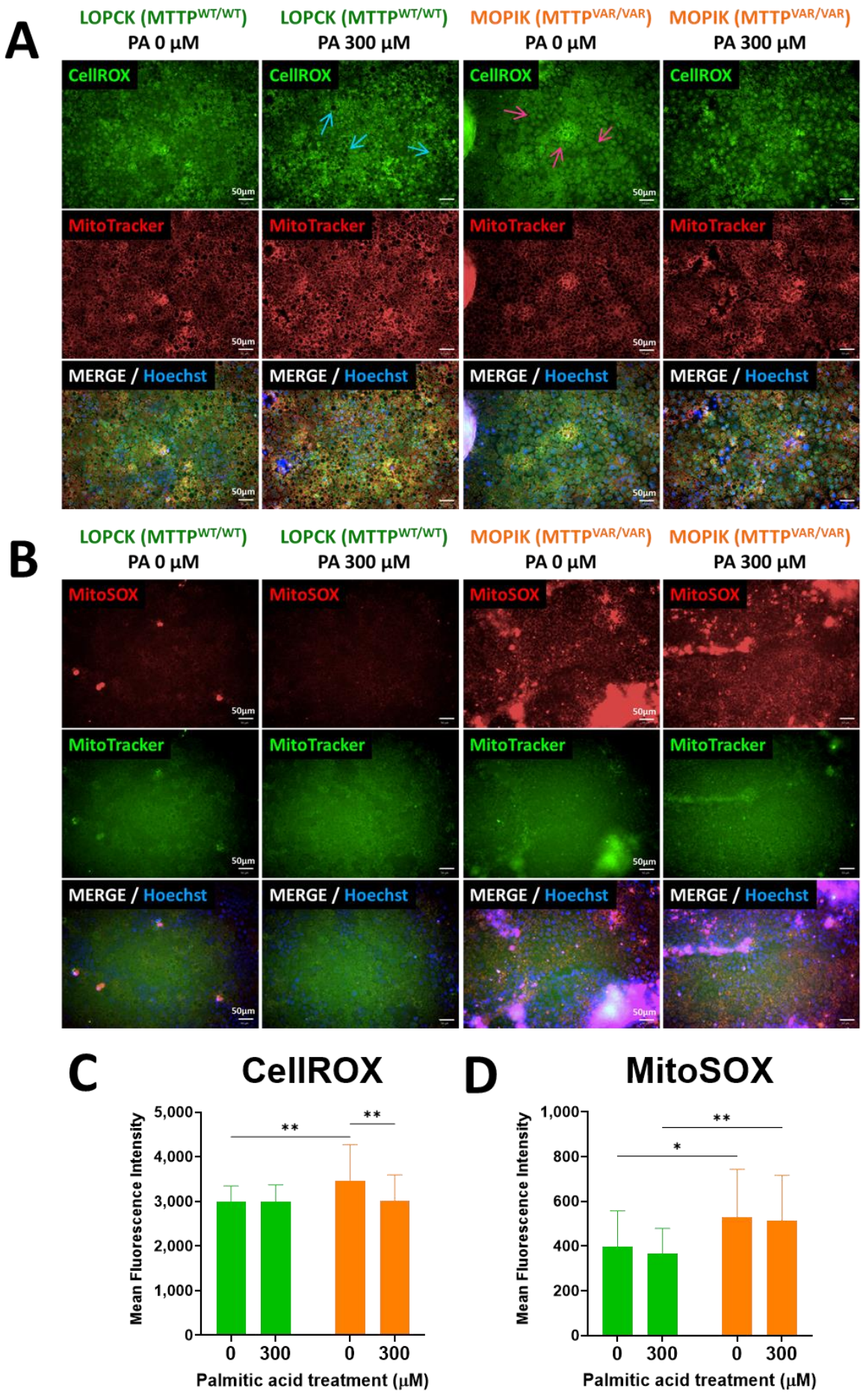

A
LOPCK (MTTP WT/WT) PA 0 µM
LOPCK (MTTP WT/WT) PA 300 µM
MOPIK (MTTP VAR/VAR) PA 0 µM
MOPIK (MTTP VAR/VAR) PA 300 µM
CellROX
MitoTracker
MERGE / Hoechst
50µm
B
MitoSOX
MitoTracker
MERGE / Hoechst
C
CellROX
Mean Fluorescence Intensity
5,000
4,000
3,000
2,000
1,000
0
**
**
0
300
0
300
Palmitic acid treatment (µM)
D
MitoSOX
Mean Fluorescence Intensity
1,000
800
600
400
200
0
**
*
0
300
0
300
Palmitic acid treatment (µM)

Figure 5.11 MOPIK (*MTTP*$^{VAR/VAR}$) HLCs display signs of cellular and mitochondrial oxidative stress. (above) Live cell staining is performed on LOPCK and MOPIK HLCs at maturation day 10 (M10, equivalent to differentiation D19) using **(A)** CellROX and **(B)** MitoSOX reagents to detect reactive oxygen species (ROS) in cells or superoxide in mitochondria. Blue arrows indicates nuclei that do not have CellROX, pink arrows indicate nuclei that have CellROX localisation. HLCs are double stained with MitoTracker in either deep red or green colour, counterstained with Hoeschst 33342 solution for nuclei staining. Fluorescence intensity is quantified for **(C)** CellROX green and (D) MitoSOX red with or without 48-hour PA treatment. Statistical significance: * p<0.05; ** p<0.01; ***p<0.005; ****p<0.0001.

Altered mitochondrial respiration in MOPIK (MTTP$^{VAR/VAR}$)-HLCs

Mitochondria are highly dynamic organelles involved in the regulation of cellular metabolism, redox regulation, and apoptosis in all tissues; its most prominent role is to produce adenosine triphosphate (ATP) through respiration as a source of energy for cells. Mitochondria in the liver play a critical role in the development and pathogenesis of steatosis and NAFLD; hepatic mitochondrial dysfunction may impair fatty acid β-oxidation resulting in the accumulation of FFA in the liver. To explore how the *MTTP*-p.I564T affects mitochondrial metabolic activity, we interrogate mitochondrial functions of hiPSC derived-HLCs (with or without 48-h PA treatment) by measuring oxidative phosphorylation (OXPHOS) using the Seahorse Extracellular Flux (XF) analyser (MitoStress assay).

As shown in the schematic in **Figure 5.12A**, this platform measures real-time oxygen consumption rates (OCR) of live cells at intervals of approximately 5-8 minutes. The protocol involves 3 serial injections of oligomycin (an ATP synthase inhibitor), FCCP (a protonophore that uncouples ATP synthesis from oxygen consumption), and rotenone (a Complex I inhibitor) (**Figure 5.12B**). OCR is measured prior to the addition of drugs, which states the basal respiration (**Figure 5.13A**) and then following the addition of the indicated drugs to provide measurements including maximal respiration (**Figure 5.13B**); proton (H^+) leak (**Figure 5.13C**); ATP production-coupled respiration (**Figure 5.13D**); spare respiratory capacity with percentage (**Figure 5.13E, F**); non-mitochondrial respiration (**Figure 5.13G**) and coupling efficiency (**Figure 5.13H**).

MOPIK-HLCs showed an overall increase of OCR rate compared to LOPCK-HLCs (**Figure 5.12B**), they also had higher demand of mitochondrial respiration based on significantly higher basal (**Figure 5.13A**), maximum respiration rates (**Figure 5.13B**) and ATP production rate (**Figure 5.13D**). Both LOPCK and MOPIK cell lines had relatively lower proton leak in untreated conditions compared to that of PA treatment (**Figure 5.13C**), higher rates of proton leaks in PA-treated cells depicts a disproportionate increase in oxygen consumption at high protonmotive force. This may imply that cells had an incomplete coupling of substrate oxygen to generate ATP and other metabolites as a result of processing excess lipid influx.

This is also reflected on spare capacity measurements, PA-treated cells had relatively lower spare capacity; meaning the amount of extra ATP that can be produced by oxidative phosphorylation in case of a sudden increase in energy demand were reduced (**Figure 5.13E**). The spare capacity percentage (%) is calculated as the maximal respiration divided by the basal respiration rate times 100, untreated MOPIK-HLCs had noticeably low percentage even though its ATP production rate was high, illustrated that the capability of cells respond to an energetic demand (cell fitness) is relatively low (**Figure 5.13F**). This also showed in the relatively higher rates of non-mitochondrial respiration in diseased cell line (**Figure 5.13G**). Both untreated LOPCK- and MOPIK-HLCs had significantly higher coupling efficiency, indicating that large proportions of the oxygen consumed were used to drive ATP synthesis compared with that driving proton leak; HLCs worked relatively more efficient without any PA treatment overall.

An important observation we noticed is that diseased MOPIK ($MTTP^{VAR/VAR}$) cell line had relatively higher metabolic rates compared to the healthy LOPCK ($MTTP^{WT/WT}$) in general, however, both cell lines had decreased mitochondrial respiration rates after the exposure of PA overall. This suggested that diseased cell line with the *MTTP*-p.I564T genetic variant would have higher mitochondrial activity intrinsically for lipid degradation via β-oxidation, notwithstanding PA-induced steatosis is associated with

compromising mitochondrial respiration or dysfunction extrinsically regardless of the cell line genotype.

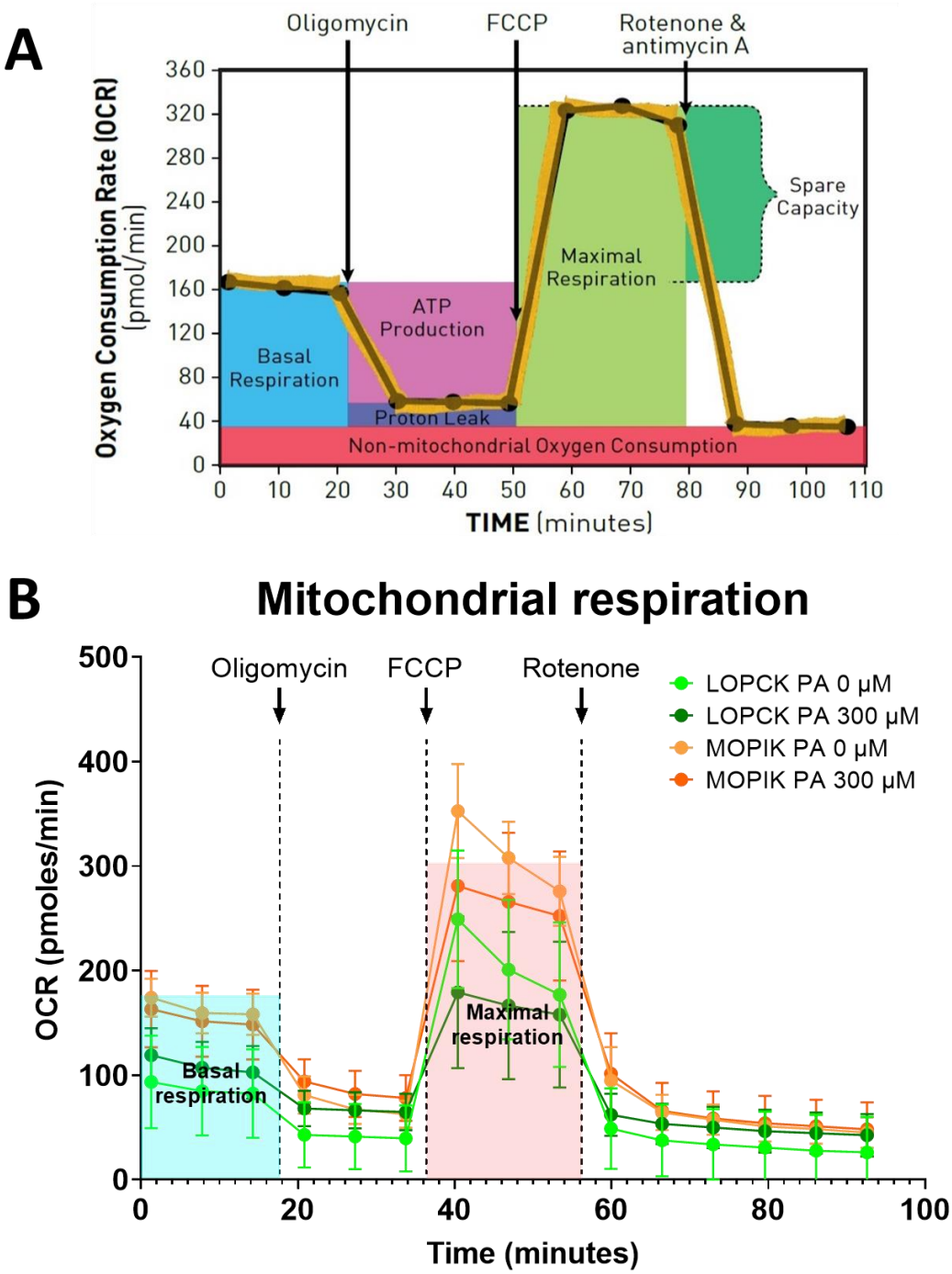
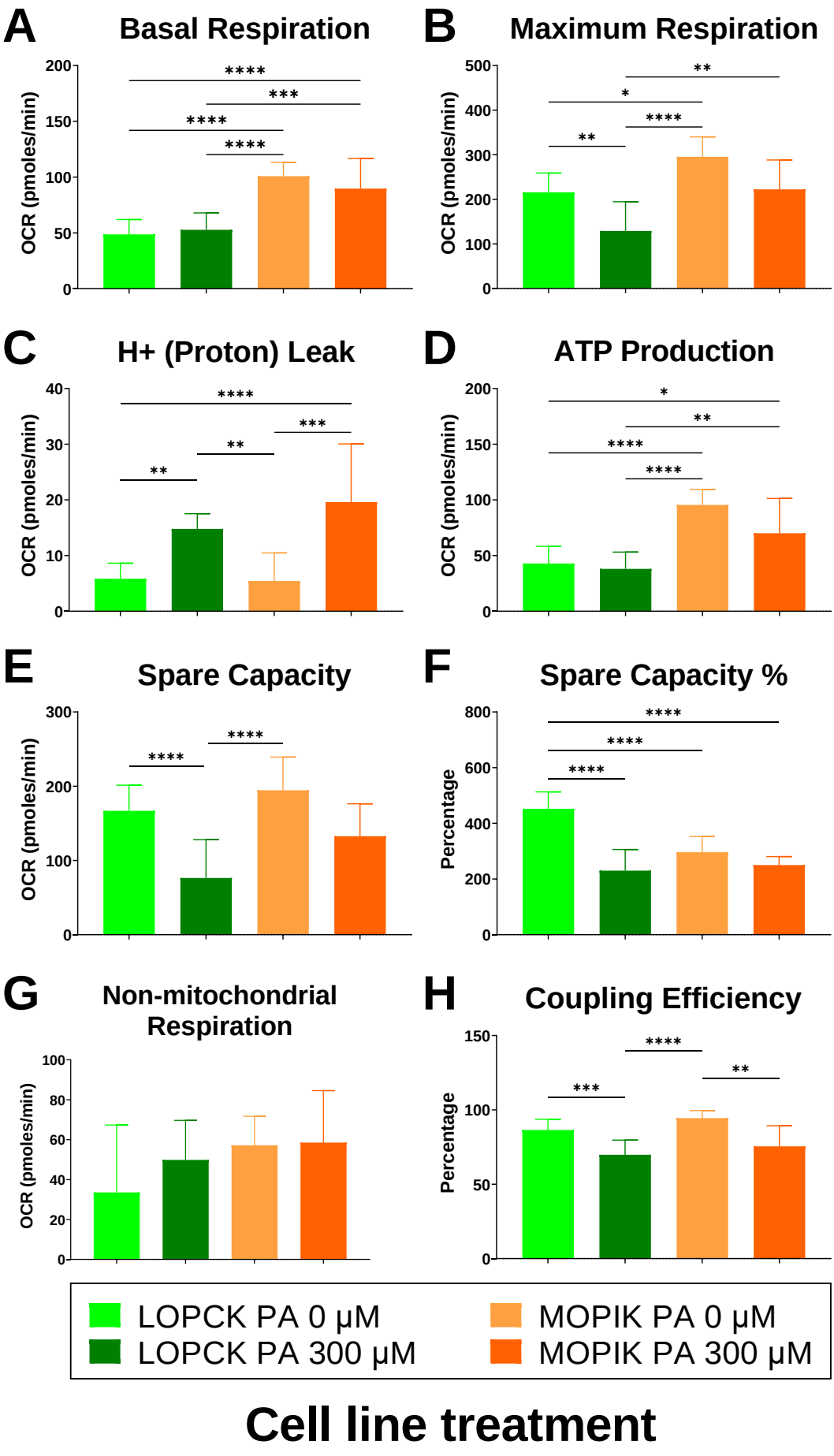


Figure 5.12 Functional analysis of mitochondrial respiration in LOPCK (*MTTP*$^{WT/WT}$)- and MOPIK (*MTTP*$^{VAR/VAR}$)-HLCs using the Seahorse platform. (above) **(A)** Test profile of the key parameters of mitochondrial respiration. Sequential compound injections enable measurement of oxygen consumption rate (OCR) in basal respiration, ATP production, proton leak, maximal respiration, spare respiratory capacity, and non-mitochondrial respiration (adapted from manufacturers' user guide). **(B)** Mitochondrial respiration profile of LOPCK- and MOPIK-HLCs with or without palmitic acid treatment at maturation day 10 (M10,

equivalent to differentiation D19). MOPIK-HLCs showed increased basal respiration and maximal respiration rates in both untreated and PA-treated conditions compared to LOPCK-HLCs. *P ⩽ 0.05, **P ⩽ 0.01, ***P ⩽ 0.001, ****P ⩽ 0.0001 of the corresponding parameters compared to LOPCK-HLCs PA untreated control; mean ± SD, n=12. One-way ANOVA/ Dunnett was used for statistical analysis.

Figure 5.13 Mitochondrial respiration parameters of LOPCK- and MOPIK-HLCs in untreated and PA-treated conditions, measured using the Seahorse platform. (below) MOPIK-HLCs show significant differences in both **(A)** basal respiration and **(B)** maximal respiration rates compared to LOPCK-HLCs overall. Calculations of **(C)** proton (H^+) leakage; **(D)** ATP production rates; **(E)** spare capacity; **(F)** spare capacity percentage; **(G)** non-mitochondrial respiration rates and **(H)** coupling efficiency are done based on the Seahorse MitoStress measurements. Statistical significance: *P ⩽ 0.05, **P ⩽ 0.01, ***P ⩽ 0.001, ****P ⩽ 0.0001; mean ± SD, n=12. One--way ANOVA with Turkey's post hoc test is used for statistical analysis.


A
Basal Respiration
OCR (pmoles/min)
B
Maximum Respiration
OCR (pmoles/min)
C
H+ (Proton) Leak
OCR (pmoles/min)
D
ATP Production
OCR (pmoles/min)
E
Spare Capacity
OCR (pmoles/min)
F
Spare Capacity %
Percentage
G
Non-mitochondrial Respiration
OCR (pmoles/min)
H
Coupling Efficiency
Percentage
LOPCK PA 0 µM
LOPCK PA 300 µM
MOPIK PA 0 µM
MOPIK PA 300 µM
Cell line treatment

Transcriptomic profiling of healthy and disease cell lines in response to lipid challenge

To obtain a more global and comprehensive transcriptomic profile of the hiPSC-derived HLCs under different PA conditions, mRNA sequencing was performed to identify differentially expressed genes, REBLPAT hiPSCs were used as reference sample set for comparison. Multi-dimensional principal component analysis (PCA) and t-distributed stochastic neighbour embedding (t-SNE) were applied to evaluate the overall relatedness of the different sample sets (**Figure 5.14A-D**). Scree plot demonstrated that most of the variability came from PC1 (**Figure 5.14A, B**), separating the REBLPAT hiPSC sample set from the rest; LOPCK and MOPIK samples were separated in PC2 (**Figure 5.14C**). Samples were clustered into three major groups altogether into hiPSC, healthy LOPCK samples and disease MOPIK samples

Pairwise comparison of untreated vs PA-treated within each cell line (Effects of PA on cells)

We then performed DESeq2 differential gene expression analysis to examine gene profiles between untreated and PA-treated conditions, statistic filter was placed to only select genes with statistical significance below 0.05 after Benjamini and Hochberg correction, 1603 genes (LOPCK) and 684 genes (MOPIK) were identified. An intensity difference filter was also set to stringently select genes with highly significant differences, results were shown as log2.

Total 192 differentially expressed genes were found in LOPCKs, 132 genes were upregulated, 60 downregulated (**Figure 5.15A**); 65 differentially expressed genes were selected in MOPIK-HLCs, with 48 upregulated and 17 downregulated (**Figure 5.15B**). We identified 6 upregulated genes and 7 downregulated genes that were overlapping between the two cell lines (**Figure 5.15C**), list of overlapping genes and their functions from the UniProt database were presented in **Table 5.1** (upregulated) and **Table 5.2** (downregulated).

To validate the cell type for the differentiated cells, a stringent filter of Shrunk log 2 fold change above 2 was added so that only genes that had increased expression during differentiation were used for gene set enrichment. Based on EnrichR comparison to the Human Cell Atlas reference, from the ARCHS4 dataset we found that the gene hit lists for LOPCK (**Figure 5.15C**) and MOPIK (**Figure 5.15D**) were both highly matching with genes that are related to liver tissue and hepatocyte; these results affirmed that our differentiated cells were indeed belong to the hepatocyte lineage.

Noticeably, genes that could stimulate lipid breakdown via ketogenesis (*HMGCS2*) and increased lipid binding and transport (*FABP1*) were upregulated; *CIDEC* upregulation could also restrict lipolysis and favouring storage of lipid droplets simultaneously (**Table 5.1**). *SOCS3* and *HAMP* upregulation could be related to inflammation; in hepatocytes, pro-inflammatory cytokine IL6 can activate JAK1/STAT3 signalling, which can then induce the negative feedback regulator *SOCS3* and expression of hepatic acute phase protein (APP, plasma proteins synthesized in the liver whose concentrations changed by 25% or more during inflammation) genes such as *HAMP* [310].

PPP1R14A encodes for the protein phosphatase 1 regulatory subunit 14A (a.k.a. CPI-17), which has an important role in the regulation of blood-glucose levels in the liver and glycogen metabolism, muscle contractility. CPI17 phosphorylation often occurs in response to agonist stimulation through activation of protein kinase C (PKC), Rho-associated protein kinase (ROCK) and integrin-linked kinase (ILK) [311]. **Table 5.2** listed the overlapping downregulated genes found in both cell lines. Reduction was found in genes that encoded for prostaglandin biosynthesis (*PTGS1*) to compensate for the influx of PA, interestingly, structural protein collagen (*COL7A1, COL1A2*) gene expressions were also downregulated. Functionally, genes related to phase I drug metabolising enzyme *CYP1A1;* activator of various lysosomal lipid degradation enzyme (*PSAPL1*); actin organisation protein (*FHOD3*) and neural axon guidance (*SEMA6B*) were reduced in response to the addition of PA.

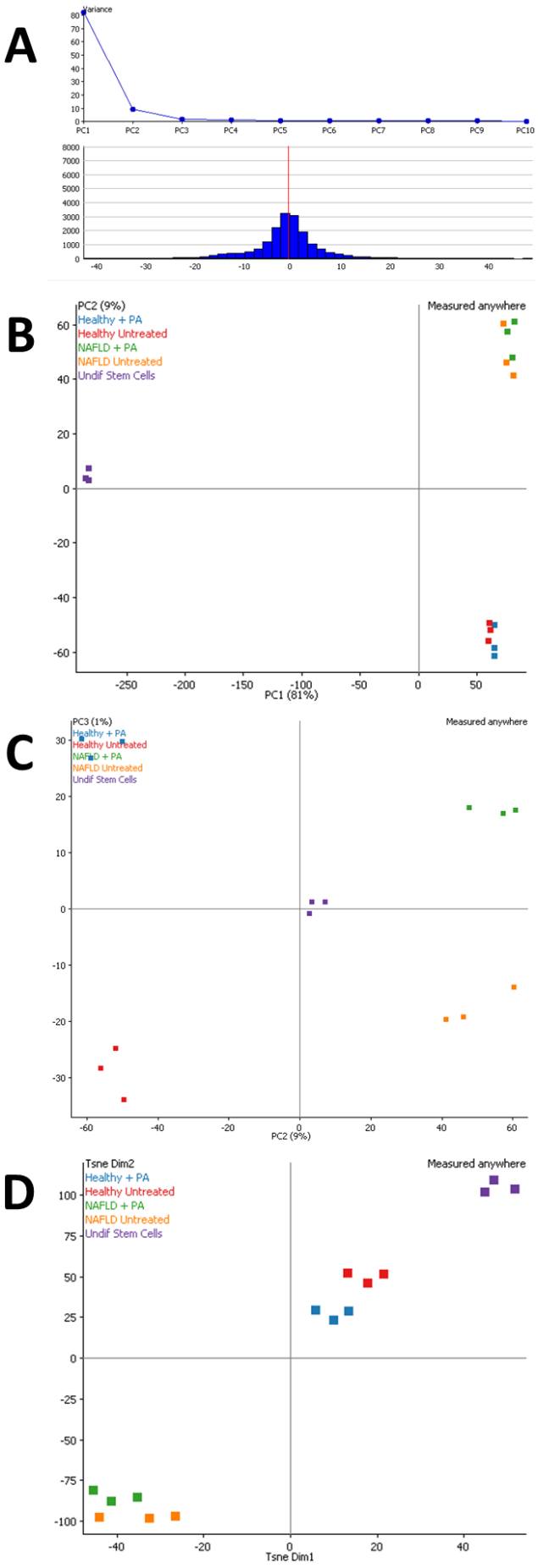
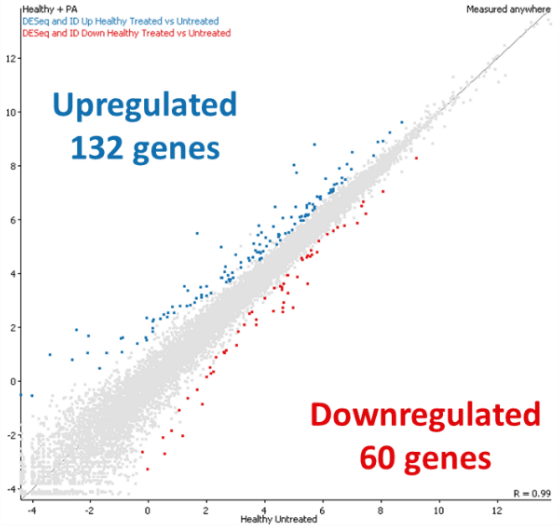


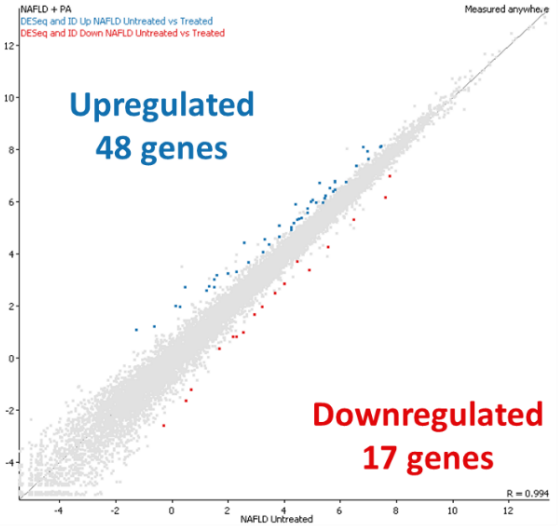
Figure 5.14 Multi-dimensional principal component analysis (PCA) and t-SNE analyses of differentially expressed genes similarities between sample sets. (left) **(A)** Scree plot representing the number of factors retained in principal components. Most of the variability comes from PC1, separating the hiPSC sample set from the rest. There is reasonable amount of difference in PC2, separating LOPCK samples from MOPIK-HLCs. Overall relatedness of the different samples is illustrated as PCA plots, **(B)** PC1/2 and **(C)** PC2/3 classes of variance between undifferentiated REBLPAT hiPSCs, M10 LOPCK- and MOPIK-HLCs treated with or without 48-hour PA. **(D)** t-SNE is analysed to explore high-dimensional data showing the samples categorised in different clusters.

Figure 5.15 Pairwise comparison of untreated and PA-treated HLCs derived from LOPCK ($MTTP^{WT/WT}$) and MOPIK ($MTTP^{VAR/VAR}$) cell lines. (below) The overall gene expression pattern differences between **(A)** LOPCK-HLCs and **(B)** MOPIK-HLCs in untreated and PA-treated conditions, dots indicate the upregulated (blue) and downregulated (red) genes that has minimum DESeq p-value below 0.05, in addition with a Log2 fold change above and below 0. **(C)** Summary table of the differentially expressed gene hits which overlap in both cell lines, 6 upregulated and 7 downregulated genes between the two sample sets match. The cell types of differentiated **(D)** LOPCK and **(E)** MOPIK cell lines are determined based on the upregulated genes using a stringent filter, where Shrunk Log2 fold change value is above 2.0 relative to undifferentiated hiPSCs.

A LOPCK (MTTP$^{WT/WT}$)-HLCs
Untreated vs PA 300 µM



B MOPIK (MTTP$^{VAR/VAR}$)-HLCs
Untreated vs PA 300 µM



C

	Upregulated LOPCK	Downregulated LOPCK	Upregulated MOPIK	Downregulated MOPIK
Upregulated LOPCK	132	0	6	0
Downregulated LOPCK	0	60	0	7
Upregulated MOPIK	6	0	48	0
Downregulated MOPIK	0	7	0	17

D LOPCK (MTTP$^{WT/WT}$)

Index	Name	P-value	Adjusted p-value	Odds Ratio	Combined score
1	LIVER (BULK TISSUE)	6.662e-163	7.194e-161	2.72	1017.19
2	HEPATOCYTE	3.025e-118	1.633e-116	2.44	661.17
3	SMALL INTESTINE (BULK TISSUE)	1.268e-78	4.564e-77	2.15	385.83
4	GASTRIC EPITHELIAL CELL	9.568e-70	2.583e-68	2.08	330.09
5	ILEUM (BULK)	4.833e-67	1.044e-65	2.05	313.59
6	LUNG (BULK TISSUE)	5.792e-58	1.042e-56	1.97	259.88
7	COLON (BULK TISSUE)	1.893e-53	2.921e-52	1.93	234.18
8	GASTRIC TISSUE (BULK)	4.762e-46	6.428e-45	1.85	193.58
9	OMENTUM	3.685e-39	4.422e-38	1.78	157.60
10	AMNIOTIC FLUID	1.454e-23	1.570e-22	1.59	83.40

E MOPIK (MTTP$^{VAR/VAR}$)

Index	Name	P-value	Adjusted p-value	Odds Ratio	Combined score
1	LIVER (BULK TISSUE)	2.363e-171	2.552e-169	2.74	1075.07
2	HEPATOCYTE	4.413e-123	2.383e-121	2.45	689.05
3	SMALL INTESTINE (BULK TISSUE)	4.644e-82	1.672e-80	2.16	403.60
4	ILEUM (BULK)	4.053e-68	1.094e-66	2.04	316.85
5	LUNG (BULK TISSUE)	1.365e-61	2.948e-60	1.99	278.23
6	GASTRIC EPITHELIAL CELL	1.754e-59	3.158e-58	1.97	266.04
7	COLON (BULK TISSUE)	2.340e-53	3.610e-52	1.91	231.44
8	GASTRIC TISSUE (BULK)	3.668e-47	4.952e-46	1.85	197.74
9	OMENTUM	6.260e-45	7.512e-44	1.83	185.93
10	SKIN (BULK TISSUE)	5.090e-28	5.497e-27	1.63	102.71

Table 5.1 Common differentially expressed genes that are upregulated in both LOPCK- and MOPIK-HLCs.

Probe	Ensembl ID	Gene Description; Corresponding protein	Function (UniProtKB)
HMGCS2	ENSG00000134240	3-Hydroxy-3-Methylglutaryl-Coa Synthase 2; Hydroxymethylglutaryl-CoA synthase, mitochondrial	• Mitochondrial enzyme that catalyses the first irreversible step in ketogenesis, a metabolic pathway that provides lipid-derived energy during the fasting. • Condensing acetyl-CoA to acetoacetyl-CoA to form HMG-CoA, which is converted by HMG-CoA reductase (HMGCR) into mevalonate.
FABP1	ENSG00000163586	Fatty Acid Binding Protein 1; Fatty acid-binding protein (liver)	• Plays a role in lipoprotein-mediated cholesterol uptake in hepatocytes (PubMed:25732850). • Binds cholesterol (PubMed:25732850). • Binds free fatty acids and their coenzyme A derivatives, bilirubin, and some other small molecules in the cytoplasm. May be involved in intracellular lipid transport (By similarity). • Important role in regulating lipid metabolism and cellular signalling pathways.
CIDEC	ENSG00000187288	Cell Death Inducing DFFA Like Effector C; Cell death activator CIDE-3	• Binds to lipid droplets and regulates their enlargement, thereby restricting lipolysis and favouring storage. • Required for unilocular lipid droplet formation and optimal energy storage in human. • CIDEC is a regulator of adipocyte lipid metabolism and may be important for the adipocyte to adapt to changes in energy availability. • Its role in neutral lipid transfer and lipid droplet enlargement is activated by the interaction with PLIN1. • May act as a CEBPB coactivator in the white adipose tissue to control the expression of a subset of CEBPB downstream target genes, including SOCS1, SOCS3, TGFB1, TGFBR1, ID2 and XDH.

SOCS3	ENSG00000184557	Suppressor of Cytokine Signalling 3	• SOCS family proteins form part of a classical negative feedback system that regulates cytokine signal transduction. • A main role of SOCS3 results from its binding to both the JAK kinase and the cytokine receptor, which results in the inhibition of STAT3 activation. • Inhibits cytokine signal transduction by binding to tyrosine kinase receptors including IL6ST/gp130, LIF, erythropoietin, insulin, IL12, GCSF and leptin receptors. • Binding to JAK2 inhibits its kinase activity and regulates IL6 signalling. Suppresses foetal liver erythropoiesis.
HAMP	ENSG00000105697	Hepcidin Antimicrobial Peptide	• The HAMP gene produces hepcidin protein, a liver-produced hormone that constitutes the main circulating regulator of iron absorption and distribution across tissues. • Acts by promoting endocytosis and degradation of ferroportin, leading to the retention of iron in iron-exporting cells and decreased flow of iron into plasma. • Controls the major flows of iron into plasma: absorption of dietary iron in the intestine, recycling of iron by macrophages, which phagocytose old erythrocytes and other cells, and mobilization of stored iron from hepatocytes (PubMed:22306005).
PPP1R14A	ENSG00000167641	Protein Phosphatase 1 Regulatory Inhibitor Subunit 14A	• Inhibitor of PPP1CA (encodes for a smooth muscle myosin phosphatase) • Has over 1000-fold higher inhibitory activity when phosphorylated, creating a molecular switch for regulating the phosphorylation status of PPP1CA substrates and smooth muscle contraction.

Table 5.2 Common differentially expressed genes that are downregulated in both LOPCK- and MOPIK-HLCs.

Probe	ID	Gene Description; Corresponding protein	Function (UniProtKB)
COL7A1	ENSG00000114270	Collagen Type VII Alpha 1 Chain	• Stratified squamous epithelial basement membrane protein that forms anchoring fibrils which may contribute to epithelial basement membrane organization and adherence by interacting with extracellular matrix (ECM) proteins such as type IV collagen.
PSAPL1	ENSG00000178597	Prosaposin Like 1 (Gene/Pseudogene); Proactivator polypeptide-like 1	• This gene encodes a protein that is related to the glycoprotein prosaposin, it is predicted that the encoded protein is a preproprotein that is proteolytically processed to generate multiple protein products. • These predicted products include saposins A-like, B-like, C-like, and D-like, which may play a role in the lysosomal degradation of sphingolipids
COL1A2	ENSG00000164692	Collagen Type I Alpha 2 Chain	• As a structural protein, type I collagen (fibrillar forming collagen) interacts with other matrix proteins including proteoglycans and fibronectin. • Type I collagen signalling to cells through its integrin receptors and other cell surface collagen receptors (CD36), inhibitory leukocyte-associated Ig-like receptor (LAIR)-1 (CD305), Endo180 (CD280), and discoidin domain receptors (DDR1 and DDR2) can regulate cell growth, motility, and differentiation.
PTGS1	ENSG00000095303	Prostaglandin-Endoperoxide Synthase 1; Prostaglandin G/H synthase 1	• Prostaglandin-endoperoxide synthase (PTGS), dual cyclooxygenase (COX) and peroxidase, is the key enzyme in prostaglandin biosynthesis. • In gastric epithelial cells, it is a key step in the generation of prostaglandins, such as prostaglandin E2 (PGE2), which plays an important role in cytoprotection. • In platelets, it is involved in the generation of thromboxane A2 (TXA2), which promotes platelet activation and aggregation, vasoconstriction, and proliferation of vascular smooth muscle cells (Probable).

CYP1A1	ENSG00000140465	Cytochrome P450 Family 1 Subfamily A Member 1	• A cytochrome P450 monooxygenase, involved in the metabolism of various endogenous substrates, including fatty acids, steroid hormones, and vitamins (PubMed:11555828, PubMed:14559847, PubMed:12865317, PubMed:15805301, PubMed:15041462, PubMed:18577768, PubMed:19965576, PubMed:20972997, PubMed:10681376). • It is one the most important xenobiotic-metabolizing enzyme of the placenta for which relevant inducible activity has been demonstrated throughout pregnancy. • Catalyses two successive oxidative transformation of all-trans retinol to all-trans retinal and then to the active form all-trans retinoic acid (PubMed:10681376). • May also participate in eicosanoids metabolism by converting hydroperoxide species into oxo metabolites (lipoxygenase-like reaction, NADPH-independent) (PubMed:21068195).
FHOD3	ENSG00000134775	Formin Homology 2 Domain Containing 3; FH1/FH2 domain-containing protein 3	• Actin-organizing protein that may cause stress fibre formation together with cell elongation (By similarity). • Isoform 4 may play a role in actin filament polymerization in cardiomyocytes.
SEMA6B	ENSG00000167680	Semaphorin-6B	• Semaphorins play a major role in axon guidance. • The protein encoded by this gene may be involved in both peripheral and central nervous system development.

LOPCK vs MOPIK comparison in untreated and PA-treated conditions (Assessment on the influence of MTTP-p.I564T genotypes to cell functionality)

Initial assessment focussed on the effects of PA treatment on cells, in this section we will be focussing on the inherent differences potentially caused by the *MTTP*-p.I564T variation and how that might have altered cellular behaviours and functions. To demonstrate the global patterns, heatmaps of differentially expressed genes with significant differences in untreated (**Figure 5.16A**) and PA-treated (**Figure 5.16B**) conditions between LOPCK and MOPIK cell lines were generated. Three main clusters were identified in untreated condition, hiPSC sample set was evidently different from the HLC samples, nevertheless, both untreated and PA-treated MOPIK-HLCs gene sets had distinctly different patterns compared to those of LOPCK, most were in the opposite expression (**Figure 5.16A**). In PA-treated condition, similar pattern was also found between LOPCK and MOPIK sample sets, however, cluster analysis showed that LOPCK sample sets were relatively closer to hiPSC instead; genes that were downregulated (pink bars) in hiPSC and LOPCK sample sets had increased expression (green bars) in MOPIK-HLCs.

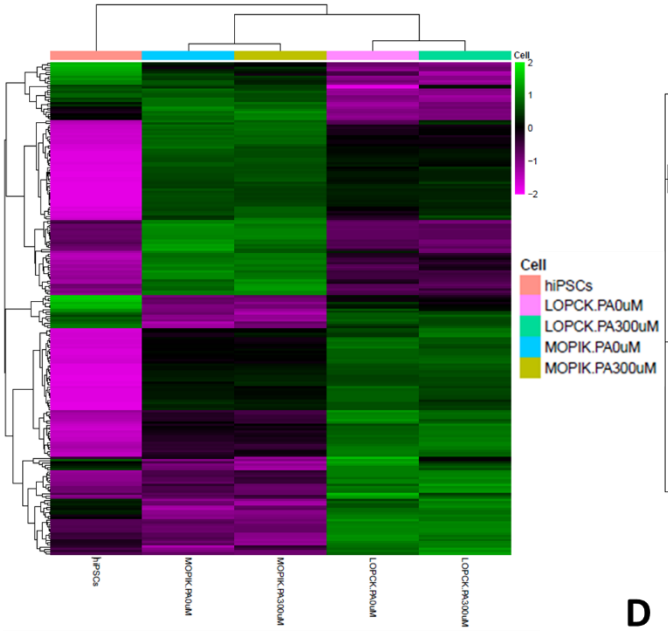
To decipher the pathways related to these gene sets, we utilised Reactome pathway analysis and obtained ReacFoam for a holistic visualisation. **Figure 5.16C** highlighted some of the most relevant pathways in untreated condition were involved in ECM organisation; regulation of insulin-like growth factor (IGF) transport and uptake by IGF binding proteins (IGFBPs); collagen biosynthesis and modifying enzymes; as well as degradation of the ECM. Under PA-treatment, we found that pathways started to change in LOPCK and MOPIK HLCs; most of the genes detected were still involved in ECM organisation and integrin cell surface interactions (**Figure 5.16D**). However, we also detected genes related to the activation of interferon α/β signalling; ER-phagosome pathway; XBP1(S) activates chaperone genes; IRE1α activates chaperones; ECM proteoglycans; regulation of cholesterol biosynthesis by SREBP; and assembly of collagen fibrils and other multimeric structures.

We have cross-validated gene ontology (GO) enrichment of the differentially expressed genes using ToppGene Suite for a more detailed report, **Figure 5.17** demonstrated hierarchy analysis of GO terms related to specific properties, including "Molecular function"; "Biological process"; "Cellular component" and "Pathway". GO terms of the differentially expressed gene sets in untreated (**Figure 5.17A**) and PA-treated (**Figure 5.17B**) conditions between LOPCK and MOPIK cell lines were coherent to Reactome results. Untreated HLCs were expressing a lot of genes related to the regulation of lipid metabolism and enzymatic activity for lipid catabolic processes; whereas after PA addition there were more gene upregulation involved in ECM remodelling and wound healing.

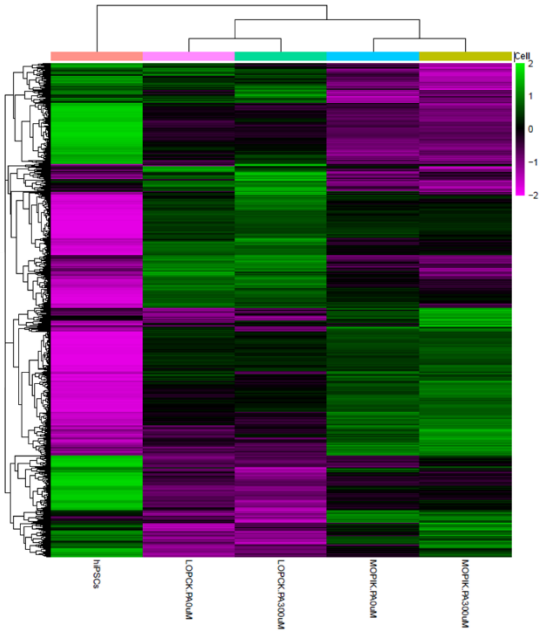
In summary, transcriptomics data revealed that there is a demand of genes related to lipolysis and lipid transport as seen with the upregulation of those genes in both LOPCK and MOPIK-HLCs after PA treatment. Upregulation of inflammatory and collagen biosynthesis related genes were also detected, suggesting that inflammation and extracellular matrix organisation may be activated due to lipotoxity.

Figure 5.16 Differentially expressed gene profiles between LOPCK (*MTTP*$^{WT/WT}$)- and MOPIK (*MTTP*$^{VAR/VAR}$)-HLCs in 48-hour untreated and PA-treated conditions at maturation day 10 (M10, equivalent to differentiation D19). (below) Differentially expressed genes are analysed by DESeq2 analysis. Heatmap of overall gene profiles between LOPCK- and MOPIK-HLCs in **(A)** PA-untreated and **(B)** with 300 µM PA treatment. Heatmap is shown as log2 fold change between sample sets. Differentially expressed gene hit outputs are analysed using web-based Reactome analysis tool, result is illustrated as a ReacFoam to present the pathways involved between LOPCK- and MOPIK-HLCs in **(C)** PA-untreated and **(D)** with 300 µM PA treatment.

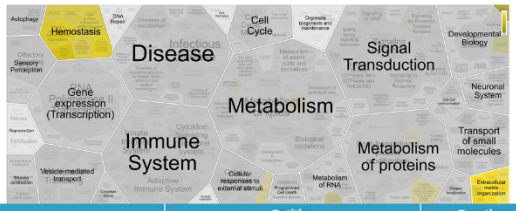
A **Differentially expressed genes in Untreated LOPCK- and MOPIK-HLCs**



B **Differentially expressed genes in PA-treated LOPCK- and MOPIK-HLCs**

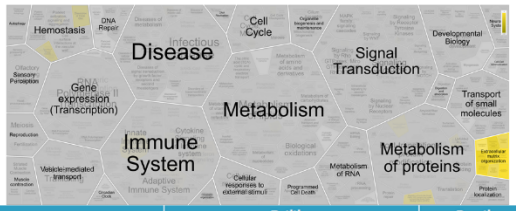


C



Pathway name	Entities				Reactions	
	found	ratio	p-value	FDR*	found	ratio
Regulation of Insulin-like Growth Factor (IGF) transport and uptake by Insulin-like Growth Factor Binding Proteins (IGFBPs)	15 / 127	0.009	5.25e-07	1.71e-04	14 / 14	0.001
Extracellular matrix organization	15 / 329	0.023	1.39e-05	0.004	119 / 319	0.024
Post-translational protein phosphorylation	9 / 109	0.008	1.10e-04	0.019	1 / 1	7.45e-05
Metallothioneins bind metals	4 / 16	0.001	1.69e-04	0.022	9 / 27	0.002
Response to metal ions	4 / 21	0.001	4.71e-04	0.049	9 / 31	0.002
Collagen formation	7 / 104	0.007	0.002	0.139	43 / 77	0.006
MET activates PTK2 signaling	4 / 32	0.002	0.002	0.139	1 / 5	3.72e-04
ECM proteoglycans	6 / 79	0.005	0.002	0.139	11 / 23	0.002
Platelet degranulation	5 / 137	0.009	0.002	0.139	3 / 11	8.19e-04
Response to elevated platelet cytosolic Ca2+	5 / 144	0.01	0.003	0.167	3 / 14	0.001
Integrin cell surface interactions	6 / 86	0.006	0.004	0.167	20 / 55	0.004
Degradation of the extracellular matrix	5 / 148	0.01	0.004	0.167	20 / 105	0.008
Defective B3GALTL causes Peters-plus syndrome (PpS)	4 / 89	0.005	0.004	0.174	1 / 1	7.45e-05
Activation of NOXA and translocation to mitochondria	2 / 6	4.13e-04	0.005	0.174	5 / 5	3.72e-04
O-glycosylation of TSR domain-containing proteins	4 / 41	0.003	0.005	0.185	2 / 2	1.49e-04
Assembly of collagen fibrils and other multimeric structures	5 / 67	0.005	0.006	0.189	18 / 26	0.002
Activation of C3 and C5	2 / 7	4.82e-04	0.006	0.195	3 / 3	2.23e-04
Collagen chain trimerization	4 / 44	0.003	0.007	0.195	5 / 28	0.002
MET promotes cell motility	4 / 45	0.003	0.007	0.196	1 / 12	8.94e-04
Common Pathway of Fibrin Clot Formation	3 / 25	0.002	0.009	0.231	14 / 29	0.002
Collagen biosynthesis and modifying enzymes	5 / 76	0.005	0.01	0.239	25 / 51	0.004
PPARA activates gene expression	5 / 175	0.012	0.01	0.239	4 / 41	0.003
Regulation of lipid metabolism by PPARalpha	5 / 177	0.012	0.011	0.244	5 / 44	0.003
Syndecan interactions	3 / 29	0.002	0.013	0.29	3 / 15	0.001

D



Pathway name	Entities				Reactions	
	found	ratio	p-value	FDR*	found	ratio
Endosomal/Vacuolar pathway	5 / 62	0.006	8.73e-07	0.002	4 / 4	2.98e-04
Antigen Presentation: Folding, assembly and peptide loading of class I MHC	11 / 102	0.007	3.88e-06	0.004	14 / 16	0.001
Interferon alpha/beta signaling	58 / 188	0.013	1.05e-04	0.061	20 / 22	0.002
Extracellular matrix organization	90 / 329	0.023	1.22e-04	0.061	256 / 319	0.024
Syndecan interactions	14 / 29	0.002	0.001	0.364	14 / 15	0.001
Polo-like kinase mediated events	12 / 23	0.002	0.001	0.364	15 / 15	0.001
Regulation of Insulin-like Growth Factor (IGF) transport and uptake by Insulin-like Growth Factor Binding Proteins (IGFBPs)	39 / 127	0.009	0.001	0.364	14 / 14	0.001
Integrin cell surface interactions	29 / 86	0.006	0.001	0.364	49 / 55	0.004
Platelet degranulation	41 / 137	0.009	0.002	0.364	5 / 11	8.19e-04
ER-Phagosome pathway	49 / 178	0.012	0.002	0.364	5 / 10	7.45e-04
TP53 Regulates Transcription of Death Receptors and Ligands	10 / 18	0.001	0.002	0.364	7 / 7	5.21e-04
Response to elevated platelet cytosolic Ca2+	42 / 144	0.01	0.002	0.399	11 / 14	0.001
XBP1(S) activates chaperone genes	30 / 95	0.007	0.003	0.484	15 / 47	0.004
Post-translational protein phosphorylation	33 / 109	0.008	0.004	0.506	1 / 1	7.45e-05
NGF-stimulated transcription	20 / 56	0.004	0.004	0.506	30 / 37	0.003
IRE1alpha activates chaperones	31 / 101	0.007	0.004	0.506	16 / 53	0.004
Antigen processing-Cross presentation	52 / 195	0.013	0.005	0.566	15 / 23	0.002
ECM proteoglycans	25 / 79	0.005	0.006	0.709	22 / 23	0.002
Common Pathway of Fibrin Clot Formation	11 / 25	0.002	0.007	0.728	27 / 29	0.002
Non-integrin membrane-ECM interactions	20 / 61	0.004	0.01	0.849	21 / 22	0.002
Regulation of cholesterol biosynthesis by SREBP (SREBF)	26 / 87	0.006	0.011	0.849	26 / 52	0.004
Neutrophil degranulation	109 / 480	0.033	0.011	0.849	10 / 10	7.45e-04
Assembly of collagen fibrils and other multimeric structures	21 / 67	0.005	0.013	0.849	24 / 26	0.002

A

GO: Molecular Function			
ID	Name	p-value	q-value Bonferroni
GO:0005201	extracellular matrix structural constituent	1.03E-07	7.32E-05
GO:0004175	endopeptidase activity	3.72E-07	2.64E-04
GO:0008233	peptidase activity	9.43E-07	6.69E-04
GO:0008237	metallopeptidase activity	3.82E-05	2.71E-02
GO:0004222	metalloendopeptidase activity	4.14E-05	2.94E-02
GO:0002020	protease binding	6.57E-05	4.66E-02
GO:0005539	glycosaminoglycan binding	1.01E-04	7.17E-02
GO:0004866	endopeptidase inhibitor activity	2.38E-04	1.69E-01
GO:0060230	lipoprotein lipase activator activity	2.54E-04	1.80E-01
GO:0061134	peptidase regulator activity	2.54E-04	1.80E-01

GO: Biological Process			
ID	Name	p-value	q-value Bonferroni
GO:0019216	regulation of lipid metabolic process	4.12E-08	1.66E-04
GO:0050996	positive regulation of lipid catabolic process	1.70E-07	6.86E-04
GO:0042060	wound healing	2.37E-07	9.52E-04
GO:0009887	animal organ morphogenesis	2.91E-07	1.17E-03
GO:0061687	detoxification of inorganic compound	3.41E-07	1.37E-03
GO:0006954	inflammatory response	3.48E-07	1.40E-03
GO:0001501	skeletal system development	4.02E-07	1.62E-03
GO:0006629	lipid metabolic process	4.42E-07	1.78E-03
GO:0046903	secretion	4.55E-07	1.83E-03
GO:0098754	detoxification	7.90E-07	3.18E-03

GO: Cellular Component			
ID	Name	p-value	q-value Bonferroni
GO:0062023	collagen-containing extracellular matrix	2.69E-16	1.08E-13
GO:0031012	extracellular matrix	3.06E-16	1.23E-13
GO:0031091	platelet alpha granule	1.72E-06	6.89E-04
GO:0005903	brush border	4.02E-06	1.61E-03
GO:0045177	apical part of cell	4.65E-06	1.86E-03
GO:0005788	endoplasmic reticulum lumen	4.94E-06	1.98E-03
GO:0098862	cluster of actin-based cell projections	1.32E-05	5.31E-03
GO:0072562	blood microparticle	5.42E-05	2.17E-02
GO:0005902	microvillus	1.36E-04	5.47E-02
GO:0031093	platelet alpha granule lumen	3.33E-04	1.34E-01

Pathway			
ID	Name	p-value	q-value Bonferroni
M5889	Ensemble of genes encoding extracellula	6.50E-11	6.36E-08
M3468	Genes encoding enzymes and their regula	1.56E-08	1.52E-05
M5884	Ensemble of genes encoding core extrac	6.80E-07	6.66E-04
1268755	Regulation of Insulin-like Growth Factor	3.42E-06	3.35E-03
1339158	Metallothioneins bind metals	5.36E-06	5.25E-03
1339157	Response to metal ions	5.36E-06	5.25E-03
1270244	Extracellular matrix organization	9.24E-06	9.05E-03
M5885	Ensemble of genes encoding ECM-associ	1.68E-05	1.64E-02
1269367	Platelet degranulation	1.47E-04	1.44E-01
83042	PPAR signaling pathway	1.82E-04	1.78E-01
1269365	Response to elevated platelet cytosolic C	1.91E-04	1.87E-01
212237	Mineral absorption	2.99E-04	2.92E-01
PW:0000238	insulin-like growth factor signaling	3.11E-04	3.04E-01
1269340	Hemostasis	4.29E-04	4.20E-01
M3008	Genes encoding structural ECM glycopro	4.59E-04	4.49E-01
1270256	ECM proteoglycans	5.03E-04	4.93E-01
169349	Validated transcriptional targets of AP1 f	6.13E-04	6.00E-01
1270088	Synthesis of Prostaglandins (PG) and Thro	6.26E-04	6.13E-01
1270245	Collagen formation	7.28E-04	7.13E-01
1457776	Miscellaneous digestion events	7.88E-04	7.72E-01

B

GO: Molecular Function			
ID	Name	p-value	q-value Bonferroni
GO:0050839	cell adhesion molecule binding	5.48E-16	1.21E-12
GO:0008092	cytoskeletal protein binding	1.45E-15	3.20E-12
GO:0016301	kinase activity	9.00E-14	1.99E-10
GO:0016773	phosphotransferase activity, alcohol group as acceptor	9.25E-14	2.04E-10
GO:0004672	protein kinase activity	1.90E-12	4.20E-09
GO:0042802	identical protein binding	4.60E-12	1.02E-08
GO:0045296	cadherin binding	4.96E-12	1.10E-08
GO:0003779	actin binding	8.82E-12	1.95E-08
GO:0019900	kinase binding	1.28E-11	2.83E-08
GO:0019901	protein kinase binding	1.41E-11	3.12E-08

GO: Biological Process			
ID	Name	p-value	q-value Bonferroni
GO:0022610	biological adhesion	2.36E-28	2.43E-24
GO:0007155	cell adhesion	1.27E-27	1.30E-23
GO:0009611	response to wounding	7.44E-24	7.64E-20
GO:0006629	lipid metabolic process	1.42E-21	1.45E-17
GO:0000902	cell morphogenesis	3.71E-21	3.80E-17
GO:0042060	wound healing	5.83E-21	5.98E-17
GO:0098609	cell-cell adhesion	2.88E-20	2.95E-16
GO:0032989	cellular component morphogenesis	4.07E-20	4.18E-16
GO:0006082	organic acid metabolic process	9.71E-20	9.97E-16
GO:0043436	oxoacid metabolic process	2.84E-19	2.92E-15

GO: Cellular Component			
ID	Name	p-value	q-value Bonferroni
GO:0005884	actin filament	2.18E-22	2.54E-19
GO:0062023	collagen-containing extracellular matrix	1.85E-21	2.16E-18
GO:0015629	actin cytoskeleton	4.73E-21	5.52E-18
GO:0032432	actin filament bundle	6.61E-21	7.71E-18
GO:0030054	cell junction	4.60E-18	5.37E-15
GO:0098858	actin-based cell projection	1.07E-17	1.24E-14
GO:0031012	extracellular matrix	1.09E-17	1.27E-14
GO:0005902	microvillus	6.62E-17	7.73E-14
GO:0099080	supramolecular complex	6.91E-17	8.06E-14
GO:0099081	supramolecular polymer	1.12E-16	1.31E-13

Pathway			
ID	Name	p-value	q-value Bonferroni
1270244	Extracellular matrix organization	7.87E-13	2.71E-09
1269340	Hemostasis	3.18E-11	1.09E-07
M18	Beta1 integrin cell surface interactions	6.39E-11	2.20E-07
1269367	Platelet degranulation	3.30E-09	1.14E-05
1269365	Response to elevated platelet cytosolic Ca2+	3.31E-09	1.14E-05
138045	HIF-1-alpha transcription factor network	7.14E-09	2.46E-05
M255	HIF-1-alpha transcription factor network	1.05E-08	3.60E-05
P00012	Cadherin signaling pathway	4.41E-08	1.52E-04
1319988	AGE-RAGE signaling pathway in diabetic complications	6.07E-08	2.09E-04
M19580	Pentose and glucuronate interconversions	1.04E-07	3.57E-04
782000	Proteoglycans in cancer	1.20E-07	4.13E-04
1457780	Neutrophil degranulation	1.27E-07	4.37E-04
1270001	Metabolism of lipids and lipoproteins	1.44E-07	4.95E-04
M176	FOXM1 transcription factor network	1.76E-07	6.05E-04
82929	Pentose and glucuronate interconversions	4.00E-07	1.38E-03
997799	Glucuronate pathway (uronate pathway)	4.75E-07	1.63E-03
M53	Beta3 integrin cell surface interactions	6.64E-07	2.28E-03
1270255	Syndecan interactions	8.04E-07	2.77E-03
132956	Metabolic pathways	9.36E-07	3.22E-03
137935	FOXM1 transcription factor network	1.65E-06	5.66E-03

Figure 5.17 Gene list term enrichment analysis based on functional annotations and protein interactions network. Gene ontology (GO) of differentially expressed genes between LOPCK (*MTTP*$^{WT/WT}$) and MOPIK (*MTTP*$^{VAR/VAR}$) in **(A)** PA-untreated and **(B)** 300 µM PA-treated conditions. GO term hierarchy analysis within "Molecular function"; "Biological process"; "Cellular component" and "Pathway" is performed using ToppGene Suite.

High throughput proteomics profiling using antibody microarrays

NFκB-associated proteins

To better understand the underlying mechanism of lipid accumulation caused by the *MTTP*-p.I564T variation and cellular responses of the derived HLCs after external lipid challenge , we utilised different R&D's proteome profiler antibody arrays to examine the changes in proteome and secretome between LOPCK and MOPIK HLCs under untreated and PA-treated condition after 48 hours. We performed human NFκB (**Figure 5.18**), phospho-kinase (**Figure 5.19**) and cytokine (**Figure 5.20**) proteome arrays using cell lysates or cell culture supernate to explore and identify what signalling pathway was activated, results were represented as the fold change of mean pixel intensity of the sample duplicates normalised to untreated LOPCK-HLCs (as 1).

We detected the higher levels of proteins related to the NFκB and TLR inflammatory pathways particularly in untreated MOPIK-HLCs (**Figure 5.18**), including RelA/p65 (involved in NFκB heterodimer formation, nuclear translocation and activation); IKKγ/nemo (activates NFκB); IRAK1 (involved in TLR and IL1 receptor pathways); and NFκB1. Activation of IRAK1 could potentially switch on the IKK complex and leading to activation of downstream RelA/p65 subunits (RelA/p65 and RelA/p65 S529) and NFκB (NFκB1 and NFκB2), forming the NF-kB transcription factor complex.

In addition, apoptosis related proteins such as ASC (Apoptosis-associated speck-like protein containing a CARD); TRAIL R2/DR5 (TNF-related apoptosis-inducing ligand 2 (TRAIL receptor 2 or death receptor 5, DR5); Fas/TNFRSF6/CD95 were most abundantly found in MOPIK-HLCs lysate compared to other conditions. Fas and TRAIL R2 both are receptors that involved in mediating apoptosis via the extrinsic Fas or TNF pathways. ASC is a key adaptor protein for inflammasome receptors essential for inducing caspase-1 activation and the consequent secretion of interleukin-1β (IL-1β). These proteins regulate the expression of genes influencing a broad range of biological processes such as innate and adaptive immunity, inflammation, and stress responses; upregulation of these proteins indicates that NFκB signalling is inherently

more stimulated in MOPIK-HLCs even without the additional PA treatment, resulting in potential apoptosis-related cell death.

Increased levels of inflammatory proteins such as RelA/p65; SHARPIN; STING/TMEM173; IRAK1; MYD88; and FADD/MORT1 (Fas-associated protein with death domain) in PA-treated LOPCK (*MTTP*$^{WT/WT}$)-HLCs demonstrated that with the addition of lipid influx, healthy cell line was also able to model lipid-induced inflammation. Interestingly, we observed relatively lower level of inflammatory proteins in PA-treated MOPIK-HLCS compared to untreated LOPCK-HLCs, notwithstanding pro-apoptotic proteins including TRAIL R1/D94 and TRAIL R2/DR5 were increased in PA-treated MOPIK-HLCs, this may imply that apoptosis pathway could be activated in HLCs with *MTTP*$^{VAR/VAR}$ genotype after lipid challenge.

Protein phosphorylation

Protein phosphorylation is a reversible post-translational modification of proteins, it is an important regulatory mechanism that can active or deactivate signalling pathways for many cellular processes such as protein synthesis and signal transduction; this is achieved by phosphorylation and dephosphorylation many enzymes and receptor via the help of kinases and phosphatases. Hyperactivity, malfunction, or overexpression of protein phosphorylation may be a manifestation of pathological responses.

We detected phosphorylation in proteins that are related to hepatic stellate cell (HSC) activation and fibrosis in MOPIK cell line under both untreated and PA-treated conditions (relatively higher in untreated MOPIK-HLCs) (**Figure 5.19**); lymphocyte-specific protein tyrosine kinase (Lck); platelet-derived growth factor receptor beta precursor (PDGFRβ); Lyn (tyrosine kinase); Src (proto-oncogene tyrosine-protein kinase); and PYK2 (proline- rich protein tyrosine kinase 2). Quiescent HSCs are lipid-storing cells with the presence of large lipid droplets (LDs), activation of HSC could be a result of processing lipid overload, LD size can be reduced or degraded upon this activation. Not only that, transition of HSC from a quiescent to a proliferative and

migratory state could lead to liver fibrogenesis. In PA-treated MOPIK-HLCs, we noticed cAMP-responsive Element-binding Protein (CREB) level was at the highest, followed by untreated MOPIK-HLCs; phosphorylated CREB can enhance hepatic glucogenesis, which could be due to the lipid influx.

AMP-activated protein kinases (AMPK) is a master regulator of cellular energy homeostasis; increased phosphorylated AMPKα1 and AMPKα2 levels in both untreated and PA-treated MOPIK-HLCs may be a response to compensate for lipid accumulation [312]. Addition of PA also caused an increased c-JUN phosphorylation in MOPIK-HLCs, potentially activate inflammation via the JNK/c-Jun phosphorylation pathway. We found an opposite effect on MOPIK-HLCs without the addition of PA, instead, decreased phosphorylated c-JUN was found and that might have in turn caused an increase p38α level through negative feedback of the c-JUN/ATF2 pathway; hyperactivation of p38 activity is related to aberrant cell survival and growth, which may explain the increased phosphorylation we also observed in fibrogenic proteins such as PDGFRβ in untreated MOPIK-HLCs.

The *MTTP*-p.I564T genotype seemed to have activated fibrogenic activity inherently, whereas excess PA influx would have caused in induction in inflammation more severely. On the other hand, healthy LOPCK ($MTTP^{WT/WT}$) cell line reacted differently upon PA treatment, we noticed a significant increased phosphorylation in ribosomal protein S6 kinases (RSKs): RSK1/2/3, RSK is a downstream target of the extracellular signal-regulated kinase (ERK) signalling, which involved in the regulation of lipid synthesis.

A strikingly low levels of endothelial nitric oxide synthase (eNOS) phosphorylation was detected in both untreated and PA-treated MOPIK-HLCs, which is highly likely related to the *MTTP*.p.I564T genetic variation compared to LOPCK cell line. Downregulation of eNOS could impair hepatic endothelial cell function and exacerbates multiple features of NAFLD progression by altering glucose and lipid homeostasis [313]. Overall reduced phosphorylation of PI3K/Akt pathway kinases in

MOPIK-HLCs have indirectly decreased the level of their downstream target eNOS, this is also reflected in the secretome dynamics shown in the next section.

Cytokine secretion

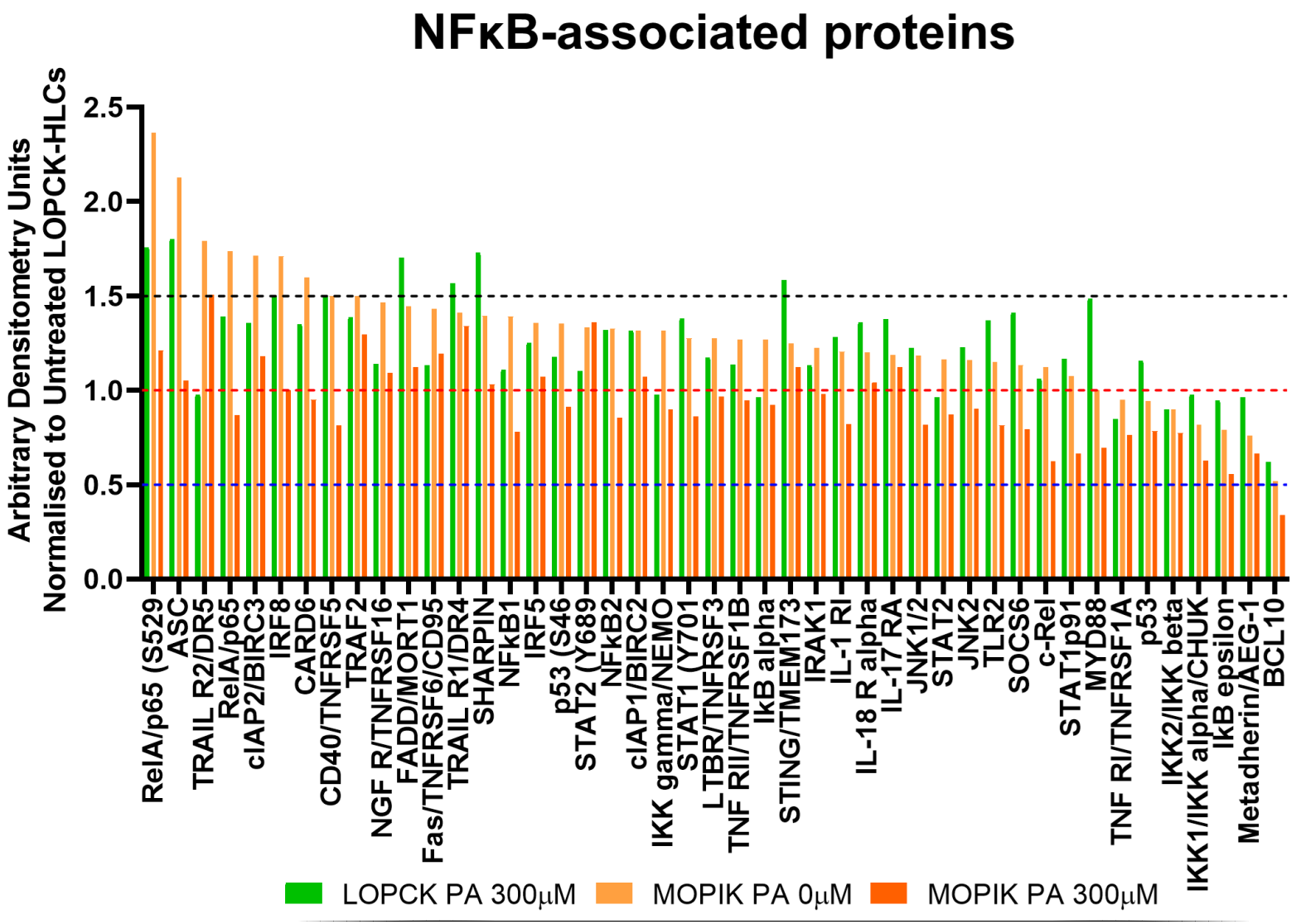
Human XL Cytokine array kit was used for the detection of secreted protein in cell culture supernate (**Figure 5.20A, B and C**). Cytokine arrays revealed that macrophage inflammatory proteins (MIPs) were detected at various levels in hiPSC-HLCs, all very high. MIP-1α/MIP-1β was at the highest in PA-treated LOPCK-HLCs (18.1 folds increase ↑), followed by untreated (15.6↑) and PA-treated (15↑) MOPIK-HLCs, compared to untreated LOPCK-HLCs control (**Figure 5.20A**). MIP-1α and MIP-1β are major factors produced by macrophages and monocytes after they are stimulated with proinflammatory cytokines such as IL-1β or bacterial endotoxin, which crucial for immune responses towards inflammation and infection [314]. Interestingly, MIP-3α and MIP-3β levels were decreased in both untreated and PA-treated MOPIK-HLCs (**Figure 5.20B**), but PA-treated LOPCK-HLCs detected an increase of MIP-3α (2.7↑) and MIP-3β (1.7↑), which are crucial in the regulation of dendritic cells [315].

B-cell activating factor (BAFF) was significantly higher in MOPIK-HLCs in both untreated (11.1↑) and PA-treated (5.82↑) conditions, whereas its level was down 3.9↓ fold in PA-treated LOPCK-HLCs compared to the control. Over-production of BAFF has been linked to murine and human autoimmunity, excess BAFF could stimulate autoreactive B cells emergence [316], [317]. Untreated MOPIK (*MTTP*$^{VAR/VAR}$) HLCs secreted high level of CD30 (8.3↑), which could be an innate mechanism to counteract with lipid accumulation due to the genetic variation, as CD30 can function as a lipid-lowering agent [318]. Apolipoprotein A-I (ApoA, 0.33↓) was detected significantly low in MOPIK-HLCs supernate compared to LOPCK-HLCs, decreased ApoA secretion may indicate that the diseased cell line has difficulty in exporting lipids compared to normal cells (**Figure 5.20C**).

When we examined the effects of external lipid challenge on HLCs with different *MTTP*-p.I564T genotype, we detected relatively higher levels of secretory proteins

related to liver inflammation in PA-treated LOPCK-HLCs compared to the control (**Figure 5.20A, B and C**). These proteins included C-reactive protein (10.5↑); vascular cell adhesion molecule 1 (VCAM-1, 4.7↑); complement factor D (7.0↑); granulocyte-macrophage colony-stimulating factor (GM-CSF, 4.0↑); IL18 binding protein (IL18 BPa, 9.5↑) and Fas ligand (3.8↑). PA-treated (13.8↑) MOPIK-HLCs had noticeably high levels of Endoglin (Eng), notwithstanding untreated MOPIK-HLCs also had an increased amount of Eng (8.5↑) but slightly less; conversely, PA-treated LOPCK-HLCs had a reduction (5.5↓). Eng has a key role in endothelium-mediated vascular reactivity as it regulates the expression of eNOS [319]. Addition of PA resulted in intracellular lipid accumulation and potentially causing the activation of inflammatory pathways via slightly different mechanisms depending on the *MTTP*-p.I564T genotypes.

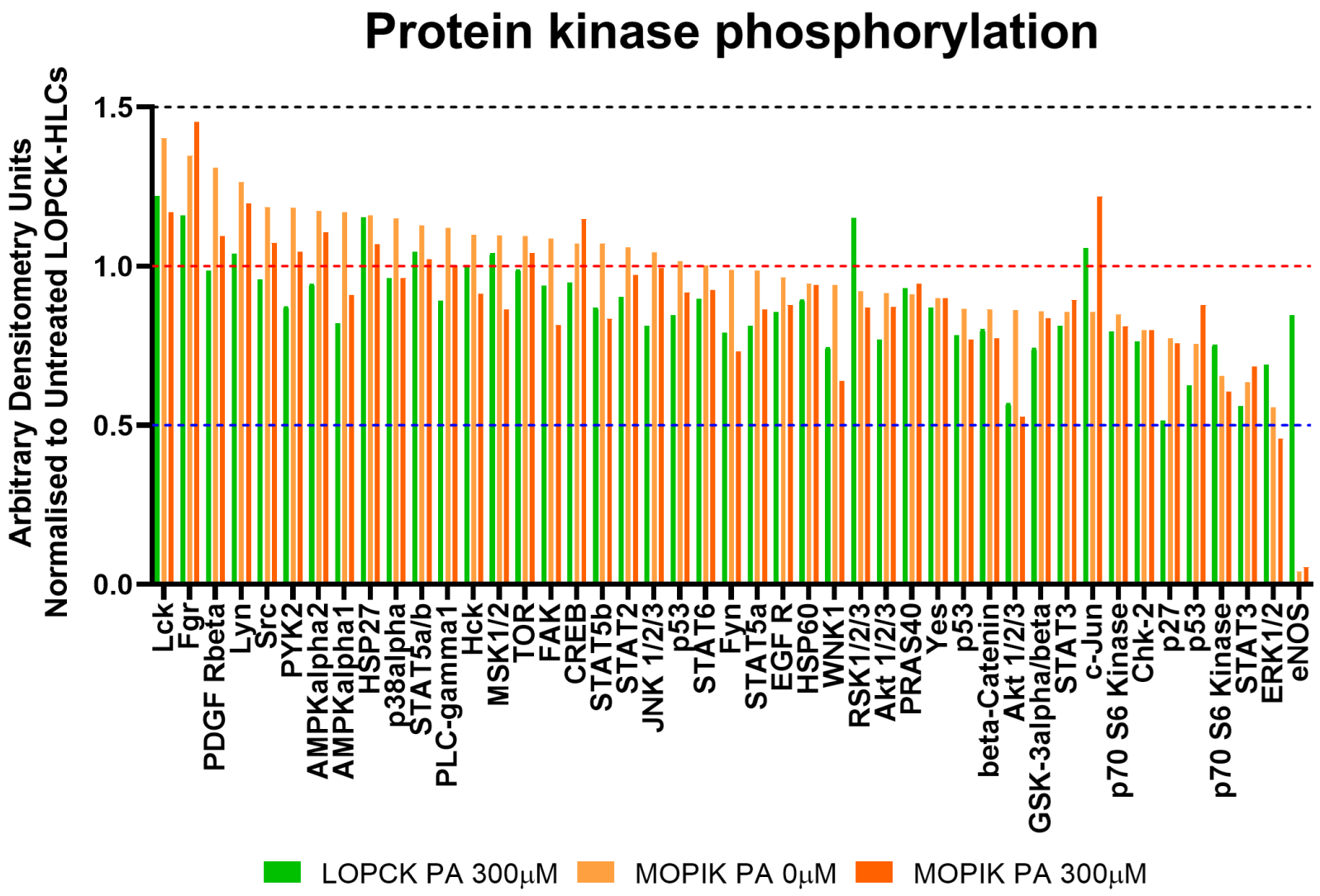
In summary, combined proteome array data suggested that MOPIK-HLCs displayed an altered proteome profile, as seen in the activation of pro-apoptotic and pro-inflammatory signalling pathways in MOPIK-HLCs compared to healthy LOPCK-HLCs.



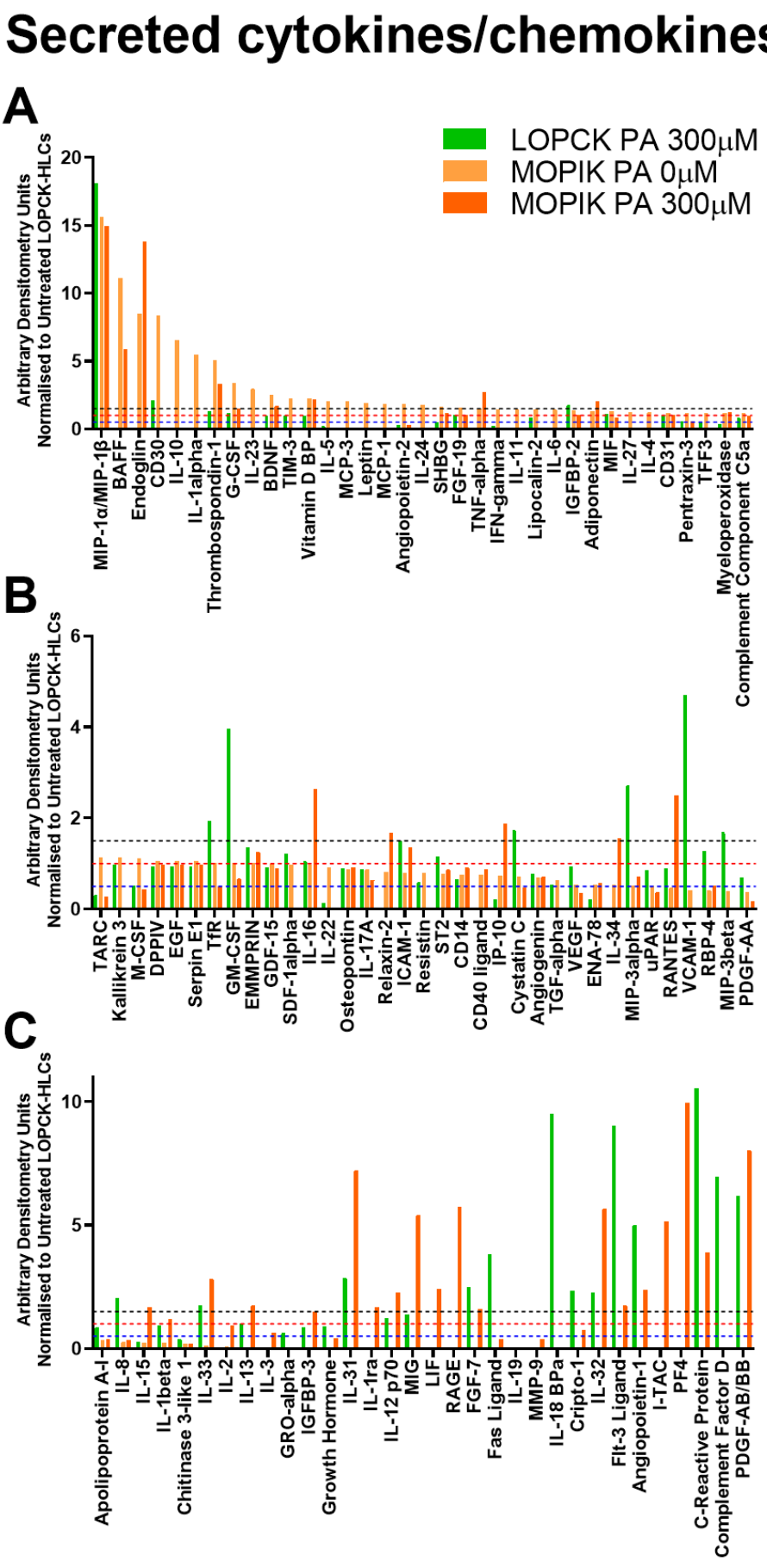
NFκB array	LOPCK PA 300μM	MOPIK PA 0μM	MOPIK PA 300μM
ASC	1.80	2.13	1.05
BCL10	0.62	0.52	0.34
CARD6	1.35	1.60	0.95
CD40/TNFRSF5	1.50	1.50	0.81
cIAP1/BIRC2	1.32	1.32	1.07
cIAP2/BIRC3	1.36	1.71	1.18
c-Rel	1.06	1.13	0.63
FADD/MORT1	1.70	1.45	1.12
Fas/TNFRSF6/CD95	1.13	1.43	1.20
IkB alpha	0.96	1.27	0.92
IkB epsilon	0.94	0.79	0.56
IKK gamma/NEMO	0.97	1.31	0.90
IKK1/IKK alpha/CHUK	0.98	0.82	0.63
IKK2/IKK beta	0.90	0.90	0.77
IL-1 RI	1.28	1.21	0.82
IL-17 RA	1.38	1.19	1.13
IL-18 R alpha	1.36	1.20	1.04
IRAK1	1.13	1.22	0.98
IRF5	1.25	1.36	1.07
IRF8	1.50	1.71	1.00
JNK1/2	1.22	1.18	0.82
JNK2	1.23	1.16	0.90
LTBR/TNFRSF3	1.17	1.28	0.97
Metadherin/AEG-1	0.96	0.76	0.67
MYD88	1.48	1.00	0.70
NFkB1	1.11	1.39	0.78
NFkB2	1.32	1.33	0.86
NGF R/TNFRSF16	1.14	1.47	1.09
p53	1.16	0.94	0.78
p53 (S46	1.18	1.35	0.91
RelA/p65	1.39	1.74	0.87
RelA/p65 (S529	1.76	2.36	1.21
SHARPIN	1.73	1.39	1.03
SOCS6	1.41	1.13	0.80
STAT1 (Y701	1.38	1.28	0.86
STAT1p91	1.17	1.07	0.67
STAT2	0.96	1.16	0.87
STAT2 (Y689	1.10	1.33	1.36
STING/TMEM173	1.58	1.25	1.13
TLR2	1.37	1.15	0.81
TNF RI/TNFRSF1A	0.85	0.95	0.76
TNF RII/TNFRSF1B	1.14	1.27	0.95
TRAF2	1.39	1.50	1.30
TRAIL R1/DR4	1.57	1.41	1.34
TRAIL R2/DR5	0.98	1.79	1.51

Figure 5.18 Expression of NFκB-associated signalling proteins in HLCs under different PA treatments at maturation day 10 (M10). (above) Comparison is relative to the expression in untreated LOPCK (*MTTP*$^{WT/WT}$) HLCs, signal quantification is completed using densitometry of NFκB protein array. Quantification of four NFκB arrays, each array contains 41 proteins and 4 serine or tyrosine phosphorylation sites antibodies involved in NFκB signal transduction, each antibody is printed in duplicate. 400μg of cell lysate of each culture condition was used on individual array. Array spots were visualised and the intensity of each set of antibodies was calculated as mean ± SD. The graph shows the relative fold change compared to untreated LOPCK-HLCs, set at 1 for control (LOPCK PA 0 μM). Protein levels with higher than ± 0.5 folds are indicated by dotted lines (⩾1.5, black line; 1, control in red; ⩽0.5, blue line) compared to control. Fold change values are listed in a table in alphabetical order.

Figure 5.19 Protein phosphorylation in HLCs, normalised to untreated LOPCK (*MTTP*$^{WT/WT}$)-HLCs quantified using densitometry of phosphokinase array. (below) Quantification of four sample sets (array A and B as one set) of Phospho-kinase arrays, each set of array contains 43 phosphorylated kinase antibodies printed in duplicates. 2000μg of cell lysate of each culture condition was used on individual array. Array spots were visualised and the intensity of each set of antibodies was calculated as mean ± SD. The graph shows the relative fold change compared to LOPCK-HLCs without PA treatment (control), setting at 1. Protein levels with higher than ± 0.5 folds are indicated by dotted lines (⩾1.5, black line; 1, control in red; ⩽0.5, blue line) compared to control. Fold change values are listed in a table in alphabetical order.



Phos-phokinase array	LOPCK PA 300μM	MOPIK PA 0μM	MOPIK PA 300μM
Akt 1/2/3	0.77	0.92	0.87
Akt 1/2/3	0.57	0.86	0.53
AMPKalpha1	0.82	1.17	0.91
AMPKalpha2	0.94	1.17	1.11
beta-Catenin	0.80	0.86	0.77
Chk-2	0.76	0.80	0.80
c-Jun	1.06	0.86	1.22
CREB	0.95	1.07	1.15
EGF R	0.86	0.96	0.88
eNOS	0.85	0.04	0.05
ERK1/2	0.69	0.56	0.46
FAK	0.94	1.09	0.81
Fgr	1.16	1.35	1.45
Fyn	0.79	0.99	0.73
GSK-3alpha/beta	0.74	0.86	0.84
Hck	1.00	1.10	0.91
HSP27	1.15	1.16	1.07
HSP60	0.90	0.95	0.94
JNK 1/2/3	0.81	1.04	1.00
Lck	1.22	1.40	1.17
Lyn	1.04	1.26	1.20
MSK1/2	1.04	1.10	0.86
p27	0.52	0.77	0.76
p38alpha	0.96	1.15	0.96
p53	0.85	1.02	0.92
p53	0.78	0.86	0.77
p53	0.62	0.76	0.88
p70 S6 Kinase	0.79	0.85	0.81
p70 S6 Kinase	0.75	0.66	0.61
PDGF Rbeta	0.99	1.31	1.09
PLC-gamma1	0.89	1.12	1.00
PRAS40	0.93	0.91	0.94
PYK2	0.87	1.18	1.05
RSK1/2/3	1.15	0.92	0.87
Src	0.96	1.19	1.07
STAT2	0.90	1.06	0.97
STAT3	0.81	0.86	0.89
STAT3	0.56	0.64	0.69
STAT5a	0.81	0.99	0.86
STAT5a/b	1.05	1.13	1.02
STAT5b	0.87	1.07	0.84
STAT6	0.90	1.00	0.93
TOR	0.99	1.09	1.04
WNK1	0.75	0.94	0.64
Yes	0.87	0.90	0.90



Cytokine array	LOPCK PA 300µM	MOPIK PA 0µM	MOPIK PA 300µM
Adiponectin	-0.21	1.29	2.00
Angiogenin	0.78	0.69	0.70
Angiopoietin-1	5.00	-3.29	2.37
Angiopoietin-2	0.27	1.79	0.26
Apolipoprotein A-I	0.87	0.33	0.36
BAFF	-3.86	11.09	5.82
BDNF	0.98	2.47	1.66
CD14	0.66	0.76	0.90
CD30	2.12	8.32	-0.88
CD31	0.97	1.17	1.03
CD40 ligand	-0.31	0.75	0.87
Chitinase 3-like 1	0.39	0.21	0.19
Complement C5/C5a	0.84	1.16	0.97
Complement Factor D	6.97	-5.28	-3.34
C-Reactive Protein	10.53	-5.16	3.89
Cripto-1	2.34	-1.78	0.75
Cystatin C	1.74	0.71	0.46
DPPIV	0.93	1.06	0.96
EGF	0.93	1.06	0.96
EMMPRIN	1.36	1.00	1.24
ENA-78	0.22	0.54	0.57
Endoglin	-5.50	8.50	13.81
Fas Ligand	3.81	-1.09	0.36
FGF-19	1.05	1.58	1.01
FGF-7	2.48	-1.07	1.60
Flt-3 Ligand	9.03	-2.09	1.72
G-CSF	1.15	3.35	1.49
GDF-15	0.90	0.99	0.89
GM-CSF	3.95	1.00	0.66
GRO-alpha	0.62	-0.14	-0.76
Growth Hormone	0.91	-0.32	0.42
ICAM-1	1.49	0.80	1.34
IFN-gamma	0.21	1.45	-0.44
IGFBP-2	1.79	1.35	1.03
IGFBP-3	0.87	-0.24	1.49
IL-10	-10.16	6.53	-12.53
IL-11	-0.92	1.42	-3.20
IL-12 p70	1.23	-0.37	2.26
IL-13	0.99	-0.04	1.72
IL-15	0.26	0.23	1.67
IL-16	1.06	0.96	2.64
IL-17A	0.88	0.86	0.63
IL-18 BPa	9.50	-1.70	-16.00
IL-19	-3.37	-1.16	-7.56
IL-1alpha	-5.68	5.44	-4.48
IL-1beta	0.95	0.22	1.18
IL-1ra	-0.69	-0.32	1.65
IL-2	-1.70	0.06	0.91
IL-22	0.13	0.91	-2.04
IL-23	-4.87	2.94	-6.23
IL-24	-1.07	1.74	-2.34
IL-27	0.01	1.21	-1.05
IL-3	-2.67	-0.05	0.63
IL-31	2.86	-0.32	7.19
IL-32	2.27	-1.89	5.64
IL-33	1.74	0.13	2.80
IL-34	-0.14	0.52	1.56
IL-4	-0.53	1.17	-0.71
IL-5	0.22	2.03	-1.27
IL-6	-2.43	1.40	-3.64
IL-8	2.02	0.24	0.34
IP-10	0.22	0.73	1.87
I-TAC	-0.61	-3.83	5.13
Kallikrein 3	0.98	1.12	-0.33
Leptin	-2.08	1.89	-3.06
LIF	-0.20	-0.78	2.39
Lipocalin-2	0.81	1.42	-0.30
MCP-1	-0.24	1.85	0.03
MCP-3	-1.46	2.02	-2.45
M-CSF	0.50	1.11	0.43
MIF	1.10	1.28	0.83
MIG	1.37	-0.45	5.39
MIP-1alpha/MIP-1beta	18.09	15.59	14.95
MIP-3alpha	2.72	0.51	0.71
MIP-3beta	1.68	0.39	-0.73
MMP-9	-3.83	-1.60	0.36
Myeloperoxidase	0.36	1.16	1.19
Osteopontin	0.89	0.87	0.91
PDGF-AA	0.70	0.38	0.17
PDGF-AB/BB	6.20	-26.60	8.00
Pentraxin-3	0.58	1.17	0.55
PF4	-1.52	-5.00	9.96
RAGE	-0.12	-1.03	5.74
RANTES	0.90	0.46	2.50
RBP-4	1.27	0.40	0.50
Relaxin-2	-3.47	0.81	1.66
Resistin	0.60	0.79	-0.32
SDF-1alpha	1.21	0.97	-0.01
Serpin E1	0.93	1.06	0.96
SHBG	0.51	1.60	1.16
ST2	1.16	0.76	0.86
TARC	0.32	1.14	0.27
TFF3	0.50	1.17	-0.14
TfR	1.94	1.01	0.50
TGF-alpha	0.53	0.62	-1.38
Thrombospondin-1	1.31	5.05	3.31
TIM-3	0.97	2.24	-1.34
TNF-alpha	-1.00	1.46	2.68
uPAR	0.85	0.50	0.36
VCAM-1	4.71	0.41	-0.39
VEGF	0.93	0.54	0.34
Vitamin D BP	0.98	2.20	2.14

Figure 5.20 Cytokine proteome array Levels of proteins secreted into tissue culture medium in HLCs. (above) Data is normalised to LOPCK (*MTTP*$^{WT/WT}$)-HLCs quantified using densitometry of cytokine arrays. Comparison of extracellular cytokines and growth factors proteome between LOPCK-HLCS and MOPIK-HLCS in different PA treatments. (A, B, C) Quantification of four R&D Human XL Cytokine arrays (1 array for each sample), each array contains 105 different capture antibodies printed in duplicate. 1.5 ml of cell culture supernate was run on each array. Array spots were visualised and the intensity of each set of antibodies was calculated as mean ± SD. Due to the number of antibodies used were too many, the full arrays' results were split into 3 graphs. The graph shows the relative fold change of extracellular secreted proteins compared to untreated LOPCK-HLCs, setting at 1 as the control. Protein levels with higher than ± 0.5 folds are indicated by dotted lines (⩾1.5, black line; 1, control in red; ⩽0.5, blue line) compared to control. Fold change values are listed in a table in alphabetical order (blue = increase, red = decrease).

Metabolomics profiling of LOPCK (MTTP$^{WT/WT}$) and MOPIK (MTTP$^{VAR/VAR}$)

To further characterise and understand the influence of PA treatment in healthy and diseased cell lines, liquid chromatography-mass spectrometry (LC-MS) based analytical approach was used to assess their secretome components. Spent culture media were collected at maturation day 10 (M10) from LOPCK and MOPIK HLCs, with six biological replicates from each condition, LC-MS analysis was then executed (**Figure 5.21**).

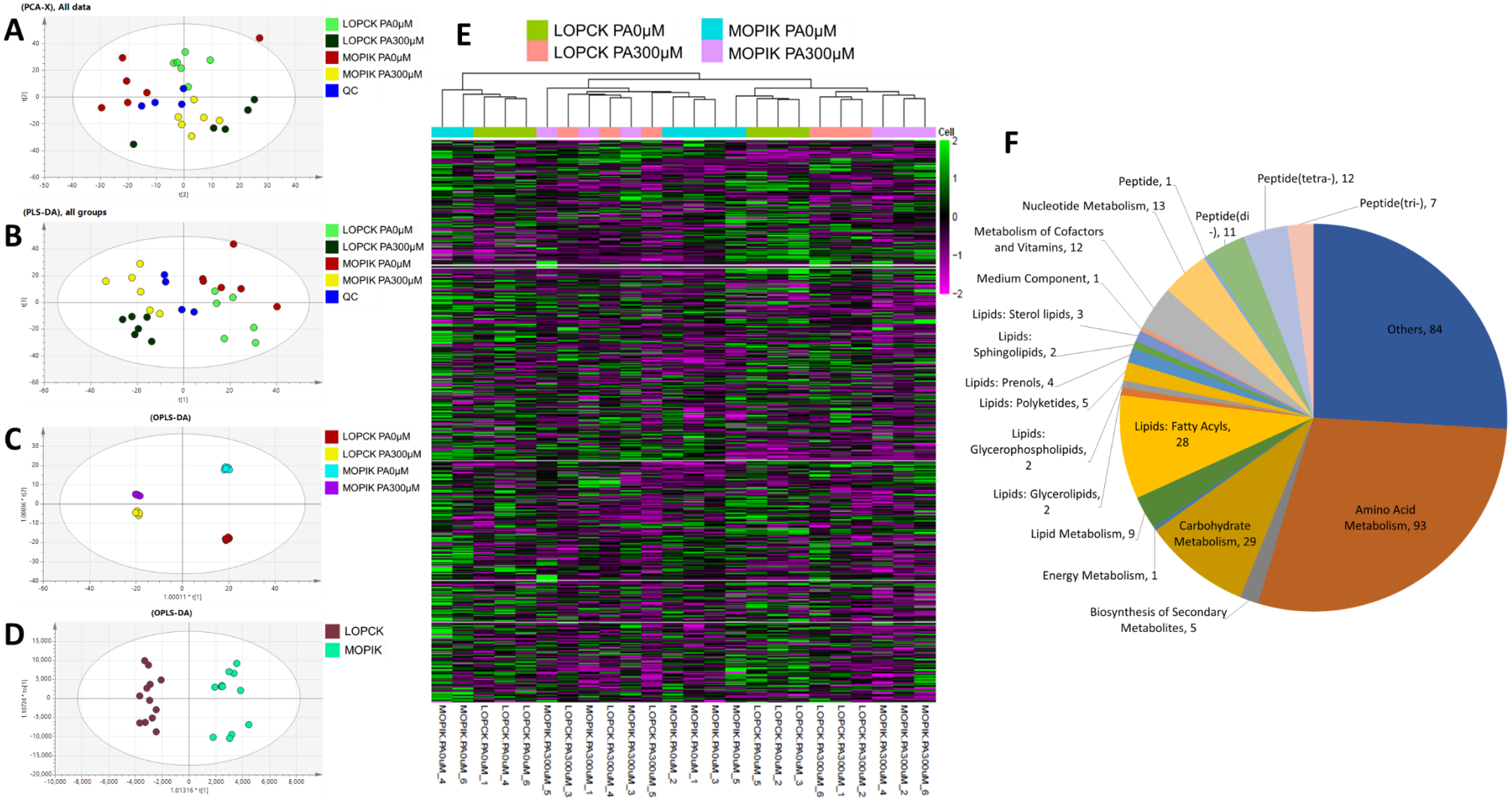
Control sets for LC-MS include quality control (QC) samples with a small quantity mix of the actual cell culture samples, standards were also tested to help predict and determine the tested molecules. Multivariate analysis were performed to evaluate how closely the sample groups are related, PCA and Orthogonal Projections to Latent Structures Discriminant Analysis (OPLS-DA) approaches were utilised. HLC samples were examined regarding to their relatedness and similarity as depicted in **Figure 5.21A-D**, PCA and OPLS-DA analyses showed that there were distinct disparity between untreated and PA-treated LOPCK and MOPIK HLCs, however the R2 value was not particularly high (R2 = 0.658, R2Y = 0.997, Q2 = 0.505, **Figure 5.21C**).

For a visual representation, we plotted a heatmap containing all the metabolites identified (3349 in total) and performed cluster analysis (**Figure 5.21E**). We found that there was discrepancy within each spent media sample set, metabolite levels were

found to be slightly different even though cells were undergoing the same differentiation protocol and collected on the same day, which could be either be related to the differentiated cell yield, or alternatively due to mishandling of sample preparation before the LC-MS analysis. Nevertheless, we have performed a search on the metabolites to be identified with significant differences and summarise their main biological functions and roles, a pie chart showing the classification of 325 metabolites is generated (**Figure 5.21F**).

Majority of the metabolites were involved or related to amino acid (93 metabolites) and carbohydrate (29 metabolites) metabolism, which are all crucial in energy production in the liver. Additionally, we have found a lot of metabolites related to different classes of lipids, possibly because of increased exportation within the serum offloading from cells. The LC-MS data showed that differentiated HLCs were indeed going through metabolic processes and functionally capable of secreting extracellular metabolites.

Figure 5.21 Extracellular metabolite profiling between LOPCK- and MOPIK-HLCs in untreated and PA-treated conditions using LC-MS-based method. (below) Spent medium samples of HLCs were harvested after 10 days of maturation to identify the secreted extracellular metabolites. Principal component analysis (PCA) and orthogonal projections to latent structures discriminant analysis (OPLS-DA) score plots were analysed against HLCs and their quality control (QC) samples. (A) PCA plot of combined LOPCK, MOPIK samples and QC samples (R2 = 0.502, Q2 = 0.264). (B) Partial Least-Squares Discriminant Analysis (PLS-DA) plot of LOPCK, MOPIK and QC samples (R2 = 0621, R2y = 0.989 Q2 = 0.778). (C) OPLS-DA plot of LOPCK- and MOPIK-HLCs with and without PA treatment (R2 = 0.658, R2Y = 0.997, Q2 = 0.505). (D) OPLS-DA score plot of overall LOPCK and MOPIK samples (R2X = 0.474, R2Y = 0.958, Q2 = 0.689). (E) Heatmap of extracellular metabolites detected in LOPCK and MOPIK cells under different PA treatments, result is shown as log2 fold change between sample sets. (F) Functional categorisation of the nutrients and metabolites produced by LOPCK- and MOPIK-HLCs under untreated or 300 μM PA treatment, 325 metabolites are categorised based on their biological function.


A
(PCA-X), All data
LOPCK PA0μM
LOPCK PA300μM
MOPIK PA0μM
MOPIK PA300μM
QC
B
(PLS-DA), all groups
LOPCK PA0μM
LOPCK PA300μM
MOPIK PA0μM
MOPIK PA300μM
QC
C
(OPLS-DA)
LOPCK PA0μM
LOPCK PA300μM
MOPIK PA0μM
MOPIK PA300μM
D
(OPLS-DA)
LOPCK
MOPIK
E
LOPCK PA0μM
LOPCK PA300μM
MOPIK PA0μM
MOPIK PA300μM
Cell
MOPIK.PA0uM_4
MOPIK.PA0uM_6
LOPCK.PA0uM_1
LOPCK.PA0uM_4
LOPCK.PA0uM_6
MOPIK.PA300uM_5
LOPCK.PA300uM_3
MOPIK.PA300uM_1
LOPCK.PA300uM_4
MOPIK.PA300uM_3
LOPCK.PA300uM_5
MOPIK.PA0uM_2
MOPIK.PA0uM_1
MOPIK.PA0uM_3
MOPIK.PA0uM_5
LOPCK.PA0uM_5
LOPCK.PA0uM_2
LOPCK.PA0uM_3
LOPCK.PA300uM_6
LOPCK.PA300uM_1
LOPCK.PA300uM_2
MOPIK.PA300uM_4
MOPIK.PA300uM_2
MOPIK.PA300uM_6
F
Peptide, 1
Peptide(tetra-), 12
Peptide(tri-), 7
Nucleotide Metabolism, 13
Peptide(di-), 11
Metabolism of Cofactors and Vitamins, 12
Medium Component, 1
Lipids: Sterol lipids, 3
Lipids: Sphingolipids, 2
Lipids: Prenols, 4
Lipids: Polyketides, 5
Lipids: Glycerophospholipids, 2
Lipids: Glycerolipids, 2
Lipid Metabolism, 9
Energy Metabolism, 1
Biosynthesis of Secondary Metabolites, 5
Others, 84
Lipids: Fatty Acyls, 28
Amino Acid Metabolism, 93
Carbohydrate Metabolism, 29

5.4 Discussion

In this chapter, we focussed on creating the NAFLD disease model and the subsequent functional characterisation in a multi-omics approach to elucidate the underlying mechanisms (**Figure 5.22**). NAFLD was modelled in two ways; by utilising HLCs generated from healthy LOPCK (*MTTP*$^{WT/WT}$) and diseased MOPIK (*MTTP*$^{VAR/VAR}$) hiPSCs with different *MTTP*-p.I564T genotypes, we could evaluate the intrinsic influence of this single nucleotide variation; to examine the extrinsic effects of high fat diet we have employed the use of fatty acids to induce hepatic steatosis in our cell models.

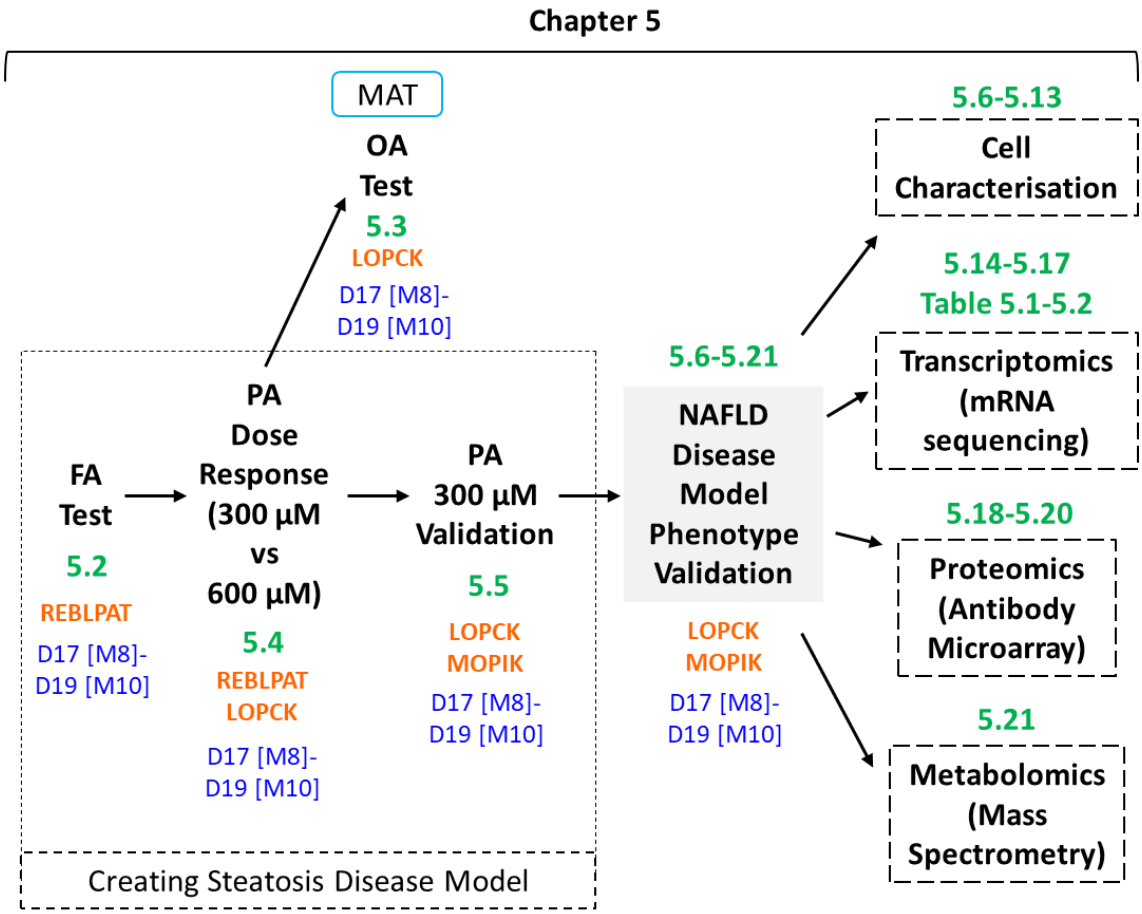


Figure 5.22 Schematic illustration of the experimental timeline of chapter 5. Experiments conducted are stated in black letters. Green letters represent the result figures related to that particular experiment. Orange letters represent the cell lines that are used in those experiments. Blue letters represent the specific period of hepatic differentiation that are tested. Blue boxes represent the differentiation stages that are of interest. Key: FA, fatty acid; OA, oleic acid; PA, palmitic acid; MAT, maturation.

Different dietary fatty acids have diverse biological properties and bioactive roles in cell signalling pathways. We first explored the effects of various types of fatty acids, including MUFA, PUFA and SFA on our generated hiPSC-HLCs, these are some of the common components found in modern western diet [297].

Monosaturated fatty acids (MUFAs) such as oleic acid (OA) is an essential element in the Mediterranean diet, it naturally occurs in various animal and vegetable fats and oils. Various studies have shown that OA could have dual beneficial or harmful effects under different circumstances. When OA was used as a concomitant supplement with PA in HepG2 cells, it was demonstrated to have a protective effect and alleviate PA-induced cellular apoptosis, oxidative stress, ER stress, mitochondrial dysfunction and inflammation [320]; similar phenomenon was also observed, downregulation of *TGF-β* and *TNF-α* gene expression were found in our cell model when we combined the use of OA, LA and PA, while mature hepatic markers *ALB, A1AT* and *AADAC* expressions increased.

We subsequently explored the possibility of using OA as a culture media supplement to improve HLC maturity during differentiation. We want to evaluate whether 5 days of OA treatment would suffice to upregulate hepatic markers in comparison to M10 OA-untreated HLCs. Addition of OA for 5 days was able to increase mature marker in HLCs mainly at the lowest dosage of 25 µM, nevertheless we also observed emergence of lipid droplets, we were concerned that OA may have a negative effect during long-term differentiation and decided not to include it as a culture supplement. Literature have also shown that use of OA alone could have an adverse effect and induce hepatic steatosis through aquaporin 3 and 9 via p38-signaling regulation [321]. Due to the ambiguous nature and unpredictability of OA, we rejected the idea of using it for developing our model. Tighter range of OA concentrations starting from 5µM should be considered if we want to investigate further in the future, additionally cells should be compared at the same timepoint either at M5 or M10 to eliminate variation in experimental set up. Lower dosage of OA may be sufficient to facilitate hepatocyte maturation along with other supplements, without causing excessive lipid accumulation. However, assessment on the influence of OA was not the main

focus of this chapter, henceforward we shall be continuing this work in the future to explore its potential as a maturation inducer.

PA is the most common saturated FA found in animals, plants and microorganisms [297], it has been used in several studies to induce cellular lipid accumulation in the past [118], [292], [322]. Indeed, when hiPSC-HLCs were treated with 300µM PA for 48 hours, we observed deposition of microvascular and macrovascular lipid droplets in both LOPCK and MOPIK cell lines. It has been reported that the choice of exogenous FA is a critical point for developing NAFLD model *in vitro*, use of SFA typically induced higher degree of steatosis and cellular damage due to their different steatotic and toxic activity with respect to USFA [323], therefore we elected PA as the induction agent. The relative concentration of FA also has been demonstrated to have an impact on hepatic lipid accumulation and cytotoxicity *in vitro* [324], [325]. Indisputably, we also observed loss of cellular structural support and detachment when we supplemented HLCs with high dose of PA (600µM) versus lower dose (300µM). It is therefore essential to screen for suitable exogenous FA candidates as a preliminary examination for creating an *in vitro* NAFLD model.

Once we have established the cell model, we then performed phenotypic validation screening to evaluate if the differentiated hiPSC-HLCs can represent the disease phenotypes faithfully. Immunostaining results showed that HLCs generated from both LOPCK and MOPIK cell lines were expressing relevant foetal and adult liver markers such as AFP and ALB. We have also measure MTTP protein and gene expression of LOPCK and MOPIK HLCs to authenticate whether the cell models display the expected phenotypes, indeed, diseased MOPIK-HLCs have relative lower MTTP protein level. Nonetheless, *MTTP* mRNA level was relatively higher in untreated MOPIK-HLCs, which had a negative correlation, implicating that the increase of gene transcripts could be a representation of MTTP protein activity demand.

Screening for significant differences in mRNA expression between conditions is commonly used as a promising technique for biological discovery or diagnostic tool for NAFLD [326]. The reliance on mRNA measurements is based on the assumption

that differential expression would directly reflect on their respective protein products, however, it has been shown that certain classes of genes such as secreted proteins would have higher mRNA-protein correlation coefficients and that mRNA and protein expression can sometimes be discordant [327]–[329].

This discrepancy between mRNA and protein levels could be attributed to other levels of regulation between transcript and protein products. ELISA data also supported our theory that MTTP activity was required, as we have measured an overall reduction of apoB-100 levels not only in NAFLD patient GF10's serum and VLDL samples compared to those of healthy individual GF06, but this state was also exacerbated in our hiPSC-HLC model; apoB-100 levels in MOPIK (*MTTP*$^{VAR/VAR}$)-HLCs were very low in relation to LOPCK (*MTTP*$^{WT/WT}$)-HLCs under both untreated and PA-treated conditions. Interestingly, we measured significantly high expression of *APOB* transcript but apoB-100 lipoprotein was barely detected in untreated MOPIK-HLCs, indicating that either there was a fault during APOB protein translation in MOPIK-HLCs or it could be that apoB was not secreted in the form of VLDL due to the *MTTP*-p.I564T variation. ELISA results showed that our cell model was undoubtedly able to reflect the relevant NAFLD phenotypes *in vitro*.

For a deeper mechanistic insight, multi-omics profiling was achieved by qPCR, mRNA sequencing (transcriptomics), high-throughput proteome arrays (proteomics) and LC-MS (metabolomics) to survey the combined effects of *MTTP*-p.I564T and lipid challenge in a more comprehensive approach. Based on our systemic assessments, we found that healthy LOPCK (*MTTP*$^{WT/WT}$) and diseased MOPIK (*MTTP*$^{VAR/VAR}$) cell lines operated in slightly different signalling pathways under different culture conditions.

Hepatic FFA can be converted to TG as cytoplasmic lipid droplets for energy storage or secreted as VLDL transported to other tissues, alternatively, excess FFA can be metabolised via mitochondrial β-oxidation [330]. Through ORO and NR lipid staining, we observed greater intracellular lipid droplet deposition within MOPIK-HLCs compared to LOPCK-HLCs inherently even without the addition of PA.

In order to break down excess fatty acid accumulation, mitochondrial β-oxidation was required. Seahorse mitochondrial respiration assay showed that MOPIK (*MTTP*$^{VAR/VAR}$) had a significant higher basal respiration rate compared to LOPCK (*MTTP*$^{WT/WT}$) overall to compensate for the mass amount of lipid, whereas the basal respiration rates of untreated and PA-treated LOPCK-HLCs were similar. Additionally, both LOPCK and MOPIK cell lines had lower mitochondrial maximal respiration after PA exposure, a similar finding was also reported in LPO (lactate, pyruvate and octanoate)-induced steatotic model [131], implying that external induction of steatosis would result in lower respiration.

PA-treated HLCs also experienced lower coupling efficiency to produce ATP, this was due to mitochondrial proton leaks during the process of electron transport chain (ETC), incomplete coupling resulting in lower ATP energy generated which results in disproportionate increase in oxygen consumption; this phenomenon suggests potential mitochondrial oxidative stress and dysfunction occurred under PA treatment [331]. In additional to the accelerated respiration rates for mitochondrial β-oxidation, lysosomal lipid catabolism was also increased to release free cholesterol and fatty acids, as indicated from the upregulation of *LIPA* (encode for lysosomal acid lipase) in MOPIK-HLCs relative to LOPCK-HLCs during both fasting (PA 0μM) and fed (PA 300μM) states. This is also a sign of activated macrophages (including liver Kupffer cells) to release free cholesterol and fatty acids via the regulation of hepatocyte VLDL secretion [332], [333].

Sustained intracellular lipid accumulation due to the *MTTP*-p.I564T genetic variation (restrict VLDL secretion) or external lipid challenge (increasing the availability of FFA) lead to increased β-oxidation activity and subsequently could affect different reactive oxygen species (ROS) generators; organelles including ER, mitochondria and peroxisomes, as well as certain enzymes such as NADPH oxidase (NOX), cyclooxygenases, and lipoxygenases [334], [335]. ROS are formed and emitted during the redox reactions such as mitochondrial β-oxidation, protein synthesis in the ER, which we have also observed with the use of CellROX and MitoSOX fluorescence dyes.

Superoxide was produced as a by-product of mitochondrial respiration in both untreated and PA-treated MOPIK-HLCs significantly; sub-localisation of CellROX within the nucleus was also noted particularly in MOPIK cell line, whereas LOPCK-HLCs had relatively lower of CellROX nuclear deposition. These data suggest that *MTTP*$^{VAR/VAR}$ variation in MOPIK-HLCs exacerbated the cytotoxic effect of oxidative stress even without external lipid influx compared to healthy cell line, which has been shown that localised ROS production within the nuclear is more detrimental compared to the cytoplasm [336], [337].

ROS production could induce unfolded protein response resulting in ER stress, which we have also found UPR-related genes (*IRE1, ATF6, XBP1, ATF4,* etc.) were upregulated relatively higher in MOPIK-HLCs under both untreated and PA-treated conditions. The autophagy-initiating kinase ULK1 (UNC51-like kinase 1) is a direct transcriptional target of ATF4, which can drive autophagosome formation and activates autophagy [338]. Autophagy is an important process that degrades damaged organelle or protein aggregation to maintain essential activity [339], autophagy is promoted by AMPK signalling and negatively controlled by mTORC1 (mammalian target of rapamycin complex 1 or mechanistic target of rapamycin complex 1) activity; AMPK and mTORC1 regulate autophagy through coordinated phosphorylation of ULK1 (a direct transcriptional target of ATF4) [340], [341]. AMPK and mTORC1 are two important sensors that control cellular homeostasis; mTORC1 is one of the master regulators of protein synthesis, while AMPK is involved in cellular energy homeostasis by sensing the intracellular levels of AMP, ADP and ATP, such as in the case of energy stress or nutrient deprivation [342].

We detected relatively higher levels of AMPKα1 and AMPKα2 in untreated MOPIK-HLCs using phosphor-kinase proteome array, while mTOR pathway was inhibited as we have also measured a reduction of its downstream target p70S6 kinase in MOPIK cell line simultaneously, suggesting there could be a demand for degradation of damaged organelles such as mitochondria in MOPIK-HLCs. Interestingly, AMPK activity was reduced in both LOPCK and MOPIK HLCs upon PA exposure, overnutrition of lipid could have potentially lowered the need for energy production via AMPK

activation. Activation of AMPK while inhibiting mTOR can restore energy balance by inhibiting anabolic processes such as protein synthesis that consume ATP in untreated MOPIK-HLCs, while promoting catabolic processes of lipid droplets (lipophagy) to generate ATP [342], [343].

Nutrient excess can trigger ER stress and oxidative stress as we have demonstrated, this also has a direct impact to the activation of pro-inflammatory and fibrogenic pathways. We detected increased *NFkB* gene expression, as well as NFκB1 and NFκB2 and related NFκB-pathway targets (RelA/p65, IKKγ/nemo, etc.) in MOPIK-HLCs overall. The release of mediators of inflammation and fibrosis could trigger macrophages, subsequently activated TLR4 receptor which we have detected using qPCR. In addition to that, we measured higher level of the inflammasome adaptor ASC in untreated MOPIK-HLCs using proteome arrays; lipotoxicity-induced injury in hepatocytes may release danger-activated molecular patterns (DAMPs) such as IL-1α (5.4 fold ↑), together with the pattern recognition receptor TLR4 activity could activate the NOD-like receptor protein 3 (NLRP3) inflammasome cascade and pro-apoptotic pathway, which lead to hepatic inflammation [344], [345].

Other pro-inflammatory mediators BAFF, CD30, IL-10, IL-23, and leptin levels were all increased in untreated MOPIK-HLCs. Prolonged inflammation could then contribute to the pathogenesis of non-alcoholic steatohepatitis (NASH) and potentially lead to fibrosis in the long term, as we have shown that fibrotic gene (*TGF-β, COL1*) expression were upregulated in MOPIK cell line [346]. Indeed, MOPIK ($MTTP^{VAR/VAR}$) donor was a patient who had NAFLD, progressed to hepatocellular carcinoma (HCC) and developed cirrhosis, consequently she received a liver transplantation and her health was improved.

Healthy LOPCK ($MTTP^{WT/WT}$) might have undergone a different pathway in response to PA exposure, as we detected activation of hepatic stellate cell markers including granulocyte-macrophage colony-stimulating factor (GM-CSF; 3.95 fold ↑), platelet-derived growth factor (PDGF)-AB/BB (6.2↑), VCAM-1 (4.71↑), chemokine CCL20 (CC chemokine ligand 20 or MIP-3α; 2.72 ↑) [19], [347]–[350], whereas MOPIK

(*MTTP*$^{VAR/VAR}$) cell line had relatively low expression of these proteins, indicating that hiPSC-HLCs behaved differently possibly due to the *MTTP*-p.I564T genetic variations.

Another noticeable finding is that MOPIK cell line produced over 20-fold lower expression of phosphorylated eNOS (PA 0µM = 0.04, PA 300µM = 0.05) in comparison to the untreated LOPCK-HLC control (reference set as 1). Emerging studies reported that eNOS plays an important role in mitochondrial dynamics as a potent mediator to maintain mitochondrial function in the liver, reduction of eNOS could be related to impaired liver endothelial cells; reduced eNOS activity lead to decreased nitric oxide (NO) production and subsequently restrict vascular blood vessels within the liver [313], [351]–[354]. ENOS-derived nitric oxide (NO) is an endogenous vasodilatory gas that mains an anti-proliferative and anti-apoptotic environment in the vessel wall by continuous regulation of the diameter of blood vessels [355]. Animal model also shown that *eNOS*-knockout (*eNOS-/-*) mice had significantly suppressed hepatic tissue blood flow and deficiency of eNOS-derived NO had contributed to the pathogenesis of early-stage of NASH by changing the fat distribution within the liver, as well as an association with hepatic mitochondrial dysfunction; MTTP activity was also downregulated in *eNOS-/-* mice [19], [356].

Proteome array results coincide with our theory, as we have measured significant increase of endoglin (Eng) in both untreated (8.5↑) and PA-treated (13.81↑) MOPIK-HLCs, while level of Eng was decreased in PA-treated LOPCK-HLCs (-5.5↓); Eng can promote coupling of eNOS activity by facilitating its association with Hsp90 [319], [357], [358]. Induction of eNOS is dependent on Eng at the transcriptional level and it is mediated by the type I TGF-β receptor ALK5 and its downstream substrate Smad2 signalling [357], in which we have also observed relatively higher upregulation of *TGF-β* in MOPIK-HLCs compared to LOPCK-HLCs in both untreated and PA-treated conditions.

On the other note, we also detected reduction of vascular cell adhesion molecule 1 (VCAM-1) in untreated (0.41↓) and PA-treated (-0.39↓) MOPIK-HLCs, in comparison to the increase of VCAM-1 within PA-treated LOPCK-HLCs (4.71↑). VCAM-1 is cell

surface glycoprotein predominantly expressed in endothelial cells [359], [360], it was reported in a another study that *eNOS*-knockout mice was lacking the characteristics of activated endothelial cells as they did not increase their surface expression of E-selectin, P-selectin, VCAM-1, or ICAM-1 [361].

Gathering these results, we concluded that *MTTP*-p.I564T may have contributed to the impairment of liver sinusoidal endothelial cells (LSEC) as observed in the lack of eNOS expression within MOPIK ($MTTP^{VAR/VAR}$)-HLCs and may lead to liver fibrogenesis via TGF-β/Smad2 phosphorylation [16].

Chapter 6.

General Discussion

Chapter 6. General Discussion

6.1 Fulfilment of thesis objectives

The aim of this thesis was to generate new *in vitro* model for NAFLD to gain mechanistic insights in two main aspects; to explore the interrelationship between genetic predisposition with the novel *MTTP*-p.I564T SNV, as well as the cellular and molecular responses upon exogenous lipid challenge using fatty acids. The main experimental stages of this PhD project are depicted in **Figure 6.1**.

In this section, key experimental findings of each chapter will be integrated towards establishing the generated NAFLD disease models, relevance of the generated model in potential diagnostic biomarker discovery and therapeutic target will be discussed. Moreover, experimental considerations and limitations addressed. Finally, methods for further investigation of the proposed models of NAFLD will be suggested.

In chapter 3, we first derived human dermal fibroblasts from healthy individual, patients with homozygous and heterozygous *MTTP*-p.I564T genotypes (**Figure 3.2**). Reprogramming was then performed to produce hiPSC lines (**Figure 3.3**), which later then differentiated into HLCs using our optimised differentiation protocol. HDF-derived LOPCK, MOPIK, and HETIK hiPSCs were characterised to prove that they were pluripotent, their ability to differentiate into three germ layer lineages was assessed by using karyotyping, qPCR and immunocytochemistry (**Figure 3.4**, **Figure 3.5**). In addition to these three hiPSC lines, we also wanted to generate an extra cell line using healthy LOPCK hiPSC with *MTTP*$^{-/-}$ knockout as an external isogenic *MTTP* negative control (**Figure 3.11**). However, only a heterozygous knockout was achieved using a commercially available kit. Due to limited time moving forward to creating NAFLD disease model, we thereby did not use the heterozygous *MTTP* control and continued with the next stage.

Chapter 4 depicted the optimisation of our hepatic differentiation platform to generate HLCs that are relatively more mature and functionally more relevant for

downstream experiments. We found that optimisation was essential for each cell line to produce HLC populations that are comparable with improved maturity. By examining cell proliferation and growth rates, we manipulated the initial seeding density (**Figure 4.3**), and BMP4 concentration (**Figure 4.4**) for each cell line during hepatic endoderm development.

In addition to that, we wanted to reduce the overall cost and time of our hepatic differentiation protocol, that would be beneficial for scale-up in the future for drug screening and potential therapeutic purposes. Differentiation time during foregut differentiation was reduced and it was proven that two days of Activin A treatment would suffice to drive foregut formation (**Figure 4.2**). BMP4 concentration
We compared the use of small molecules PNU-74654 and LDN-193189 in replacement of two of the more costly recombinant proteins DKK and Noggin (**Figure** 4.5, **Figure 4.6**). It was however proven that even just with minor changes of the supplement component would have a significant reduction in differentiation efficiency (**Figure 4.7**, **Figure 4.8**). Therefore, we kept the recombinant protein-based medium formula and compared how effective it was in comparison to the alternative protocol that we used to use. Immunostaining, qPCR transcriptomics and metabolomics data all showed that HLCs generated using the New protocol are more related to primary liver samples and more mature compared to that of the Old protocol (**Figure 4.10-Figure 4.14**).

After the optimisation process, we generated hiPSC-HLCs with specific *MTTP*-p.I564T genotypes that is associated with an inherited form of NAFLD in chapter 5, subsequently induced intracellular lipid accumulation within HLCs using palmitic acid to model the additional effect of Western diet (**Figure 5.2**). Palmitic acid-induced steatosis HLC models with either wildtype or homozygous *MTTP*-p.I564T variants were characterised (**Figure 5.4-Figure 5.7**) and compared phenotypically using transcriptomics (Figure 5.14-Figure 5.16), proteomics (**Figure 5.18-Figure 5.20**), and metabolomics profiling (**Figure 5.21**). Our investigation has revealed that this SNV lead to a reduction of apoB-containing lipoprotein (apoB-100) secretion in homozygous MOPIK ($MTTP^{VAR/VAR}$)-HLCs compared to wildtype LOPCK ($MTT^{WT/WTT}$)-

HLCs overall, though apoB-100 level was slightly increased after PA treatment similar to patients' serum samples (**Figure 5.8**). This is a unique phenomenon in comparison to other typical *MTTP* mutations in abetalipoproteinemia where apoB level is undetectable [151], [152], [362]. Although *MTTP*-p.I564T variant was identified in the past in clinical case report and transcriptomic study, no phenotypic characteristics related to our findings are previously reported [363], [364]. Further discussion on proposed mechanistic model will be covered in later section.

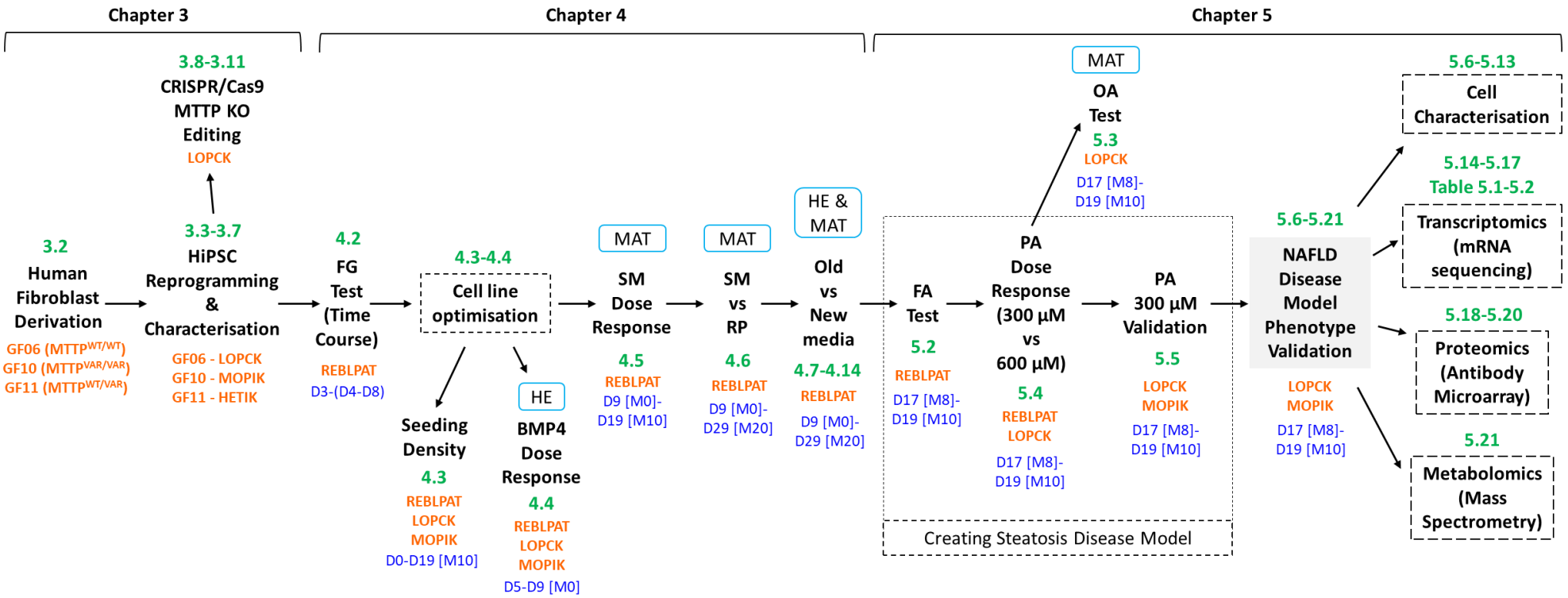


Figure 6.1 Schematic illustration of the experimental timeline of chapter 3 to 5. Experiments conducted are stated in black letters. Green letters represent the result figures related to that particular experiment. Orange letters represent the cell lines that are used in those experiments. Blue letters represent the specific period of hepatic differentiation that are tested. Blue boxes represent the differentiation stages that are of interest. Key: MTTP, microsomal triglyceride transfer protein FG, foregut; HE, hepatic endoderm; MAT, maturation; SM, small molecule; RP, recombinant protein; BMP4, bone morphogenetic protein 4; FA, fatty acid; OA, oleic acid; PA, palmitic acid.

6.2 Proposed mechanistic model of *MTTP*-p.I564T NAFLD

Protein modelling via DynaMut suggests that missense mutation of T to C results in a substitution of amino acid isoleucine to threonine though may affect MTP structure, the change does not occur in the active site or in functional regions as previously described [92], [93], [365], it only seems to influence protein stability, which consequently may reduce its enzymatic activity overall. This subtle difference impacted on hepatic lipid imbalance as we have observed upregulation of *APOB* gene expression (**Figure 5.9**), but with significantly low apoB-100 secretion (**Figure 5.8)**, accompanied with increased lipid droplets deposition (**Figure 5.4**) in MOPIK cell line, once again, these evidence showed that *MTTP*-p.I564T variant is clearly distinct from ABL [362], [366]. Through these results, reduced saturated dietary fat intake may be a potential treatment to mitigate clinical manifestation of liver steatosis in NAFLD patient with this variant.

MOPIK-HLCs was detected with relatively high expression of *MTTP* compared to LOPCK-HLCs, and yet the protein expression of MTTP was a lot lower based on immunostaining results. This indicates that the *MTTP*-p.I564T defect may lead to reduction of lipid export. QPCR data of lipid metabolism related markers suggests that there is a demand of lipoprotein packaging and lipid export in MOPIK-HLCs compared to LOPCK-HLCs (*APOB* ↑, *VLDLR* ↑, **Figure 5.9B**). Detection of the very-low-density-lipoprotein receptor (*VLDLR*) in PA-untreated MOPIK-HLCs but with almost absent level of apoB-100 tested in MOPIK-HLCs spent medium, suggesting that there could be a lack of VLDL protein rather than the lack of VLDL ligand binding and transport by the VLDL receptor. This indicates that there is an insufficient export of packaged lipoproteins from HLCs to the culture media supernatant. At the same time lipolysis (LIPC ↓) is potentially inhibited by the increase of apolipoprotein C-III, the expression of *APOC3* functions as a VLDL component to inhibit lipoprotein lipase and hepatic lipase [306], resulting in higher lipid accumulation within MOPIK-HLCs and prolonged lipid overload could result in lipotoxicity.

Using proteome microarray, we detected phosphorylation in proteins that are related to hepatic stellate cell (HSC) activation and fibrosis (Lck ↑, PDGFRβ ↑, Lyn ↑, Src ↑, PYK2 ↑) in MOPIK cell line under both untreated and PA-treated conditions (relatively higher in untreated MOPIK-HLCs) (**Figure 5.19**). Quiescent HSCs are lipid-storing cells with the presence of large lipid droplets (LDs), activation of HSC could be a result of processing lipid overload. Not only that, transition of HSC from a quiescent to a proliferative and migratory state could lead to liver fibrogenesis. In PA-treated MOPIK-HLCs, we noticed CREB level was at the highest, followed by untreated MOPIK-HLCs; phosphorylated CREB can enhance hepatic glucogenesis, which could be due to the lipid influx.

Overall upregulation of UPR activators (*IRE1, ATF6*) and mediators (*ATF4, XBP1*) in MOPIK-HLCs indicated that although ERAD degradation was working efficiently, there was a greater stimulation of UPR activity and ER stress, which consequently could lead to activation of inflammatory signalling pathways. As a matter of fact, qPCR data and proteome arrays also showed signs of NFκB pathway activation in MOPIK-HLCs, the levels of *NFκB* were significantly higher in MOPIK-HLCs compared to LOPCK-HLCs in both PA-treated and untreated conditions. We detected the higher levels of proteins related to the NFκB and TLR inflammatory pathways particularly in untreated MOPIK-HLCs (**Figure 5.18**), including RelA/p65; IKKγ/nemo; IRAK1 and NFκB1. Activation of IRAK1 could potentially switch on the IKK complex and leading to activation of downstream RelA/p65 subunits (RelA/p65 and RelA/p65 S529) and NFκB (NFκB1 and NFκB2), forming the NF-kB transcription factor complex.

In addition, apoptosis related proteins such as ASC; TRAIL R2/DR5; Fas/TNFRSF6/CD95 were most abundantly found in MOPIK-HLCs lysate compared to other conditions based on proteome array data. Fas and TRAIL R2 both are receptors that involved in mediating apoptosis via the extrinsic Fas or TNF pathways. ASC is a key adaptor protein for inflammasome receptors essential for inducing caspase-1 activation and the consequent secretion of interleukin-1β (IL-1β). Upregulation of these proteins indicates that NFκB signalling is inherently more stimulated in MOPIK-

HLCs even without the additional PA treatment, resulting in potential apoptosis-related cell death.

Pattern recognition receptors such as toll-like receptors (*TLR*) 1-5 gene expressions were also measured to detect any potential stimulation of immune response. We found that *TLR4* was highly upregulated (> 100 folds) particularly in MOPIK-HLCs in comparison to LOPCK-HLCs, with a slight reduction after PA treatment. Significant increase of *TLR4* gene expression in both untreated and PA-treated MOPIK-HLCs compared to LOPCK-HLCs indicating that there may be an activation of damage-associated molecular pattern molecules (DAMPs) caused by endogenous intracellular triggers released by injured tissues and necrotic cells. Strong pro-inflammatory response could be activated through interaction with *TLR4.* It has been reported that in monocytes and macrophages, TLR4 activation was associated with the activation of IRE1α, one of the three branches of downstream UPR/ER stress signalling [367]. Aligned with our qPCR data, upregulation of *IRE1* and other ER stress related genes could lead to an intracellular signalling pathway NFκB and inflammatory cytokine production which is responsible for activating the innate immune system.

On the other hand, we have also detected relatively higher level of MitoSOX in MOPIK-HLCs; increased ROS production may be caused by the UPR activation in diseased cell line. Seahorse analysis showed that diseased MOPIK-HLCs had relatively higher metabolic rates compared to the healthy LOPCK-HLCs in general, however, both cell lines had decreased mitochondrial respiration rates after the exposure of PA overall. This suggested that diseased cell line with the *MTTP*-p.I564T genetic variant would have higher mitochondrial activity intrinsically for lipid degradation via β-oxidation. Notwithstanding PA-induced steatosis is associated with compromising mitochondrial respiration or dysfunction extrinsically in both LOPCK- and MOPIK-HLCs. This is also reflected on spare capacity measurements, PA-treated cells had relatively lower spare capacity; meaning the amount of extra ATP that can be produced by oxidative phosphorylation in case of a sudden increase in energy demand were reduced (**Figure 5.13E**). Metabolomics profiling also identified that majority of the metabolites were involved or related to amino acid (93 metabolites)

and carbohydrate (29 metabolites) metabolism, which are all crucial in energy production in the liver, suggesting that HLCs are metabolically active to overcome lipid accumulation.

Nutrient excess can trigger ER stress and oxidative stress as we have demonstrated, this also has a direct impact to the activation of pro-inflammatory and fibrogenic pathways. We detected increased *NFkB* gene expression, as well as NFκB1 and NFκB2 and related NFκB-pathway targets (RelA/p65, IKKγ/nemo) in MOPIK-HLCs overall. The release of mediators of inflammation and fibrosis could trigger macrophages, subsequently activated TLR4 receptor which we have detected using qPCR. In addition to that, we measured higher level of the inflammasome adaptor ASC in untreated MOPIK-HLCs using proteome arrays; lipotoxicity-induced injury in hepatocytes may release danger-activated molecular patterns (DAMPs) such as IL-1α, together with the pattern recognition receptor TLR4 activity could activate the NOD-like receptor protein 3 (NLRP3) inflammasome cascade and pro-apoptotic pathway, which lead to hepatic inflammation [344], [345].

Expression of *TGF-β* in MOPIK-HLCs were significantly higher statistically compared to LOPCK-HLCs, indicating there may be a need for cell proliferation, tissue repair and survival, alternatively, upregulation of *TGF-β* could be an indication of promoting fibrosis by enhancing type I collagen (*COL1*). Indeed, mRNA level of *COL1* was also upregulated in MOPIK-HLCs relative to LOPCK-HLCs in both untreated and PA-treated conditions, whereas PA-treated LOPCK-HLCs had a downregulation of *COL1* instead; this may suggest an activation of extracellular matrix (ECM) protein synthesis in MOPIK-HLCs for structural remodelling. The *MTTP*-p.I564T genotype seemed to have activated fibrogenic activity inherently, whereas excess PA influx would have caused in induction in inflammation more severely.

Through proteomics analysis we also found a noticeable observation that eNOS phosphorylation was strikingly low in in both untreated and PA-treated homozygous MOPIK-HLCs compared to wildtype LOPCK-HLCs (**Figure 5.19**). Downregulation of eNOS could impair hepatic endothelial cell function and exacerbates multiple

features of NAFLD progression by altering glucose and lipid homeostasis [313]. Gathering these results, we concluded that *MTTP*-p.I564T may have contributed to the impairment of liver sinusoidal endothelial cells (LSEC) as observed in the lack of eNOS expression within MOPIK ($MTTP^{VAR/VAR}$)-HLCs and may lead to liver fibrogenesis via TGF-β/Smad2 phosphorylation [16].

Decreased eNOS phosphorylation may be a suitable as a biomarker for diagnosis and prognosis evaluation for NAFLD and NASH, as well as a potential therapeutic target for drug screening to increase eNOS expression. We can cross-validate eNOS quantification with patient's blood samples as an indication of disease progression, which is a lot less invasive and cost-effective. Several other studies also showed that deficiency of eNOS function can exacerbates NAFLD pathogenesis by altering hepatic tissue blood flow and sequentially changing the fat distribution within the liver [313], [352], [354], [356]. Reduction of eNOS can lead to decreased nitric oxide (NO) production, it is therefore apparent that increasing NO bioavailability and antioxidant status in vascular tissue can potentially prevent the onset of vascular dysfunction [368].

6.3 Study limitations and improvements

In chapter 3, besides the generation of hiPSC lines via reprogramming, we also attempted to create a positive control as *MTTP-/-* to compare and evaluate the effects of *MTTP* knockout. We purchased a commercially available CRISPR/Cas9 gene knockout kit, however, we found that the procedure of creating a homozygous knockout clone was very time-consuming and ineffective (most of the generated clones were heterozygous). Since we were given the reagents, gRNA vectors, and donor DNA template, limited modification or adjustment could be done. In an ideal situation, perhaps instead of the complete *MTTP* knockout, it would be wise to create an isogenic pair of controls by simultaneously correcting the *MTTP*-p.I564T variation in the homozygous MOPIK ($MTTP^{VAR/VAR}$) hiPSC line, as well as installing this specific SNV into the healthy LOPCK ($MTTP^{WT/WT}$) cell line. This would enable a us to develop a more physiologically relevant and accurate humanised model to distinguish variant-dependent effects from secondary effects, such as patient age, sex, or other genetic

background that may contribute to phenotypic variation of NAFLD. This approach was conducted in creating hypertrophic cardiomyopathy (HCM) disease model [370]; the use of isogenic hiPSC-cardiomyocytes proved to be crucial as they have found that age of the donor patient might have influenced the pathogenic phenotype causing arrhythmogenesis and illustrated the value of isogenic control in genotype-phenotype correlations.

In this study, we have employed HDR-mediated CRISPR/Cas9 programme to generate KO clone. Although HDR is the more preferred pathway for precise knock-in using donor DNA cassette as it can reduce random integration and off-site effect [371], [372], efficiency may be compromised and could display three-fold reduction compared to NHEJ and potentially causes greater damage to cells [373], it was reported that site-specific Cas9 nucleases were no longer able to cut in HDR-mediated editing due to the targeted DSB site was destroyed [374].

The emergence of newer genome editing technologies such as base editing poses an attractive option for the generation of isogenic control, as well as a more efficient route for genetic modification. DNA base editors use components from CRISPR system of a catalytically disabled CRISPR–Cas nuclease, incorporated to a single-stranded DNA deaminase enzyme, and in some cases with a DNA glycosylase inhibitor, to directly introduce specific and precise point mutations into cellular DNA or RNA without making DSBs [375]. Base editors can be categorised into two main classes as cytosine base editors (CBEs) and adenine base editors (ABEs), where CBE catalyses the conversion of C•G base pairs to T•A base pairs (C→T, G→A) [376]; and ABEs catalyses A•T-to-G•C conversions (A→G, T→C) [377]. Correction of the *MTTP*-p.I564T variant in MOPIK hiPSCs can be achieved using CBE by converting the pathogenic T allele back into C, whereas ABE can introduce conversion of wildtype C to variant T. This allows the conversion of one base or base pair into another even in non-dividing cells without generating excess undesired editing by-products; application of base editing to engineer isogenic control NAFLD model would

therefore be advantageous relative to traditional CRISPR/Cas9 HDR-mediated editing techniques.

One of the cell culture aspects we haven't looked into in chapter 4 is the choice of biomaterial to support cell-cell interaction and enhance structural organisation. Matrigel was used in this study as it is readily available and it has been used in many other studies to culture adult hepatocytes and hiPSC-HLCs in the past [378]–[380]. Nonetheless, we need to take into consideration that its composition is undefined and is animal-derived, indeed, our experiments were hindered on several occasions due to the batch-to-batch variability of Matrigel, which has cost us significant time and money to investigate the cause of inefficient differentiation.

On the other hand, if we needed to scale-up the production of HLCs for biomedical applications such as drug screening or potential clinical-grade cell therapy, a defined and sustainable extracellular matrix alternative must be found. Recombinant laminin (laminin-521 and -511) is a promising substrate that has been shown to improve cell organisation, functionality and phenotype by supressing unfavourable gene regulatory networks that are involved in controlling cell proliferation, migration, fibroblast and colon specification in HLCs [217], [381]. Other viable natural or synthetic biomaterial candidates include cellulose nanofibril hydrogel [382], polyisocyanopeptides (PIC)/ laminin-111 hydrogel mixture [383] have reported to produce functional hepatic organoids in a 3D setting, we could also explore the use of these surface substrates in current 2D platform to see if cellular architecture and maturation can be improved.

6.4 Conclusion and future perspective

Finally, due to the time constrain enforced by the global pandemics COVID19, further experiments were not able to be completed. The next step would include validation of eNOS as a biomarker, eNOS protein level can be evaluated by western blot. Ideally,

we would also want to cross-validate patient's serum samples for eNOS to determine whether low level of eNOS in MOPIK-HLCs correlates to homozygous *MTTP*-p.I564T SNV. Furthermore, we could generate MOPIK-HLCs and screen for potential new drug or do target gene editing to correct *MTTP*-p.I564T mutation.

Our *in vitro* model not only is an attractive model for cellular consequences in NAFLD steatosis, but the flexibility of our cell culture also allows modification and adjustment to model other liver diseases and their combined effects, such as alcoholic-liver fatty liver disease (AFLD) and hepatitis, with the addition of ethanol and hepatitis C virus exposure [384]–[386]. Additionally we can also examine how the inherent steatosis or fibrotic condition may play a role in the susceptibility of new type of pathogens, for example the severe acute respiratory syndrome coronavirus 2 (SARS-CoV-2) infection, resulting in current COVID-19 pandemics and elicit associated immune dysfunction contributing to higher mortality [387]. Use of hiPSC-HLCs steatosis model would be a much safer and sustainable approach to investigate the correlation between NAFLD and other diseases, as well as potential mechanical challenges to search for new therapeutic targets.

References

[1] M. L. Petroni, L. Brodosi, E. Bugianesi, and G. Marchesini, "Management of non-alcoholic fatty liver disease," *The BMJ*, vol. 372. BMJ Publishing Group, Jan. 18, 2021, doi: 10.1136/bmj.m4747.

[2] X. Ge, L. Zheng, M. Wang, Y. Du, and J. Jiang, "Prevalence trends in non-alcoholic fatty liver disease at the global, regional and national levels, 1990–2017: a population-based observational study," *BMJ Open*, vol. 10, no. 8, p. e036663, Aug. 2020, doi: 10.1136/BMJOPEN-2019-036663.

[3] M. A. Tincopa, J. Wong, M. Fetters, and A. S. Lok, "Patient disease knowledge, attitudes and behaviours related to non-alcoholic fatty liver disease: a qualitative study," *BMJ Open Gastro*, vol. 0, p. e000634, 2021, doi: 10.1136/bmjgast-2021-000634.

[4] K. Riazi, M. Raman, L. Taylor, M. G. Swain, and A. A. Shaheen, "Dietary Patterns and Components in Nonalcoholic Fatty Liver Disease (NAFLD): What Key Messages Can Health Care Providers Offer?," *Nutrients*, vol. 11, no. 12, Dec. 2019, doi: 10.3390/NU11122878.

[5] S. K. Sarin, M. Prasad, A. Ramalingam, and U. Kapil, "Integration of public health measures for NAFLD into India's national programme for NCDs," *Lancet Gastroenterol. Hepatol.*, vol. 6, no. 10, pp. 777–778, Oct. 2021, doi: 10.1016/S2468-1253(21)00264-8.

[6] E. Trefts, M. Gannon, and D. H. Wasserman, *The Liver*, vol. 27, no. 21. Cell Press, 2017, pp. R1147–R1151.

[7] K. Si-Tayeb, F. P. Lemaigre, and S. A. Duncan, "Organogenesis and Development of the Liver," *Dev. Cell*, vol. 18, no. 2, pp. 175–189, 2010, doi: 10.1016/j.devcel.2010.01.011.

[8] A. M. Zorn and J. M. Wells, "Molecular Basis of Vertebrate Endoderm Development," *Int. Rev. Cytol.*, vol. 259, pp. 49–111, 2007, doi: 10.1016/S0074-7696(06)59002-3.

[9] T. Kietzmann, "Metabolic zonation of the liver: The oxygen gradient revisited," *Redox Biol.*, vol. 11, pp. 622–630, Apr. 2017, doi: 10.1016/J.REDOX.2017.01.012.

[10] W. Birchmeier, "Orchestrating Wnt signalling for metabolic liver zonation," *Nat. Cell Biol. 2016 185*, vol. 18, no. 5, pp. 463–465, Apr. 2016, doi: 10.1038/NCB3349.

[11] M. Gordillo, T. Evans, and V. Gouon-Evans, "Orchestrating liver development.," *Development*, vol. 142, no. 12, pp. 2094–2108, Jun. 2015, doi: 10.1242/dev.114215.

[12] P. A. Gruppuso and J. A. Sanders, "Regulation of liver development: Implications for liver biology across the lifespan," *Journal of Molecular Endocrinology*, vol. 56, no. 3. BioScientifica Ltd., pp. R115–R125, Apr. 01, 2016, doi: 10.1530/JME-15-0313.

[13] L. Maroni *et al.*, "Functional and Structural Features of Cholangiocytes in Health and Disease," *CMGH*, vol. 1, no. 4. Elsevier Inc, pp. 368–380, Jul. 01, 2015, doi: 10.1016/j.jcmgh.2015.05.005.

[14] J. E. Puche, Y. Saiman, and S. L. Friedman, "Hepatic stellate cells and liver

fibrosis," *Compr. Physiol.*, vol. 3, no. 4, pp. 1473–1492, 2013, doi: 10.1002/cphy.c120035.

[15] C. Yin, K. J. Evason, K. Asahina, and D. Y. R. Stainier, "Hepatic stellate cells in liver development, regeneration, and cancer," *Journal of Clinical Investigation*, vol. 123, no. 5. American Society for Clinical Investigation, pp. 1902–1910, May 01, 2013, doi: 10.1172/JCI66369.

[16] B. Dewidar, C. Meyer, S. Dooley, and A. N. Meindl-Beinker, "TGF-β in Hepatic Stellate Cell Activation and Liver Fibrogenesis-Updated 2019," *Cells*, vol. 8, no. 11. NLM (Medline), Nov. 11, 2019, doi: 10.3390/cells8111419.

[17] A. T. Nguyen-Lefebvre and A. Horuzsko, "Kupffer Cell Metabolism and Function.," *J. Enzymol. Metab.*, vol. 1, no. 1, 2015, Accessed: Apr. 18, 2021. [Online]. Available: http://www.ncbi.nlm.nih.gov/pubmed/26937490.

[18] S. Shetty, P. F. Lalor, and D. H. Adams, "Liver sinusoidal endothelial cells — gatekeepers of hepatic immunity," *Nature Reviews Gastroenterology and Hepatology*, vol. 15, no. 9. Nature Publishing Group, pp. 555–567, Sep. 01, 2018, doi: 10.1038/s41575-018-0020-y.

[19] A. Hammoutene and P.-E. E. Rautou, "Role of liver sinusoidal endothelial cells in non-alcoholic fatty liver disease," *Journal of Hepatology*, vol. 70, no. 6. Elsevier B.V., pp. 1278–1291, Jun. 01, 2019, doi: 10.1016/j.jhep.2019.02.012.

[20] M. J. Watt, P. M. Miotto, W. De Nardo, and M. K. Montgomery, "The Liver as an Endocrine Organ - Linking NAFLD and Insulin Resistance," *Endocrine Reviews*, vol. 40, no. 5. Oxford University Press, pp. 1367–1393, May 10, 2019, doi: 10.1210/er.2019-00034.

[21] M. J. Armstrong, L. A. Adams, A. Canbay, and W.-K. Syn, "Extrahepatic complications of nonalcoholic fatty liver disease," *Hepatology*, vol. 59, no. 3, pp. 1174–1197, Mar. 2014, doi: 10.1002/hep.26717.

[22] Z. M. Younossi *et al.*, "The economic and clinical burden of nonalcoholic fatty liver disease in the United States and Europe," *Hepatology*, vol. 64, no. 5, pp. 1577–1586, 2016, doi: 10.1002/hep.28785.

[23] U. Frevert *et al.*, "Intravital Observation of Plasmodium berghei Sporozoite Infection of the Liver," *PLoS Biol.*, vol. 3, no. 6, p. e192, May 2005, doi: 10.1371/journal.pbio.0030192.

[24] S. M. Illustration, "Liver Structure – Sawchyn Medical Illustration," 2020. https://www.sawchynmi.com/sawchynportfolios/liver-structure/ (accessed Apr. 18, 2021).

[25] K. R. Feingold and C. Grunfeld, "Introduction to Lipids and Lipoproteins," *Endotext*, no. Figure 1, pp. 1–19, Feb. 2000, Accessed: Feb. 11, 2020. [Online]. Available: http://www.ncbi.nlm.nih.gov/pubmed/26247089.

[26] A. Zhyvotovska, D. Yusupov, and S. I. McFarlane, "Introductory Chapter: Overview of Lipoprotein Metabolism," in *Dyslipidemia*, IntechOpen, 2019.

[27] M. M. Hussain, P. Rava, M. Walsh, M. Rana, and J. Iqbal, "Multiple functions of microsomal triglyceride transfer protein," *Nutr.Metab (Lond).*, vol. 9:14. doi:, pp. 14–19, 2012, doi: 1743-7075-9-14 [pii];10.1186/1743-7075-9-14 [doi].

[28] A. Remmerie and C. L. Scott, "Macrophages and lipid metabolism," *Cell. Immunol.*, vol. 330, pp. 27–42, Aug. 2018, doi: 10.1016/j.cellimm.2018.01.020.

[29] V. Kumar, A. Abul, and A. Jon, *Robbins Basic Pathology*, 9th ed. Philadelphia, PA: Elsevier Saunders, 2012.

[30] N. Toshikuni, M. Tsutsumi, and T. Arisawa, “Clinical differences between alcoholic liver disease and nonalcoholic fatty liver disease,” *World J. Gastroenterol.*, vol. 20, no. 26, pp. 8393–8406, 2014, doi: 10.3748/wjg.v20.i26.8393.

[31] S. M. Abd El-Kader and E. M. S. El-Den Ashmawy, “Non-alcoholic fatty liver disease: The diagnosis and management,” *World J. Hepatol.*, vol. 7, no. 6, pp. 846–858, 2015, doi: 10.4254/wjh.v7.i6.846.

[32] D. Singh, C. J. Das, and M. P. Baruah, “Imaging of non alcoholic fatty liver disease: A road less travelled.,” *Indian J. Endocrinol. Metab.*, vol. 17, no. 6, pp. 990–5, 2013, doi: 10.4103/2230-8210.122606.

[33] T. Wilkins, A. Tadkod, I. Hepburn, and R. R. Schade, “Nonalcoholic fatty liver disease: diagnosis and management,” *Am Fam Physician*, vol. 88, no. 1, pp. 35–42, 2013, [Online]. Available: http://www.aafp.org/afp/2013/0701/p35.pdf%5Cnhttp://www.ncbi.nlm.nih.gov/pubmed/23939604%5Cnhttp://www.aafp.org/afp/2013/0701/p35.pdf.

[34] A. C. Tuyama and C. Y. Chang, “Non-alcoholic fatty liver disease,” *J. Diabetes*, vol. 4, no. 3, pp. 266–280, 2012, doi: 10.1111/j.1753-0407.2012.00204.x.

[35] Y. Takahashi and T. Fukusato, “Histopathology of nonalcoholic fatty liver disease/nonalcoholic steatohepatitis,” *World J. Gastroenterol.*, vol. 20, no. 42, pp. 15539–15548, 2014, doi: 10.3748/wjg.v20.i42.15539.

[36] F. Perla, M. Prelati, M. Lavorato, D. Visicchio, and C. Anania, “The Role of Lipid and Lipoprotein Metabolism in Non-Alcoholic Fatty Liver Disease,” *Children*, vol. 4, no. 6, p. 46, 2017, doi: 10.3390/children4060046.

[37] U. Iqbal, B. Perumpail, D. Akhtar, D. Kim, and A. Ahmed, “The Epidemiology, Risk Profiling and Diagnostic Challenges of Nonalcoholic Fatty Liver Disease,” *Medicines*, vol. 6, no. 1, p. 41, Mar. 2019, doi: 10.3390/medicines6010041.

[38] Z. M. Younossi, A. B. Koenig, D. Abdelatif, Y. Fazel, L. Henry, and M. Wymer, “Global epidemiology of nonalcoholic fatty liver disease—Meta-analytic assessment of prevalence, incidence, and outcomes,” *Hepatology*, vol. 64, no. 1, pp. 73–84, 2016, doi: 10.1002/hep.28431.

[39] British Society of Gastroenterology, “Commissioning report of NASH and non-alcoholic fatty liver disease,” 2009. [Online]. Available: http://www.bsg.org.uk/clinical/commissioning-report/nash-and-non-alcoholic-fatty-liver-disease.html.

[40] E. De la Cruz-Cano *et al.*, “Association between obesity and depression in patients with diabetes mellitus type 2; a study protocol,” *F1000Research*, 2015, doi: 10.12688/f1000research.5995.1.

[41] S. Mitra, A. De, and A. Chowdhury, “Epidemiology of non-alcoholic and alcoholic fatty liver diseases,” *Translational Gastroenterology and Hepatology*, vol. 5. AME Publishing Company, Jan. 05, 2020, doi: 10.21037/TGH.2019.09.08.

[42] M. C. S. Wong *et al.*, “The changing epidemiology of liver diseases in the Asia–Pacific region,” *Nature Reviews Gastroenterology and Hepatology*, vol. 16, no. 1. Nature Publishing Group, pp. 57–73, Jan. 01, 2019, doi: 10.1038/s41575-018-0055-0.

[43] J. Li *et al.*, “Prevalence, incidence, and outcome of non-alcoholic fatty liver disease in Asia, 1999–2019: a systematic review and meta-analysis,” *Lancet Gastroenterol. Hepatol.*, vol. 4, no. 5, pp. 389–398, May 2019, doi:

10.1016/S2468-1253(19)30039-1.
[44] J. G. Fan, S. U. Kim, and V. W. S. Wong, “New trends on obesity and NAFLD in Asia,” *Journal of Hepatology*, vol. 67, no. 4. Elsevier B.V., pp. 862–873, Oct. 01, 2017, doi: 10.1016/j.jhep.2017.06.003.
[45] C. Estes *et al.*, “Modelling NAFLD disease burden in four Asian regions—2019-2030,” *Aliment. Pharmacol. Ther.*, vol. 51, no. 8, pp. 801–811, Apr. 2020, doi: 10.1111/apt.15673.
[46] NHS Digital, “Health Survey for England 2014: Health, social care and lifestyles Summary of key findings,” 2015, [Online]. Available: http://www.hscic.gov.uk/catalogue/PUB19295/HSE2014-Sum-bklet.pdf.
[47] R. Williams *et al.*, “Addressing liver disease in the UK: A blueprint for attaining excellence in health care and reducing premature mortality from lifestyle issues of excess consumption of alcohol, obesity, and viral hepatitis,” *Lancet*, vol. 384, no. 9958, pp. 1953–1997, 2014, doi: 10.1016/S0140-6736(14)61838-9.
[48] K. Das *et al.*, “Nonobese population in a developing country has a high prevalence of nonalcoholic fatty liver and significant liver disease,” *Hepatology*, vol. 51, no. 5, pp. 1593–1602, May 2010, doi: 10.1002/hep.23567.
[49] K. Das and A. Chowdhury, “Lean NASH: Distinctiveness and clinical implication,” *Hepatology International*, vol. 7, no. 2. Springer India, pp. S806–S813, Dec. 01, 2013, doi: 10.1007/s12072-013-9477-5.
[50] Y. Eguchi *et al.*, “Visceral fat accumulation and insulin resistance are important factors in nonalcoholic fatty liver disease,” *J. Gastroenterol.*, vol. 41, no. 5, pp. 462–469, 2006, doi: 10.1007/s00535-006-1790-5.
[51] C. P. Day and O. F. W. James, “Steatohepatitis: A tale of two ‘Hits’?,” *Gastroenterology*, vol. 114, no. 4 I, pp. 842–845, 1998, doi: 10.1016/S0016-5085(98)70599-2.
[52] K. Fon Tacer and D. Rozman, “Nonalcoholic Fatty Liver Disease: Focus on Lipoprotein and Lipid Deregulation,” *J. Lipids*, vol. 2011, pp. 1–14, 2011, doi: 10.1155/2011/783976.
[53] J. P. Arab, M. Arrese, and M. Trauner, “Recent Insights into the Pathogenesis of Nonalcoholic Fatty Liver Disease,” *Annu. Rev. Pathol. Mech. Dis*, vol. 13, pp. 321–50, 2018, doi: 10.1146/annurev-pathol-020117.
[54] N. Magee, A. Zou, and Y. Zhang, “Pathogenesis of Nonalcoholic Steatohepatitis: Interactions between Liver Parenchymal and Nonparenchymal Cells,” *Biomed Res. Int.*, vol. 2016, 2016, doi: 10.1155/2016/5170402.
[55] C. L. Gentile, M. A. Frye, and M. J. Pagliassotti, “Fatty acids and the Endoplasmic Reticulum in Non-Alcoholic Fatty Liver Disease,” *Science (80-.).*, vol. 37, no. 1, pp. 8–16, 2011, doi: 10.1002/biof.135.Fatty.
[56] B. W. Smith and L. A. Adams, “Non-alcoholic fatty liver disease,” *Crit. Rev. Clin. Lab. Sci.*, vol. 48, no. 3, pp. 97–113, 2011, doi: 10.3109/10408363.2011.596521.
[57] H. Tilg and A. R. Moschen, “Evolution of inflammation in nonalcoholic fatty liver disease: The multiple parallel hits hypothesis,” *Hepatology*, vol. 52, no. 5, pp. 1836–1846, 2010, doi: 10.1002/hep.24001.
[58] B. A. Neuschwander-Tetri, “Hepatic lipotoxicity and the pathogenesis of nonalcoholic steatohepatitis: The central role of nontriglyceride fatty acid metabolites,” *Hepatology*, vol. 52, no. 2, pp. 774–788, 2010, doi:

10.1002/hep.23719.
[59] K. L. Donnelly, C. I. Smith, S. J. Schwarzenberg, J. Jessurun, M. D. Boldt, and E. J. Parks, “Sources of fatty acids stored in liver and secreted via lipoproteins in patients with nonalcoholic fatty liver disease,” *J. Clin. Invest.*, vol. 115, no. 5, pp. 1343–1351, 2005, Accessed: Apr. 19, 2021. [Online]. Available: /pmc/articles/PMC1087172/.
[60] C. Ress and S. Kaser, “Mechanisms of intrahepatic triglyceride accumulation,” *World J. Gastroenterol.*, vol. 22, no. 4, pp. 1664–1673, 2016, doi: 10.3748/wjg.v22.i4.1664.
[61] R. J. Thomas *et al.*, “Automated, scalable culture of human embryonic stem cells in feeder-free conditions,” *Biotechnol. Bioeng.*, vol. 102, no. 6, pp. 1636–1644, Apr. 2009, doi: 10.1002/bit.22187.
[62] S. L. Friedman, B. A. Neuschwander-Tetri, M. Rinella, and A. J. Sanyal, “Mechanisms of NAFLD development and therapeutic strategies,” *Nat. Med.*, vol. 24, no. 7, pp. 908–922, Jul. 2018, doi: 10.1038/s41591-018-0104-9.
[63] R. F. Schwabe, I. Tabas, and U. B. Pajvani, “Mechanisms of Fibrosis Development in Nonalcoholic Steatohepatitis,” *Gastroenterology*, vol. 158, no. 7, pp. 1913–1928, 2020, doi: 10.1053/j.gastro.2019.11.311.
[64] M. Ganz *et al.*, “Progression of non-alcoholic steatosis to steatohepatitis and fibrosis parallels cumulative accumulation of danger signals that promote inflammation and liver tumors in a high fat-cholesterol-sugar diet model in mice.,” *J. Transl. Med.*, vol. 13, p. 193, 2015, doi: 10.1186/s12967-015-0552-7.
[65] R. J. Perry, V. T. Samuel, K. F. Petersen, and G. I. Shulman, “The role of hepatic lipids in hepatic insulin resistance and type 2 diabetes,” *Nature*, vol. 510, no. 7503, pp. 84–91, 2014, doi: 10.1038/nature13478.
[66] P. Nguyen *et al.*, “Liver lipid metabolism,” vol. 92, pp. 272–283, 2008, doi: 10.1111/j.1439-0396.2007.00752.x.
[67] F. Nassir and J. Ibdah, “Role of Mitochondria in Nonalcoholic Fatty Liver Disease,” *Int. J. Mol. Sci.*, vol. 15, no. 5, pp. 8713–8742, 2014, doi: 10.3390/ijms15058713.
[68] X.-Q. Zhang, C.-F. Xu, C.-H. Yu, W.-X. Chen, and Y.-M. Li, “Role of endoplasmic reticulum stress in the pathogenesis of nonalcoholic fatty liver disease.,” *World J. Gastroenterol.*, vol. 20, no. 7, pp. 1768–1776, 2014, doi: 10.3748/wjg.v20.i7.1768.
[69] S. Jeyapal *et al.*, “Chronic consumption of fructose in combination with trans fatty acids but not with saturated fatty acids induces nonalcoholic steatohepatitis with fibrosis in rats,” *Eur. J. Nutr.*, Jul. 2017, doi: 10.1007/s00394-017-1492-1.
[70] K. Jarukamjorn, N. Jearapong, C. Pimson, and W. Chatuphonprasert, “A High-Fat, High-Fructose Diet Induces Antioxidant Imbalance and Increases the Risk and Progression of Nonalcoholic Fatty Liver Disease in Mice,” *Scientifica (Cairo).*, vol. 2016, 2016, doi: 10.1155/2016/5029414.
[71] M. F. Abdelmalek *et al.*, “Increased fructose consumption is associated with fibrosis severity in patients with nonalcoholic fatty liver disease,” *Hepatology*, vol. 51, no. 6, pp. 1961–1971, 2010, doi: 10.1002/hep.23535.
[72] J. S. Lee, D. W. Jun, E. K. Kim, H. J. Jeon, H. H. Nam, and W. K. Saeed, “Histologic and metabolic derangement in high-fat, high-fructose, and combination diet

animal models," *Sci. World J.*, vol. 2015, 2015, doi: 10.1155/2015/306326.
[73] S. BasuRay, E. Smagris, J. C. Cohen, and H. H. Hobbs, "The PNPLA3 variant associated with fatty liver disease (I148M) accumulates on lipid droplets by evading ubiquitylation," *Hepatology*, vol. 66, no. 4, pp. 1111–1124, Oct. 2017, doi: 10.1002/hep.29273.
[74] S. Prill *et al.*, "The TM6SF2 E167K genetic variant induces lipid biosynthesis and reduces apolipoprotein B secretion in human hepatic 3D spheroids," *Sci. Rep.*, vol. 9, no. 1, Dec. 2019, doi: 10.1038/s41598-019-47737-w.
[75] N. L. Beer *et al.*, "The P446L variant in GCKR associated with fasting plasma glucose and triglyceride levels exerts its effect through increased glucokinase activity in liver," *Hum. Mol. Genet.*, vol. 18, no. 21, pp. 4081–4088, Nov. 2009, doi: 10.1093/hmg/ddp357.
[76] P. Pingitore and S. Romeo, "The role of PNPLA3 in health and disease," *Biochimica et Biophysica Acta - Molecular and Cell Biology of Lipids*, vol. 1864, no. 6. Elsevier B.V., pp. 900–906, Jun. 01, 2019, doi: 10.1016/j.bbalip.2018.06.018.
[77] H. C. Lee *et al.*, "Caenorhabditis elegans mboa-7, a member of the MBOAT family, is required for selective incorporation of polyunsaturated fatty acids into phosphatidylinositol," *Mol. Biol. Cell*, vol. 19, no. 3, pp. 1174–1184, Mar. 2008, doi: 10.1091/mbc.E07-09-0893.
[78] S. Buch *et al.*, "A genome-wide association study confirms PNPLA3 and identifies TM6SF2 and MBOAT7 as risk loci for alcohol-related cirrhosis," *Nat. Genet.*, vol. 47, no. 12, pp. 1443–1448, Dec. 2015, doi: 10.1038/ng.3417.
[79] F. S. Macaluso, M. Maida, and S. Petta, "Genetic background in nonalcoholic fatty liver disease: A comprehensive review," *World J. Gastroenterol.*, vol. 21, no. 39, pp. 11088–11111, 2015, doi: 10.3748/wjg.v21.i39.11088.
[80] A. J. Hooper, L. a Adams, and J. R. Burnett, "Genetic determinants of hepatic steatosis in man.," *J. Lipid Res.*, vol. 52, pp. 593–617, 2011, doi: 10.1194/jlr.R008896.
[81] R. S. Mcleod and Z. Yao, "Assembly and Secretion of Triglyceride-Rich Lipoproteins," in *Biochemistry of Lipids, Lipoproteins and Membranes.*, 6th ed., J. Leonard, Ed. 2016, pp. 459–488.
[82] M. M. Hussain, J. Shi, and P. Dreizen, "Microsomal triglyceride transfer protein and its role in apoB-lipoprotein assembly," *J. Lipid Res.*, vol. 44, no. 1, pp. 22–32, 2003, doi: 10.1194/jlr.R200014-JLR200.
[83] S. Rustaeus, P. Stillemark, K. Lindberg, D. Gordon, and S. O. Olofsson, "The microsomal triglyceride transfer protein catalyzes the post- translational assembly of apolipoprotein B-100 very low density lipoprotein in McA-RH7777 cells," *J. Biol. Chem.*, vol. 273, no. 9, pp. 5196–5203, Feb. 1998, doi: 10.1074/jbc.273.9.5196.
[84] J. R. Burnett, A. J. Hooper, and R. A. Hegele, *Abetalipoproteinemia*. University of Washington, Seattle, 2018.
[85] M. Di Filippo *et al.*, "Molecular and functional analysis of two new MTTP gene mutations in an atypical case of abetalipoproteinemia," *J. Lipid Res.*, vol. 53, no. 3, pp. 548–555, Mar. 2012, doi: 10.1194/jlr.M020024.
[86] M. Di Filippo *et al.*, "Homozygous MTTP and APOB mutations may lead to hepatic steatosis and fibrosis despite metabolic differences in congenital

hypocholesterolemia," 2014. Accessed: Oct. 22, 2020. [Online]. Available: http://genetics.bwh.harvard.edu/pph/.

[87] A. Aminoff *et al.*, "Allele-specifi c regulation of MTTP expression infl uences the risk of ischemic heart disease," *J. Lipid Res.*, vol. 51, pp. 103–111, 2010, doi: 10.1194/jlr.M900195-JLR200.

[88] T. V. G. Prata *et al.*, "MTTP polymorphisms and hepatic steatosis in individuals chronically infected with hepatitis C virus," *Arch. Virol.*, vol. 164, no. 10, pp. 2559–2563, Oct. 2019, doi: 10.1007/s00705-019-04352-4.

[89] C. Namikawa *et al.*, "Polymorphisms of microsomal triglyceride transfer protein gene and manganese superoxide dismutase gene in non-alcoholic steatohepatitis," *J. Hepatol.*, vol. 40, no. 5, pp. 781–786, May 2004, doi: 10.1016/j.jhep.2004.01.028.

[90] A. J. Hooper, J. R. Burnett, and G. F. Watts, "Contemporary aspects of the biology and therapeutic regulation of the microsomal triglyceride transfer protein," *Circ. Res.*, vol. 116, no. 1, pp. 193–205, 2015, doi: 10.1161/CIRCRESAHA.116.304637.

[91] C. J. Mann *et al.*, "The structure of vitellogenin provides a molecular model for the assembly and secretion of atherogenic lipoproteins," *J. Mol. Biol.*, vol. 285, no. 1, pp. 391–408, Jan. 1999, doi: 10.1006/jmbi.1998.2298.

[92] P. Bradbury *et al.*, "A common binding site on the microsomal triglyceride transfer protein for apolipoprotein B and protein disulfide isomerase," *J. Biol. Chem.*, vol. 274, no. 5, pp. 3159–3164, Jan. 1999, doi: 10.1074/jbc.274.5.3159.

[93] E. I. Biterova *et al.*, "The crystal structure of human microsomal triglyceride transfer protein," *Proc. Natl. Acad. Sci. U. S. A.*, vol. 116, no. 35, pp. 17251–17260, 2019, doi: 10.1073/pnas.1903029116.

[94] C. H. M. Rodrigues, D. E. V. Pires, and D. B. Ascher, "DynaMut: Predicting the impact of mutations on protein conformation, flexibility and stability," *Nucleic Acids Res.*, vol. 46, no. W1, pp. W350–W355, Jul. 2018, doi: 10.1093/nar/gky300.

[95] K. Nagaoka *et al.*, "The metabolite, alpha-ketoglutarate inhibits non-alcoholic fatty liver disease progression by targeting lipid metabolism," *Liver Res.*, vol. 4, no. 2, pp. 94–100, Jun. 2020, doi: 10.1016/j.livres.2020.04.001.

[96] F. Haczeyni *et al.*, "The selective peroxisome proliferator-activated receptor-delta agonist seladelpar reverses nonalcoholic steatohepatitis pathology by abrogating lipotoxicity in diabetic obese mice," *Hepatol. Commun.*, vol. 1, no. 7, pp. 663–674, Sep. 2017, doi: 10.1002/hep4.1072.

[97] R. B. d. Oliveira *et al.*, "Impaired compensatory beta-cell function and growth in response to high-fat diet in LDL receptor knockout mice," *Int. J. Exp. Pathol.*, vol. 95, no. 4, pp. 296–308, 2014, doi: 10.1111/iep.12084.

[98] X. Pan, J. Queiroz, and M. M. Hussain, "Nonalcoholic fatty liver disease in CLOCK mutant mice," *J. Clin. Invest.*, vol. 140, no. 8, pp. 4282–4300, Aug. 2020, doi: 10.1172/JCI132765.

[99] L. Grumet *et al.*, "Lysosomal acid lipase hydrolyzes retinyl ester and affects retinoid turnover," *J. Biol. Chem.*, vol. 291, no. 34, pp. 17977–17987, Aug. 2016, doi: 10.1074/jbc.M116.724054.

[100] M. Liebig, D. Dannenberger, B. Vollmar, and K. Abshagen, "Endogenously increased n-3 PUFA levels in fat-1 transgenic mice do not protect from non-

alcoholic steatohepatitis," *HepatoBiliary Surg. Nutr.*, vol. 8, no. 5, pp. 447–458, Oct. 2019, doi: 10.21037/hbsn.2019.04.03.
[101] "Lack of Efficacy of an Inhibitor of PDE4 in Phase 1 and 2 Trials ofPatients With Nonalcoholic Steatohepatitis," *Clin. Gastroenterol. Hepatol.*, vol. 12, no. 10, pp. 1724-1730.e5, Oct. 2014, doi: 10.1016/j.cgh.2014.01.040.
[102] Y. Nakade *et al.*, "Ezetimibe for the treatment of non-alcoholic fatty liver disease: A meta-analysis," *Hepatol. Res.*, vol. 47, no. 13, pp. 1417–1428, Dec. 2017, doi: 10.1111/hepr.12887.
[103] V. S. Chachay *et al.*, "Resveratrol Does Not Benefit Patients With Nonalcoholic Fatty Liver Disease," *Clin. Gastroenterol. Hepatol.*, vol. 12, no. 12, pp. 2092-2103.e6, Dec. 2014, doi: 10.1016/j.cgh.2014.02.024.
[104] T. Kostrzewski *et al.*, "A Microphysiological System for Studying Nonalcoholic Steatohepatitis," *Hepatol. Commun.*, vol. 4, no. 1, pp. 77–91, Jan. 2020, doi: 10.1002/hep4.1450.
[105] A. Kermanizadeh, D. M. Brown, W. Moritz, and V. Stone, "The importance of inter-individual Kupffer cell variability in the governance of hepatic toxicity in a 3D primary human liver microtissue model," *Sci. Rep.*, vol. 9, no. 1, pp. 1–9, Dec. 2019, doi: 10.1038/s41598-019-43870-8.
[106] B. M. Kim, A. M. Abdelfattah, R. Vasan, B. C. Fuchs, and M. Y. Choi, "Hepatic stellate cells secrete Ccl5 to induce hepatocyte steatosis," *Sci. Rep.*, vol. 8, no. 1, pp. 1–10, Dec. 2018, doi: 10.1038/s41598-018-25699-9.
[107] M. Kozyra, I. Johansson, Å. Nordling, S. Ullah, V. M. Lauschke, and M. Ingelman-Sundberg, "Human hepatic 3D spheroids as a model for steatosis and insulin resistance," *Sci. Rep.*, vol. 8, no. 1, p. 14297, Dec. 2018, doi: 10.1038/s41598-018-32722-6.
[108] A. Zou, N. Magee, F. Deng, S. Lehn, C. Zhong, and X. Yuxia Zhang, "Hepatocyte nuclear receptor SHP suppresses inflammation and fibrosis in a mouse model of nonalcoholic steatohepatitis and the," *J. Biol. Chem*, no. 22, pp. 8656–8671, 2018, doi: 10.1074/jbc.RA117.001653.
[109] F. Jung, T. Lippmann, A. Brandt, C. J. Jin, A. J. Engstler, and A. Baumann, "Moderate consumption of fermented alcoholic beverages diminishes diet-induced non-alcoholic fatty liver disease through mechanisms involving hepatic adiponectin signaling in mice," *Eur. J. Nutr.*, vol. 59, no. 2, pp. 787–799, Mar. 2020, doi: 10.1007/s00394-019-01945-2.
[110] E. M. Maldonado *et al.*, "Multi-scale, whole-system models of liver metabolic adaptation to fat and sugar in non-alcoholic fatty liver disease," *npj Syst. Biol. Appl.*, vol. 4, no. 1, p. 33, Dec. 2018, doi: 10.1038/s41540-018-0070-3.
[111] D. Knobeloch *et al.*, "Human hepatocytes: Isolation, culture, and quality procedures," *Methods Mol. Biol.*, vol. 806, pp. 99–120, 2012, doi: 10.1007/978-1-61779-367-7_8.
[112] M. Kiamehr *et al.*, "Dedifferentiation of primary hepatocytes is accompanied with reorganization of lipid metabolism indicated by altered molecular lipid and miRNA profiles," *Int. J. Mol. Sci.*, vol. 20, no. 12, p. 2910, Jun. 2019, doi: 10.3390/ijms20122910.
[113] E. Ramboer, T. Vanhaecke, V. Rogiers, and M. Vinken, "Immortalized human hepatic cell lines for in vitro testing and research purposes," *Methods Mol Biol.*, vol. 1250, pp. 53–76, 2015, doi: 10.1007/978-1-4939-2074-7.

[114] E. Ramboer *et al.*, “Strategies for immortalization of primary hepatocytes,” *Journal of Hepatology*, vol. 61, no. 4. Elsevier B.V., pp. 925–943, 2014, doi: 10.1016/j.jhep.2014.05.046.
[115] A. Molinaro, B. Becattini, and G. Solinas, “Insulin signaling and glucose metabolism in different hepatoma cell lines deviate from hepatocyte physiology toward a convergent aberrant phenotype,” *Sci. Rep.*, vol. 10, no. 1, pp. 1–10, Dec. 2020, doi: 10.1038/s41598-020-68721-9.
[116] G. Pettinato, R. Ramanathan, R. A. Fisher, M. J. Mangino, N. Zhang, and X. Wen, “Scalable Differentiation of Human iPSCs in a Multicellular Spheroid-based 3D Culture into Hepatocyte-like Cells through Direct Wnt/β-catenin Pathway Inhibition,” *Sci. Rep.*, vol. 6, Sep. 2016, doi: 10.1038/srep32888.
[117] M. Kiamehr *et al.*, “hiPSC-derived hepatocytes closely mimic the lipid profile of primary hepatocytes: A future personalised cell model for studying the lipid metabolism of the liver,” *J. Cell. Physiol.*, vol. 234, no. 4, pp. 3744–3761, Apr. 2019, doi: 10.1002/jcp.27131.
[118] M. Parafati, R. J. Kirby, S. Khorasanizadeh, F. Rastinejad, and S. Malany, “A nonalcoholic fatty liver disease model in human induced pluripotent stem cell-derived hepatocytes, created by endoplasmic reticulum stress-induced steatosis,” *Dis. Model. Mech.*, vol. 11, no. 9, p. dmm033530, Sep. 2018, doi: 10.1242/dmm.033530.
[119] N. Graffmann *et al.*, “Modeling Nonalcoholic Fatty Liver Disease with Human Pluripotent Stem Cell-Derived Immature Hepatocyte-Like Cells Reveals Activation of PLIN2 and Confirms Regulatory Functions of Peroxisome Proliferator-Activated Receptor Alpha,” *Stem Cells Dev.*, vol. 25, no. 15, pp. 1119–1133, Aug. 2016, doi: 10.1089/scd.2015.0383.
[120] A. Carpentier, I. Nimgaonkar, V. Chu, Y. Xia, Z. Hu, and T. J. Liang, “Hepatic differentiation of human pluripotent stem cells in miniaturized format suitable for high-throughput screen.,” *Stem Cell Res.*, vol. 16, no. 3, pp. 640–650, 2016, doi: 10.1016/j.scr.2016.03.009.
[121] A. C. De L’hortet, K. Takeishi, J. Guzman-Lepe, C.-X. Deng, D. Nagrath, and A. Soto-Gutierrez, “Generation of Human Fatty Livers Using Custom-Engineered Induced Pluripotent Stem Cells with Modifiable SIRT1 Metabolism,” *Cell Metab.*, vol. 30, pp. 385–401, 2019, doi: 10.1016/j.cmet.2019.06.017.
[122] S. J. Forbes, S. Gupta, and A. Dhawan, “Cell therapy for liver disease: From liver transplantation to cell factory,” *J. Hepatol.*, vol. 62, no. S1, pp. S157–S169, 2015, doi: 10.1016/j.jhep.2015.02.040.
[123] F. Sampaziotis, C.-P. Segeritz, and L. Vallier, “Potential of human induced pluripotent stem cells in studies of liver disease,” *Hepatology*, vol. 62, no. 1, pp. 303–311, 2015, doi: 10.1002/hep.27651.
[124] C. Nicolas, Y. Wang, J. Luebke-Wheeler, and S. Nyberg, “Stem Cell Therapies for Treatment of Liver Disease,” *Biomedicines*, vol. 4, no. 1, p. 2, 2016, doi: 10.3390/biomedicines4010002.
[125] J. Meseguer-Ripolles, S. R. Khetani, J. G. Blanco, M. Iredale, and D. C. Hay, “Pluripotent Stem Cell-Derived Human Tissue: Platforms to Evaluate Drug Metabolism and Safety,” *AAPS J.*, vol. 20, no. 1, p. 20, 2018, doi: 10.1208/s12248-017-0171-8.
[126] A. Messina, E. Luce, M. Hussein, and A. Dubart-Kupperschmitt, “Pluripotent-

Stem-Cell-Derived Hepatic Cells: Hepatocytes and Organoids for Liver Therapy and Regeneration," *Cells*, vol. 9, no. 2. NLM (Medline), Feb. 12, 2020, doi: 10.3390/cells9020420.

[127] M. Kiamehr *et al.*, "Lipidomic profiling of patient-specific induced pluripotent stem cell-derived hepatocyte-like cells," *Dis. Model. Mech.*, p. dmm.030841, 2017, doi: 10.1242/dmm.030841.

[128] Y. Choudhury *et al.*, "Patient-specific hepatocyte-like cells derived from induced pluripotent stem cells model pazopanib-mediated hepatotoxicity," *Sci. Rep.*, vol. 7, p. 41238, 2017, doi: 10.1038/srep41238.

[129] D. J. Messner, B. H. Rhieu, and K. V Kowdley, "Iron overload causes oxidative stress and impaired insulin signaling in AML-12 hepatocytes," doi: 10.1007/s10620-013-2648-3.

[130] M. N. Bin Ramli *et al.*, "Human Pluripotent Stem Cell-Derived Organoids as Models of Liver Disease," *Gastroenterology*, vol. 159, no. 4, pp. 1471-1486.e12, Oct. 2020, doi: 10.1053/j.gastro.2020.06.010.

[131] M. C. Sinton *et al.*, "A human pluripotent stem cell model for the analysis of metabolic dysfunction in hepatic steatosis," *iScience*, vol. 24, no. 1, p. 101931, Jan. 2021, doi: 10.1016/j.isci.2020.101931.

[132] R. Ouchi, S. Togo, M. Kimura, H. Y. Yoshikawa, and J. M. Wells, "Modeling Steatohepatitis in Humans with Pluripotent Stem Cell-Derived Organoids," *Cell Metab.*, vol. 30, pp. 374–384, 2019, doi: 10.1016/j.cmet.2019.05.007.

[133] B. Lucendo-Villarin *et al.*, "Development of a cost-effective automated platform to produce human liver spheroids for basic and applied research," *Biofabrication*, vol. 13, no. 1, p. 015009, Dec. 2020, doi: 10.1088/1758-5090/abbdb2.

[134] G. Chen *et al.*, "Chemically defined conditions for human iPSC derivation and culture," *Nat. Methods*, vol. 8, no. 5, pp. 424–429, May 2011, doi: 10.1038/nmeth.1593.

[135] P. W. Burridge *et al.*, "Chemically defned generation of human cardiomyocytes," *Nat. Methods*, vol. 11, no. 8, pp. 855–860, 2014, doi: 10.1038/nMeth.2999.

[136] L. Vallier *et al.*, "Early cell fate decisions of human embryonic stem cells and mouse epiblast stem cells are controlled by the same signalling pathways," *PLoS One*, vol. 4, no. 6, p. e6082, 2009, doi: 10.1371/journal.pone.0006082.

[137] D. C. Hay *et al.*, "Highly efficient differentiation of hESCs to functional hepatic endoderm requires ActivinA and Wnt3a signaling," *Proc. Natl. Acad. Sci. U. S. A.*, vol. 105, no. 34, pp. 12301–12306, Aug. 2008, doi: 10.1073/pnas.0806522105.

[138] N. R. F. Hannan *et al.*, "Generation of multipotent foregut stem cells from human pluripotent stem cells," *Stem Cell Reports*, vol. 1, no. 4, pp. 293–306, 2013, doi: 10.1016/j.stemcr.2013.09.003.

[139] R. L. Gieseck *et al.*, "Maturation of induced pluripotent stem cell derived hepatocytes by 3D-culture," *PLoS One*, vol. 9, no. 1, p. e86372, 2014, doi: 10.1371/journal.pone.0086372.

[140] K. L. Fair, J. Colquhoun, and N. R. F. Hannan, "Intestinal organoids for modelling intestinal development and disease," 2018.

[141] J. R. Spence *et al.*, "Directed differentiation of human pluripotent stem cells

into intestinal tissue in vitro," *Nature*, vol. 470, no. 7332, pp. 105–110, Feb. 2011, doi: 10.1038/nature09691.
[142] G. Chen *et al.*, "Chemically defined conditions for human iPS cell derivation and culture," *Nat Methods*, vol. 8, no. 5, pp. 424–429, 2011, doi: 10.1038/nmeth.1593.Chemically.
[143] V. R. Cicinnati, Q. Shen, G. C. Sotiropoulos, A. Radtke, G. Gerken, and S. Beckebaum, "Validation of putative reference genes for gene expression studies in human hepatocellular carcinoma using real-time quantitative RT-PCR," *BMC Cancer*, vol. 8, Nov. 2008, doi: 10.1186/1471-2407-8-350.
[144] S. Wang, B. Wang, H. He, A. Sun, and C. Guo, "A new set of reference housekeeping genes for the normalization RT-qPCR data from the intestine of piglets during weaning," *PLoS One*, vol. 13, no. 9, Sep. 2018, doi: 10.1371/JOURNAL.PONE.0204583.
[145] H. R. Ahn *et al.*, "HMBS is the most suitable reference gene for RT-qPCR in human HCC tissues and blood samples," *Oncol. Lett.*, vol. 22, no. 5, Nov. 2021, doi: 10.3892/OL.2021.13052.
[146] J. Zhang, Y. Y. Gao, Y. Q. Huang, Q. Fan, X. T. Lu, and C. K. Wang, "Selection of housekeeping genes for quantitative gene expression analysis in yellow-feathered broilers," *https://doi-org.nottingham.idm.oclc.org/10.1080/1828051X.2017.1365633*, vol. 17, no. 2, pp. 540–546, Apr. 2017, doi: 10.1080/1828051X.2017.1365633.
[147] H. Priddle *et al.*, "Derivation and characterisation of the human embryonic stem cell lines, NOTT1 and NOTT2," *Vitr. Cell. Dev. Biol. - Anim.*, vol. 46, pp. 367–375, 2010, doi: 10.1007/s11626-010-9290-6.
[148] ISCN, *ISCN 2005 : an international system for human cytogenetic nomenclature (2005) : recommendations of the International Standing Committee on Human Cytogenetic Nomenclature*. Karger, 2005.
[149] R. J. Havel, H. A. Eder, and J. H. Bragdon, "The distribution and chemical composition of ultracentrifugally separated lipoproteins in human serum.," *J. Clin. Invest.*, vol. 34, no. 9, pp. 1345–1353, 1955, doi: 10.1172/JCI103182.
[150] A. Surrati, R. Linforth, I. D. Fisk, V. Sottile, and D.-H. Kim, "Non-destructive characterisation of mesenchymal stem cell differentiation using LC-MS-based metabolite footprinting," *Analyst*, vol. 141, no. 12, pp. 3776–3787, Jun. 2016, doi: 10.1039/C6AN00170J.
[151] J. R. Burnett, D. A. Bell, A. J. Hooper, and R. A. Hegele, "Clinical utility gene card for: Abetalipoproteinaemia," *Eur. J. Hum. Genet.*, vol. 20, p. 20, 2012, doi: 10.1038/ejhg.2012.30.
[152] C. C. Shoulders *et al.*, "Abetalipoproteinemia is caused by defects of the gene encoding the 97 kDa subunit of a microsomal triglyceride transfer protein," 1993. Accessed: Oct. 18, 2020. [Online]. Available: https://academic.oup.com/hmg/article/2/12/2109/649158.
[153] D. Sharp *et al.*, "Cloning and gene defects in microsomal triglyceride transfer protein associated with abetalipoproteinaemia," *Nature*, vol. 365, pp. 65–69, 1993, Accessed: Jul. 06, 2020. [Online]. Available: https://www-nature-com.ezproxy.nottingham.ac.uk/articles/365065a0.pdf.
[154] M. Gene *et al.*, "Functional Analysis of Promoter Variants in the Microsomal Triglyceride Transfer Protein," vol. 29, no. September 2007, pp. 123–129, 2008,

doi: 10.1002/humu.
[155] K. Takahashi and S. Yamanaka, “Induction of Pluripotent Stem Cells from Mouse Embryonic and Adult Fibroblast Cultures by Defined Factors,” *Cell*, vol. 126, no. 4, pp. 663–676, 2006, doi: 10.1016/j.cell.2006.07.024.
[156] K. Takahashi *et al.*, “Induction of Pluripotent Stem Cells from Adult Human Fibroblasts by Defined Factors,” *Cell*, vol. 131, no. 5, pp. 861–872, 2007, doi: 10.1016/j.cell.2007.11.019.
[157] J. Yu *et al.*, “Human Induced Pluripotent Stem Cells Free of Vector and Transgene Sequences,” *Science (80-.).*, vol. 324, no. 5928, pp. 797–801, 2009, doi: 10.1126/science.1172482.
[158] J. Toombs *et al.*, “Lab Resource: Multiple Cell Lines Generation of twenty four induced pluripotent stem cell lines from twenty four members of the Lothian Birth Cohort 1936,” *Stem Cell Res.*, vol. 46, p. 101851, 2020, doi: 10.1016/j.scr.2020.101851.
[159] J. M. Churko, P. W. Burridge, and J. C. Wu, “Generation of human iPSCs from human peripheral blood mononuclear cells using non-integrative sendai virus in chemically defined conditions,” *Methods Mol. Biol.*, vol. 1036, pp. 81–88, 2013, doi: 10.1007/978-1-62703-511-8_7.
[160] I. H. Park *et al.*, “Reprogramming of human somatic cells to pluripotency with defined factors,” *Nature*, vol. 451, no. 7175, pp. 141–146, Jan. 2008, doi: 10.1038/nature06534.
[161] T. Zhou *et al.*, “Generation of human induced pluripotent stem cells from urine samples,” *Nat. Protoc.*, vol. 7, no. 12, pp. 2080–2089, 2012, doi: 10.1038/nprot.2012.115.
[162] R. V. Pisal *et al.*, “Directed reprogramming of comprehensively characterized dental pulp stem cells extracted from natal tooth,” *Sci. Rep.*, vol. 8, no. 1, pp. 1–13, Dec. 2018, doi: 10.1038/s41598-018-24421-z.
[163] S. Re *et al.*, “Improved generation of induced pluripotent stem cells from hair derived keratinocytes – A tool to study neurodevelopmental disorders as ADHD,” *Front. Cell. Neurosci.*, vol. 12, 2018, doi: 10.3389/fncel.2018.00321.
[164] N. Sun *et al.*, “Feeder-free derivation of induced pluripotent stem cells from adult human adipose stem cells,” *Proc. Natl. Acad. Sci. U. S. A.*, vol. 106, no. 37, pp. 15720–15725, Sep. 2009, doi: 10.1073/pnas.0908450106.
[165] K. Y. Kim, E. Hysolli, and I. H. Park, “Reprogramming human somatic cells into induced pluripotent stem cells (iPSCs) using retroviral vector with GFP,” *J. Vis. Exp.*, no. 62, p. 3804, Apr. 2012, doi: 10.3791/3804.
[166] A. Hotta and J. Ellis, “Retroviral vector silencing during iPS cell induction: An epigenetic beacon that signals distinct pluripotent states,” *Journal of Cellular Biochemistry*, vol. 105, no. 4. John Wiley & Sons, Ltd, pp. 940–948, Jan. 11, 2008, doi: 10.1002/jcb.21912.
[167] K. Takahashi, T. Ichisaka, and S. Yamanaka, “Identification of genes involved in tumor-like properties of embryonic stem cells.,” *Methods Mol. Biol.*, vol. 329, pp. 449–458, 2006, doi: 10.1385/1-59745-037-5:449.
[168] S. Yamanaka, “A Fresh Look at iPS Cells,” *Cell*, vol. 137, no. 1. Cell Press, pp. 13–17, Apr. 03, 2009, doi: 10.1016/j.cell.2009.03.034.
[169] W. Zhou and C. R. Freed, “Adenoviral gene delivery can reprogram human fibroblasts to induced pluripotent stem cells,” *Stem Cells*, vol. 27, no. 11, pp.

2667–2674, Nov. 2009, doi: 10.1002/stem.201.
[170] K. Kaji, K. Norrby, A. Paca, M. Mileikovsky, P. Mohseni, and K. Woltjen, “Virus-free induction of pluripotency and subsequent excision of reprogramming factors,” *Nature*, vol. 458, no. 7239, pp. 771–775, Apr. 2009, doi: 10.1038/nature07864.
[171] K. Woltjen *et al.*, “PiggyBac transposition reprograms fibroblasts to induced pluripotent stem cells,” *Nature*, vol. 458, no. 7239, pp. 766–770, Apr. 2009, doi: 10.1038/nature07863.
[172] J. S. Bang *et al.*, “Optimization of episomal reprogramming for generation of human induced pluripotent stem cells from fibroblasts,” *Animal Cells Syst. (Seoul).*, vol. 22, no. 2, pp. 132–139, Mar. 2018, doi: 10.1080/19768354.2018.1451367.
[173] L. Warren *et al.*, “Highly efficient reprogramming to pluripotency and directed differentiation of human cells with synthetic modified mRNA,” *Cell Stem Cell*, vol. 7, no. 5, pp. 618–630, Nov. 2010, doi: 10.1016/j.stem.2010.08.012.
[174] D. Kim *et al.*, “Generation of Human Induced Pluripotent Stem Cells by Direct Delivery of Reprogramming Proteins,” *Cell Stem Cell*, vol. 4, no. 6. Cell Stem Cell, pp. 472–476, Jun. 05, 2009, doi: 10.1016/j.stem.2009.05.005.
[175] N. Fusaki, H. Ban, A. Nishiyama, K. Saeki, and M. Hasegawa, “Efficient induction of transgene-free human pluripotent stem cells using a vector based on Sendai virus, an RNA virus that does not integrate into the host genome.,” *Proc. Jpn. Acad. Ser. B. Phys. Biol. Sci.*, vol. 85, no. 8, pp. 348–362, 2009, doi: 10.2183/PJAB.85.348.
[176] T. Okumura *et al.*, “Robust and highly efficient hiPSC generation from patient non-mobilized peripheral blood-derived CD34+ cells using the auto-erasable Sendai virus vector,” *Stem Cell Res. Ther.*, vol. 10, no. 1, p. 185, Jun. 2019, doi: 10.1186/s13287-019-1273-2.
[177] K. Nishimura *et al.*, “Simple and effective generation of transgene-free induced pluripotent stem cells using an auto-erasable Sendai virus vector responding to microRNA-302-NC-ND license (http://creativecommons.org/licenses/by-nc-nd/4.0/),” 2017, doi: 10.1016/j.scr.2017.06.011.
[178] J. Sochacki, S. Devalle, M. Reis, P. Mattos, and S. Rehen, “Generation of urine iPS cell lines from patients with Attention Deficit Hyperactivity Disorder (ADHD) using a non-integrative method,” *Stem Cell Res.*, vol. 17, no. 1, pp. 102–106, Jul. 2016, doi: 10.1016/j.scr.2016.05.015.
[179] A. Al Abbar, S. C. Ngai, N. Nograles, S. Y. Alhaji, and S. Abdullah, “Induced Pluripotent Stem Cells: Reprogramming Platforms and Applications in Cell Replacement Therapy,” *Biores. Open Access*, vol. 9, no. 1, pp. 121–136, Apr. 2020, doi: 10.1089/biores.2019.0046.
[180] Q. Liu, D. J. Segal, J. B. Ghiara, and C. F. Barbas, “Design of polydactyl zinc-finger proteins for unique addressing within complex genomes,” *Proc. Natl. Acad. Sci. U. S. A.*, vol. 94, no. 11, pp. 5525–5530, May 1997, doi: 10.1073/pnas.94.11.5525.
[181] J. K. Joung and J. D. Sander, “TALENs: A widely applicable technology for targeted genome editing,” *Nature Reviews Molecular Cell Biology*, vol. 14, no. 1. NIH Public Access, pp. 49–55, Jan. 2013, doi: 10.1038/nrm3486.
[182] R. Barrangou and J. A. Doudna, “Applications of CRISPR technologies in

research and beyond," *Nat. Biotechnol.*, vol. 34, no. 9, pp. 933–941, Sep. 2016, doi: 10.1038/nbt.3659.
[183] N. Brookhouser, S. Raman, C. Potts, and D. Brafman, "May I Cut in? Gene Editing Approaches in Human Induced Pluripotent Stem Cells," *Cells*, vol. 6, no. 1, p. 5, 2017, doi: 10.3390/cells6010005.
[184] B. Wiedenheft, S. H. Sternberg, and J. A. Doudna, "RNA-guided genetic silencing systems in bacteria and archaea," *Nature*, vol. 482, no. 7385, pp. 331–338, 2012, doi: 10.1038/nature10886.
[185] F. A. Ran, P. D. Hsu, J. Wright, V. Agarwala, D. A. Scott, and F. Zhang, "Genome engineering using the CRISPR-Cas9 system," *Nat. Protoc.*, vol. 8, no. 11, pp. 2281–2308, 2013, doi: 10.1038/nprot.2013.143.
[186] K. P. Ringer *et al.*, "Comparative analysis of lipid-mediated CRISPR-Cas9 genome editing techniques," *Cell Biol. Int.*, vol. 42, no. 7, pp. 849–858, Jul. 2018, doi: 10.1002/cbin.10952.
[187] X. Xu *et al.*, "Efficient homology-directed gene editing by CRISPR/Cas9 in human stem and primary cells using tube electroporation," *Sci. Rep.*, vol. 8, no. 1, pp. 1–11, Dec. 2018, doi: 10.1038/s41598-018-30227-w.
[188] T. Borgonovo, I. M. Vaz, A. C. Senegaglia, C. L. K. Rebelatto, and P. R. S. Brofman, "Genetic evaluation of mesenchymal stem cells by G-banded karyotyping in a Cell Technology Center," *Rev. Bras. Hematol. Hemoter.*, vol. 36, no. 3, p. 202, May 2014, doi: 10.1016/J.BJHH.2014.03.006.
[189] E. F. Vanin, "PROCESSED PSEUDOGENES: CHARACTERISTICS AND EVOLUTION," *Annu. Rev. Genet.*, vol. 19, pp. 253–272, Nov. 1985, doi: 10.1146/ANNUREV.GE.19.120185.001345.
[190] Y. Tutar, "Pseudogenes," *Comp. Funct. Genomics*, vol. 2012, p. 425526, 2012, doi: 10.1155/2012/424526.
[191] L. Poliseno, "Pseudogenes: Newly discovered players in human cancer," *Sci. Signal.*, vol. 5, no. 242, Sep. 2012, doi: 10.1126/SCISIGNAL.2002858.
[192] E. M. Poursani, B. M. Soltani, and S. J. Mowla, "Differential Expression of OCT4 Pseudogenes in Pluripotentand Tumor Cell Lines," *Cell J.*, vol. 18, no. 1, p. 28, Apr. 2016, doi: 10.22074/CELLJ.2016.3984.
[193] F. Wezel, J. Pearson, L. A. Kirkwood, and J. Southgate, "Differential Expression of Oct4 Variants and Pseudogenes in Normal Urothelium and Urothelial Cancer," *Am. J. Pathol.*, vol. 183, no. 4, pp. 1128–1136, 2013, doi: 10.1016/j.ajpath.2013.06.025.
[194] S. Liedtke, J. Enczmann, S. Waclawczyk, P. Wernet, and G. Kögler, "Oct4 and Its Pseudogenes Confuse Stem Cell Research," *Cell Stem Cell*, vol. 1, no. 4, pp. 364–366, Oct. 2007, doi: 10.1016/J.STEM.2007.09.003.
[195] D. Pain, G. W. Chirn, C. Strassel, and D. M. Kemp, "Multiple Retropseudogenes from Pluripotent Cell-specific Gene Expression Indicates a Potential Signature for Novel Gene Identification," *J. Biol. Chem.*, vol. 280, no. 8, pp. 6265–6268, Feb. 2005, doi: 10.1074/JBC.C400587200.
[196] J. Zhang *et al.*, "The human pluripotency gene NANOG/NANOGP8 is expressed in gastric cancer and associated with tumor development," *Oncol. Lett.*, vol. 1, no. 3, p. 457, May 2010, doi: 10.3892/OL_00000081.
[197] I. Marjanovič, M. Kandušer, D. Miklavčič, M. M. Keber, and M. Pavlin, "Comparison of Flow Cytometry, Fluorescence Microscopy and

Spectrofluorometry for Analysis of Gene Electrotransfer Efficiency," *J Membr. Biol*, vol. 247, pp. 1259–1267, 2014, doi: 10.1007/s00232-014-9714-4.
[198] S. Meyer, P. Wörsdörfer, K. Günther, M. Thier, and F. Edenhofer, "Derivation of Adult Human Fibroblasts and their Direct Conversion into Expandable Neural Progenitor Cells.," *J. Vis. Exp.*, no. 101, pp. 1–10, 2015, doi: 10.3791/52831.
[199] M. Vangipuram, D. Ting, S. Kim, R. Diaz, and B. Schüle, "Skin Punch Biopsy Explant Culture for Derivation of Primary Human Fibroblasts," *J. Vis. Exp.*, no. 77, p. e3779, 2013, doi: 10.3791/3779.
[200] L. Kisselbach, M. Merges, A. Bossie, and A. Boyd, "CD90 Expression on human primary cells and elimination of contaminating fibroblasts from cell cultures," *Cytotechnology*, vol. 59, no. 1, p. 31, Jan. 2009, doi: 10.1007/S10616-009-9190-3.
[201] H. Alam, L. Sehgal, S. T. Kundu, S. N. Dalal, and M. M. Vaidya, "Novel function of keratins 5 and 14 in proliferation and differentiation of stratified epithelial cells," *Mol. Biol. Cell*, vol. 22, no. 21, pp. 4068–4078, Nov. 2011, doi: 10.1091/MBC.E10-08-0703/ASSET/IMAGES/LARGE/4068FIG7.JPEG.
[202] E. T. Strässler, K. Aalto-Setälä, M. Kiamehr, U. Landmesser, and N. Kränkel, "Age Is Relative—Impact of Donor Age on Induced Pluripotent Stem Cell-Derived Cell Functionality," *Frontiers in Cardiovascular Medicine*, vol. 5. Frontiers Media S.A., p. 25, Jan. 25, 2018, doi: 10.3389/fcvm.2018.00004.
[203] V. Turinetto, L. Orlando, and C. Giachino, "Induced pluripotent stem cells: Advances in the quest for genetic stability during reprogramming process," *International Journal of Molecular Sciences*, vol. 18, no. 9. MDPI AG, Sep. 13, 2017, doi: 10.3390/ijms18091952.
[204] A. Gore *et al.*, "Somatic coding mutations in human induced pluripotent stem cells," *Nature*, vol. 471, no. 7336, pp. 63–67, Mar. 2011, doi: 10.1038/nature09805.
[205] Y. Mayshar *et al.*, "Identification and Classification of Chromosomal Aberrations in Human Induced Pluripotent Stem Cells," *Cell Stem Cell*, vol. 7, no. 4, pp. 521–531, 2010, doi: 10.1016/j.stem.2010.07.017.
[206] S. Ruiz *et al.*, "Analysis of protein coding mutations in hiPSCs and their possible role during somatic cell reprogramming," *Nat Commun*, vol. 4, 2013, doi: 10.1038/ncomms2381.Analysis.
[207] W. Liu *et al.*, "The suppression of medium acidosis improves the maintenance and differentiation of human pluripotent stem cells at high density in defined cell culture medium," *Int. J. Biol. Sci.*, vol. 14, no. 5, pp. 485–496, Apr. 2018, doi: 10.7150/ijbs.24681.
[208] A. Beenken and M. Mohammadi, "The FGF family: Biology, pathophysiology and therapy," *Nature Reviews Drug Discovery*, vol. 8, no. 3. NIH Public Access, pp. 235–253, 2009, doi: 10.1038/nrd2792.
[209] M. A. Bush *et al.*, "Pharmacokinetics and pharmacodynamics of recombinant FGF-2 in a phase I trial in coronary artery disease," *J. Clin. Pharmacol.*, vol. 41, no. 4, pp. 378–385, Jan. 2001, doi: 10.1177/00912700122010230.
[210] M. A. Nugent and E. R. Edelmant, "Kinetics of Basic Fibroblast Growth Factor Binding to Its Receptor and Heparan Sulfate Proteoglycan: A Mechanism for Cooperativity," *Biochemistry*, vol. 31, no. 37, pp. 8876–8883, Feb. 1992, doi:

10.1021/bi00152a026.
[211] L. Wang *et al.*, "Fatty acid synthesis is critical for stem cell pluripotency via promoting mitochondrial fission," *EMBO J.*, vol. 36, no. 10, pp. 1330–1347, May 2017, doi: 10.15252/embj.201695417.
[212] Y. Nakatake *et al.*, "Kinetics of drug selection systems in mouse embryonic stem cells," *BMC Biotechnol.*, vol. 13, no. 1, p. 1, 2013, doi: 10.1186/1472-6750-13-64.
[213] Y. Fu *et al.*, "High-frequency off-target mutagenesis induced by CRISPR-Cas nucleases in human cells," *Nat. Biotechnol.*, vol. 31, no. 9, pp. 822–826, Sep. 2013, doi: 10.1038/nbt.2623.
[214] P. D. Hsu *et al.*, "DNA targeting specificity of RNA-guided Cas9 nucleases," *Nat. Biotechnol.*, vol. 31, no. 9, pp. 827–832, Sep. 2013, doi: 10.1038/nbt.2647.
[215] V. Pattanayak *et al.*, "High-throughput profiling of off-target DNA cleavage reveals RNA-programmed Cas9 nuclease specificity HHS Public Access Author manuscript," *Nat Biotechnol*, vol. 31, no. 9, pp. 839–843, 2013, doi: 10.1038/nbt.2673.
[216] R. Gopalappa, B. Suresh, S. Ramakrishna, and H. H. Kim, "Paired D10A Cas9 nickases are sometimes more efficient than individual nucleases for gene disruption," *Nucleic Acids Res.*, vol. 46, no. 12, p. 71, Jul. 2018, doi: 10.1093/nar/gky222.
[217] K. Cameron *et al.*, "Recombinant Laminins Drive the Differentiation and Self-Organization of hESC-Derived Hepatocytes," *Stem Cell Reports*, vol. 5, no. 6, pp. 1250–1262, 2015, doi: 10.1016/j.stemcr.2015.10.016.
[218] K. Ooeda *et al.*, "A two-dimensional multiwell cell culture method for the production of CYP3A4-expressing hepatocyte-like cells from HepaRG cells," no. July, pp. 1–12, 2020, doi: 10.1002/prp2.652.
[219] H. Rashidi *et al.*, "3D human liver tissue from pluripotent stem cells displays stable phenotype in vitro and supports compromised liver function in vivo," *Arch. Toxicol.*, vol. 92, pp. 3117–3129, 2018, doi: 10.1007/s00204-018-2280-2.
[220] H. Ardalani, S. Sengupta, V. Harms, V. Vickerman, J. A. Thomson, and W. L. Murphy, "3-D culture and endothelial cells improve maturity of human pluripotent stem cell-derived hepatocytes," *Acta Biomater.*, vol. 95, pp. 371–381, Sep. 2019, doi: 10.1016/j.actbio.2019.07.047.
[221] N. Davoodian, A. S. Lotfi, M. Soleimani, and S. J. Mowla, "MicroRNA-122 Overexpression Promotes Hepatic Differentiation of Human Adipose Tissue-Derived Stem Cells," *J. Cell. Biochem.*, vol. 115, no. 9, pp. 1582–1593, Sep. 2014, doi: 10.1002/jcb.24822.
[222] C. Du *et al.*, "Highly efficient and expedited hepatic differentiation from human pluripotent stem cells by pure small-molecule cocktails," *Stem Cell Res. Ther.*, vol. 9, no. 1, pp. 1–15, 2018, doi: 10.1186/s13287-018-0794-4.
[223] G. Wang *et al.*, "Co-culture system of hepatocytes and endothelial cells: two in vitro approaches for enhancing liver-specific functions of hepatocytes," *Cytotechnology*, vol. 70, no. 4, pp. 1279–1290, Aug. 2018, doi: 10.1007/s10616-018-0219-3.
[224] S. Sengupta *et al.*, "Co-culture with mouse embryonic fibroblasts improves maintenance of metabolic function of human small hepatocyte progenitor cells," *Curr. Res. Toxicol.*, vol. 1, pp. 70–84, Jun. 2020, doi:

10.1016/j.crtox.2020.08.001.
[225] T. Mu *et al.*, "Embryonic liver developmental trajectory revealed by single-cell RNA sequencing in the Foxa2eGFP mouse," *Commun. Biol.*, vol. 3, no. 1, pp. 1–12, Dec. 2020, doi: 10.1038/s42003-020-01364-8.
[226] L. Han *et al.*, "Single cell transcriptomics identifies a signaling network coordinating endoderm and mesoderm diversification during foregut organogenesis," *Nat. Commun.*, vol. 11, no. 1, pp. 1–16, Dec. 2020, doi: 10.1038/s41467-020-17968-x.
[227] T. Hurrell, C.-P. P. Segeritz, L. Vallier, K. S. Lilley, and A. D. Cromarty, "A proteomic time course through the differentiation of human induced pluripotent stem cells into hepatocyte-like cells," *Sci. Rep.*, vol. 9, no. 1, pp. 1–11, Dec. 2019, doi: 10.1038/s41598-019-39400-1.
[228] K. Shahzad *et al.*, "Hepatic metabolomics and transcriptomics to study susceptibility to ketosis in response to prepartal nutritional management," *J. Anim. Sci. Biotechnol.*, vol. 10, no. 1, p. 96, Dec. 2019, doi: 10.1186/s40104-019-0404-z.
[229] R. Mesnage *et al.*, "Integrated transcriptomics and metabolomics reveal signatures of lipid metabolism dysregulation in HepaRG liver cells exposed to PCB 126," *Arch. Toxicol.*, vol. 92, no. 8, pp. 2533–2547, Aug. 2018, doi: 10.1007/s00204-018-2235-7.
[230] X. Gao, R. Li, P. Cahan, Y. Zhao, J. J. Yourick, and R. L. Sprando, "Hepatocyte-like cells derived from human induced pluripotent stem cells using small molecules: Implications of a transcriptomic study," *Stem Cell Res. Ther.*, vol. 11, no. 1, pp. 1–21, Sep. 2020, doi: 10.1186/s13287-020-01914-1.
[231] N. R. F. Hannan, C.-P. Segeritz, T. Touboul, and L. Vallier, "Production of hepatocyte-like cells from human pluripotent stem cells.," *Nat. Protoc.*, vol. 8, no. 2, pp. 430–437, 2013, doi: 10.1038/nprot.2012.153.
[232] D. Shin *et al.*, "Bmp and Fgf signaling are essential for liver specification in zebrafish.," *Development*, vol. 134, no. 11, pp. 2041–50, Jun. 2007, doi: 10.1242/dev.000281.
[233] V. Gouon-Evans *et al.*, "BMP-4 is required for hepatic specification of mouse embryonic stem cell-derived definitive endoderm," *Nat. Biotechnol.*, vol. 24, no. 11, pp. 1402–1411, 2006, doi: 10.1038/nbt1258.
[234] A. M. Zorn, "Liver Development," *StemBook*, pp. 1–30, 2008, doi: 10.3824/stembook.1.25.1.
[235] L. T. Ang *et al.*, "A Roadmap for Human Liver Differentiation from Pluripotent Stem Cells," *Cell Rep.*, vol. 22, no. 8, pp. 2190–2205, Feb. 2018, doi: 10.1016/j.celrep.2018.01.087.
[236] A. Suzuki, S. Sekiya, D. Büscher, J. C. Izpisúa Belmonte, and H. Taniguchi, "Tbx3 controls the fate of hepatic progenitor cells in liver development by suppressing p19ARF expression.," *Development*, vol. 135, no. 9, pp. 1589–1595, 2008, doi: 10.1242/dev.016634.
[237] T. H. W. Lüdtke, V. M. Christoffels, M. Petry, and A. Kispert, "Tbx3 promotes liver bud expansion during mouse development by suppression of cholangiocyte differentiation," *Hepatology*, vol. 49, no. 3, pp. 969–978, 2009, doi: 10.1002/hep.22700.
[238] D. Shin and S. P. S. Monga, "Cellular and molecular basis of liver development,"

Compr. Physiol., vol. 3, no. 2, pp. 799–815, 2013, doi: 10.1002/cphy.c120022.
[239] Z. Jaafarpour *et al.*, "Overexpression of microRNA-375 and microRNA-122 promotes the differentiation of human induced pluripotent stem cells into hepatocyte-like cells," *Biologicals*, vol. 63, pp. 24–32, Jan. 2020, doi: 10.1016/j.biologicals.2019.12.005.
[240] M. Gjorgjieva, C. Sobolewski, D. Dolicka, M. Correia De Sousa, and M. Foti, "MiRNAs and NAFLD: From pathophysiology to therapy," *Gut*, vol. 68, no. 11. BMJ Publishing Group, pp. 2065–2079, Nov. 01, 2019, doi: 10.1136/gutjnl-2018-318146.
[241] A. Asai *et al.*, "Paracrine signals regulate human liver organoid maturation from induced pluripotent stem cells," 2017, doi: 10.1242/dev.142794.
[242] G. Pettinato *et al.*, "Generation of fully functional hepatocyte-like organoids from human induced pluripotent stem cells mixed with Endothelial Cells," *Sci. Rep.*, vol. 9, no. 1, pp. 1–21, Dec. 2019, doi: 10.1038/s41598-019-45514-3.
[243] K. Si-Tayeb *et al.*, "Highly efficient generation of human hepatocyte-like cells from induced pluripotent stem cells," *Hepatology*, vol. 51, no. 1, pp. 297–305, Jan. 2010, doi: 10.1002/hep.23354.
[244] F. G. Torizal, K. Kimura, I. Horiguchi, and Y. Sakai, "Size-dependent hepatic differentiation of human induced pluripotent stem cells spheroid in suspension culture," *Regen. Ther.*, vol. 12, pp. 66–73, Dec. 2019, doi: 10.1016/j.reth.2019.04.011.
[245] M. Vosough *et al.*, "Generation of functional hepatocyte-like cells from human pluripotent stem cells in a scalable suspension culture.," *Stem Cells Dev.*, vol. 22, no. 20, pp. 2693–705, 2013, doi: 10.1089/scd.2013.0088.
[246] M. N. Labour *et al.*, "Development of 3D hepatic constructs within polysaccharide-based scaffolds with tunable properties," *Int. J. Mol. Sci.*, vol. 21, no. 10, 2020, doi: 10.3390/ijms21103644.
[247] S. J. Mun, Y.-H. Hong, H.-S. Ahn, J.-S. Ryu, K.-S. Chung, and M. J. Son, "Long-Term Expansion of Functional Human Pluripotent Stem Cell-Derived Hepatic Organoids," *Int. J. Stem Cells*, Apr. 2020, doi: 10.15283/ijsc20060.
[248] F. Meier *et al.*, "Hepatic differentiation of human iPSCs in different 3D models: A comparative study," *Int. J. Mol. Med.*, vol. 40, no. 6, pp. 1759–1771, Dec. 2017, doi: 10.3892/ijmm.2017.3190.
[249] M. Vinken *et al.*, "Involvement of cell junctions in hepatocyte culture functionality," *Critical Reviews in Toxicology*, vol. 36, no. 4. Taylor & Francis, pp. 299–318, Apr. 2006, doi: 10.1080/10408440600599273.
[250] N. E. Ryu, S. H. Lee, and H. Park, "Spheroid Culture System Methods and Applications for Mesenchymal Stem Cells," *Cells*, vol. 8, no. 12. NLM (Medline), p. 1620, Dec. 12, 2019, doi: 10.3390/cells8121620.
[251] N. Freyer *et al.*, "Microscale 3D Liver Bioreactor for In Vitro Hepatotoxicity Testing under Perfusion Conditions," *Bioengineering*, vol. 5, no. 1, p. 24, Mar. 2018, doi: 10.3390/bioengineering5010024.
[252] R. M. Tostões *et al.*, "Human liver cell spheroids in extended perfusion bioreactor culture for repeated-dose drug testing," *Hepatology*, vol. 55, no. 4, pp. 1227–1236, Apr. 2012, doi: 10.1002/hep.24760.
[253] D. Wendt, A. Marsano, M. Jakob, M. Heberer, and I. Martin, "Oscillating perfusion of cell suspensions through three-dimensional scaffolds enhances

cell seeding efficiency and uniformity," *Biotechnol. Bioeng.*, vol. 84, no. 2, pp. 205–214, Oct. 2003, doi: 10.1002/bit.10759.

[254] Y. L. Xiao, J. Riesle, and C. A. Van Blitterswijk, "Static and dynamic fibroblast seeding and cultivation in porous PEO/PBT scaffolds," in *Journal of Materials Science: Materials in Medicine*, 1999, vol. 10, no. 12, pp. 773–777, doi: 10.1023/A:1008946832443.

[255] S. M. Warren, A. M. Sailon, A. C. Allori, E. H. Davidson, D. D. Reformat, and R. J. Allen, "A novel flow-perfusion bioreactor supports 3D dynamic cell culture," *J. Biomed. Biotechnol.*, vol. 2009, 2009, doi: 10.1155/2009/873816.

[256] J. Arrowsmith and P. Miller, "Efficacy Safety Strategic Commercial Operational BIOBUSINESS BRIEFS," Nature Publishing Group, Aug. 2013. doi: 10.1038/nrd4090.

[257] C. Olgasi, A. Cucci, and A. Follenzi, "Ipsc-derived liver organoids: A journey from drug screening, to disease modeling, arriving to regenerative medicine," *Int. J. Mol. Sci.*, vol. 21, no. 17, pp. 1–30, 2020, doi: 10.3390/ijms21176215.

[258] D. Zhao *et al.*, "Promotion of the efficient metabolic maturation of human pluripotent stem cell-derived hepatocytes by correcting specification defects," *Cell Research*, vol. 23, no. 1. Nature Publishing Group, pp. 157–161, Jan. 2013, doi: 10.1038/cr.2012.144.

[259] A. M. Zorn and J. M. Wells, "Vetebrate endoderm development," pp. 221–251, 2010, doi: 10.1146/annurev.cellbio.042308.113344.Vertebrate.

[260] K. S. Zaret, "Liver specification and early morphogenesis," *Mech. Dev.*, vol. 92, no. 1, pp. 83–88, 2000, doi: 10.1016/S0925-4773(99)00326-3.

[261] M. J. Marvin, G. Di Rocco, A. Gardiner, S. M. Bush, and A. B. Lassar, "Inhibition of Wnt activity induces heart formation from posterior mesoderm," *Genes Dev.*, vol. 15, no. 3, pp. 316–327, Feb. 2001, doi: 10.1101/gad.855501.

[262] F. Lemaigre and K. S. Zaret, "Liver development update: new embryo models, cell lineage control, and morphogenesis," 2004, doi: 10.1016/j.gde.2004.08.004.

[263] A. Palaria, J. R. Angelo, T. M. Guertin, J. Mager, and K. D. Tremblay, "Patterning of the hepato-pancreatobiliary boundary by BMP reveals heterogeneity within the murine liver bud," *Hepatology*, vol. 68, no. 1, pp. 274–288, Jul. 2018, doi: 10.1002/hep.29769.

[264] L. F. Leal, A. C. Bueno, D. C. Gomes, R. Abduch, M. de Castro, and S. R. Antonini, "Inhibition of the Tcf/beta-catenin complex increases apoptosis and impairs adrenocortical tumor cell proliferation and adrenal steroidogenesis," *Oncotarget*, vol. 6, no. 40, pp. 43016–43032, 2015, doi: 10.18632/oncotarget.5513.

[265] A. Narytnyk *et al.*, "Differentiation of Human Epidermal Neural Crest Stem Cells (hEPI-NCSC) into Virtually Homogenous Populations of Dopaminergic Neurons," *Stem Cell Rev. Reports*, vol. 10, no. 2, pp. 316–326, Apr. 2014, doi: 10.1007/s12015-013-9493-9.

[266] J. E. Frith, D. M. Titmarsh, H. Padmanabhan, and J. J. Cooper-White, "Microbioreactor Array Screening of Wnt Modulators and Microenvironmental Factors in Osteogenic Differentiation of Mesenchymal Progenitor Cells," *PLoS One*, vol. 8, no. 12, p. e82931, Dec. 2013, doi: 10.1371/journal.pone.0082931.

[267] C. E. Sanvitale *et al.*, "A New Class of Small Molecule Inhibitor of BMP Signaling," *PLoS One*, vol. 8, no. 4, Apr. 2013, doi: 10.1371/journal.pone.0062721.
[268] C. Chen, A. Soto-Gutierrez, P. M. Baptista, and B. Spee, "Biotechnology Challenges to In Vitro Maturation of Hepatic Stem Cells," *Gastroenterology*, vol. 154, no. 5, pp. 1258–1272, Apr. 2018, doi: 10.1053/J.GASTRO.2018.01.066.
[269] M. Baxter *et al.*, "Phenotypic and functional analyses show stem cell-derived hepatocyte-like cells better mimic fetal rather than adult hepatocytes," *J. Hepatol.*, vol. 62, no. 3, pp. 581–589, 2015, doi: 10.1016/j.jhep.2014.10.016.
[270] A. I. Wayne Wiens Lawrence Gilbert, "Glycerol metabolism in the human liver: Inhibition by ethanol," *Science (80-.).*, vol. 150, no. 3696, pp. 616–617, Oct. 1965, doi: 10.1126/science.150.3696.616.
[271] Y. Urasaki, G. Pizzorno, and T. T. Le, "Uridine Affects Liver Protein Glycosylation, Insulin Signaling, and Heme Biosynthesis," *PLoS One*, vol. 9, no. 6, p. e99728, Jun. 2014, doi: 10.1371/journal.pone.0099728.
[272] A. Blanco and G. Blanco, "Amino Acid Metabolism," in *Medical Biochemistry*, Elsevier, 2017, pp. 367–399.
[273] Y. Zhang, S. Guo, C. Xie, and J. Fang, "Uridine Metabolism and Its Role in Glucose, Lipid, and Amino Acid Homeostasis," *BioMed Research International*, vol. 2020. Hindawi Limited, 2020, doi: 10.1155/2020/7091718.
[274] C. N. Medine, B. Lucendo-Villarin, W. Zhou, C. C. West, and D. C. Hay, "Robust generation of hepatocyte-like cells from human embryonic stem cell populations.," *J. Vis. Exp.*, no. 56, p. e2969, 2012, doi: 10.3791/2969.
[275] S. Agarwal, K. L. Holton, and R. Lanza, "Efficient differentiation of functional hepatocytes from human embryonic stem cells.," *Stem Cells*, vol. 26, no. 5, pp. 1117–1127, May 2008, doi: 10.1634/stemcells.2007-1102.
[276] N. L. Magner, Y. Jung, J. Wu, J. A. Nolta, M. A. Zern, and P. Zhou, "Insulin and IGFs enhance hepatocyte differentiation from human embryonic stem cells via the PI3K/AKT Pathway," *Stem Cells*, vol. 31, no. 10, pp. 2095–2103, 2013, doi: 10.1002/stem.1478.
[277] E. Świderska, J. Strycharz, A. Wróblewski, J. Szemraj, J. Drzewoski, and A. Śliwińska, "Role of PI3K/AKT Pathway in Insulin-Mediated Glucose Uptake," in *Blood Glucose Levels*, IntechOpen, 2020.
[278] Z. Hu, R. P. Evarts, K. Fujio, E. R. Marsden, and S. S. Thorgeirsson, "Expression of hepatocyte growth factor and c-met genes during hepatic differentiation and liver development in the rat," *Am. J. Pathol.*, vol. 142, no. 6, pp. 1823–1830, 1993, Accessed: Feb. 24, 2021. [Online]. Available: /pmc/articles/PMC1886980/?report=abstract.
[279] A. Suzuki, A. Iwana, H. Miyashita, H. Nakauchi, and H. Taniguchi, "Role for growth factors and extracellular matrix in controlling differentiation of prospectively isolated hepatic stem cells," *Development*, vol. 130, no. 11, pp. 2513–2524, Jun. 2003, doi: 10.1242/dev.00459.
[280] A. Kamiya, T. Kinoshita, and A. Miyajima, "Oncostatin M and hepatocyte growth factor induce hepatic maturation via distinct signaling pathways," *FEBS Lett.*, vol. 492, no. 1–2, pp. 90–94, Mar. 2001, doi: 10.1016/S0014-5793(01)02140-8.
[281] M. Takigawa, T. Takano, K. Nakagawa, M. Sakuda, and F. Suzuki, "Hydrocortisone stimulation of proliferation and glycosaminoglycan synthesis

in rabbit craniofacial chondrocytes in vitro," *Arch. Oral Biol.*, 1988, doi: 10.1016/0003-9969(88)90019-2.
[282] P. Podevin *et al.*, "Production of infectious hepatitis C virus in primary cultures of human adult hepatocytes," *Gastroenterology*, vol. 139, no. 4, pp. 1355-1364.e6, Oct. 2010, doi: 10.1053/j.gastro.2010.06.058.
[283] M. López-Riera *et al.*, "New microRNA biomarkers for drug-induced steatosis and their potential to predict the contribution of drugs to non-alcoholic fatty liver disease," *Front. Pharmacol.*, vol. 8, no. JAN, Jan. 2017, doi: 10.3389/fphar.2017.00003.
[284] M. Benet *et al.*, "A simple transcriptomic signature able to predict drug-induced hepatic steatosis," *Arch. Toxicol.*, vol. 88, no. 4, pp. 967–982, Jan. 2014, doi: 10.1007/s00204-014-1197-7.
[285] J. Liu *et al.*, "HSPA12A attenuates lipopolysaccharide-induced liver injury through inhibiting caspase-11-mediated hepatocyte pyroptosis via PGC-1α-dependent acyloxyacyl hydrolase expression," *Cell Death Differ.*, vol. 27, no. 9, pp. 2651–2667, Sep. 2020, doi: 10.1038/s41418-020-0536-x.
[286] P. Kanmani and H. Kim, "Protective effects of lactic acid bacteria against TLR4 induced inflammatory response in hepatoma HepG2 cells through modulation of toll-like receptor negative regulators of mitogen-activated protein kinase and NF-κB signaling," *Front. Immunol.*, vol. 9, no. JUL, p. 1, Jul. 2018, doi: 10.3389/fimmu.2018.01537.
[287] S. Bucher *et al.*, "Bisphenol a induces steatosis in HepaRG cells using a model of perinatal exposure," *Environ. Toxicol.*, vol. 32, no. 3, pp. 1024–1036, Mar. 2017, doi: 10.1002/tox.22301.
[288] P. Chienwichai, S. Topanurak, O. Reamtong, U. Boonyuen, S. Worakhunpiset, and P. Tharnpoophasiam, "Effects of low bisphenol A concentration on protein expression profiles in an in vitro model of non-alcoholic fatty liver disease," *Mol. Cell. Toxicol.*, vol. 14, no. 1, pp. 61–70, Jan. 2018, doi: 10.1007/s13273-018-0008-2.
[289] A. Montesano *et al.*, "l-Carnitine counteracts in vitro fructose-induced hepatic steatosis through targeting oxidative stress markers," *J. Endocrinol. Invest.*, vol. 43, no. 4, pp. 493–503, Apr. 2020, doi: 10.1007/s40618-019-01134-2.
[290] R. C. Su *et al.*, "Hyperglycemia induces key genetic and phenotypic changes in human liver epithelial HepG2 cells which parallel the Leprdb/J mouse model of non-alcoholic fatty liver disease (NAFLD)," *PLoS One*, vol. 14, no. 12, p. e0225604, Dec. 2019, doi: 10.1371/journal.pone.0225604.
[291] P. Pingitore, K. Sasidharan, M. Ekstrand, S. Prill, D. Lindén, and S. Romeo, "Human Multilineage 3D Spheroids as a Model of Liver Steatosis and Fibrosis," *Int. J. Mol. Sci.*, vol. 20, no. 7, p. 1629, Apr. 2019, doi: 10.3390/ijms20071629.
[292] Y. Zhang *et al.*, "Inhibition of MD2-dependent inflammation attenuates the progression of non-alcoholic fatty liver disease," *J. Cell. Mol. Med.*, vol. 22, no. 2, pp. 936–947, Feb. 2018, doi: 10.1111/jcmm.13395.
[293] M. J. Lyall *et al.*, "Modelling non-alcoholic fatty liver disease in human hepatocyte-like cells.," *Philos. Trans. R. Soc. Lond. B. Biol. Sci.*, vol. 373, no. 1750, p. 20170362, Jul. 2018, doi: 10.1098/rstb.2017.0362.
[294] H. Rafiei, K. Omidian, and B. Bandy, "Dietary Polyphenols Protect Against Oleic Acid-Induced Steatosis in an in Vitro Model of NAFLD by Modulating Lipid

Metabolism and Improving Mitochondrial Function," *Nutrients*, vol. 11, no. 541, 2019, doi: 10.3390/nu11030541.

[295] B. Anfuso, C. Tiribelli, L. Adorini, and N. Rosso, "Obeticholic acid and INT-767 modulate collagen deposition in a NASH in vitro model," *Sci. Rep.*, vol. 10, no. 1, pp. 1–12, Dec. 2020, doi: 10.1038/s41598-020-58562-x.

[296] N. Kaur, V. Chugh, and A. K. Gupta, "Essential fatty acids as functional components of foods- a review," *Journal of Food Science and Technology*, vol. 51, no. 10. Springer, pp. 2289–2303, Oct. 01, 2014, doi: 10.1007/s13197-012-0677-0.

[297] A. C. Rustan and C. A. Drevon, "Fatty Acids: Structures and Properties," *ENCYCLOPEDIA OF LIFE SCIENCES*. 2005, doi: 10.1038/npg.els.0003894.

[298] R. Valenzuela and A. Valenzuela, "Overview About Lipid Structure," in *Lipid Metabolism*, InTech, 2013.

[299] B. Bulutoglu, C. Rey-Bedón, Y. B. Kang, S. Mert, M. L. Yarmush, and O. B. Usta, "A microfluidic patterned model of non-alcoholic fatty liver disease: Applications to disease progression and zonation," *Lab Chip*, vol. 19, no. 18, pp. 3022–3031, Sep. 2019, doi: 10.1039/c9lc00354a.

[300] Q. Tu *et al.*, "Palmitic acid induces autophagy in hepatocytes via JNK2 activation," *Nat. Publ. Gr.*, vol. 35, no. 4, pp. 504–512, 2014, doi: 10.1038/aps.2013.170.

[301] S. Carotti *et al.*, "An overview of deregulated lipid metabolism in nonalcoholic fatty liver disease with special focus on lysosomal acid lipase," *American Journal of Physiology - Gastrointestinal and Liver Physiology*, vol. 319, no. 4. American Physiological Society, pp. G469–G480, Oct. 01, 2020, doi: 10.1152/ajpgi.00049.2020.

[302] S. Santamarina-Fojo, H. González-Navarro, L. Freeman, E. Wagner, and Z. Nong, "Hepatic lipase, lipoprotein metabolism, and atherogenesis," *Arteriosclerosis, Thrombosis, and Vascular Biology*, vol. 24, no. 10. Lippincott Williams & Wilkins, pp. 1750–1754, Oct. 01, 2004, doi: 10.1161/01.ATV.0000140818.00570.2d.

[303] A. Delik, H. Akkız, and S. Dinçer, "The effect of PNPLA3 polymorphism as gain in function mutation in the pathogenesis of non-alcoholic fatty liver disease," *Indian J. Gastroenterol.*, vol. 39, no. 1, pp. 84–91, Feb. 2020, doi: 10.1007/s12664-020-01026-x.

[304] H. Mahdessian *et al.*, "TM6SF2 is a regulator of liver fat metabolism influencing triglyceride secretion and hepatic lipid droplet content," *Proc. Natl. Acad. Sci. U. S. A.*, vol. 111, no. 24, pp. 8913–8918, Jun. 2014, doi: 10.1073/pnas.1323785111.

[305] J. L. Pitman, D. J. Bonnet, L. K. Curtiss, and N. Gekakis, "Reduced cholesterol and triglycerides in mice with a mutation in Mia2, a liver protein that localizes to ER exit sites," *J. Lipid Res.*, vol. 52, no. 10, pp. 1775–1786, Oct. 2011, doi: 10.1194/jlr.M017277.

[306] W. Dai, Z. Zhang, C. Yao, and S. Zhao, "Emerging evidences for the opposite role of apolipoprotein C3 and apolipoprotein A5 in lipid metabolism and coronary artery disease," *Lipids in Health and Disease*, vol. 18, no. 1. BioMed Central Ltd., p. 220, Dec. 13, 2019, doi: 10.1186/s12944-019-1166-5.

[307] I. Fabregat *et al.*, "TGF-β signalling and liver disease," *FEBS J.*, vol. 283, no. 12, pp. 2219–2232, Jun. 2016, doi: 10.1111/febs.13665.

[308] A. Weng Chuan Peng *et al.*, "Inflammatory Cytokine TNFa Promotes the Long-Term Expansion of Primary Hepatocytes in 3D Culture Article Inflammatory Cytokine TNFa Promotes the Long-Term Expansion of Primary Hepatocytes in 3D Culture," *Cell*, vol. 175, 2018, doi: 10.1016/j.cell.2018.11.012.

[309] S. Zhao *et al.*, "The concentration of tumor necrosis factor-α determines its protective or damaging effect on liver injury by regulating Yap activity," *Cell Death Dis.*, vol. 11, no. 1, pp. 1–13, Jan. 2020, doi: 10.1038/s41419-020-2264-z.

[310] S. Sobotta *et al.*, "Model based targeting of IL-6-induced inflammatory responses in cultured primary hepatocytes to improve application of the JAK inhibitor ruxolitinib," *Front. Physiol.*, vol. 8, no. OCT, p. 775, Oct. 2017, doi: 10.3389/fphys.2017.00775.

[311] M. Eto, "Regulation of cellular protein phosphatase-1 (PP1) by phosphorylation of the CPI-17 family, C-kinase-activated PP1 Inhibitors," *J. Biol. Chem.*, vol. 284, no. 51, pp. 35273–35277, 2009, doi: 10.1074/jbc.R109.059972.

[312] L. Agius, B. E. Ford, and S. S. Chachra, "The metformin mechanism on gluconeogenesis and AMPK activation: The metabolite perspective," *Int. J. Mol. Sci.*, vol. 21, no. 9, 2020, doi: 10.3390/ijms21093240.

[313] R. P. Cunningham, R. D. Sheldon, and R. S. Rector, "The Emerging Role of Hepatocellular eNOS in Non-alcoholic Fatty Liver Disease Development," *Front. Physiol.*, vol. 11, p. 767, Jul. 2020, doi: 10.3389/fphys.2020.00767.

[314] P. Menten, A. Wuyts, and J. Van Damme, "Macrophage inflammatory protein-1," *Cytokine Growth Factor Rev.*, vol. 13, no. 6, pp. 455–481, 2002, doi: 10.1016/S1359-6101(02)00045-X.

[315] R. Song, S. Liu, and K. W. Leong, "Effects of MIP-1α, MIP-3α, and MIP-3β on the induction of HIV gag-specific immune response with DNA vaccines," *Mol. Ther.*, vol. 15, no. 5, pp. 1007–1015, May 2007, doi: 10.1038/mt.sj.6300129.

[316] S. L. Kalled, "The role of BAFF in immune function and implications for autoimmunity," *Immunol. Rev.*, vol. 204, no. 1, pp. 43–54, Apr. 2005, doi: 10.1111/j.0105-2896.2005.00219.x.

[317] Y. Nakamura *et al.*, "Depletion of B cell-activating factor attenuates hepatic fat accumulation in a murine model of nonalcoholic fatty liver disease," *Sci. Rep.*, vol. 9, no. 1, pp. 1–12, Dec. 2019, doi: 10.1038/s41598-018-37403-y.

[318] B. von Tresckow *et al.*, "Depletion of Cellular Cholesterol and Lipid Rafts Increases Shedding of CD30," *J. Immunol.*, vol. 172, no. 7, pp. 4324–4331, Apr. 2004, doi: 10.4049/jimmunol.172.7.4324.

[319] D. Beiroa *et al.*, "Heterozygous Deficiency of Endoglin Decreases Insulin and Hepatic Triglyceride Levels during High Fat Diet," *PLoS One*, vol. 8, no. 1, pp. 1–11, 2013, doi: 10.1371/journal.pone.0054591.

[320] X. Chen *et al.*, "Oleic acid protects saturated fatty acid mediated lipotoxicity in hepatocytes and rat of non-alcoholic steatohepatitis," *Life Sci.*, vol. 203, pp. 291–304, Jun. 2018, doi: 10.1016/j.lfs.2018.04.022.

[321] E. Juárez-Hernández, N. C. Chávez-Tapia, M. Uribe, and V. J. Barbero-Becerra, "Role of bioactive fatty acids in nonalcoholic fatty liver disease," *Nutr. J.*, vol. 15, p. 72, 2016, doi: 10.1186/s12937-016-0191-8.

[322] S. Joshi-Barve *et al.*, "Palmitic acid induces production of proinflammatory cytokine interleukin-8 from hepatocytes," *Hepatology*, vol. 46, no. 3, pp. 823–

830, Sep. 2007, doi: 10.1002/hep.21752.
[323] H. Malhi, S. F. Bronk, N. W. Werneburg, and G. J. Gores, “Free fatty acids induce JNK-dependent hepatocyte lipoapoptosis,” *J. Biol. Chem.*, vol. 281, no. 17, pp. 12093–12101, Apr. 2006, doi: 10.1074/jbc.M510660200.
[324] M. J. Gómez-Lechón, M. T. Donato, A. Martínez-Romero, N. Jiménez, J. V. Castell, and J. E. O’Connor, “A human hepatocellular in vitro model to investigate steatosis,” *Chem. Biol. Interact.*, vol. 165, no. 2, pp. 106–116, Jan. 2007, doi: 10.1016/j.cbi.2006.11.004.
[325] F. Chiappini *et al.*, “Metabolism dysregulation induces a specific lipid signature of nonalcoholic steatohepatitis in patients,” *Sci. Rep.*, vol. 7, p. 46658, 2017, doi: 10.1038/srep46658.
[326] L. Li *et al.*, “Identification of key genes in non-alcoholic fatty liver disease progression based on bioinformatics analysis,” *Mol. Med. Rep.*, vol. 17, no. 6, pp. 7708–7720, Jun. 2018, doi: 10.3892/mmr.2018.8852.
[327] G. Chen *et al.*, “Discordant protein and mRNA expression in lung adenocarcinomas.,” *Mol. Cell. Proteomics*, vol. 1, no. 4, pp. 304–313, Apr. 2002, doi: 10.1074/mcp.M200008-MCP200.
[328] R. Lichtinghagen *et al.*, “Different mRNA and protein expression of matrix metalloproteinases 2 and 9 and tissue inhibitor of metalloproteinases 1 in benign and malignant prostate tissue,” *Eur. Urol.*, vol. 42, no. 4, pp. 398–406, Oct. 2002, doi: 10.1016/S0302-2838(02)00324-X.
[329] U. T. Shankavaram *et al.*, “Transcript and protein expression profiles of the NCI-60 cancer cell panel: An integromic microarray study,” *Mol. Cancer Ther.*, vol. 6, no. 3, pp. 820–832, Mar. 2007, doi: 10.1158/1535-7163.MCT-06-0650.
[330] P. Tessari, A. Coracina, A. Cosma, and A. Tiengo, “Hepatic lipid metabolism and non-alcoholic fatty liver disease,” *Nutr. Metab. Cardiovasc. Dis.*, vol. 19, no. 4, pp. 291–302, 2009, doi: 10.1016/j.numecd.2008.12.015.
[331] J. Cheng *et al.*, “Mitochondrial proton leak plays a critical role in pathogenesis of cardiovascular diseases,” *Adv. Exp. Med. Biol.*, vol. 982, pp. 359–370, May 2017, doi: 10.1007/978-3-319-55330-6_20.
[332] H. Zhang, “Lysosomal acid lipase and lipid metabolism: New mechanisms, new questions, and new therapies,” *Current Opinion in Lipidology*, vol. 29, no. 3. Lippincott Williams and Wilkins, pp. 218–223, Jun. 01, 2018, doi: 10.1097/MOL.0000000000000507.
[333] F. Li and H. Zhang, “Lysosomal Acid Lipase in Lipid Metabolism and beyond,” *Arterioscler. Thromb. Vasc. Biol.*, vol. 39, no. 5, pp. 850–856, May 2019, doi: 10.1161/ATVBAHA.119.312136.
[334] C. Quijano, M. Trujillo, L. Castro, and A. Trostchansky, “Interplay between oxidant species and energy metabolism,” *Redox Biol.*, vol. 8, pp. 28–42, Aug. 2016, doi: 10.1016/j.redox.2015.11.010.
[335] M. Masarone *et al.*, “Role of oxidative stress in pathophysiology of nonalcoholic fatty liver disease,” *Oxidative Medicine and Cellular Longevity*, vol. 2018. Hindawi Limited, 2018, doi: 10.1155/2018/9547613.
[336] L. M. Paardekooper, E. Van Vroonhoven, M. Ter Beest, and G. Van Den Bogaart, “Radical stress is more cytotoxic in the nucleus than in other organelles,” *Int. J. Mol. Sci.*, vol. 20, no. 17, p. 4147, Sep. 2019, doi: 10.3390/ijms20174147.
[337] C. Provost, F. Choufani, L. Avedanian, G. Bkaily, F. Gobeil, and D. Jacques,

"Nitric oxide and reactive oxygen species in the nucleus revisited," *Canadian Journal of Physiology and Pharmacology*, vol. 88, no. 3. Canadian Science Publishing, pp. 296–304, 2010, doi: 10.1139/Y10-011.

[338] M. Luhr *et al.*, "The kinase PERK and the transcription factor ATF4 play distinct and essential roles in autophagy resulting from tunicamycin-induced ER stress," *J. Biol. Chem.*, vol. 294, no. 20, pp. 8197–8217, May 2019, doi: 10.1074/jbc.RA118.002829.

[339] H. Wang *et al.*, *The Upstream Pathway of mTOR-Mediated Autophagy in Liver Diseases*, vol. 8, no. 12. 2019.

[340] J. Kim, M. Kundu, B. Viollet, and K. L. Guan, "AMPK and mTOR regulate autophagy through direct phosphorylation of Ulk1," *Nat. Cell Biol.*, vol. 13, no. 2, pp. 132–141, Feb. 2011, doi: 10.1038/ncb2152.

[341] M. Holczer, B. Hajdú, T. Lőrincz, A. Szarka, G. Bánhegyi, and O. Kapuy, "A double negative feedback loop between MTORC1 and AMPK kinases guarantees precise autophagy induction upon cellular stress," *Int. J. Mol. Sci.*, vol. 20, no. 22, Nov. 2019, doi: 10.3390/ijms20225543.

[342] D. Garcia and R. J. Shaw, "AMPK: Mechanisms of Cellular Energy Sensing and Restoration of Metabolic Balance," *Molecular Cell*, vol. 66, no. 6. Cell Press, pp. 789–800, Jun. 15, 2017, doi: 10.1016/j.molcel.2017.05.032.

[343] M. Jang *et al.*, "AMPK contributes to autophagosome maturation and lysosomal fusion," *Sci. Rep.*, vol. 8, p. 12637, Dec. 2018, doi: 10.1038/s41598-018-30977-7.

[344] J. Pan *et al.*, "Fatty acid activates NLRP3 inflammasomes in mouse Kupffer cells through mitochondrial DNA release," *Cell. Immunol.*, no. July, pp. 0–1, 2018, doi: 10.1016/j.cellimm.2018.08.006.

[345] T. Csak *et al.*, "Both bone marrow-derived and non-bone marrow-derived cells contribute to AIM2 and NLRP3 inflammasome activation in a MyD88-dependent manner in dietary steatohepatitis," *Liver Int.*, vol. 34, no. 9, pp. 1402–1413, 2014, doi: 10.1111/liv.12537.

[346] X. Zhou, S. Fouda, D. Li, K. Zhang, and J. M. Ye, "Involvement of the autophagy-er stress axis in high fat/carbohydrate diet-induced nonalcoholic fatty liver disease," *Nutrients*, vol. 12, no. 9, pp. 1–12, 2020, doi: 10.3390/nu12092626.

[347] E. Borkham-Kamphorst and R. Weiskirchen, "The PDGF system and its antagonists in liver fibrosis," *Cytokine and Growth Factor Reviews*, vol. 28. Elsevier Ltd, pp. 53–61, Apr. 01, 2016, doi: 10.1016/j.cytogfr.2015.10.002.

[348] A. Tan-Garcia *et al.*, "Liver fibrosis and CD206+ macrophage accumulation are suppressed by anti-GM-CSF therapy," *JHEP Reports*, vol. 2, no. 1, p. 100062, Feb. 2020, doi: 10.1016/j.jhepr.2019.11.006.

[349] Z. Zhou *et al.*, "Neutrophil–Hepatic Stellate Cell Interactions Promote Fibrosis in Experimental Steatohepatitis," *CMGH*, vol. 5, no. 3, pp. 399–413, Mar. 2018, doi: 10.1016/j.jcmgh.2018.01.003.

[350] X. Chu *et al.*, "CCL20 is up-regulated in non-alcoholic fatty liver disease fibrosis and is produced by hepatic stellate cells in response to fatty acid loading," *J. Transl. Med.*, vol. 16, no. 1, p. 108, Apr. 2018, doi: 10.1186/s12967-018-1490-y.

[351] M. Persico *et al.*, "Non alcoholic fatty liver disease and eNOS dysfunction in humans," *BMC Gastroenterol.*, vol. 17, no. 1, Mar. 2017, doi: 10.1186/s12876-

017-0592-y.
[352] M. Ruart *et al.*, "Impaired endothelial autophagy promotes liver fibrosis by aggravating the oxidative stress response during acute liver injury," *J. Hepatol.*, vol. 70, no. 3, pp. 458–469, Mar. 2019, doi: 10.1016/j.jhep.2018.10.015.
[353] O. Tirosh, E. Ilan, N. Budick-Harmelin, G. Ramadori, and Z. Madar, "Downregulation of eNOS in a nutritional model of fatty liver," *E. Spen. Eur. E. J. Clin. Nutr. Metab.*, vol. 4, no. 2, pp. e101–e104, Apr. 2009, doi: 10.1016/j.eclnm.2009.02.001.
[354] R. D. Sheldon, M. H. Laughlin, and R. S. Rector, "Reduced hepatic eNOS phosphorylation is associated with NAFLD and type 2 diabetes progression and is prevented by daily exercise in hyperphagic OLETF rats," *J. Appl. Physiol.*, vol. 116, no. 9, pp. 1156–1164, May 2014, doi: 10.1152/japplphysiol.01275.2013.
[355] W. C. Sessa, "eNos at a glance," *J. Cell Sci.*, vol. 117, no. 12, pp. 2427–2429, May 2004, doi: 10.1242/jcs.01165.
[356] Y. Nozaki *et al.*, "Deficiency of eNOS exacerbates early-stage NAFLD pathogenesis by changing the fat distribution," *BMC Gastroenterol.*, vol. 15, no. 1, p. 177, Dec. 2015, doi: 10.1186/s12876-015-0409-9.
[357] J. F. Santibanez *et al.*, "Endoglin increases eNOS expression by modulating Smad2 protein levels and Smad2-dependent TGF-β signaling," *J. Cell. Physiol.*, vol. 210, no. 2, pp. 456–468, Feb. 2007, doi: 10.1002/jcp.20878.
[358] M. Toporsian *et al.*, "A role for endoglin in coupling eNOS activity and regulating vascular tone revealed in hereditary hemorrhagic telangiectasia," *Circ. Res.*, vol. 96, no. 6, pp. 684–692, Apr. 2005, doi: 10.1161/01.RES.0000159936.38601.22.
[359] D. H. Kong, Y. K. Kim, M. R. Kim, J. H. Jang, and S. Lee, "Emerging roles of vascular cell adhesion molecule-1 (VCAM-1) in immunological disorders and cancer," *International Journal of Molecular Sciences*, vol. 19, no. 4. MDPI AG, Apr. 01, 2018, doi: 10.3390/ijms19041057.
[360] R. M. Carr, "VCAM-1: Closing the gap between lipotoxicity and endothelial dysfunction in nonalcoholic steatohepatitis," *Journal of Clinical Investigation*, vol. 131, no. 6. American Society for Clinical Investigation, Mar. 15, 2021, doi: 10.1172/JCI147556.
[361] P. J. Kuhlencordt *et al.*, "Role of endothelial nitric oxide synthase in endothelial activation: insights from eNOS knockout endothelial cells," *Am. J. Physiol. Physiol.*, vol. 286, no. 5, pp. C1195–C1202, May 2004, doi: 10.1152/ajpcell.00546.2002.
[362] R. Zamel, R. Khan, R. L. Pollex, and R. A. Hegele, "Abetalipoproteinemia: Two case reports and literature review," *Orphanet J. Rare Dis.*, vol. 3, no. 1, p. 19, 2008, doi: 10.1186/1750-1172-3-19.
[363] O. Sakamoto *et al.*, "An atypical case of abetalipoproteinaemia with severe fatty liver in the absence of steatorrhoea or acanthocytosis," *Eur. J. Pediatr.*, vol. 165, pp. 68–70, 2006, doi: 10.1007/s00431-005-1751-7.
[364] P. G. Rodríguez Gutiérrez, J. R. González García, Y. A. Castillo De León, J. R. Zárate Guerrero, and M. T. Magaña Torres, "A novel p.Gly417Valfs*12 mutation in the MTTP gene causing abetalipoproteinemia: Presentation of the first patient in Mexico and analysis of the previously reported cases," *J. Clin. Lab. Anal.*, vol. 35, no. 3, Mar. 2021, doi: 10.1002/jcla.23672.

[365] J. Read *et al.*, "A mechanism of membrane neutral lipid acquisition by the microsomal triglyceride transfer protein," *J. Biol. Chem.*, vol. 275, no. 39, pp. 30372–30377, Sep. 2000, doi: 10.1074/jbc.C000364200.
[366] I. Khatun, M. T. Walsh, and M. M. Hussain, "Loss of both phospholipid and triglyceride transfer activities of microsomal triglyceride transfer protein in abetalipoproteinemia," *J. Lipid Res.*, vol. 54, no. 6, pp. 1541–1549, Jun. 2013, doi: 10.1194/jlr.M031658.
[367] C. Shen, W. Ma, L. Ding, S. Li, X. Dou, and Z. Song, "The TLR4-IRE1α pathway activation contributes to palmitate-elicited lipotoxicity in hepatocytes," *J. Cell. Mol. Med.*, pp. 1–10, 2018, doi: 10.1111/jcmm.13636.
[368] T. Ramprasath, V. Vasudevan, S. Sasikumar, S. Puhari, L. Saso, and G. Selvam, "Regression of Oxidative Stress by Targeting eNOS and Nrf2/ARE Signaling: A Guided Drug Target for Cardiovascular Diseases," *Curr. Top. Med. Chem.*, vol. 15, no. 9, pp. 857–871, Feb. 2015, doi: 10.2174/1568026615666150220114417.
[369] M. Qader, J. Xu, Y. Yang, Y. Liu, and S. Cao, "Natural nrf2 activators from juices, wines, coffee, and cocoa," *Beverages*, vol. 6, no. 4, pp. 1–24, 2020, doi: 10.3390/beverages6040068.
[370] J. G. W. Smith *et al.*, "Isogenic Pairs of hiPSC-CMs with Hypertrophic Cardiomyopathy/LVNC-Associated ACTC1 E99K Mutation Unveil Differential Functional Deficits," *Stem Cell Reports*, vol. 11, no. 5, pp. 1226–1243, Nov. 2018, doi: 10.1016/j.stemcr.2018.10.006.
[371] D. H. Lackner *et al.*, "A generic strategy for CRISPR-Cas9-mediated gene tagging," *Nat. Commun.*, vol. 6, Dec. 2015, doi: 10.1038/ncomms10237.
[372] U. Ray and S. C. Raghavan, "Modulation of DNA double-strand break repair as a strategy to improve precise genome editing," *Oncogene*, vol. 39, no. 41. Springer Nature, pp. 6393–6405, Oct. 08, 2020, doi: 10.1038/s41388-020-01445-2.
[373] H. Wang *et al.*, "One-step generation of mice carrying mutations in multiple genes by CRISPR/cas-mediated genome engineering," *Cell*, vol. 153, no. 4, pp. 910–918, May 2013, doi: 10.1016/j.cell.2013.04.025.
[374] B. Wang *et al.*, "Highly efficient CRISPR/HDR-mediated knock-in for mouse embryonic stem cells and zygotes," *Biotechniques*, vol. 59, no. 4, pp. 201–208, Oct. 2015, doi: 10.2144/000114339.
[375] E. M. Porto, A. C. Komor, I. M. Slaymaker, and G. W. Yeo, "Base editing: advances and therapeutic opportunities," *Nature Reviews Drug Discovery*, vol. 19, no. 12. Nature Research, pp. 839–859, Dec. 01, 2020, doi: 10.1038/s41573-020-0084-6.
[376] A. C. Komor, Y. B. Kim, M. S. Packer, J. A. Zuris, and D. R. Liu, "Programmable editing of a target base in genomic DNA without double-stranded DNA cleavage," *Nature*, vol. 533, no. 7603, pp. 420–424, Apr. 2016, doi: 10.1038/nature17946.
[377] N. M. Gaudelli *et al.*, "Programmable base editing of T to G C in genomic DNA without DNA cleavage," *Nature*, vol. 551, no. 7681, pp. 464–471, Nov. 2017, doi: 10.1038/nature24644.
[378] D. Garnier *et al.*, "Expansion of human primary hepatocytes in vitro through their amplification as liver progenitors in a 3D organoid system," *Sci. Rep.*, vol.

8, no. 1, p. 8222, Dec. 2018, doi: 10.1038/s41598-018-26584-1.
[379] P. Sun, G. Zhang, X. Su, M. Zhang, W. Wei, and W. L. Correspondence, "Maintenance of Primary Hepatocyte Functions In Vitro by Inhibiting Mechanical Tension-Induced YAP Activation In Brief," *Cell Rep.*, vol. 29, pp. 3212–3222, 2019, doi: 10.1016/j.celrep.2019.10.128.
[380] M. Kajiwara *et al.*, "Donor-dependent variations in hepatic differentiation from human-induced pluripotent stem cells," *Proc. Natl. Acad. Sci.*, vol. 109, no. 31, pp. 12538–12543, 2012, doi: 10.1073/pnas.1209979109.
[381] L. K. Kanninen *et al.*, "Laminin-511 and laminin-521-based matrices for efficient hepatic specification of human pluripotent stem cells," *Biomaterials*, vol. 103, pp. 86–100, Oct. 2016, doi: 10.1016/j.biomaterials.2016.06.054.
[382] M. Krüger *et al.*, "Cellulose Nanofibril Hydrogel Promotes Hepatic Differentiation of Human Liver Organoids," *Adv. Healthc. Mater.*, vol. 9, no. 6, p. 1901658, Mar. 2020, doi: 10.1002/adhm.201901658.
[383] S. Ye *et al.*, "A Chemically Defined Hydrogel for Human Liver Organoid Culture," *Adv. Funct. Mater.*, vol. 30, no. 48, p. 2000893, Nov. 2020, doi: 10.1002/adfm.202000893.
[384] L. Tian, N. Prasad, and Y. Y. Jang, "In Vitro Modeling of Alcohol-Induced Liver Injury using Human-Induced Pluripotent Stem Cells," in *Methods in Molecular Biology*, vol. 1353, Humana Press Inc., 2016, pp. 271–283.
[385] A. Carpentier, J. Sheldon, F. W. R. Vondran, R. J. P. Brown, and T. Pietschmann, "Efficient acute and chronic infection of stem cell-derived hepatocytes by hepatitis C virus," *Gut*, vol. 69, no. 9, pp. 1659–1666, Sep. 2020, doi: 10.1136/gutjnl-2019-319354.
[386] A. Schöbel, K. Rösch, and E. Herker, "Functional innate immunity restricts Hepatitis C Virus infection in induced pluripotent stem cell-derived hepatocytes," *Sci. Rep.*, vol. 8, no. 1, p. 3893, Dec. 2018, doi: 10.1038/s41598-018-22243-7.
[387] T. Marjot *et al.*, "COVID-19 and liver disease: mechanistic and clinical perspectives," *Nature Reviews Gastroenterology and Hepatology*. Nature Research, pp. 1–17, Mar. 10, 2021, doi: 10.1038/s41575-021-00426-4.

Appendix I – Publications

Articles

Lara C. Lewis, **Peggy Cho Kiu Lo**, Jeremy M. Foster, Nan Dai, Ivan R. Corrêa, Paulina M. Durczak, Gary Duncan, Ashley Ramsawhook, Guruprasad Padur Aithal, Chris Denning, Nicholas R. F. Hannan, Alexey Ruzov, "Dynamics of 5-carboxylcytosine during hepatic differentiation: Potential general role for active demethylation by DNA repair in lineage specification." *Epigenetics*, vol. 12, no. 4, pp. 277–286, 2017, DOI: 10.1080/15592294.2017.1292189.

Jane I. Grove, **Peggy Cho Kiu Lo**, Nick Shrine, Julian Barwell, Louise V. Wain, Martin D. Tobin, Andrew M. Salter, Neil Bennett, Catherine John, Ioanna Ntalla, Gabriela E. Jones, Christopher P. Neal, Mervyn G. Thomas, Helen Kuht, Pankaj Gupta, Vishwaraj M. Vemala, Allister Grant, Adeolu B. Adewoye, Kotacherry T. Shenoy, Leena K., Balakumaran, Edward J. Hollox, Nicholas R.F. Hannan, Guruprasad P. Aithal, "Identification and functional characterisation of a rare *MTTP* variant underlying hereditary non-alcoholic fatty liver disease."
(Manuscript submitted to *Nature Genetics*, under review)

Conference abstract

Peggy Cho Kiu Lo, Jane I. Grove, Guruprasad P. Aithal, Nicholas R. Hannan "Modelling Non-Alcoholic Fatty Liver Disease (NAFLD) using Human Induced Pluripotent Stem Cells (hiPSCs)." *ISSCR 2019 Annual Meeting Poster Abstract book* , F-3164, 2019.

Appendix II – Other scientific contributions

Grants and Awards

- National Institute for Health Research (NIHR) award (2016-2019).
- The University of Nottingham Graduate School Travel Prize 2019 – funded with maximum amount £600.
- European Cooperation in Science and Technology (COST) action 2nd Training course – funded €860 in 2019.

Conference attendance, Presentations and Outreach

- Oral presentation at the 11th International Meeting of the Portuguese Society for Stem Cells and Cell Therapies (October 2019)
- Poster presentation at the ISSCR Annual Meeting (June 2019)
- Oral presentation at the Sue Watson Postgraduate Presentation Prize (March 2019)
- Poster presentation at the Annual CBS Symposium (January 2019)
- Poster presentation at the Mercia Stem Cell Alliance (MSCA) Annual Scientific Meeting (December 2018)
- Oral presentation at the Cancer and Stem Cells Departmental seminar (April 2018)
- Oral presentation at the NDDC lunchtime seminar (March 2018)
- Poster presentation at the Medicine & Health Sciences Faculty Postgraduate Research Forum (June 2017)
- Mercia Stem Cell Alliance (MSCA) Annual Scientific Meeting (December 2016)